Title
Measurement of the High-Energy Neutron Flux Above and Below Ground

Author
Roecker, Caleb Daniel

Publication Date
2016

Peer reviewed|Thesis/dissertation

Measurement of the High-Energy Neutron Flux Above and Below Ground

by

Caleb Daniel Roecker

A dissertation submitted in partial satisfaction of the

requirements for the degree of

Doctor of Philosophy

in

Engineering – Nuclear Engineering

in the

Graduate Division

of the

University of California, Berkeley

Committee in charge:

Professor Kai Vetter, Chair
Professor Rick Norman
Assistant Professor Gabriel Orebi Gann
Doctor Peter Marleau

Summer 2016

Measurement of the High-Energy Neutron Flux Above and Below Ground

Abstract

Measurement of the High-Energy Neutron Flux Above and Below Ground

by

Caleb Daniel Roecker

Doctor of Philosophy in Engineering – Nuclear Engineering

University of California, Berkeley

Professor Kai Vetter, Chair

High-energy neutrons produce secondary particles through spallation, which create a ubiquitous and prominent background in a wide range of rare-event particle and nuclear physics experiments. Above ground, the high-energy neutron energy-dependent flux has been measured, but with significantly varying results. Below ground, only two previous measurements have succeeded in observing these neutrons, and communicated their results in a fashion useful to others. In a separate effort, a model of the neutron energy-dependent flux was previously developed for measurements below 1000 m.w.e. No comparisons to this model and the measured neutron flux have been performed.

In an effort to provide new and independent measurements above and below ground, the Multiplicity and Recoil Spectrometer (MARS) was designed, constructed, and deployed to the Kimballton Underground Research Facility (KURF). MARS is a transportable $\sim$1 m^3 detector composed of plastic scintillator Gd based neutron detectors, and a lead spallation target. MARS uses neutron spallation in the lead to transform an incident high-energy neutron into many lower energy secondary neutrons. By recording the secondary neutron multiplicity over many incident neutron events, the incident neutron energy spectrum can be inferred. This multiplicity method employed by MARS represents a new approach in high-energy neutron spectroscopy, which requires a new algorithm to correct the observed signal into a neutron spectrum. A recently developed Markov Chain Monte Carlo (MCMC) inversion algorithm, with a calibrated Monte Carlo model of MARS, is used to perform this inversion.

Using this new multiplicity method, MARS performed measurements at the surface of Earth and at depths of 377 meters water equivalent (m.w.e.), 540 m.w.e., and 1450 m.w.e. Due to the transportable nature of MARS, minimal detector related systematic bias exists between these measurements. The minimal bias between these measurements at multiple depths will allow for the creation of a depth-dependent predictive model of the high-energy neutron energy-dependent flux.

This dissertation introduces the new multiplicity measurement approach, the MCMC inversion algorithm, the Monte Carlo model and associated calibrations, and presents results

from the four measurements. Above ground, the MARS measurement results agree with most of the previous measurements in the energy range between 90 MeV and 250 MeV. Above 250 MeV the MARS results report slightly lower flux than most of the previous measurements, but are still within the spread of all previous measurements. Below ground, no direct comparison can be made to the MARS results at 377 m.w.e. The MARS result at 540 m.w.e. appears to be in rough agreement with one of the previous below ground measurements, at the one measured energy where the results overlap. At 1450 m.w.e., the MARS results shows reasonable agreement with previous simulation predictions.

The rough agreement of the MARS results, at all relevant locations, with previous measurements and existing simulation where applicable, provide confidence that all MARS measurements have produced the correct high-energy neutron energy-dependent flux. Above ground, the new independent results strengthen the results of previous measurements. Below ground, the three measurements provide consistent results with minimal detector related bias between measurements due to the transportable nature of MARS, that will be used to produce a depth-dependent model of the high-energy neutron energy-dependent flux. For the rare-event particle and nuclear physics experiments affected by high-energy neutron backgrounds, this model will allow for the prediction of the high-energy neutron background at different measurement locations, a more robust instrumental design, and the ability to estimate the high-energy neutron background contribution in their final measured data; the confidence in the results of these experiments will be improved.

To My Parents

Contents

Contents **ii**

List of Figures **iv**

List of Tables **xii**

1 Motivation **1**

2 Introduction to High-Energy Neutrons **4**
2.1 Sources of High-Energy Neutrons 4
2.2 High-Energy Neutrons as a Background 7
2.3 Traditional Methods for High-Energy Neutron Detection 9

3 Measurement Concept **13**
3.1 The Multiplicity Method 14
3.2 The Inverse Problem 17
3.3 Identifying Multiplicity Events 22
3.4 The General MCMC Algorithm 27
3.5 The Specific MCMC Algorithm 29

4 The Multiplicity and Recoil Spectrometer **33**
4.1 Detector Design 34
4.2 Electronics and Read-Out 35
4.3 Experimental Data Adjustments 36
4.4 Energy Calibration of the Experiment 41
4.5 Neutron Capture-Efficiency and Capture-Time Calibrations 44
4.6 Charged Particle Veto 46

5 The MARS Monte Carlo Model and Simulation **49**
5.1 The Geometric Model 49
5.2 The Physics Models 51
5.3 Simulating the MARS DAQ 54
5.4 Effective Area Predictions 55

5.5 MCMC Reconstruction of Simulated Spectra 59

6 Measurement of the High-Energy Neutron Energy-Dependent Flux Above Ground 62
6.1 Previous Measurements 63
6.2 Measurement Campaign 64
6.3 The Measured Data and MCMC Preliminary Results 65
6.4 Final Results and Discussion 73

7 Measurement of the High-Energy Neutron Energy Dependent Flux Below Ground 75
7.1 Previous Measurements 75
7.2 Measurement Campaign 77
7.3 Results 79
7.4 Summary and Comparison to Previous Work 96
7.5 MARS Results Implications 97

8 Summary 100

9 Future Work 103
9.1 Continuation of Measurements 103
9.2 Improvements in Modeling and System Response 103

A MARS Results Data 106

B Modeling of the Gamma-Ray and Cosmogenic Charged Particle Noise 130

C Determination of Depth Below Ground 133

D PMT Gain Drift 136

E PMT Non-Linearity 143

F Position-Dependent Energy Calibration 147
F.1 Top Neutron Detector 148
F.2 Veto Detectors 151

G Convergence Criteria Above Ground 153

H Convergence Criteria Below Ground 158

Bibliography 165

List of Figures

2.1 The measured and inferred solar cycles based upon the number of sunspots from 1750 to 2016. This figure was taken from D. Hathaway's NASA web article "The Sunspot Cycle" [26]. 5
2.2 The three components of an example cosmic ray shower taken from Fig. 1b of [27]. Above ground, MARS measures the high-energy neutron component from the hadronic showers. Below ground, MARS measures the high-energy neutron component created by mesonic shower particle interactions in rock. 6
2.3 An example set of three Bonner spheres and associated preamplifiers taken from Fig. 1 of [39]. 10
2.4 An example of a capture-gated neutron detector taken from Fig. 2 of [43]. The grey rectangular prism is a light-guide and the signal readout, the blue rectangular prism is the active detector scintillator, and the red tubes are the He-3 neutron capture component. 12

3.1 Depicts a high-energy neutron initiating a spallation reaction in the lead and generating secondary neutrons. These secondary neutrons down-scatter in the scintillator and are captured on a Gd nucleus in the paint. The Gd de-excitation produces 1-5 gamma rays which further interact in the scintillator. 15
3.2 The simulated energy of the secondary neutrons exiting the lead spallation target. Incident high-energy neutrons were simulated with a uniform energy distribution between 20 MeV and 1000 MeV. 15
3.3 Depicts the timing characteristics of a high-energy neutron multiplicity event. The two part time-dependent signature of the multiplicity signal is observed: the prompt component is the large energy deposition at time 0, the delayed component is the subsequent neutron captures after the prompt component. . . 16
3.4 An illustration of the timing characteristics of a high-energy neutron multiplicity event. The two part time-dependent signature of the multiplicity signal is observed. The three measured parameters: multiplicity, capture energy, and thermalization energy, of the two part signature are denoted. 21

3.5 (a) The FOM_{Trig} described in Eq. 3.9 for a variety of triggering algorithms described in Sec. 3.3. (b) The expected background multiplicity rate due to the uncorrelated gamma-ray flux. Fixed length time ranges of 25, 65, and 125 μs are shown. Expanding time ranges are denoted with the initial range before and the secondary range after a + symbol. 24
3.6 The time between depositions in $\geq$3 multiplicity events and the previous veto deposition. The signal is composed of two exponential distributions. The exponential with the faster time constant is due to charged particle induced neutron captures in the detector. The long time constant exponential is due to the ambient gamma ray flux. 26
3.7 The ratio of the capture energy to the multiplicity. This is the average energy deposited by Gd de-excitations on a per event basis. The above ground data is assumed to be predominately from neutrons. The tail below 2.2 MeV/# for the 377 m.w.e. data is assumed to be from the ambient gamma ray noise. 26

4.1 An exploded view illustration of the detectors, frame, and lead. 33
4.2 A view of the MARS deployment platform below ground. 34
4.3 A view from one end of the assembled MARS veto. 35
4.4 (a) The total neutron detector energy spectrum is shown. The edge at 1,000 PE is due to Gd de-excitations and the peak at 10,000 PE is due to through going muons. (b) A representative gain correction plot for a PMT in the neutron detector is shown. The blue data with no marker is the pre-corrected data, the red data with a triangular marker is the template data, and the black data with the square marker is the corrected data. (c) Displays the gain correction factor G as a function of time in weeks for the same PMT (b). The gain degradation is assumed to be due to mechanical decoupling. 38
4.5 Gain drift average for all PMTs as a function of time. 39
4.6 The apparatus for measuring the PMT linearity is shown above. The LEDs are closely spaced together and the PMTs are firmly held. A light-tight black cover was placed around the setup. 40
4.7 The measured PMT non-linear response as a function of light. The black line shows a perfectly linear response. The red triangular data points correspond to the PMT measured non-linearity. Errors for the red triangular data are too small to be observed over the marker. 41
4.8 The experimental and simulated Cs-137 and Co-60 spectra in the center of the detector with the collimator are shown from left to right respectively. The experimental data is red with a triangle marker and the simulation data is a black solid line. 43
4.9 Capture time distribution for the experimental data and simulation from tagged multiplicity events from a Cf-252 neutron multiplicity source. Some disagreement exists at short capture times but the exponential shape matches reasonably well. 46
4.10 The recorded veto energy spectrum at the 377 m.w.e. depth 47

5.1 A computer rendering of the full geometry Monte Carlo Model. Axes are labeled and the scale is included. 50
5.2 A computer rendering of the partial geometry Monte Carlo Model. Axes are labeled and the scale is included. The steel table and lead are included in the model; the rendering struggled to effectively display these components. 51
5.3 A comparison of the total kinetic energy of all particles produced in a Gd de-excitation between the evaporation and default final state model. The Evaporation model correctly predicts the Q-values of the reactions. 52
5.4 A comparison of the gamma ray multiplicity produced in a Gd de-excitation between the evaporation and default final state model. 53
5.5 A comparison of the high energy neutron response on NE213 using MENATE_R and the default Geant4 shielding physics list. (a) Depicts a simulation with incident neutrons of energy between 29 and 30 MeV. (b) Depicts a simulation with incident neutrons of energy between 74 and 78 MeV. (c) Depicts a simulation with incident neutrons of energy between 131 and 133 MeV. (d) Depicts a simulation with incident neutrons of energy between 206 and 208 MeV. Experimental comparisons can be found in Nakao *et al.* [74]. 54
5.6 (a) Depicts the multiplicity response as a function of the incident neutron energy. (b) Depicts the capture energy response as a function of the incident neutron energy. (c) Depicts the thermalization energy response as a function of the incident neutron energy. All three components are binned in the same manner used in the MCMC reconstruction algorithm. Each column of the respective histogram is a probability distribution of the events at that respective energy. 57
5.7 The histogram representation of the MARS detector response matrix $\mathbf{A}$. Note the matrix looks like the superposition of several upper triangular matrices. The matrix in this representation is not quasi-diagonal. 58
5.8 The predicted effective area for incident high-energy neutrons with angular distributions of isotropic, $\cos^2(\theta)$, $\cos^3(\theta)$, and $\cos^4(\theta)$. 58
5.9 (a) Depicts the simulated 3 component response ($\vec{g}$) from 100 MeV neutrons incident on MARS. (b) Depicts the simulated 3 component response ($\vec{g}$) from 700 MeV neutrons incident on MARS. Higher values of the simulated $\vec{g}$ are populated as the incident neutron energy increases. 60
5.10 The reconstructed counts/ΔE of the 5 mono-energetic neutron simulations. The input spectra in the basis spline space is displayed as a blue line. Reconstructed spectra are displayed in a dash black line. Confidence intervals around the reconstructed spectra are displayed as a patterned red area. 61

6.1 A Google maps quasi 3-D representation of the above ground KURF measurement location. The measurement location is near the center of the figure. The mine entrance is near the top right of the figure. Significant elevation increases are observed at the bottom right and top left of the figure. 65

6.2 The measured neutron data and the predicted gamma ray contaminated events from the measurement above ground at KURF. (a) Depicts the measured multiplicity and the predicted contaminated multiplicity data. (b) Depicts the measured capture energy and the predicted contaminated capture energy data. (c) Depicts the measured thermalization energy and the predicted contaminated thermalization energy data. The three components of each x-axis represents the measured binning for the respective component. A similar percent of contaminated events is observed across the range of measured data consistent with a small constant probability for contamination. 67
6.3 The measured three component data vector $\vec{g}_{meas}$ and the predicted background $\vec{b}$. It appears the predicted background is a nearly constant percentage of the measured vector bin value. 68
6.4 The regularization parameter α iteration update values from step 2c of the MCMC algorithm from Sec. 3.5. 68
6.5 The percent difference between the final bias reduced answer $\vec{f}^{5}_{BC}$ and the previous iterations $\vec{f}^{n}_{BC}$ where n varies from 0 to 4. A minimal amount of bias was removed from the solution. This is probably due to conservative knot spacing of the final answer. 69
6.6 (a) Depicts the autocorrelation of $\vec{f}_0$ as a function of the post burn-in iteration. (b) Depicts the running average of $\vec{f}_0$ as a function of the post burn-in iteration. (c) Depicts the value of $\vec{f}_0$ as a function of the post burn-in iteration. (d) Depicts the histogram of $\vec{f}_0$ values. As described in the text the sub-figures are representative of all parameters and indicate sufficient convergence. 70
6.7 The percent difference in the reconstructed neutron flux versus energy, between the preferred ($\cos^3(\theta)$) and alternative choices of the neutron angular distribution. The partial geometry model was used for this comparison. 71
6.8 The percent difference in the reconstructed neutron flux versus energy, between the partial and full geometry models given an incident angular distribution of $\cos^3(\theta)$. 72
6.9 The percent difference in the reconstructed neutron flux versus energy, between the default initial time range structure of 25 μs and initial time ranges of 22 μs and 28 μs given an incident angular distribution of $\cos^3(\theta)$. 73
6.10 The above ground reconstructed neutron energy-dependent flux at KURF compared to previous experiments. The previous experimental data correspond to the following shapes: Ashton *et al.* ■[78], Gordon *et al.* +[39], Heidbreder *et al.* ▲[80], Hess *et al.* ●[10, 41], Preszler *et al.* ○[81], and R. Saxena □[83]. The results from Ashton [78] were scaled by Ziegler [12] due to the unknown incident angular distribution. 74

7.1 A picture of the cavern before construction of the KURF scientific facility. . . . 78

7.2 A picture of the inside of the KURF scientific facility. The MARS deployment platform was parked at location B. 79
7.3 The measured neutron data and the simulation predicted gamma-ray and muon background from the measurement at 377 m.w.e. depth at KURF. (a) Depicts the measured multiplicity and the predicted contaminated multiplicity data. (b) Depicts the measured capture energy and the predicted contaminated capture energy data. (c) Depicts the measured thermalization energy and the predicted contaminated thermalization energy data. The three components of each x-axis represents the measured binning for the respective component. A similar percent of contaminated events is observed across the range of measured data consistent with a small constant probability for contamination. 81
7.4 For the 377 m.w.e. depth: Redo (a)(a) depicts the regularization parameter α iteration update values from step 2c of the MCMC algorithm from Sec. 3.5. (b) Depicts the percent difference between the final bias reduced answer $\vec{f}_{BC}^{5}$ and the previous iterations $\vec{f}_{BC}^{n}$ where n varies from 0 to 4. 82
7.5 For the 377 m.w.e. depth: (a) depicts the autocorrelation of $\vec{f}_0$ as a function of the post burn-in iteration. (b) Depicts the running average of $\vec{f}_0$ as a function of the post burn-in iteration. (c) Depicts the value of $\vec{f}_0$ as a function of the post burn-in iteration. (d) Depicts the histogram of $\vec{f}_0$ values. As described in the text the sub-figures are representative of all parameters and indicate sufficient convergence. 83
7.6 For the 377 m.w.e. depth: (a) Depicts the percent difference in the reconstructed neutron flux versus energy, between the preferred ($\cos^2(\theta)$) and alternative choices of the neutron angular distribution. The partial geometry model was used for this comparison. (b) Depicts the reconstructed neutron energy-dependent flux for the partial and full geometry models given an incident angular distribution of $\cos^2(\theta)$. (c) Depicts the reconstructed neutron energy-dependent flux with variation in the initial gate triggering time given an incident angular distribution of $\cos^2(\theta)$. . . 84
7.7 The reconstructed high-energy neutron energy-dependent flux with total uncertainty at 377 m.w.e. 85
7.8 The measured neutron data and the simulation predicted gamma-ray and muon background from the measurement at 540 m.w.e. depth at KURF. (a) Depicts the measured multiplicity and the predicted contaminated multiplicity data. (b) Depicts the measured capture energy and the predicted contaminated capture energy data. (c) Depicts the measured thermalization energy and the predicted contaminated thermalization energy data. The three components of each x-axis represents the measured binning for the respective component. A similar percent of contaminated events is observed across the range of measured data consistent with a small constant probability for contamination. No muon predicted background events were observed. This is an artifact of the simulation time and small muon contamination probability. 86

7.9 For the 540 m.w.e. depth: (a) depicts the regularization parameter α iteration update values from step 2c of the MCMC algorithm from Sec. 3.5. (b) Depicts the percent difference between the final bias reduced answer $\vec{f}_{BC}^{5}$ and the previous iterations $\vec{f}_{BC}^{n}$ where n varies from 0 to 4. 87
7.10 For the 540 m.w.e. depth: (a) depicts the autocorrelation of $\vec{f}_0$ as a function of the post burn-in iteration. (b) Depicts the running average of $\vec{f}_0$ as a function of the post burn-in iteration. (c) Depicts the value of $\vec{f}_0$ as a function of the post burn-in iteration. (d) Depicts the histogram of $\vec{f}_0$ values. As described in the text the sub-figures are representative of all parameters and indicate sufficient convergence. 88
7.11 For the 540 m.w.e. depth: (a) Depicts the percent difference in the reconstructed neutron flux versus energy, between the preferred ($\cos^2(\theta)$) and alternative choices of the neutron angular distribution. The partial geometry model was used for this comparison. (b) Depicts the reconstructed neutron energy-dependent flux for the partial and full geometry models given an incident angular distribution of $\cos^2(\theta)$. (c) Depicts the reconstructed neutron energy-dependent flux with variation in the initial gate triggering time given an incident angular distribution of $\cos^2(\theta)$. . . 89
7.12 The reconstructed high-energy neutron energy-dependent flux with total uncertainty at 540 m.w.e. 90
7.13 The measured neutron data and the simulation predicted gamma-ray and muon background from the measurement at 1450 m.w.e. depth at KURF. (a) Depicts the measured multiplicity and the predicted contaminated multiplicity data. (b) Depicts the measured capture energy and the predicted contaminated capture energy data. (c) Depicts the measured thermalization energy and the predicted contaminated thermalization energy data. The three components of each x-axis represents the measured binning for the respective component. A similar percent of contaminated events was observed across the range of measured data consistent with a small constant probability for contamination. 91
7.14 For the 1450 m.w.e. depth: (a) depicts the regularization parameter α iteration update values from step 2c of the MCMC algorithm from Sec. 3.5. (b) Depicts the percent difference between the final bias reduced answer $\vec{f}_{BC}^{5}$ and the previous iterations $\vec{f}_{BC}^{n}$ where n varies from 0 to 4. 92
7.15 For the 1450 m.w.e. depth: (a) depicts the autocorrelation of $\vec{f}_0$ as a function of the post burn-in iteration. (b) Depicts the running average of $\vec{f}_0$ as a function of the post burn-in iteration. (c) Depicts the value of $\vec{f}_0$ as a function of the post burn-in iteration. (d) Depicts the histogram of $\vec{f}_0$ values. As described in the text the sub-figures are representative of all parameters and indicate sufficient convergence. 93

7.16 For the 1450 m.w.e. depth: (a) Depicts the percent difference in the reconstructed neutron flux versus energy, between the preferred ($\cos^2(\theta)$) and alternative choices of the neutron angular distribution. The partial geometry model was used for this comparison. (b) Depicts the reconstructed neutron energy-dependent flux for the partial and full geometry models given an incident angular distribution of $\cos^2(\theta)$. (c) Depicts the reconstructed neutron energy-dependent flux with variation in the initial gate triggering time given an incident angular distribution of $\cos^2(\theta)$. . . 94
7.17 The reconstructed high-energy neutron energy-dependent flux with total uncertainty at 1450 m.w.e. . . . 95
7.18 The reconstructed high-energy neutron energy-dependent flux at 377, 540, and 1450 m.w.e. at KURF compared to previous measurements [15, 14, 13] and simulation predictions [16]. . . . 97
7.19 (a) The energy integrated neutron flux and the muon flux versus the depth for the three MARS measurements. The neutron flux is represented by the square markers and the right y-axis. The muon flux is represented by the triangle markers and the left y-axis. The neutron energy integration was performed over the energy range of 90 MeV to 300 MeV. (b) The ratio of the integrated neutron flux and the muon flux versus the measurement depth. . . . 98

8.1 The MARS reconstructed high-energy neutron energy-dependent flux above ground and at depths of 377 m.w.e, 540 m.w.e, and 1450 m.w.e. at KURF. The previous experimental data above ground correspond to the following shapes: Ashton *et al.* ■[78], Gordon *et al.* +[39], Heidbreder *et al.* ▲[80], Hess *et al.* ●[10, 41], Preszler *et al.* ○[81], and R. Saxena □[83]. The previous experimental data below ground correspond to the following shapes: Garrison ◆[13] and Malgin ▼[15, 14]. The previous simulation predictions are by Mei and Hime [16] and correspond to the cyan curve and systematic uncertainty. . . . 102

B.1 The energy distribution in PE of ambient gamma rays at the 377 m.w.e. depth. 131

C.1 A depiction of the measured 377 m.w.e. overburden profile. MARS is located at the (0,0,0) position directly below ∼150 m of rock. All dimensions are in meters, not m.w.e. . . . 134
C.2 A depiction of the measured 540 m.w.e. overburden profile. MARS is located at the (0,0,0) position directly above ∼250 m of rock. All dimensions are in meters, not m.w.e. . . . 135

D.1 The measured gain drift of neutron detector PMTs. . . . 137
D.2 The measured gain drift of neutron detector PMTs. . . . 138
D.3 The measured gain drift of neutron detector PMTs. . . . 139
D.4 The measured gain drift of neutron detector PMTs. . . . 140
D.5 The measured gain drift of veto PMTs 141
D.6 The measured gain drift of veto PMTs 142

E.1 The measured saturation of PMTs 144
E.2 The measured saturation of PMTs 145
E.3 The measured saturation of PMTs 146

F.1 A labeled view from one end of the assembled MARS veto. 147
F.2 The position-dependent energy calibration of the top neutron detector. 148
F.3 The position-dependent energy calibration of the top neutron detector. 149
F.4 The position-dependent energy calibration of the top neutron detector. 150
F.5 The position-dependent energy calibration of veto detectors. 151
F.6 The position-dependent energy calibration of veto detectors. 152

G.1 The autocorrelation of each basis spline coefficient of the above ground measurement. 154
G.2 The running mean of each basis spline coefficient of the above ground measurement. 155
G.3 The value of each basis spline coefficient as a function of the MCMC iteration post burn-in of the above ground measurement. 156
G.4 The distribution of each basis spline coefficient of the above ground measurement. 157

H.1 The autocorrelation of each basis spline coefficient at the 377 m.w.e. depth. . . 158
H.2 The running mean of each basis spline coefficient at the 377 m.w.e. depth. . . . 159
H.3 The value of each basis spline coefficient as a function of the MCMC iteration post burn-in at the 377 m.w.e. depth. 159
H.4 The distribution of each basis spline coefficient at the 377 m.w.e. depth. 160
H.5 The autocorrelation of each basis spline coefficient at the 540 m.w.e. depth. . . 160
H.6 The running mean of each basis spline coefficient at the 540 m.w.e. depth. . . . 161
H.7 The value of each basis spline coefficient as a function of the MCMC iteration post burn-in at the 540 m.w.e. depth. 161
H.8 The distribution of each basis spline coefficient at the 540 m.w.e. depth. 162
H.9 The autocorrelation of each basis spline coefficient at the 1450 m.w.e. depth. . . 162
H.10 The running mean of each basis spline coefficient at the 1450 m.w.e. depth. . . . 163
H.11 The value of each basis spline coefficient as a function of the MCMC iteration post burn-in at the 1450 m.w.e. depth. 163
H.12 The distribution of each basis spline coefficient at the 1450 m.w.e. depth. 164

List of Tables

3.1 The FOM_{SVD} for permutations of the three measured observables. The optimal FOM_{SVD} was found when using all three measured observables. 22

4.1 Various multiplicity ratios were used to calculate the total neutron detection efficiency measured with a Cf-252 source. 45

5.1 The integral number of neutrons simulated for the 5 mono-energetic neutron energies. The truth, bias corrected reconstruction, and the integral of the $\pm 1\sigma$ confidence interval functions are displayed. 61

A.1 The high-energy neutron energy-dependent flux results from the four MARS measurements at KURF. All results are quoted in units of [#/cm^2/sec/MeV]. 106

A.2 The high-energy neutron energy-dependent flux positive uncertainty σ_+ results from the four MARS measurements at KURF. All results are quoted in units of [#/cm^2/sec/MeV]. 114

A.3 The high-energy neutron energy-dependent flux negative uncertainty σ_- results from the four MARS measurements at KURF. All results are quoted in units of [#/cm^2/sec/MeV]. 121

Acknowledgments

The work presented here would have been significantly more challenging, if not impossible, without the contributions of several individuals.

Kai Vetter, thank you for being the advisor that I needed: you gave me enough space to think and explore topics related to this work, but did not let me stray too far or waste too much time. Your guidance and persistent advice to think about the big picture was invaluable. Additionally, thank you for sending me to quite a few conferences to present posters and talks. The introduction and interaction you facilitated, with the field of radiation detection, will serve to further my ability to contribute to this community in the future.

Rick Norman, thank you for chairing my qualifying exam and reviewing my dissertation. Additionally, thank you for asking me questions that pointed me towards reading the PDG report on cosmic rays. I feel that these questions greatly improved the content of this work.

Peter Marleau, thank you for sitting on my qualifying exam, reviewing my dissertation, reviewing journal papers, and questioning the analysis decisions I made. Additionally, thank you for taking the time to meet with me on multiple Fridays, when you were supposed to have the day off.

Nathaniel Bowden, thank you for your advice over years and several projects. Your contributions to any detector operational knowledge or data analysis skills I posses can not be overstated.

Adam Bernstein, thank you for your advice, review of journal papers, and persistent questioning about the results presented here. Also, thank you for connecting me with the Union of Concerned Scientist Summer Symposium; it was a truly valuable experience to interact with individuals who have been at the forefront of citizen based advocacy of nuclear nonproliferation.

Melinda Sweany, thank you for introducing me to a significant portion of the work that went into the literature review, field specific knowledge, and early work you performed for this project. Without the work performed in your thesis and your advice, the work presented here would have taken significantly longer.

Mark Gerling, thank you for your early data analysis on the project, help with calibrating the detector, and help with setting up and moving the detector below ground.

Jim Brennan, John Steele, and Kevin Hulin, thank you for your work in making MARS a working detector. Without your efforts the project would have been significantly delayed.

Don Gunter, thank you for taking the time to teach me about inverse problems. Your advice and insight significantly improved the results presented here.

Melissa Connelly, thank you for moving to California with me. The support you offered made incredibly stressful times much more bearable. Thank you for exploring new places and pastimes with me. I'm excited for our future.

Dan and Sandy Roecker, thank you for instilling in me a love of learning and a desire to succeed from a very early age. You laid the initial groundwork that made all of this possible.

Chapter 1

Motivation

Everything on Earth is exposed to a wide range of ionizing radiation. From the natural decay of nuclei, to extragalactic charged particles bombarding the atmosphere creating showers of highly energetic particles, to man-made sources of radiation: this radiation field is inescapable. The scientific community has spent many years designing and deploying radiation detectors to measure natural and man-made radiation sources. Man-made source measurements benefit from the ability to turn off the source (e.g. radiation produced in a nuclear reactor). The natural radioactive background, due to its persistent nature, can be more challenging to quantify.

Due to electromagnetic interactions of charged particles, early efforts in quantifying the natural radioactive background focused on measuring the charged particle flux in the atmosphere [1, 2, 3, 4, 5], on the surface of Earth [6], and below the surface of Earth [7, 8]. The measurement of electrically neutral particles is significantly more challenging. Neutral particles, for example: neutrons, neutrinos/antineutrinos, etc., typically require the particle to interact with a detector to produce charged particles. These charged particles are then used to infer the presence and reaction of neutral particles. More recent efforts have measured the naturally occurring low-energy neutron flux and gamma-ray flux[1]. Measurements have even characterized these fluxes in a location dependent manner [9].

Due to the low interaction probability of high-energy neutrons, measurements of the high-energy neutron flux are sparse. A series of measurements of the high-energy neutron flux were performed by many different experimenters, primarily during the 1950's to 1960's. Measurements have been made quantifying the high-energy neutron flux at the altitude frequented by commercial aircraft [10, 11]. At Earth's surface, several high-energy neutron flux measurements were performed by various groups and later summarized by Ziegler [12]; significant disagreement exists between these measurements particular between 100 MeV and 300 MeV. Below ground, high-energy neutron flux measurements are sparse and have only been successfully performed at shallow depth [13, 14, 15]. Depth is conventionally described in terms of a location's equivalent flat overburden depth in water: meters water

[1]Low energy versus high energy is ambiguous and largely based upon the scientific community being addressed. Here high energy implies energies above 20 MeV and low energy implies energies below 20 MeV.

equivalent (m.w.e.). The conversion factor is typically 2.65: the density of standard rock in g/cm^3 [2]. At deep depths, no measurements exist of the high-energy energy-dependent neutron flux. In the absence of measurements, Monte Carlo simulation has been used to predict the high-energy neutron flux using derived parameters from several experiments [16]. These experiments measured the muon-induced neutrons produced in liquid scintillator, not the neutron flux from the cavern walls; a fact often misinterpreted by some in the rare-event physics community [17].

The largely unknown and poorly measured high-energy neutron flux presents a potentially significant source of background to a wide variety of experiments above and below the surface of Earth. These high-energy neutrons induce lower-energy radiation: gamma rays and neutrons, by interacting with the experiment and surrounding environment. To further complicate matters the flux is dependent upon the location on Earth, the surrounding environment, and whether the experiment is above or below ground. The location dependence on Earth is a function of the geomagnetic rigidity [18]. The variation in the isotopes of the surrounding environment affects the energy and multiplicity of secondary neutrons and gamma rays. The variation due to being above or below Earth's surface is a function of high-energy neutron production mechanism. Cosmic rays strike the atmosphere and initiate showers of high-energy particles. Some of these particles decay into high-energy neutrons and reach the surface of Earth. These neutrons produced above ground are attenuated by the Earth; they do not significantly contribute to the neutron flux below ground. However, muons are also created through the decay of particles produced in cosmic ray interactions with the atmosphere. Muons are capable of penetrating below ground, and produce high-energy neutrons through muon spallation and muon capture on rock.

Above ground, the high-energy neutron induced secondary particles have the potential to affect neutron and gamma-ray measurements. Below ground, these secondary particles may affect rare-event physics searches: antineutrino nuclear reactor monitors [19], WIMP dark matter detectors [20], and neutrinoless double beta decay detectors [21]. In particular, antineutrino nuclear reactor monitoring experiments present an interesting scenario, where accurately predicting the expected high-energy neutron flux is critical to performing a measurement [19]. These experiments monitor the operation of the nuclear plant by detecting the antineutrino signal, an indicative product of the fission reaction occurring in nuclear reactors. The fission process used in nuclear reactors produces Plutonium; an essential component of a modern nuclear weapon. The ultimate concern is any undeclared activity by the nuclear reactor operator: operation of the reactor or removal of the fuel. In order to demonstrate the feasibility of using the antineutrino flux to determine compliance of the reactor operator, antineutrino nuclear reactor monitoring experiments have been built in relative proximity to the reactor being monitoring [22, 23, 24]. To stretch the distance at which such a measurement could be performed and increase the utility of a monitoring effort, an experiment must be buried to avoid cosmogenic charged particles. However, one unknown factor controlling

[2]Here, shallow depths denotes any depth less than 1000 m.w.e. Deep denotes any depth greater than 1000 m.w.e.

the depth the experiment must be buried is the high-energy neutron flux [19].

The following dissertation describes an effort to measure the high-energy neutron energy-dependent flux, above and below Earth's surface. The motivation for measuring these high-energy neutron fluxes is twofold: a broad scientific mission to understand the depth-dependent variation in the high-energy neutron flux and produce a depth-dependent model, and a specific applied mission to measure a significant source of background for below ground rare-event physics experiments. The remainder of this dissertation is as follows: in Chapter 2 sources of high-energy neutrons, the process by which high-energy neutrons induce background in rare-event experiments, and traditional high-energy neutron detection methods are presented. In Chapter 3 the new multiplicity measurement concept and the associated MCMC inversion algorithm used to measure and infer the high-energy neutron flux is presented. In Chapter 4 the measurement apparatus: the Multiplicity and Recoil Spectrometer (MARS) and calibrations of MARS are presented. In Chapter 5 the MARS Monte Carlo model is presented and simulated data is used to infer a simulated high-energy neutron energy-dependent flux. In Chapter 6 the result from the above ground measurement performed at Earth's surface above the Kimballton Underground Research Facility (KURF) is presented. In Chapter 7 results from three below ground measurements at KURF are presented. These measurements were made at depths of 377 m.w.e., 540 m.w.e., and 1450 m.w.e. spanning the transition from shallow to deep depths. Comparisons for both the above and below ground results are made to the previous sparse measurements. Finally in Chapter 8 the results and implications of this work are summarized.

Chapter 2

Introduction to High-Energy Neutrons

The following chapter briefly introduces the reader to high-energy neutrons. In Sec. 2.1 the process by which high-energy neutrons are created is presented. In Sec. 2.2 the process by which high-energy neutrons induce background in measurements is described. Experiments which are concerned with this high-energy neutron induced background are also discussed. Finally, in Sec. 2.3 traditional methods for detecting high-energy neutrons are presented. The short-comings of these methods are discussed, which motivates the new measurement method described in Chapter 3.

2.1 Sources of High-Energy Neutrons

As described in the Chapter 1, this work focuses on the naturally occurring not man-made, high-energy neutron flux. At all locations on Earth, the high-energy neutron flux is indirectly created by high-energy charged particles interacting in Earth's atmosphere. These high-energy cosmogenic charged particles are primarily due to extragalactic sources. The Sun is a second-order contribution to the high-energy charged particle flux. The flux of these charged particles is anti-correlated with solar activity; increased solar activity increases the magnetic field of the heliosphere deflecting or stopping some of the charged particle flux [18]. Solar activity has cycle with an 11-year period, typically characterized by the number of sun spots (Fig. 2.1) [25].

After propagation through the heliosphere, these high-energy charged particles interact in Earth's atmosphere generating electromagnetic, hadronic, and mesonic showers as shown in Fig. 2.2, which was taken from Fig. 1b of [27]. Penetration of the high-energy charged particles into Earth's atmosphere is a function of Earth's magnetic field. Thus, the rate of these showers are a function of time and of latitude and longitude. Components of these showers decay, others are partially attenuated by Earth's atmosphere. For the purposes of the discussion presented here, the important components and associated labels of these

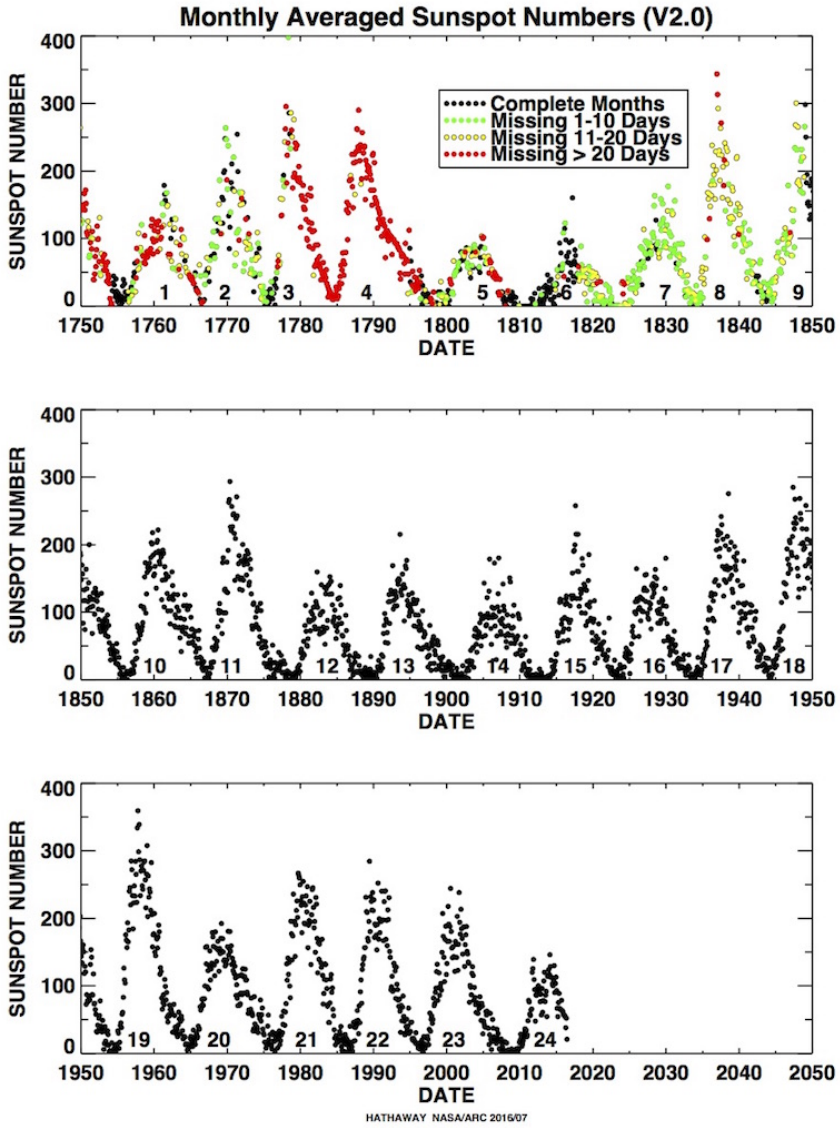

Figure 2.1: The measured and inferred solar cycles based upon the number of sunspots from 1750 to 2016. This figure was taken from D. Hathaway's NASA web article "The Sunspot Cycle" [26].

showers are high-energy neutrons (n), muons ($\mu^{\pm}$), and muon neutrinos (ν) as displayed in Fig. 2.2.

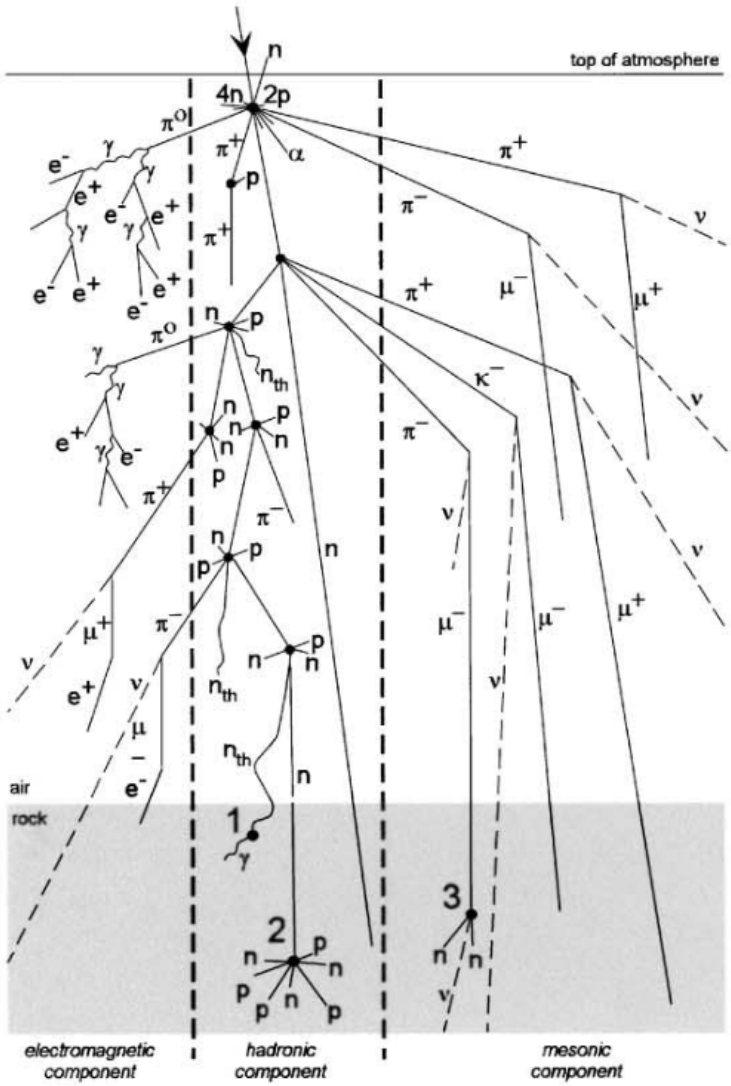

Figure 2.2: The three components of an example cosmic ray shower taken from Fig. 1b of [27]. Above ground, MARS measures the high-energy neutron component from the hadronic showers. Below ground, MARS measures the high-energy neutron component created by mesonic shower particle interactions in rock.

Above ground, the high-energy neutron flux is primarily due to spallation reactions by high-energy charged particles on Oxygen and Nitrogen. Within tens of meter of rock, high-energy neutrons from hadronic showers are attenuated through scattering (Fig. 2.2 path 2). Below ground, the high-energy neutron flux is due to the muon component of the mesonic

showers (Fig. 2.2 path 3). High-energy neutrons are produced through muon spallation and muon capture. Most muons are created by pion decay in mesonic showers. A very small percentage of muons are created through charged-current interactions of ν_μ with rock [28], which is not shown in Fig. 2.2. Thus, an experiment can never truly escape the high-energy neutron flux by going deeper below ground. The energy spectrum of muon-induced neutrons is not well measured [16].

2.2 High-Energy Neutrons as a Background

The problem with high-energy neutrons is not just their ubiquitous nature; it is the fact that they are electrically neutral [1]: unlike charged particles, neutrons are difficult to identify. For some experiments the neutron induced signal may be difficult to remove from the desired data. To further complicate the problem, high-energy neutrons are capable of inducing spallation reactions inside the experiment or in the surrounding environment. These spallation reactions produce lower-energy neutrons as well as excited nuclei, which may further decay by neutron or gamma-ray emission.

These secondary neutrons and gamma rays induce background in most experiments. Due to the weak macroscopic cross section of high-energy neutrons, detector fiducialization [2] may not be successful at removing this background. Shielding near experiments, particularly high-Z materials, may provide a spallation target increasing the background due to secondary spallation particles. Additionally since there may be multiple spallation products, experiments that use correlation may still be susceptible to this background. Given these challenges, high-energy neutron induced background is particularly problematic for low-statistics measurements. Furthermore, low-statistic measurements with poor energy resolution may be at a greater disadvantage. Without the ability to identify and veto high-energy neutron induced events, measurements must rely on modeling of the high-energy neutron flux to predict the high-energy neutron induced background.

As discussed in Chapter 1, high-energy neutrons are capable of mimicking the desired signal from a host of rare-event physics experiments. The following text describes how high-energy neutrons induce background in a variety of experiments.

Nuclear Reactor Monitoring

Extensive efforts in the last two decades have been made to demonstrate the feasibility of monitoring nuclear reactors using the antineutrino flux [22, 23, 24]. Successful experiments have been located very close to the reactor core. Antineuntrinos are produced in copious quantities as by-products of the fission process used in nuclear reactors. These antineutrinos

[1] Neutrons do have a non-zero magnetic moment. However, interactions using the magnetic nature of neutrons are typically performed at thermal neutron energies.

[2] Fidicualization is a concept often used in rare-event physics experiments. Events which are identified to occur at the edge of the detector are discarded to remove certain background components.

are produced when the neutron-rich fission products decay by β^- decay

$$n \rightarrow p + e^- + \overline{\nu}_e. \tag{2.1}$$

Antineutrinos, having a small interaction probability, rarely interact and easily exit the reactor. Traditionally these antineutrinos have been measured by large hydrogenous detectors: water or liquid scintillator based experiments. In addition to the large hydrogenous target these detectors are generally loaded with a neutron capture agent. Antineutrinos passing through the detector occasionally undergo inverse β decay:

$$\overline{\nu}_e + p \rightarrow e^+ + n, \tag{2.2}$$

producing a neutron (n) and a positron (e^+). The detection of antineutrinos is dependent upon the correlated signal of the e^+ annihilation and the subsequent n capture by the neutron capture agent. Fiducialization is used to identify interactions away from the edge of the detector. Any non-antineutrino based signal that can mimic this correlated process inside the fiducalized volume is potentially problematic. When in close proximity to the reactor, these background signals are generally not problematic due to an acceptable signal-to-noise ratio. As the distance is increased from the reactor core, the antineutrino event rate decreases at a rate $\propto 1/r^2$ where r is the distance from the reactor.

If one wanted to measure the antineutrino signal from kilometer-scale distances these non-antineutrino based signals become challenging: the signal-to-noise ratio becomes poor. A kilometer-scale measurement has already been performed by KamLAND at a depth of 2700 m.w.e. [29]. The WATCHMAN collaboration proposal [19] attempts to quantify how a long distance measurement could be made with minimal overburden. The WATCHMAN white paper identifies an extensive list of background signals (See Fig. 5 of [19]). High-energy neutrons represent a significant source of background due to their ability to interact in the fiducial volume. High-energy neutron interacting in the fiducial volume can produce multiple lower-energy neutrons. These lower-energy neutrons can be captured on the neutron capture agent mimicking the correlated signal from inverse β decay.

Other Rare-Event Detection

Other rare-event detection searches are susceptible to background induced by high-energy neutrons. Weakly Interacting Massive Particle (WIMP) dark matter searches are susceptible to nuclear recoils by low-energy neutrons created by high-energy neutron spallation on detector materials. Data reduction based upon the number of nuclear scatters may be possible to remove some of this high-energy neutron induced background. Significant simulation work has been performed to estimate high-energy neutron induced background in a host of WIMP dark matter experiments: EDELWEISS [30, 31], CDMS [32], and LUX [17]. Particularly concerning is the LUX [17] high-energy neutron prediction which states: "The muon-induced high-energy neutron flux from the rock has been measured at several underground sites, and both the total flux and energy distribution can be fitted with empirical

depth-dependent functions". The paper then references Mei and Hime [16]. Unfortunately for LUX, Mei and Hime did not measure the muon-induced high-energy neutron flux from the rock. They compared measured data and Monte Carlo simulations of the muon-induced high-energy neutron flux produced in liquid scintillator. Mei and Hime used the Monte Carlo code FLUKA [33, 34]. It was assumed that if FLUKA acceptably predicted muon-induced neutrons in liquid scintillator, it might correctly predict muon-induced neutrons in rock. Significant uncertainty exists in the predictions of Mei and Hime.

Besides WIMP dark matter detectors, neutrinoless double beta decay experiments are particularly interested in the high-energy neutron flux. MAJORANA [35], a double beta decay experiment, uses Germanium detectors enriched in Ge^{76} in a high-purity copper cryostat deep below ground. Of particular concern for MAJORANA, high-energy neutrons may interact in the copper cryostat producing gamma rays very near or above the Q-value of the proposed Ge^{76} decay, potentially reducing the signal-to-noise ratio of the measurement. Boswell *et al.* [36] measured the total and level cross-sections for gamma decay from high-energy neutron inelastic scattering on natural Copper at LANSCE [37]. This measurement was intended to benchmark ENDF/B-VII data, which Monte Carlo codes use. If the measurement correctly predicted the cross-sections, reliable estimates of the high-energy neutron induced background could be predicted. Their total cross-section results compared favorably to published ENDF/B-VII data. However, the individual level cross-sections, particularly above 2 MeV, showed significant discrepancies with published ENDF/B-VII data. If the ENDF/B-VII data can be improved and a reliable estimate of the high-energy neutron flux existed, a better prediction of the high-energy neutron induced background would become possible.

2.3 Traditional Methods for High-Energy Neutron Detection

Motivated by obtaining a better understanding of the high-energy neutron flux above and below ground, previous high-energy neutron measurement techniques were investigated. Again, most of these measurements were summarized by Ziegler [12]. They comprise two types of experiments: detectors that operate by converting the high-energy neutron into lower-energy secondary neutrons or experiments which measure the recoil of high-energy neutrons. Given the review below, previous methods appear unattractive for measuring the high-energy neutron flux above and below ground based primarily on two conclusions: the efficiency may not be sufficient to measure the high-energy neutron flux below ground, and if the efficiency is sufficient the detector may not be transportable. The effort described here is motivated by characterizing the high-energy neutron flux at a variety of locations and depths: the detector must be transportable.

Bonner Spheres

Bonner sphere experiments have been the traditional workhorse of above ground high-energy neutron measurements [38, 11, 39]. These detectors are composed of a set of moderating spheres each surrounding a neutron capture detector. An example subset of spheres is shown in Fig. 2.3; the figure was taken from [39]. Each sphere is a slightly different size and has a specific sensitive neutron energy range. Typical Bonner sphere arrays have 10-14 spheres. High-energy sensitivity is obtained by incorporating a steel or lead insert into two of the largest spheres. High-energy neutrons undergo spallation on the lead or steel inserts, generating secondary neutrons of lower energy. These lower-energy neutrons thermalize on the moderating sphere and are captured by the internal neutron detectors. The energy-dependent neutron flux is obtained by comparing the measured count rate between each detector, given the estimated or measured detector response. A common code used to unfold the measured count rate is MAXED [40].

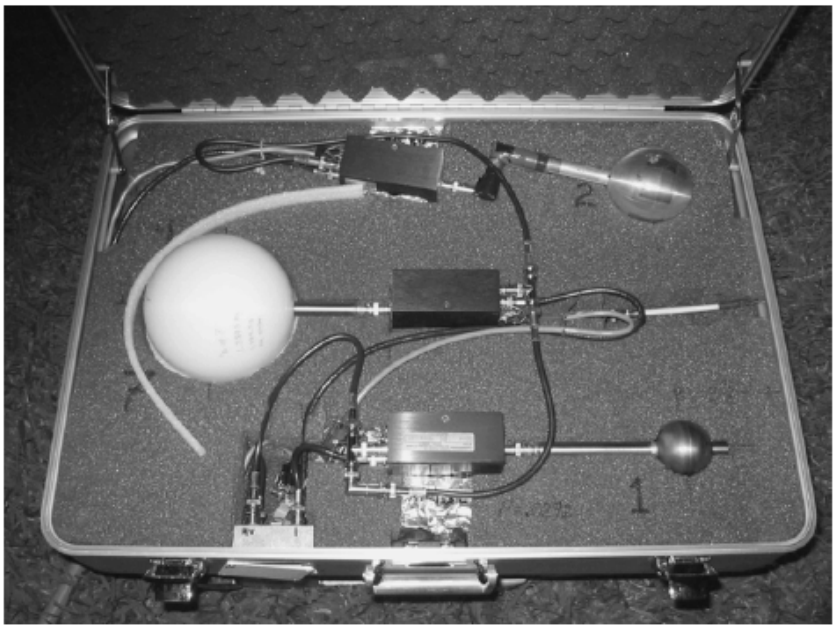

Figure 2.3: An example set of three Bonner spheres and associated preamplifiers taken from Fig. 1 of [39].

There are several problems with most Bonner sphere measurements. First, a significant number of Bonner sphere measurements do not report statistical or systematic uncertainty estimates. MAXED [40] calculates these uncertainty values, but experiments neglect to report these values. Second, only two spheres are sensitive to high-energy neutrons limiting the high-energy resolution. Third, these high-energy neutron spheres are also susceptible to cosmogenic charged particle spallation in the lead and steel inserts. Traditionally these

detectors are not used in anti-coincidence with charged particle detectors surrounding the spheres. A separate charged particle detector may be incorporated, but the charged particle background subtraction is performed in a statistical manner: the measured charged particle flux is used with a Monte Carlo model of the Bonner spheres to predict the charged particle induced signal. Finally, Bonner sphere experiments may not have the required efficiency to measure high-energy neutron fluxes at shallow or deep depths below ground, given the predicted flux from Mei and Hime [16] [3]. However, the method of converting high-energy neutrons into lower energy neutrons seems particularly attractive as a detection strategy.

Similar experiments used International Geophysical Year (IGY) neutron meters to detect high-energy neutrons. These experiments operate on a similar principle: high-energy neutron spallation on a lead target to create lower-energy secondary neutrons [41]. However, the detectors where not configured in a spherical fashion. For the remainder of this work the term "Bonner sphere" will be used to refer to both measurements.

Recoil Spectrometers

Recoil based spectrometers can be categorized based upon their respective detection method: telescope, capture-gated, or pure recoil. Telescopes measure at least two neutron scatters in separate detectors [42]. The energy is inferred by the energy deposited in the first detector and the time between the two recoils. Capture-gated detectors operate in a similar manner: the energy of the first recoil is used to infer the incident neutron energy. However, after the first neutron scatter, the neutron must capture on a neutron capture agent to confirm that the recoil was due to a neutron [43, 44]. Finally, purely recoil based methods, without a subsequent capture, can be used to detect high-energy neutrons [45]. The construction and size of these detectors varies based upon whether the detector is transportable or fixed. An example capture-gated neutron detector is displayed in Fig. 2.4, which was taken from Fig. 2 of [43].

Each of the above detection methods has several problems. Telescopes, in order to have energy resolution at high-energy, must separate the two detection planes or detectors. This decreases the efficiency of the telescope or requires the addition of larger detectors or more detectors. If more or larger detectors are used, the interactions of uncorrelated gamma rays or neutrons may reduce the signal-to-noise ratio of the measurement. In general telescopes that are transportable lack the efficiency to make high-energy neutron measurements below ground. Transportable capture-gated detectors may suffer from reduced efficiency at neutron energies above $>\sim$150 MeV [15]. Finally, pure recoil detectors may have problems with background rejection due to not requiring a second scatter or capture. In the presence of a particularly weak high-energy neutron flux, this method may be sensitive to stopped charged particle (muon) decay.

[3] As an aside, the claim that Bonner sphere experiments can measure high-energy neutrons at 10-15 GeV [11, 39] seems particularly dubious when examining the detector response functions given in [11] and the measurement statistics quoted in [39].

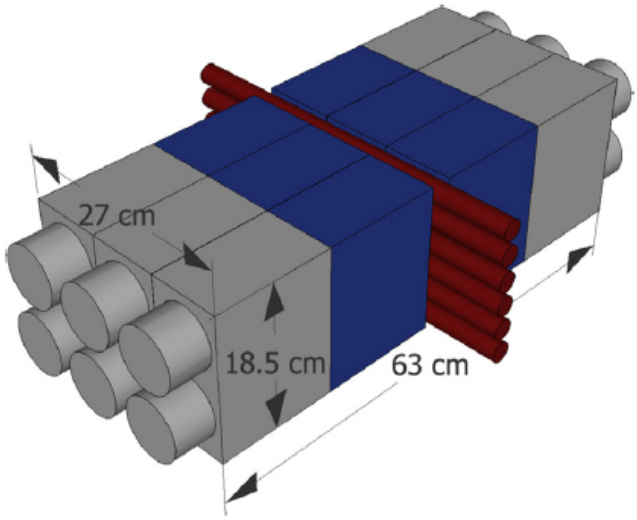

Figure 2.4: An example of a capture-gated neutron detector taken from Fig. 2 of [43]. The grey rectangular prism is a light-guide and the signal readout, the blue rectangular prism is the active detector scintillator, and the red tubes are the He-3 neutron capture component.

Ignoring the response of pure recoil detectors, telescopes and capture-gated detectors are not attractive methods because they require two time correlated interactions. While this reduces uncorrelated background, it also reduces the detection probability: two interactions must occur, which make measurements requiring a transportable high-efficiency detector difficult. As a final note, most of the listed recoil spectrometers use liquid scintillator which is flammable. Flammable material, due to a safety hazard, should be avoided in below ground measurements.

Chapter 3

Measurement Concept

Traditional high-energy neutron spectrometers have certain characteristics that would make it extremely difficult to measure a low high-energy neutron flux in the presence of relatively strong uncorrelated gamma-ray or charged particle background. This is the environment encountered when measuring the ambient high-energy neutron flux. Traditional methods tend to require long measurement times in order to obtain reasonable statistics. Below ground this scenario becomes more challenging. These backgrounds are particularly problematic for recoil spectrometers and telescopes due to their reliance on two correlated time signatures. To overcome this limitation, an acceptable option could be an array of Bonner spheres with a charged particle veto. However, at high energies Bonner sphere arrays have unacceptably low efficiency. This inadequate efficiency, at the same below ground locations measured by MARS, would require an integration time of at least several years per location. MARS accomplishes three below ground measurements in just under 2 years of operation.

In order to overcome the limitations of traditional high-energy neutron spectroscopic approaches, MARS uses a spallation based multiplicity technique to transform an incident high-energy neutron into many lower energy secondary neutrons. These secondary neutrons can be thermalized in a short time window and efficiently captured in a detector. MARS identifies high-energy neutrons by recording a significant number of correlated neutron captures in a short time window. A large number of correlated neutron captures is a particularly strong indicator of an incident high-energy neutron; the method has a high signal-to-noise ratio. The multiplicity technique was proposed and demonstrated for high-energy neutron integrated flux measurements, but not for energy spectra measurements [46, 47]. It has the previously unexploited potential for spectral unfolding of the incident neutron energy spectrum based on the secondary neutron multiplicity and other associated characteristics of the spallation event. If spectral unfolding can be achieved, the multiplicity method promises superior sensitivity as compared to other transportable high-energy neutron spectrometers.

While this technique sounds promising, there is one significant challenge: the transformation from the incident high-energy neutron to the measured secondary neutron multiplicity is not injective. A mono-energetic high-energy neutron spectrum incident on MARS will produce a wide non-symmetric multiplicity distribution. However, the challenge is the inverse of

this transformation: a far more difficult problem commonly referred to as the "inverse problem". To unfold the incident high-energy neutron energy-dependent flux, a new approach was developed which uses a Markov Chain Monte Carlo (MCMC) technique to solve the MARS inverse problem. This particular technique is attractive due to its ability to reconstruct the incident neutron energy-dependent flux, incorporate a priori information, reduce bias induced from the a priori information, and calculate the uncertainty.

The rest of the chapter focuses on the methodology to detect and infer the high-energy neutron energy-dependent flux. Section 3.1 describes the multiplicity method in detail. Section 3.2 describes inverse problems in general and introduces Singular Value Decomposition (SVD). SVD, due to its non-iterative nature, was used to optimize the measured observables of the multiplicity method in MARS. Section 3.3 describes the triggering algorithm to identify multiplicity events. Section 3.4 briefly describes general MCMC algorithms for solving the inverse problem. Finally Sec. 3.5 describes the specific MCMC algorithm used for the MARS analysis.

3.1 The Multiplicity Method

In order to initiate and detect high-energy neutron induced multiplicity events, MARS consists of two Gd containing plastic scintillator detectors arranged around a lead spallation target. The plastic scintillator provides an efficient, radiation sensitive, neutron down-scattering medium. The large thermal neutron capture cross section and energetic de-excitation of Gd nuclei allow for identification of neutron capture interactions when coupled with the light output from the plastic scintillator. The lead is an efficient fast-to-slow neutron converter.

Before describing the physics of the multiplicity event it is useful to define two terms: deposition and event. These terms are intended to bring clarity to the discussion surrounding the measured signal. The MARS analysis defines a deposition as the integrated energy deposited in 300 ns. A number of depositions closely spaced in time is considered an event, which is assumed to be initiated by a single incident high-energy neutron.

When an incident high-energy neutron interacts with the lead target as shown in Fig. 3.1, a spallation reaction can occur, resulting in multiple secondary neutrons emerging from all sides of the target. Secondary spallation neutrons are estimated by simulation to be emitted with an average energy of $\sim$1-2 MeV with a high-energy tail as displayed in Fig. 3.2 [48, 49]. A uniform incident high-energy neutron energy distribution between 20 MeV and 1000 MeV was used to create Fig. 3.2. These secondary neutrons down-scatter in the scintillator surrounding the lead and are captured by a Gd nucleus. The excited Gd nucleus then de-excites emitting 1-5 gamma rays with a total energy of $\sim$8 MeV, which may interact in the scintillator forming a deposition. In addition to secondary neutrons, a spallation reaction may rarely produce high-energy charged particles[1]. The collection of the time correlated charged particle interactions, secondary neutron thermalizations, and Gd de-excitations forms an event.

[1]The charged particles observed in Monte Carlo simulation [48, 49] were $\pi^{\pm}$. Events with the structure of Fig. 3.3 have been observed in measured data and simulation.

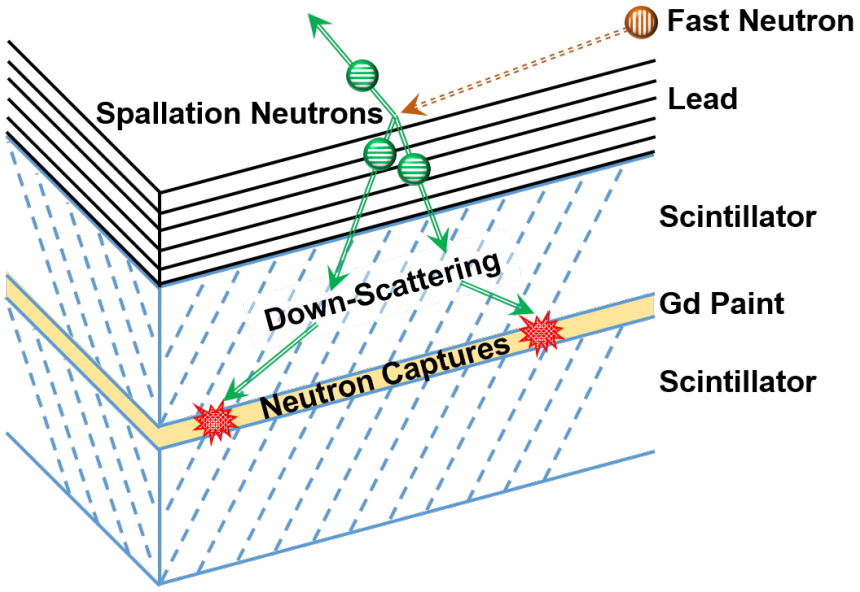

Figure 3.1: Depicts a high-energy neutron initiating a spallation reaction in the lead and generating secondary neutrons. These secondary neutrons down-scatter in the scintillator and are captured on a Gd nucleus in the paint. The Gd de-excitation produces 1-5 gamma rays which further interact in the scintillator.

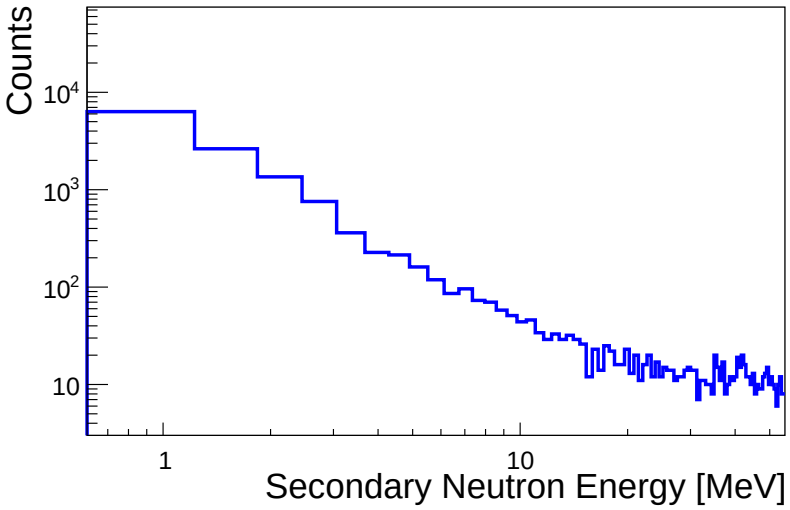

Figure 3.2: The simulated energy of the secondary neutrons exiting the lead spallation target. Incident high-energy neutrons were simulated with a uniform energy distribution between 20 MeV and 1000 MeV.

The multiplicity event sequence induces a two part time-dependent signature in MARS: the prompt and delayed components. The prompt component occurs very close in time to the initial spallation reaction and is composed of the energy deposited in MARS by the thermalization of the secondary neutrons and the interactions of the spallation created charged particles. The prompt component only records the energy; MARS does not record any waveform data. To first order the energy deposited depends upon the charged particles being created during spallation; secondary neutrons are quenched and their deposited energy will only be observable when there are a large number of secondary neutrons. The delayed component is more complex: time and energy information exist, and both are important for reconstructing the incident neutron flux. The delay component is spread over a larger time range and occurs when secondary neutrons are captured on Gd nuclei. The timing structure of an example event is displayed in Fig. 3.3.

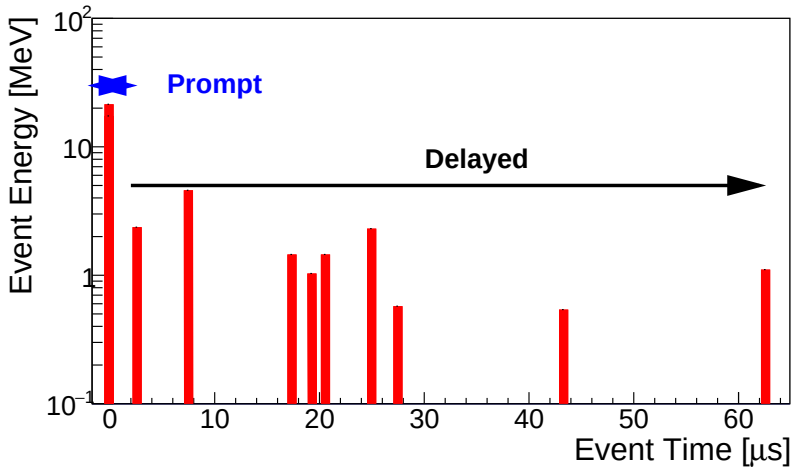

Figure 3.3: Depicts the timing characteristics of a high-energy neutron multiplicity event. The two part time-dependent signature of the multiplicity signal is observed: the prompt component is the large energy deposition at time 0, the delayed component is the subsequent neutron captures after the prompt component.

The multiplicity signal can be distorted by two noise components: cosmogenic charged particles[2] inducing spallation in the lead and the uncorrelated ambient gamma-ray flux. Spallation events due to cosmogenic charged particles have a similar event structure as a neutron multiplicity event. The only way to exclude this data is to use a cosmogenic charged particle veto around the plastic scintillator detectors and the lead. The ambient gamma-ray flux is due to naturally occurring radioactive materials surrounding the experiment. Due to its random nature, it is modeled as a Poisson process with a characteristic time constant [50]. For the rest of this paper, the characteristic Poisson time constant will be

[2]This is a reference primarily to muons and is different than the spallation charged particles. The quantifiers distinguishing the two charged particles are: spallation versus cosmogenic.

referred to as the inter-event time. For all measurements performed here, the inter-event time was $>\sim$450 μs. Due to this long inter-event time, multiple gamma-ray depositions over a time period of $\sim$100 μs is unlikely. However, all depositions in a contaminated event do not have to be due to the ambient gamma-ray flux. A more probable scenario is a single gamma ray contaminating a neutron multiplicity event.

With an understanding of the event structure and the associated noise components, an algorithm was formulated to optimize the identification and triggering of the measured observables. A separate algorithm must then invert this measured signal, over many events, into the incident high-energy neutron flux. These two algorithms are highly correlated: the identification and triggering algorithm is dependent upon identifying the components of the measured signal which contain the most information; the quantification of information can be formulated by an inversion algorithm. The inversion algorithm is dependent upon correctly classified events in order to invert the measured signal into the incident high-energy neutron energy-dependent flux.

Due to this correlation, the inverse problem is presented first. Several idealized components of the measured signal from Monte Carlo simulation [48, 49] are identified, and the permutation of these observables which contain the maximum information is identified. Then an identification and triggering algorithm is developed to accurately identify those observables, while minimizing the expected gamma-ray noise contribution; cosmogenic charged particles are assumed to be removed by the charged particle veto.

3.2 The Inverse Problem

In general, any measurement apparatus transforms the desired quantity into a measured quantity. For many problems, this transformation is easily corrected. For example, the telescope technique described in Chapter 2 is a time-of-flight measurement between two detector planes. Ignoring relativistic effects, the energy of the particle can be directly determined by $E = \Delta E + \frac{1}{2}m(\frac{\Delta x}{\Delta t})^2$, where ΔE is the energy deposited in the first interaction, m is the mass of the particle, Δx is the distance between the first and second interaction, and Δt is time between interactions. There is uncertainty in measuring ΔE and Δt that propagates through to the final answer. However the answer can be arrived at in straight-forward fashion.

This example inversion problem, and the significantly more complicated MARS problem, can be described by using the Fredholm integral [51]. This integral equation can be discretized and the solution found. The following section briefly describes the MARS inversion using the Fredholm integral. Singular Value Decomposition (SVD), a traditional non-iterative solution is introduced. Due to its speed and simplicity SVD was used to optimize the measured signal in the MARS detector.

The Fredholm First Integral

The Fredholm integral equation can be used to describe the forward problem: given a model of the transformation of the measurement apparatus and the incident quantity of interest the predicted measured quantity can be calculated [51]. The integral equation, for the case of MARS, is defined by:

$$g(\vec{y}) = \int A(E, \vec{y}) f(E) dE + b(\vec{y}), \tag{3.1}$$

$g(\vec{y})$ is the measured secondary neutron response, $A(E, \vec{y})$ is the kernel or detector response matrix, $f(E)$ is the desired energy-dependent flux, $b(\vec{y})$ is the noise in the secondary neutron response space, $\vec{y}$ is the vector of measured parameters, and E is the incident neutron energy. Because the continuous form of the parameters are generally not known, Eq. 3.1 is traditionally discretized:

$$\vec{g}_{meas} = \mathbf{A}\vec{f} + \vec{b}, \tag{3.2}$$

where $\vec{g}_{meas}$ is a vector of length N, $\mathbf{A}$ is a N by P matrix, $\vec{f}$ is a vector of length P, and $\vec{b}$ is a vector of length N. In the context of the above discretization for MARS, N is the number of voxels in the measured vector ($\vec{g}_{meas}$) and P is the number of energy bins.

To "vectorize" these components, imagine that each voxel in the measured space has an index number. These voxel values are then sorted into a vector based upon the index number. Conventionally, if rows of $\mathbf{A}$ and the corresponding element of $\vec{g}$ are composed of zeros ,the row and entry are culled. From a mathematical standpoint this reduces the sparse nature of the matrix and decreases computation time without the loss of information.

With this discretization and vectorization, the equations can be used to find a solution if $\mathbf{A}$ is invertible. The example telescope problem should have a square invertible detector response matrix ($\mathbf{A}$)[3]. However, for more complicated scenarios like the MARS measurement, $\mathbf{A}$ is not square and is singular eliminating the possibility of direct-matrix inversion.

SVD: A Non-Iterative Solution

In order to solve Eq. 3.2 for $\vec{f}$, early algorithms focused on finding a pseudo-inverse ($\mathbf{A}^+$) to $\mathbf{A}$. The most common pseudo-inverse matrix is the Moore-Penrose pseudo-inverse matrix [52]. This matrix can be formed by using Singular Value Decomposition (SVD) to factor the detector response matrix:

$$\mathbf{A} = \mathbf{U}\Sigma\mathbf{V}^*, \tag{3.3}$$

where $\mathbf{A}$ is the detector response matrix, $\mathbf{U}$ is N by N unitary matrix, $\mathbf{V}$ is a P by P unitary matrix, * designates the complex conjugate, and Σ is a N by P diagonal matrix of non-negative real numbers. By convention Σ is ordered in descending fashion starting at $\Sigma_{0,0}$. The matrices from SVD can be interpreted in the form of an eigenvector and eigenvalue

[3]Or very nearly square invertible matrix as compared to MARS. See Fig. 5.7

problem. The columns of $\mathbf{U}$ and $\mathbf{V}$ are eigenvectors associated with the eigenvalues of Σ ($\Sigma_{i,i}$). With this formulation, the pseudo-inverse can be calculated:

$$\mathbf{A}^{+} = \mathbf{V}\Sigma^{+}\mathbf{U}^{*}, \tag{3.4}$$

where $\mathbf{U}$ and $\mathbf{V}$ have been previously defined, and the elements of $\Sigma^{+}_{i,i} = \frac{1}{\Sigma_{i,i}}$. With this inverse, the desired quantity $\vec{f}$ can be calculated:

$$\vec{f} = \mathbf{A}^{+}(\vec{g}_{meas} - \vec{b}), \tag{3.5}$$

where all parameters have been previously defined.

In practice a direct solution using SVD is more tedious. The problem can be observed by solving the least-squares problem with SVD

$$\vec{f} = \sum_{i}^{P} \frac{\vec{u}_i^{*}(\vec{g}_{meas} - \vec{b})}{\Sigma_{i,i}}\vec{v}_i, \tag{3.6}$$

where $\vec{u}$ and $\vec{v}$ are the column vectors of $\mathbf{U}$ and $\mathbf{V}$ respectively and all other parameters have been previously defined. The solution is proportional to the inverse of the singular values. Weak singular values, which correspond to noise, have the potential to dominate the solution[4]. Measurement noise, due to cosmogenic charged particles and the ambient gamma-ray flux, makes this problem more difficult. These weak singular values and associated measurement noise often results in oscillatory behavior called Gibbs phenomenon [53].

However, a solution exists to limit the Gibbs phenomenon: a penalty function is added to the inverse problem. Traditionally this is called regularization; it introduces bias in order to calculate the solution. The solution to the least-squares problem with Tikhonov regularization, the most common regularization, is defined:

$$\vec{f} = \sum_{i}^{P} \frac{\Sigma_{i,i}\vec{u}_i^{*}(\vec{g}_{meas} - \vec{b})}{\Sigma_{i,i}^{2} + \tau}\vec{v}_i, \tag{3.7}$$

where τ is the regularization parameter [54].

While SVD provides a solution for inverting the Fredholm integral, it makes several assumptions that are not appropriate given the MARS data. First, it is a solution to the least-squares problem, which denotes Gaussian statistics [5]. The measured data of MARS may not posses sufficient counts to exhibit Gaussian statistics. Therefore, MARS requires an algorithm capable of using Poisson statistics, which does not require a large number of

[4]The noise here is not due to cosmogenic charged particles or the ambient gamma-ray flux. It is due to singular values which are very near zero.

[5]Gaussian statistics is the most efficient solution to the least squares problem. Therefore, it is traditionally used to solve least squares problems.

counts [6]. Second, SVD does not guarantee that the unfolded flux ($\vec{f}$) will be positive at all energies. Negative flux, in the context of the MARS measurements, is not physically possible.

Optimization of the Measured Observables

However, due to its eigenvector and eigenvalue formulation, SVD can be used to optimize the set of measured observables by calculating the effective rank of the detector response matrix ($\mathbf{A}$). The effective rank can be calculated by relating Eq. 3.6 and Eq. 3.7:

$$FOM_{SVD} = \sum_{i}^{P} \frac{\Sigma_{i,i}^2}{\Sigma_{i,i}^2 + \tau}, \tag{3.8}$$

where all parameters have been previously defined. For the purposes of the MARS analysis a regularization value of $\tau = (0.1\ \Sigma_{0,0})^2$ is used, which enforces a smooth requirement that significant singular values must be near 10% of the maximum singular value. By maximizing the effective rank over multiple sets of measured variables, an optimum detector response matrix can be found. However, the analysis must be careful not to add too many parameters to the measured observables. Adding an observable reflects a trade-off: the information in the detector response matrix may be increased, but by increasing the dimensions of the measured data space the statistics in individual bins may be significantly decreased, increasing noise.

Recalling the event structure and associated discussion from Fig. 3.3, the components of the multiplicity signal which are used in the inverse algorithm were identified: 1) the energy deposited in the prompt component of the signal due to secondary neutron thermalization and spallation charged particle interactions (thermalization energy), 2) the number of secondary neutron captures detected during the delayed component of the signal (multiplicity), and 3) the sum of all deposited energy from secondary neutron captures during the delayed component of the signal (capture energy). Individual energy depositions, from secondary neutron captures, were not considered in order to have a small number of measured observables. The total time or time between depositions was not considered, due to the measured time being susceptible to contamination from the uncorrelated ambient gamma-ray flux. Due to these constraints and with an interest in limiting the number of measured observables, the three parameters are formally defined below and displayed in Fig. 3.4:

1. Thermalization Energy: the deposited energy from the first deposition

2. Multiplicity: excluding the first deposition to not count charged particles interactions, the number of depositions with $\leq$8 MeV deposited energy

[6] Both the Poisson and Gaussian distributions are approximations to the Binomial distribution. Both assume a small success probability. However, the Gaussian distribution approximation assumes a sufficient number of counts have been recorded. The Poisson distribution approximation has no count requirement [50]

3. Capture Energy: excluding the first deposition to not count the deposited energy from charged particles, the sum of all deposited energy from all depositions

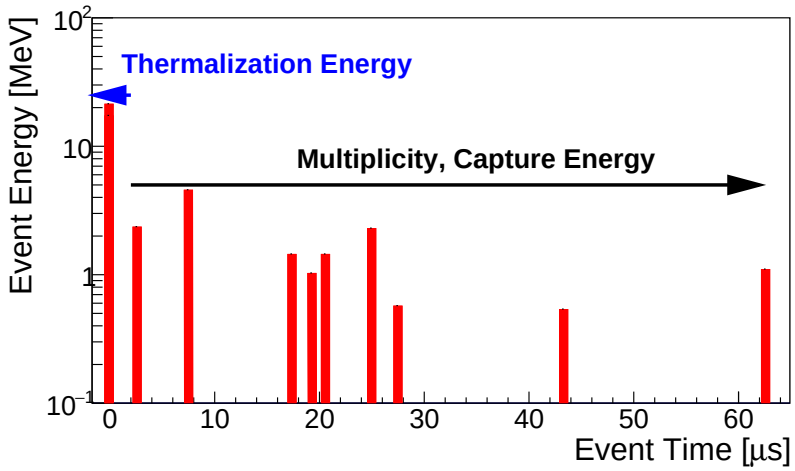

Figure 3.4: An illustration of the timing characteristics of a high-energy neutron multiplicity event. The two part time-dependent signature of the multiplicity signal is observed. The three measured parameters: multiplicity, capture energy, and thermalization energy, of the two part signature are denoted.

Given the relatively long measurement time of the example event, it would be very difficult to directly measure the high-energy neutron response (**A**) in MARS using an accelerator. Such a measurement would require a single neutron interaction per accelerator pulse, a very low accelerator repetition time ($\geq$100-200 μs), accurate knowledge of the energy of the incident neutron, and minimal feedback from the surrounding environment. Due to these complications, MARS uses Monte Carlo simulation to predict the detector response matrix **A**. Using different permutations of the three measured quantities, separate detector response matrices were constructed using the MARS Monte Carlo model (Chap. 5).

SVD was used to calculate the FOM_{SVD} for each matrix and the results are presented in Table 3.1. From Table 3.1, the optimal choice is to use all three components: the multiplicity, the capture energy, and the thermalization energy. Of the single components, the multiplicity contains the most information for inferring the incident neutron energy. The capture energy and thermalization energy contain equally useful information. However, as observed in the three component case, this information is not identical.

Table 3.1: The FOM_{SVD} for permutations of the three measured observables. The optimal FOM_{SVD} was found when using all three measured observables.

Mult.	Cap. E.	Therm. E.	FOM_{SVD}
✓	-	-	3.29
-	✓	-	2.10
-	-	✓	2.10
✓	✓	-	3.41
✓	-	✓	3.41
-	✓	✓	2.40
✓	✓	✓	3.59

3.3 Identifying Multiplicity Events

Given the expected response from Sec. 3.1 and the optimal measured components from Sec. 3.2, the MARS analysis identifies multiplicity events, while minimizing the contribution from ambient gamma-rays. A simple method to detect the highly correlated event structure of a multiplicity event is a long fixed-length time window. The window starts at a deposition; if a certain number of depositions were inside the window, the event would be recorded. The next window would start at the next deposition after the previous event.

In order to have a high detection efficiency for detecting most of the neutron captures for a high multiplicity event, the single window must be $\sim$100μs. This long window length results in the measured signal being susceptible to the uncorrelated ambient gamma-ray background, particularly for the below ground measurements at low multiplicity values.

Simple Monte Carlo Triggering Setup

A simple Monte Carlo model was constructed to optimize various triggering algorithms. The model used two parameters to estimate a recorded high-energy neutron signal: the measured neutron capture time of 18.7 $\pm$ 3.0 μs (Sec. 4.5), and a inter-event time of the uncorrelated gamma-ray background. The inter-event time used for the following analysis was 478 μs which was measured during the Cf-252 calibration (Sec. 4.5). No cosmogenic charged particle background is included in the background model; it is assumed to be removed by the charged particle veto surrounding the detector.

To analyze different triggering algorithms, the neutron capture time was sampled to simulate n neutron captures starting from time zero. The background was included by sampling the background distribution, starting two inter-event times before the first neutron capture until two inter-event times after the last neutron capture. One million sequences of

this nature were simulated with n ranging from 3 to 10.

For measurements where the neutron flux is expected to be significantly larger than the background, the effectiveness of different triggering algorithms was compared by examining the neutron detection efficiency and the number of background depositions identified as correlated neutrons. A figure of merit (FOM_{Trig}) was defined:

$$FOM_{Trig}(n) = \frac{m/n}{b+1}, \tag{3.9}$$

where n is the number of true neutron captures, m is the number of detected neutron captures, and b is the number of background depositions identified as neutron captures within a multiplicity event. Each triggering algorithm was used to process the depositions into events and calculate the figure of merit (FOM_{Trig}), which is shown in Fig. 3.5a. Due to the $FOM_{Trig} \propto \frac{1}{n}$ the optimal value will always be less than 1.

For measurements where the neutron flux is not known, or less than or on the order of the background, the FOM_{Trig} is insufficient to rank trigger algorithms. In addition to the FOM_{Trig}, the rate at which multiplicity events composed of only background depositions was used to characterize the triggering algorithms. The background multiplicity rate was determined by sampling the uncorrelated gamma-ray inter-event time distribution. The same triggering algorithms were used to detect background multiplicity events masquerading as correlated secondary neutrons. The resulting noise multiplicity spectra was normalized to the time simulated and shown in Fig. 3.5b.

An optimal triggering algorithm has a FOM_{Trig} close to 1 with the comparatively smallest background multiplicity rate. In deployment scenarios where the ambient gamma-ray background rate and a reliable estimate of the fast neutron flux is known, further optimization may be possible.

Triggering Algorithm Optimization

Given this simple Monte Carlo model, two types of multiplicity identification algorithms were investigated: a fixed length time range and an expanding length time range. Both algorithms defined an initial time range, started the range at the time of the first available deposition, and required three or more depositions to record an event. If three or more depositions were not recorded in the time range, the first deposition was discarded and the window was updated to start at the next deposition. If the three deposition threshold was reached and an event was ended, the next available deposition started the next event. The FOM_{Trig} and background multiplicity rate for several fixed and expanding time range identification algorithms are shown in Fig. 3.5.

Fixed time ranges from 25 to 200 μs were investigated. A fixed time of 65 μs was found to be optimal for measurements with a strong neutron flux compared to the background. For the expanding time range algorithm, if 3 or more depositions were reached the range was extended by a secondary time range from the time of the second to last deposition in the event. Using this algorithm the initial time range was shorter than the fixed length

algorithm, which rejected background depositions more efficiently at the cost of detection efficiency for low neutron multiplicities. The expanding nature of the time range allowed the algorithm to detect high multiplicity events more efficiently than the fixed gate algorithm as shown in Fig. 3.5a. Initial time ranges of 25 to 100 μs and secondary time ranges from 25 to 100 μs were investigated. An optimal algorithm will depend on the expected background rate and the minimum multiplicity of interest.

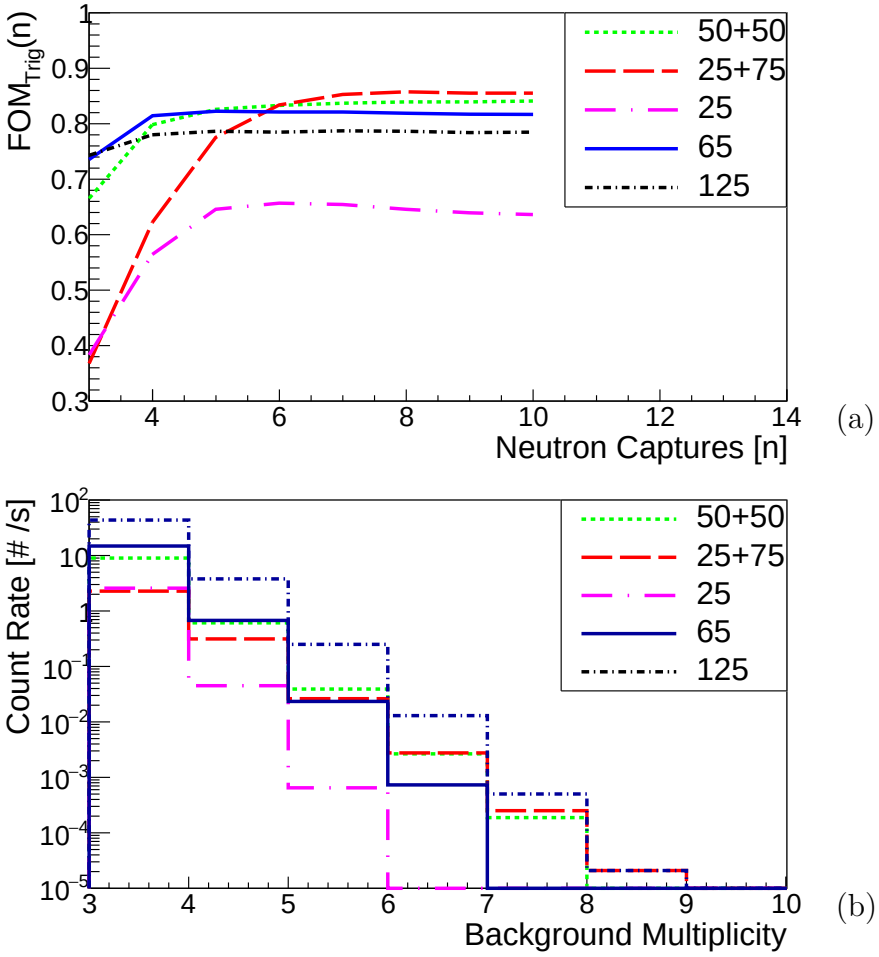

Figure 3.5: (a) The FOM_{Trig} described in Eq. 3.9 for a variety of triggering algorithms described in Sec. 3.3. (b) The expected background multiplicity rate due to the uncorrelated gamma-ray flux. Fixed length time ranges of 25, 65, and 125 μs are shown. Expanding time ranges are denoted with the initial range before and the secondary range after a + symbol.

The Triggering Algorithms

For Cf-252 calibrations described in Chapter 5 the MARS analysis used a relatively short fixed 65μs window. This was used because the signal-to-noise ratio of the measurement was high. Additionally, the constant time range made the analysis significantly easier to perform. For high-energy neutron flux measurements, MARS uses the two part expanding time range algorithm described below:

1. All individual depositions had $\geq$850 keV deposited energy
2. The start of the event must occur >200 μs from a veto deposition
3. An event is recorded if $\geq$3 depositions occur in 25 μs
4. Additional depositions can be added to an event if they occur $\leq$75 μs from the second to last deposition already recorded in an event
5. Only the first deposition may be over 8 MeV
6. An event must have a *Capture Energy/Multiplicity* ratio of:
   a) Below ground: >2.2 MeV/#
   b) Simulation or above ground if multiplicity=3: >2.0 Mev/#
   c) Simulation or above ground if multiplicity>3: Not applied

The reasoning as to why these thresholds were set will be alluded to in the following chapters. As a brief explanation, the following logic and supporting figures are provided: an energy threshold of 0.85 MeV was chosen to be safely above the hardware energy threshold which varied as the detector gain drifted (Sec. 4.3). In Fig. 3.6 the time between the start of $\geq$3 multiplicity events and the time since the previous charged particle veto deposition is displayed. By fitting the two exponential components the events due to cosmogenic charged particle spallation in the detector can be removed. A separation of >200 μs was chosen to reject these cosmogenic charged particle induced events in the experimental data. A multiplicity threshold of 3 was chosen to reduce the uncorrelated gamma-ray flux background in the experimental data. Different multiplicity thresholds could have been used. However, a threshold of 3 ensured sufficient statistics for the below ground measurements while still providing background rejection. Culling of events in which depositions, other than the first deposition, were recorded with >8 MeV deposited energy was performed to partially reject multiple incident neutrons interacting in the detector and to fully reject cosmogenic charged particle interactions during a neutron event. Finally the threshold on *Capture Energy/Multiplicity* was important for removing the ambient gamma-ray flux in the below ground measurements. This is observed in Fig. 3.7 by comparing *Capture Energy/Multiplicity* for the above ground data and the data at 377 m.w.e. using the above ground event requirements.

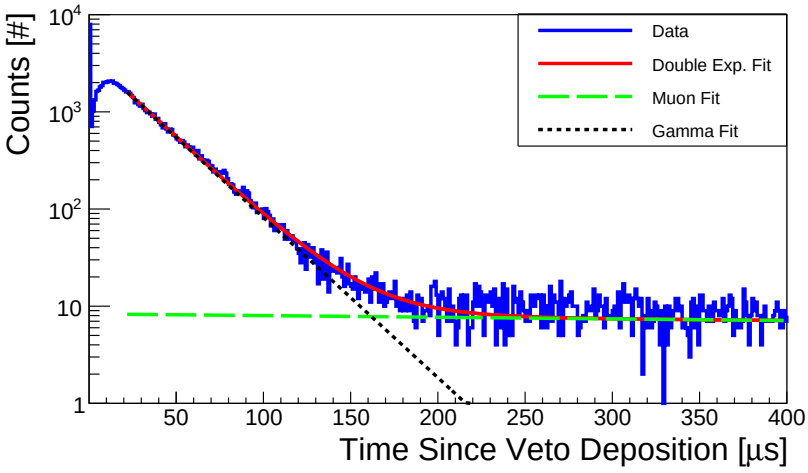

Figure 3.6: The time between depositions in ≥3 multiplicity events and the previous veto deposition. The signal is composed of two exponential distributions. The exponential with the faster time constant is due to charged particle induced neutron captures in the detector. The long time constant exponential is due to the ambient gamma ray flux.

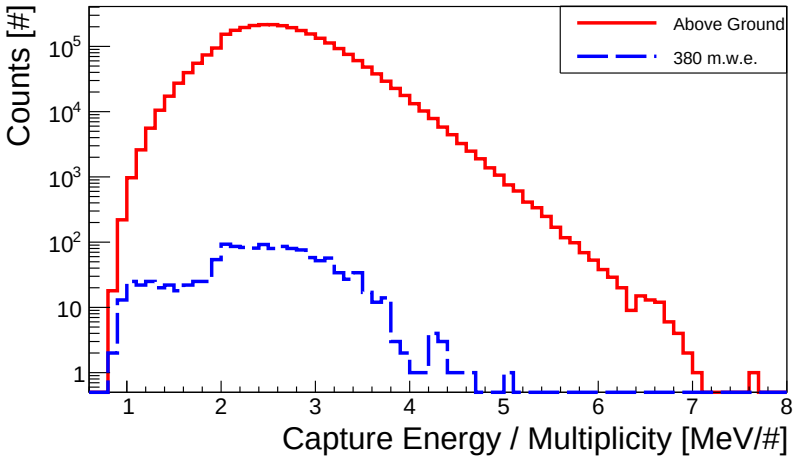

Figure 3.7: The ratio of the capture energy to the multiplicity. This is the average energy deposited by Gd de-excitations on a per event basis. The above ground data is assumed to be predominately from neutrons. The tail below 2.2 MeV/# for the 377 m.w.e. data is assumed to be from the ambient gamma ray noise.

The above ground data is assumed to be of higher quality than the below ground data: the incident neutron flux is orders of magnitude stronger, the ambient gamma ray flux is on the same order of magnitude, and the charged particle veto still removes cosmogenic charged particles. Thus the above ground data has a higher percentage of neutron induced data than

the 377 m.w.e. data; there is an unexpected number of events in the 377 m.w.e. data at values below 2 MeV/#. These events below 2 MeV/# are likely 3 depositions all due to the ambient uncorrelated gamma-ray flux. This is only possible due to the long measurement times of the below ground experiments. Above ground, the neutron flux is sufficient to not require these long measurement times. To remove this data below ground, the MARS analysis conservatively removes all events below 2.2 MeV/#.

Due to the expanding time range triggering algorithm used to identify neutron events, simple statistical analyses for the prediction of the background by ambient gamma-rays and charged particles is not possible. Simple Monte Carlo models were constructed to predict background contributions for this data and are more fully described in Appendix B.

3.4 The General MCMC Algorithm

With an optimized set of measured variables and an optimized triggering algorithm, it is time to return to solving the inverse problem. To overcome the limitations of SVD, more recent algorithms have adopted iterative approaches. By adopting an iterative approach, it is possible to constrain the reconstructed answer to the real-positive space and to account for Poisson statistics. Due to different iteration schemes, the field of iterative algorithms is littered with algorithms that are marginally different. In general these algorithms define a function to be maximized, an iterative update algorithm, and some method of incorporating a priori information, either through how many iterations the algorithm performs or explicitly including an a priori model.

The following section introduces general concepts of MCMC [55, 56], defines the iteration scheme commonly called a jump proposal, and defines how jump proposals are accepted or rejected. MCMC algorithms are attractive when compared to other iterative algorithms due to their ability to intuitively calculate uncertainty in the final result $\vec{f}$. Other iterative algorithms are not presented here.

Introduction

MCMC can be used to solve a wide array of problems. In the context of inverse problems, random-walk MCMC algorithms have historically been used [55]. Given an initial guess for $\vec{f^0}$, a random-walk algorithm produces a new guess $\vec{f^1}$ by making a small perturbation to $\vec{f^0}$. The new guess $\vec{f^{i+1}}$ is only dependent upon the previous guess $\vec{f^i}$. Additionally, the probability to move from $\vec{f^{i+1}}$ to $\vec{f^i}$ is typically required to be the same as moving from $\vec{f^i}$ to $\vec{f^{i+1}}$.

MCMC algorithms use a Bayesian approach to solve Eq. 3.2, here with regularization:

$$p(\vec{f}|\vec{g}_{meas}, \vec{b}, \alpha) = \frac{p(\vec{g}_{meas}, \vec{b}|\vec{f})p(\vec{f}|\alpha)}{p(\vec{g}_{meas}, \vec{b}|\alpha)}, \tag{3.10}$$

where α is the regularization strength, $p(\vec{f}|\vec{g}_{meas}, \vec{b}, \alpha)$ is the Bayesian posterior probability, $p(\vec{g}_{meas}, \vec{b}|\vec{f})$ is the likelihood given the Poisson statistics of the problem, $p(\vec{f}|\alpha)$ is the regularization prior, and $p(\vec{g}_{meas}, \vec{b}|\alpha)$ is the marginal likelihood.

The likelihood for Poisson statistics is defined by:

$$p(\vec{g}_{meas}, \vec{b}|\vec{f}) = \prod_{i=1}^{N} \left(e^{-\left((\mathbf{A}\vec{f})_i + \vec{b}\right)} \right) \frac{\left((\mathbf{A}\vec{f})_i + \vec{b}\right)^{\vec{g}_{meas,i}}}{(\vec{g}_{meas,i})\,!}, \tag{3.11}$$

where i is the vector element and $\mathbf{A}\vec{f}$ is the forward projected answer. This likelihood computes the probability of measuring each individual element of $\vec{g}_{meas,i}$ assuming a Poisson distribution with mean $(\mathbf{A}\vec{f} + \vec{b})_i$ The regularization can take many forms, here a Tikhonov curvature regularization is used:

$$p(\vec{f}|\alpha) \propto exp\Big(- \alpha \int f''(E) dE \Big) = exp(-\alpha \vec{f}^T \Omega \vec{f}), \tag{3.12}$$

where Ω is the curvature matrix [54]. The marginal likelihood is handled by the MCMC algorithm and is not formally defined in this work. It is not dependent upon the current answer $\vec{f}$ and is a constant value given the same measured values and regularization value: $\vec{g}_{meas}$, $\vec{b}$, α.

Satisfying the general iteration constraints, when new guesses are proposed the value of the maximization function is compared between the two states. If $\vec{f}^1$ moves into an area with a higher posterior probability value, the move is accepted. If the move is to an area with a lower posterior probability value, the move is conditionally accepted. In this manner MCMC random-walk algorithms iterate towards the maximum of the function while also exploring the function. This exploration allows for the formation of uncertainty.

Jump Proposal

In order to iterate and find the best solution, MCMC algorithms define a jump proposal that produces the translation $\vec{f}^i \rightarrow \vec{f}^{i+1}$. Many different proposals exist, but the simplest conceptual proposal is the Metropolis-Hastings algorithm [56]. This algorithm is traditionally used when the Bayesian posterior cannot be approximated by a distribution that can be easily sampled or when large correlations exist between elements of $\vec{f}$. Metropolis-Hastings conventionally defines the jump proposal to be symmetric

$$J(\vec{f}^i|\vec{f}^{i+1}) = J(\vec{f}^{i+1}|\vec{f}^i), \tag{3.13}$$

where J is the jump proposal. Note it does not have to be symmetric [56]. Typically the jump proposal is a Gaussian centered on $\vec{f}^i$ where the user must tune the widths of the n dimensional Gaussian.

Acceptance Criterion

After generating a new proposal $\vec{f}^{i+1}$, the proposal must be accepted or denied. The acceptance criteria can be formulated:

$$A(\vec{f}^{i+1}|\vec{f}^{i}) = \frac{p(\vec{f}^{i+1}|\vec{g}_{meas},\alpha)J(\vec{f}^{i}|\vec{f}^{i+1})}{p(\vec{f}^{i}|\vec{g}_{meas},\alpha)J(\vec{f}^{i+1}|\vec{f}^{i})} = \frac{p(\vec{g}_{meas}|\vec{f}^{i+1})p(\vec{f}^{i+1}|\alpha)J(\vec{f}^{i}|\vec{f}^{i+1})}{p(\vec{g}_{meas}|\vec{f}^{i})p(\vec{f}^{i}|\alpha)J(\vec{f}^{i+1}|\vec{f}^{i})}, \tag{3.14}$$

where $A(\vec{f}^{i+1}|\vec{f}^{i})$ is acceptance criteria for moving from $\vec{f}^{i}$ to $\vec{f}^{i+1}$. Recalling that the proposal is generally symmetric and has an equal probability of being reversed, the Metropolis-Hastings algorithm can drop the jump proposals from Eq. 3.14. The new accepted answer vector is assigned given the following criteria:

$$\vec{f}^{i+1} = \begin{cases} \vec{f}^{i+1}, & A(\vec{f}^{i+1}|\vec{f}^{i}) \geq 1 \\ \vec{f}^{i+1}, & A(\vec{f}^{i+1}|\vec{f}^{i}) \geq R \\ \vec{f}^{i}, & A(\vec{f}^{i+1}|\vec{f}^{i}) < R \end{cases} \tag{3.15}$$

where R is a uniform random number sampled between 0 and 1.

Given the jump proposal and acceptance criteria, the MCMC algorithm starts with an initial guess $\vec{f}^{0}$, a user defined regularization parameter α, and a user defined jump proposal Gaussian width. A new guess is proposed $\vec{f}^{1}$ and either accepted or denied. The algorithm repeats until $\vec{f}^{i}$ converges, then continues to sample until a statistically significant number of iterations have been performed. The period of iteration until convergence is commonly referred to as burn-in; these samples are discarded. The samples after burn-in can be used to determine statistically significant parameters for example the mean and variance of $\vec{f}$. Many different convergence diagnostics exist to analyze MCMC chains. The MARS analysis described in the next section uses entirely graphical means to determine convergence. These methods are simple; the analysis most likely over-iterates the chain. The four methods used after burn-in to determine convergence for each $\vec{f}_i$ are: a histogram of the value of $\vec{f}_i$, a graph of $\vec{f}_i$ as a function of iteration, a graph of the auto-correlation of $\vec{f}_i$ as a function of iteration, and a graph of the running mean of $\vec{f}_i$ as a function of iteration.

3.5 The Specific MCMC Algorithm

The MARS analysis uses a slightly more complicated MCMC algorithm, which was originally developed by Kuusela [57]. This algorithm was used because it optimizes the regularization parameter α, removes the bias introduced by the regularization using a boot-strapping technique [58], calculates uncertainty in the final unfolded answer $\vec{f}$, and defines a jump proposal with no user-based tuning parameters. Additionally the algorithm uses cubic basis splines [59] to produce a third order continuous approximation to $f(E)$ from Eq. 3.1:

$$f(E) = \sum_{i=1}^{P} \vec{f}_i \beta_i(E), \tag{3.16}$$

where $\beta_i(E)$ is the i-th cubic basis spline function and $\vec{f_i}$ is the i-th basis spline coefficient. The regularization curvature matrix Ω in the cubic basis spline parameterization is defined by:

$$\Omega_{i,j} = \int \beta_i^{''}(E)\beta_j^{''}(E)dE, \tag{3.17}$$

where $\beta_i^{''}(E)$ is the second derivative of the i-th cubic basis spline.

The Jump Proposal

Due to the MARS algorithm being nearly identical to the algorithm presented by Kuusela, only the jump proposal with noise subtraction is presented here. These elements were neglected in the original Kuusela documentation. For the finer points of the general derivation the reader is directed to [57]. The Kuusela algorithm uses a Metropolis-within-Gibbs MCMC sampler. The acceptance criterion is the same as Eq. 3.14. The conceptual design of the sampler as derived in Saquib *et al.* [60] is to approximate the Bayesian posterior $p(\vec{f}|\vec{g}_{meas}, \vec{b}, \alpha)$ by distributions that can be sampled. Saquib *et al.* described a 2-D problem with a generic regularization. However MARS is a 1-D problem with a specific regularization. Due to this difference, and in an effort for completeness, the necessary equations to use the sampler are presented below.

Metropolis-within-Gibbs sampling updates each basis spline coefficient $\vec{f_l}$ separately. By taking the second order Taylor-series expansion of the log of the full posterior probability, the sampling distribution can be formulated as a truncated Gaussian distribution for non-negative values:

$$\begin{aligned} &log\left(p(\vec{f_l}|\vec{f^i_{-l}}, \vec{g}_{meas}, \vec{b}, \alpha)\right) \approx \\ &d_1(\vec{f_l} - \vec{f^i_l}) + \frac{d_2}{2}(\vec{f_l} - \vec{f^i_l})^2 - \alpha\left(\vec{f_l}\Omega_{l,p}\vec{f_l} + \sum_{p=1,p\neq l}^{P}\vec{f_l}\Omega_{l,p}\vec{f^i_p} + \sum_{p=1,p\neq l}^{P}\vec{f^i_p}\Omega_{p,l}\vec{f_l}\right) + C, \end{aligned} \tag{3.18}$$

where the superscript i denotes the current answer, the subscript l denotes an element of the answer vector, the subscript $-l$ denotes all elements of the answer vector except l, d_1 and d_2 are the first and second derivative of the measured data as a function of $\vec{f^i_l}$, and C is a constant due to the marginal likelihood. The first and second order derivatives are defined in the following fashion:

$$d_1 = -\sum_{n=1}^{N}\mathbf{A}_{n,l}\left(1 - \frac{\vec{g}_{meas,n}}{\left((\mathbf{A}\vec{f})_l + \vec{b}\right)}\right), \tag{3.19}$$

and

$$d_2 = -\sum_{n=1}^{N}\vec{g}_{meas,n}\left(\frac{\mathbf{A}_{n,l}}{\left((\mathbf{A}\vec{f})_l + \vec{b}\right)}\right)^2, \tag{3.20}$$

where $\vec{g}_{meas,n}$ is the n-th element of the measurement vector and $(\mathbf{A}\vec{f})_l$ is the l-th element of the forward projected vector. Equation 3.18 can be formulated as a Gaussian. By taking the partial derivative of Eq. 3.18 as a function of $\vec{f_l}$ and finding the maximum, the mean of the Gaussian can be found:

$$m = \frac{d_1 - d_2\vec{f_l^i} - 2\alpha \sum\limits_{p=1,p\neq l}^{P} \Omega_{l,p}\vec{f_p}}{2\alpha\Omega_{l,l} - d_2}, \tag{3.21}$$

where m is the mean, and all parameters have been previously defined. The variance is defined by:

$$\sigma^2 = \frac{1}{2\alpha\Omega_{l,l} - d_2}. \tag{3.22}$$

The above equations result in the following jump proposal for one element of $\vec{f}$:

$$J(\vec{f_l}|\vec{f^i_{-l}}) = \begin{cases} \frac{1}{C(\sigma,m)} exp\left(\frac{-(\vec{f_l}-m,)^2}{2\sigma^2}\right), & m > 0, \vec{f_l} > 0 \\ \frac{1}{\beta} exp\left(\frac{-\vec{f_l}}{\beta}\right), & m < 0, \vec{f_l} > 0 \\ 0, & \vec{f_l} < 0 \end{cases} \tag{3.23}$$

where $C(\sigma, m)$ is the truncated Gaussian normalization coefficient and β is an exponential decay coefficient. β is defined by:

$$\beta = -m\left(2\alpha\Omega_{l,l} - d_2\right), \tag{3.24}$$

where all parameters have been previously defined.

With the above equations an iteration of the MCMC algorithm can be completed. A jump proposal is calculated for an element of the answer vector $\vec{f^i}$. If the Metropolis-Hastings acceptance criterion is met, $\vec{f_l^i}$ is updated with the new element $\vec{f_l}$. The new answer vector $\vec{f^i}$ is then used to generate jump proposals for the next element $\vec{f}_{l+1}$. This iteration is continued until all elements of the answer vector $\vec{f^i}$ have generated jump proposals which have been accepted or rejected by the Metropolis-Hastings acceptance criterion. The iteration through all vector elements is considered one MCMC iteration: the individual jump proposals are not used to update statistics or diagnostics of the MCMC algorithm.

The Steps of the Algorithm

With the above jump proposal, the general steps of the algorithm are outlined below:

1. Start with an initial guess for $\vec{f^{i=0}}$ and α
2. Optimize the regularization parameter α
    a) Run the MCMC algorithm, record S iterations after burn-in

b) Update $\alpha = \frac{PN}{2\sum_{s=1}^{S}(\vec{f}^s)^T\Omega\vec{f}^s}$

c) Start at step 2a, continue until α converges resulting in: α_{best} and $\vec{f}^{k=0}$. Use α_{best} in the rest of the algorithm.

3. Reduce the bias induced by the regularization by using a iterative bootstrapping technique

a) Set $\vec{g}^k_{sim} = \mathbf{A}\vec{f}^k$

b) Poisson sample the elements (boot-strap) of $\vec{g}^k_{sim}$ and the original $\vec{b}$ separately. Set $\vec{g}^k_{meas} = \vec{g}^k_{sim} + \vec{b}$

c) Run the MCMC algorithm

d) Perform steps 3a-c Z times and approximate the $bias^k = (\frac{1}{Z}\sum_{z=1}^{Z}\vec{f}^z) - \vec{f}^k$

e) Calculate $\vec{f}^{k+1} = \vec{f}^0 - bias^k$

f) Start at step 3a and continue until $\vec{f}^k$ converges resulting in: $\vec{f}^k_{BC}$

4. Estimate the uncertainty in the final answer $\vec{f}^k_{BC}$

a) Perform steps 3a-c multiple times to build a distribution of $\vec{f}^k_{BC}$

b) Use this distribution to construct confidence intervals

Following the convention presented earlier in the generic MCMC approach a superscript of i indicates the MCMC iteration. A superscript of k represents bias reduction iterations. For step 2, the MARS analysis records 70,000 iterations after burn-in of the MCMC iterations and performs 5-10 α update iterations. For step 3, the MARS analysis uses 20 boot-strap samples (Z) and performs the bias iteration 5-10 times. The final uncertainty analysis uses 2000 boot-strap samples as prescribed by Efron and Tibshirani [58] to generate confidence intervals. Confidence intervals are calculated by using the bootstrap percentile intervals and the third order continuous solutions of Eq. 3.16. The set of functions F from the final 2000 sample boot-strap are evaluated at E in increments of 1 MeV to find the x and $1-x$ percent evaluations at each E. Intervals are constructed by:

$$[f(E)_{BC,x}, f(E)_{BC,1-x}] \tag{3.25}$$

where $f(E)_{BC,x}$ is x percent function evaluation at E.

Chapter 4

The Multiplicity and Recoil Spectrometer

MARS was designed to be an efficient, transportable high-energy neutron spectrometer. To meet these desired characteristics MARS employs the spallation based multiplicity technique described in Chapter 3. The MARS detection medium consists of plastic scintillator sheets interleaved with Gd coated Mylar sheets. Two such units are arranged around a lead target in which secondary neutrons are generated by the incoming high-energy neutrons of interest. A schematic of MARS is shown in Fig. 4.1. The following chapter describes the physical

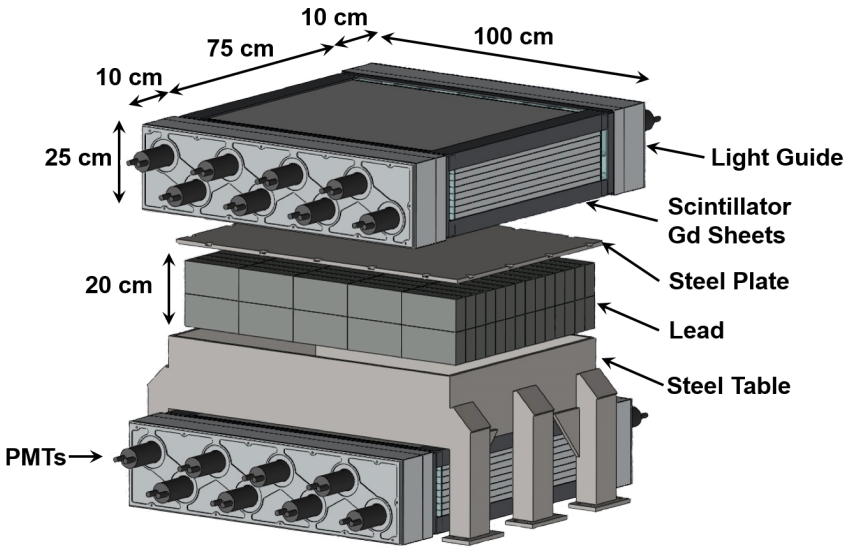

Figure 4.1: An exploded view illustration of the detectors, frame, and lead.

dimensions of MARS, the electronics and read-out used by MARS, discusses experimental adjustments to the data to provide a consistent signal, presents the position-dependent

energy calibration, presents the neutron capture efficiency and capture time calibrations, and ends with a description of the charged particle veto.

4.1 Detector Design

The neutron detection system of MARS consists of two plastic scintillator/Gd detectors with dimensions $100 \times 75 \times 25$ cm^3 mounted above and below a $101 \times 71 \times 20$ cm^3 lead converter supported by a steel table. The neutron detectors each consist of twelve 2 cm thick BC-408 plastic scintillator sheets interleaved with thin Mylar sheets coated with a Gd loaded paint. Each 100×25 cm^2 face is coupled to a $100 \times 25 \times 10$ cm^3 acrylic light guide. Eight 5 inch diameter ADIT B133D01 photo multiplier tubes (PMTs) [61] are coupled to the light guides by silicon grease.

The two neutron detectors are held together by a steel frame. The frame is mounted to the top and bottom of the lead containing steel table. An exploded view of the assembly of the detectors, table, and lead are shown in Fig. 4.1. The table is bolted to the frame of the deployment platform. The deployment platform was a ∼30 ft long stock trailer and is shown in Fig 4.2.

The muon veto system consists of seven $72 \times 24 \times 1$ inch^3 plastic scintillator paddles coupled to fishtail light guides and PMTs on each end. These seven paddles surround the detector on the top and sides. Four more paddles with dimensions $31 \times 28 \times 2$ inch^3 cover

Figure 4.2: A view of the MARS deployment platform below ground.

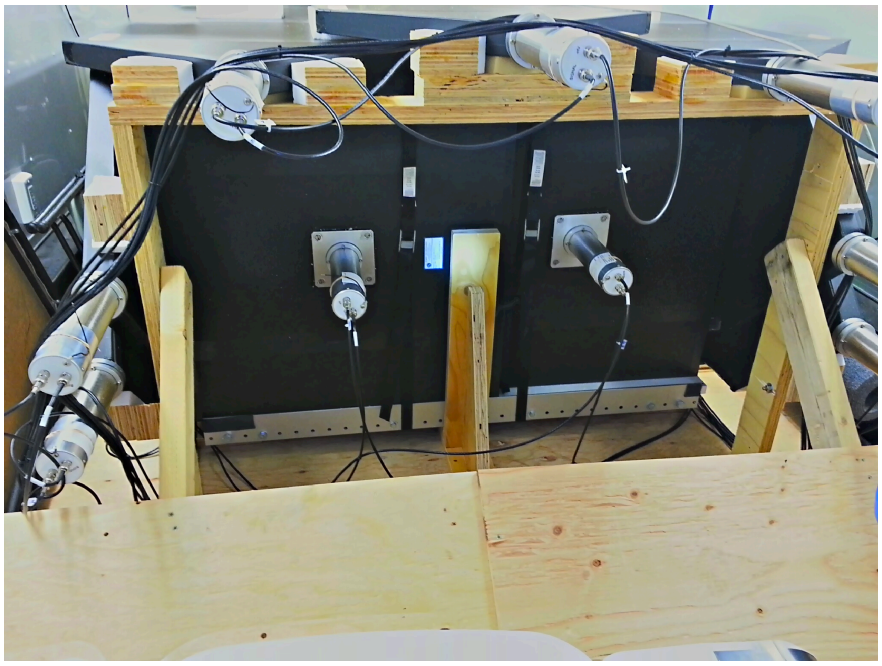

Figure 4.3: A view from one end of the assembled MARS veto.

the ends of the detector; a single PMT is mounted in the center of the paddle. A view of the assembled veto system from the back of the deployment platform is displayed in Fig. 4.3.

4.2 Electronics and Read-Out

The MARS Data Acquisition system (DAQ) is composed of four 14 bit, 250 MHz Struck SIS3316 sixteen channel Waveform Digitizers (WFD) [62] and a CAEN 1495 General Purpose Board programmed to produce a 240 MHz clock for board synchronization [63]. This clock synchronization forces all of the WFDs to record samples at 240 MHz. Each neutron detector is readout by one WFD, while the veto detectors fill the two remaining WFDs.

Firmware programming in the SIS3316 WFD calculates and records accumulated charge values for 8 independently configurable time ranges. The time ranges were:

1. 104 ns time range before the trigger
2. 25 ns time range after the trigger
3. 55 ns time range after the trigger
4. 80 ns time range after the trigger
5. 104 ns time range after the trigger

6. 208 ns time range after the trigger
7. 312 ns time range after the trigger
8. 208 ns time range starting 312 ns after the trigger

Full waveforms are not recorded to reduce data rates. To characterize the signal, three of the time ranges are used by the current analysis: a 104 ns pre-pulse recorded before the trigger to measure the WFD pedestal, 312 ns after the trigger to integrate the pulse, and a final 312 ns time range beginning 312 ns after the trigger is used to indicate pulse pileup. All WFDs use group triggering: the signals of all sixteen PMTs in a neutron detector are recorded if any group of four PMTs exceeds a threshold. The veto group triggering is slightly different: the associated group of four PMTs is recorded only if that group passes the associated threshold. The top veto fishtail panels are recorded as 2 groups. Each overlapping pair of side veto fishtail panels belong to a group and each overlapping pair of square veto panels belong to a group. By using this group triggering scheme for the detection system, dark-noise triggering is reduced.

During the course of the MARS measurements it was observed that the neutron detectors WFDs were not precisely synced with the veto WFDs. An offset of $\sim$160 ns was observed between coincident signals. This was corrected in the experimental data processing to a time separation of $\sim$10 ns. This time separation was chosen so that coincident events, most likely due to cosmogenic charged particles, are appropriated removed from the neutron data. In general this time separation and non-discrete nature of the triggering is not considered by the MARS Monte Carlo model (Chapter 5. However, it is necessary to consider this time separation for the cosmogenic charged particle background simulations (Appendix B).

4.3 Experimental Data Adjustments

To ensure a time-independent response over a large dynamic range for the PMTs in MARS, two pre-processing adjustments were made to the data: accounting for gain drift over the life of the experiment and the non-linear response of the PMTs to light. The following text describes the gain drift and linearity corrections.

Time-Dependent Gain Corrections

To account for changes in the detector configuration that cause gain drift (PMT drift, mechanical coupling, etc.), a time-independent response is traditionally achieved by gain matching the PMTs by the single photo-electron (PE) spectra before and during an experiment. However, the gain of the 5 inch diameter PMTs was not sufficient to observe single PEs over the noise of the WFD and associated electronics. A rough estimate of the measured single PE response was obtained for a subset of the PMTs using an oscilloscope in place of the WFDs. This estimated PE response is used to compare gain drift in the following text.

In the absence of a single PE peak the muon energy distribution was found to be the most consistent feature throughout a measurement period. While the mean muon energy and angular distribution can change depending on the deployment scenario, muons passing perpendicularly through both neutron detectors and the lead deposit roughly the same energy corresponding to the peak at 10,000 PE in Fig. 4.4a. The rate at which muons interact in only one neutron detector, depositing a significantly larger or smaller energy than perpendicular muons, changes the tails of the muon peak distribution in Fig. 4.4a but does not significantly change the peak position.

Muon events were identified by large energy depositions in the detector in coincidence with the surrounding veto. Each PMT's gain was adjusted based upon the position of the peak in the muon energy distribution relative to its position at the beginning of initial construction. The threshold for muon identification was applied to the detector energy (sum of all 16 PMTs) shown in Fig. 4.4a to the right of the dotted vertical line. The detector count rate with a coincident muon veto event is displayed as a function of energy in Fig. 4.4b for a representative PMT from the neutron detector. The blue data with no marker is uncorrected data from the 1450 m.w.e. depth of KURF. The red data with a triangle marker was taken at KURF at the 540 m.w.e. depth. The 540 m.w.e. depth was selected as the reference gain template. Due to the increased rock overburden, the uncorrected data from the 1450 m.w.e. depth had roughly an order of magnitude lower muon rate than the template data. A transformation described by Eq. 4.1 was applied to all points in the blue unmarked data to produce the corrected black square marker data:

$$\begin{aligned} x \rightarrow &\quad Gx, \\ y \rightarrow &\quad aGy, \end{aligned} \tag{4.1}$$

where x and y before the transformation were the measurement in PE and rate respectively, and after the transform are the corrected measurement in PE and rate respectively, a is the vertical overburden scaling factor, and G is the PMT gain factor. A χ^2 minimization, with respect to a and G, was performed using ROOT's MINUIT2 [64] package from ∼150 PE to ∼1000 PE to produce the correction. The χ^2 function used was

$$\chi^2 = \sum_i \left(\frac{y_{corr,i} - y_{temp,i}}{\sigma_{corr,i}} \right)^2, \tag{4.2}$$

where the subscript i refers to the bin number, $y_{corr,i}$ is the i-th bin of the shifted weekly count rate, $y_{temp,i}$ is the i-th bin of the template count rate, and $\sigma_{corr,i}$ is the i-th bin of the error in the shifted weekly count rate.

Gain matching the muon energy distribution was performed on a 7-14 day basis depending on the muon rate and it was assumed that the gain was relatively constant over this time span. An example time dependent gain correction is displayed in Fig. 4.4c for the same PMT as Fig. 4.4b. The detector and deployment platform were moved at week 23 resulting in the gain shift observed. Slow gain degradation was observed for a stationary detector over a many week period. The degradation was assumed to be the result of mechanical

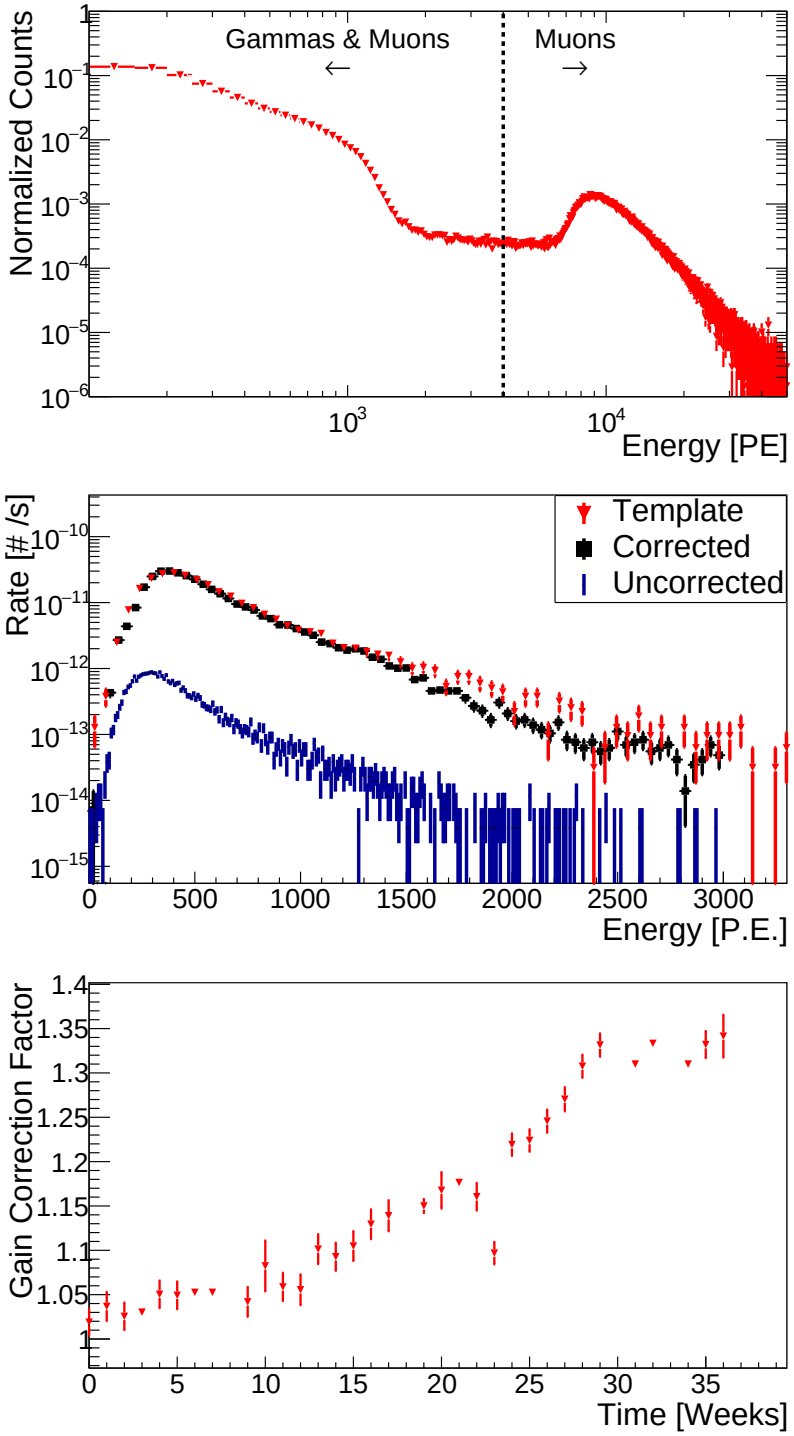

Figure 4.4: (a) The total neutron detector energy spectrum is shown. The edge at 1,000 PE is due to Gd de-excitations and the peak at 10,000 PE is due to through going muons. (b) A representative gain correction plot for a PMT in the neutron detector is shown. The blue data with no marker is the pre-corrected data, the red data with a triangular marker is the template data, and the black data with the square marker is the corrected data. (c) Displays the gain correction factor G as a function of time in weeks for the same PMT (b). The gain degradation is assumed to be due to mechanical decoupling.

decoupling. At the end of the 37 weeks displayed in Fig. 4.4c, the average gain correction for the neutron detector PMTs was 1.26 ± 0.12. The gain drift for all PMTs over the live-time of the detector is presented in Appendix D. The average gain drift for all PMTs is presented in Fig. 4.5.

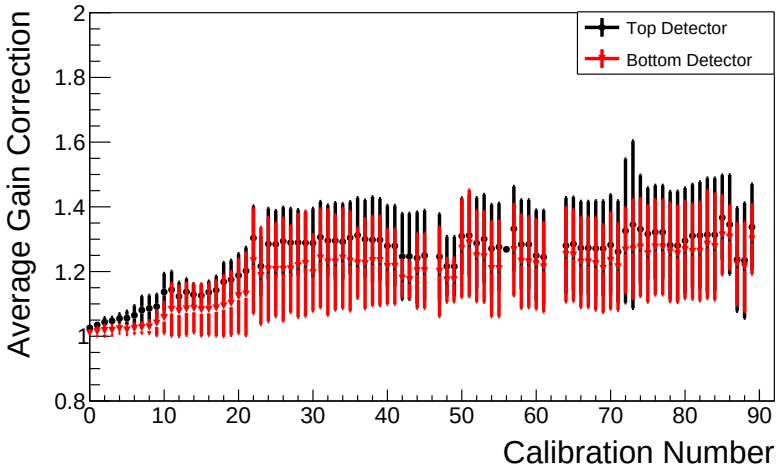

Figure 4.5: Gain drift average for all PMTs as a function of time.

Examining Fig. 4.5, the average gain correction appears to roughly stabilize 23 weeks after the template data was taken. Before this stabilization, the gain correction factor shows a steady trend towards higher values. The initial gain correction factor increase may be due to a host of problems. It is worth noting, for the initial 23 weeks the deployment platform air conditioner (AC) was turned on. This was to dissipate heat from the electronics. However, the AC air filter became clogged with diesel soot and slightly melted, which destroyed the filter. Without the filter, the AC forced diesel soot throughout the trailer, ultimately causing problems in the electronics crates. After week 23, the AC was turned off and problematic electronics components replaced. It appears that after this replacement the gain roughly stabilizes. Any gain shifts after this stabilization are most likely an artifact of the measurement times: the average gain still shifts after moving the detector. The detector was moved to different locations at weeks 23, 37, and 86.

Non-Linear PMT Response

Non-linear response in PMTs can occur when sufficient charge is introduced into the dynode structure to induce space-charge effects. In this situation, large numbers of electrons decrease the accelerating electric field limiting further electron generation on the dynodes [65]. To measure the PMT non-linearity, PMT calibrations were performed before the MARS detector was assembled. Various combinations of multiple light emitting diodes (LEDs) were used to measure the PMT response to a wide range of light levels, and to determine the relationship

between these combinations and single LEDs at a fixed drive pulse voltage. For example, if the PMT response to a pair of LEDs pulsing is less than the sum of the PMT response to those LEDs pulsing separately, that would reveal a non-linearity in the PMT response.

Each PMT and three independently driven LEDs were placed horizontally in a light tight box. The LEDs were closely spaced together as shown in Fig. 4.6 and independently connected to a fast square pulse generator. All combinations of the three LEDs were pulsed

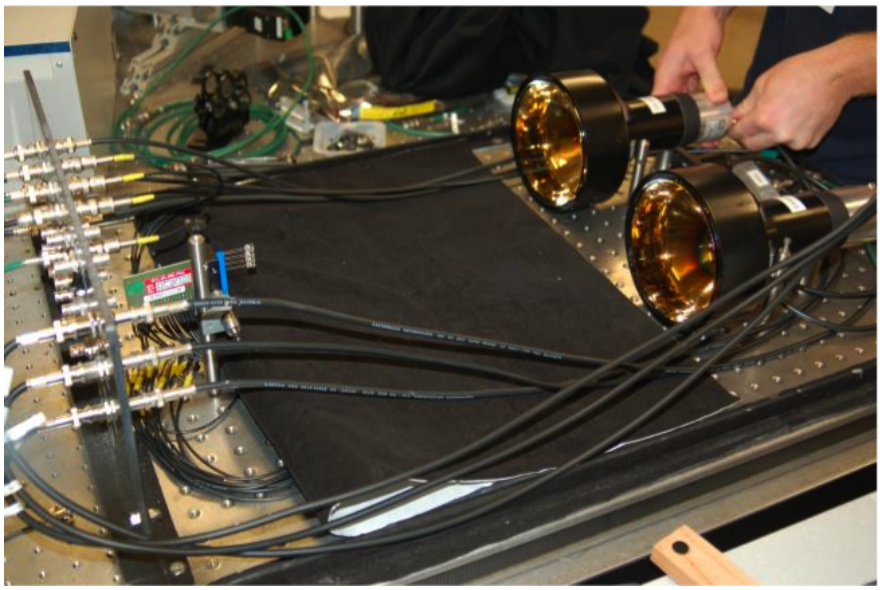

Figure 4.6: The apparatus for measuring the PMT linearity is shown above. The LEDs are closely spaced together and the PMTs are firmly held. A light-tight black cover was placed around the setup.

at a fixed LED voltage and the PMT response was recorded by the DAQ. That is, the response was recorded for each LED pulsing individually, each pair pulsing simultaneously, and all three pulsing simultaneously. All permutations were covered within a few minutes at a given drive pulse voltage to minimize the effect of the variation of LED light output with ambient temperature. Initially the LEDs were driven at low voltages so that only a small signal was observed; here the PMT was assumed to operate in a linear regime. The driving voltage was adjusted so that the range of light outputs spanned by the LED permutations at a given voltage overlapped with those at adjacent voltages. In this way the non-linear response curve of the PMT was measured via "boot-strapping" upwards from the few PE level. Results are plotted in Fig. 4.7 for a representative PMT. Linearity corrected values were found by spline interpolating Fig. 4.7 using ROOT's TGraph [64]. The non-linearity curves for all PMTs is presented in Appendix E.

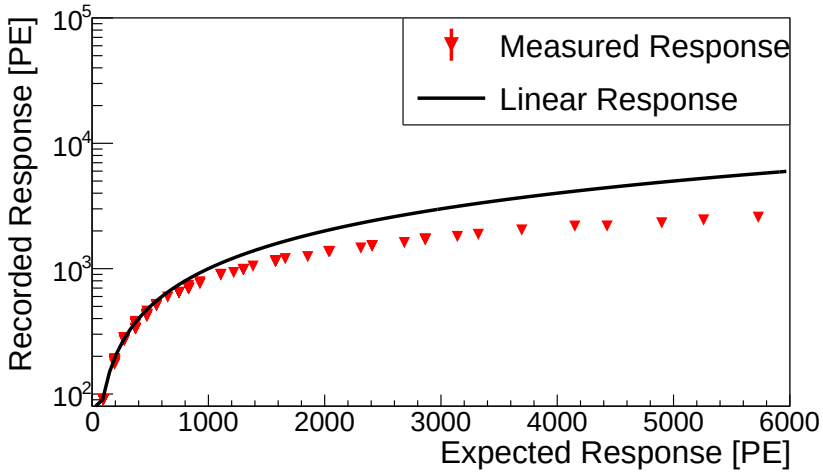

Figure 4.7: The measured PMT non-linear response as a function of light. The black line shows a perfectly linear response. The red triangular data points correspond to the PMT measured non-linearity. Errors for the red triangular data are too small to be observed over the marker.

4.4 Energy Calibration of the Experiment

Using the Monte Carlo model of MARS (Chap. 5) and the accompanying DAQ simulation (Sec. 5.3), several experimental calibrations were performed and compared to simulation in order to create and tune detector response models. A position-dependent model was created for converting the measured WFD value into measured energy. Next, an experiment was performed using a Cf-252 source to tune the Monte Carlo model Gd loading. With these two experiments, the experimental WFD values can be converted to energy, the MARS Monte Carlo model can approximate the position-dependent response to radiation in the detector, and the Monte Carlo model has an appropriate neutron capture efficiency and capture time. The following section describes the position-dependent energy calibrations.

Using the gain drift and linearity corrections, four sets of measurements and simulations were performed to characterize the detector and veto position-dependent energy response. The energy response at the center of all detector elements was used to transform the measured WFD value to energy and the position-dependent response was used on subsequent simulations to approximate the detector light transport. All energy calibrations performed in this section utilized a Co-60 and a Cs-137 gamma ray source. Due to a maximum gamma energy of 1.33 MeV the below calibrations are considered to have considerable uncertainty at energies above the Gd de-excitation Q value. For all measurements and simulations acceptable fits were found over the range of the Compton valley to the Compton Edge. The following measurements were performed:

1. The detector response in the center of the top neutron detector

2. The position dependent response relative to measurement 1 in the top neutron detector
3. The position dependent response of the 72 × 24 × 1 in^3 veto paddles
4. The position dependent response of the 31 × 28 × 2 in^3 veto paddles

All measurements used the same algorithm to determine the energy calibration and detector response: a χ^2 minimization was performed while linearly shifting the data and convolving the simulation response with a Gamma distribution. To describe the linear shift and convolution four free parameters were used:

1. m: the conversion from the WFD value to calibrated energy
2. b: the constant shift for the calibrated energy
3. c: the constant convolution parameter
4. d: the energy-dependent convolution parameter

The χ^2 function used was

$$\chi^2 = \sum_i \left(\frac{E_{exp,i} - E_{sim,i}}{\sigma_{exp,i}} \right)^2, \tag{4.3}$$

where E_{exp} is the shifted experimental spectrum, E_{sim} is the convolved simulated spectrum, and σ_{exp} is the shifted experimental energy spectrum error. The experimental WFD spectrum was shifted by

$$E_{exp} = m * WFD + b, \tag{4.4}$$

where WFD is the value of the WFD pulse integral as described in Sec. 4.2. The simulation energy spectrum was convolved with a Gamma distribution

$$E_{sim} = \int S(E) * G(E, k, \theta)\ dE, \tag{4.5}$$

where $S(E)$ is the energy dependent original simulation energy spectrum, $G(E, k, \theta)$ is the energy-dependent Gamma distribution, k is the Gamma shape parameter, and θ is the Gamma scale parameter. A Gamma distribution is the appropriate distribution due to the triggered energy and WFD values being bound to real-positive values: it is has support $(0,\infty)$. The commonly used Gaussian distribution is not appropriate because it has support $(-\infty,\infty)$. The Gamma distribution parameters were calculated using the fit parameters c and d:

$$\begin{aligned} \sigma = c + d\sqrt{E} = \sqrt{k}\theta, \\ \mu = E = k\theta. \end{aligned} \tag{4.6}$$

The first measurement for the energy calibration was in the center of the top neutron detector using the above algorithm. A collimator with slit dimension 8 × 0.4 $inch^2$ was fashioned out of four 8 × 4 × 2 $inch^3$ lead bricks to restrict the measured detector response

to the center of the detector. The four lead bricks were placed with the 8×4 inch^2 face in contact with the detector. The collimator was placed at the center of the detector, with the 8 inch length running parallel to the detector 100 cm side, and 1 μCi of Cs-137 and Co-60 were separately measured. The convolved simulated energy and calibrated experimental spectrum are shown in Fig. 4.8. The Gamma distribution used in Eq. 4.5 was found to be a poor model of the energy resolution observed in regions outside the Compton edge. A more robust model to fully describe the light collection efficiency, which controls the energy resolution, was not considered feasible given the complicated internal geometry of the scintillator sheets, acrylic, and associated air-grease boundaries.

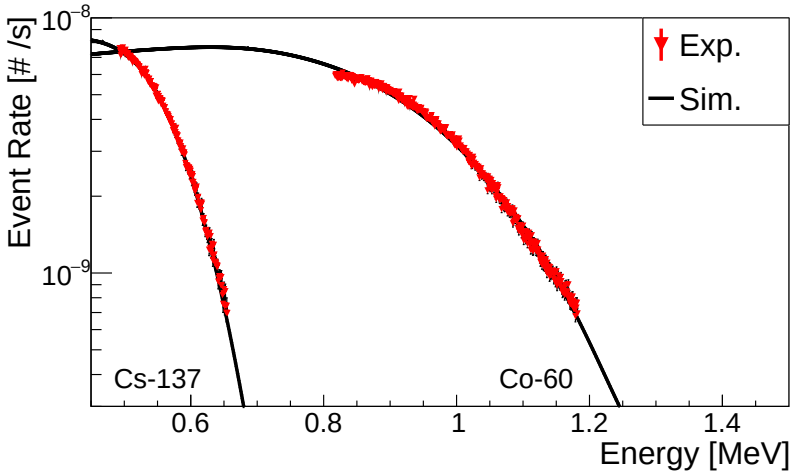

Figure 4.8: The experimental and simulated Cs-137 and Co-60 spectra in the center of the detector with the collimator are shown from left to right respectively. The experimental data is red with a triangle marker and the simulation data is a black solid line.

The second measurement accounted for the position-dependent response relative to the center calibration of the top neutron detector. Spectra from Co-60 were measured in a 5×5 grid on the top neutron detector. On the 1 m side the grid points had a pitch of 9 and 1/3 inch and on the 0.75 m side the points had a pitch of 7 and 1/8 inch. Only Co-60 was used due to a prohibitively long measurement time for the Cs-137 source that was available. Due to the position-dependent calibration only having one source, the number of fit parameters were reduced by fixing the center calibration values and adding one multiplicative factor T:

$$\begin{aligned} E_{exp} &= m_f * T * WFD + b_f, \\ \sigma &= c_f + d_f\sqrt{T * E} = \sqrt{k\theta}, \end{aligned} \tag{4.7}$$

where all parameters with the subscript f denote previously defined parameters from Eqs. 4.4 and 4.6. The subscript f parameters were fixed to the same value as the calibration in the center of the top neutron detector. The only free fit parameter was T. Position-dependent results for the top neutron detector are reported in Appendix F. Later position-dependent

measurements using Co-60, Cs-134, and Cs-137 sources differ from the above calibration by less than 5% for all fit parameters. However, due to the complexity and time required to rerun the analysis these measurements were not incorporated in the simulation response model. Comparisons were made with the bottom neutron detector by observing the change in the energy calibrated spectra using a Cf-252 neutron multiplicity source. Minimal differences in the energy spectra of the Gd de-excitations is observed between the two detectors.

The third measurement used uncollimated Cs-137 and Co-60 sources separately at the center and both edges of the $72 \times 24 \times 1$ inch^3 veto paddles. The last measurement used the same uncollimated sources at the center and one corner of the $31 \times 28 \times 2$ inch^3 paddles. Both the third and fourth measurements used the χ^2 analysis described by Eqs. 4.3-4.6. Position-dependent results for the veto paddles are reported in Appendix F.

Due to the inherent uncertainty introduced by only using one gamma ray source for the position-dependent energy calibration and only two gamma ray sources for the total energy calibration, the MARS inversion analysis bins the measured thermalization energy and capture energy in very coarse segments. This coarse binning reduces the concern of bias or systematic uncertainty in the final answer, but may negatively impact the energy resolution of the incident neutrons.

4.5 Neutron Capture-Efficiency and Capture-Time Calibrations

After determining a model for the position-dependent energy calibration, a Cf-252 source was used given the experimental setup described below to determine the neutron capture efficiency and capture time of MARS. The comparison of the simulation and experimental data given this setup allows for the determination of the Gd loading in the Monte Carlo model. An appropriate Gd loading provides the best approximation of the secondary neutron capture efficiency and capture time regardless of the experimental setup. Using the information from Sec. 3.3 a multiplicity triggering algorithm of 65 μs was chosen for two reasons: the source had a higher flux than the uncorrelated gamma ray background, and the identification algorithm had the highest FOM_{Trig} for multiplicity 3-5 events. Multiplicity 3-5 events are important for the Cf-252 analysis because the mean neutron multiplicity of Cf-252 is 3.757 ± 0.01 [66]. Additionally, for this section only, the multiplicity includes the first deposition in an event: no spallation charged particles are expected in the event.

A Cf-252 source was positioned on top of four lead bricks above the top neutron detector. Lead bricks were used to reduce the number of prompt-fission gamma rays interacting in MARS. In addition to the multiplicity event identification algorithm, a small 2×2 inch^2 cylindrical plastic scintillator detector coupled to a 2 inch PMT was used as a tagging detector to detect prompt fission gamma rays and neutrons. The tagging detector was situated as close to the Cf-252 source as possible. Multiplicity events were recorded if the first deposition started within 75 μs of a coincident deposition in the tagging detector; a

75 μs time range was necessary to ensure nearly uniform detection efficiency regardless of the true multiplicity[1]. Any depositions in the multiplicity event within 100 ns of a coincident deposition in the tagging detector were discarded to remove the prompt fission gamma-ray response. All measured parameters are a function of the solid angle of the source and detector and shielding provided by the lead. Due to this dependence, the complete system is modeled in the simulation.

The Cf-252 multiplicity distribution was determined by:

$$M(n)_{meas} = S\left(\sum_{i=n}^{N_{max}} \beta(i)\epsilon^n + \sum_{j=0}^{j<n} \sum_{i=0}^{N_{max}} \beta(i)\epsilon^j P_{bkg}(n-j)\right), \tag{4.8}$$

where n is the detected multiplicity number, $M(n)_{meas}$ is the measured multiplicity distribution, S is the source strength, N_{max} is the maximum multiplicity considered (10 neutrons), $\beta(i)$ is the Cf-252 known neutron multiplicity distribution [66], ϵ is the neutron detection total efficiency, and P_{bkg} is the Poisson probability for uncorrelated ambient gamma ray depositions. The source strength S and the total efficiency ϵ are unknown. The source noise P_{bkg} is modeled using the measured inter-event time of 478 μs and $\beta(i)$ is modeled using the parameters in Holden [66]. To eliminate the unknown source term S a ratio between different bins of the measured multiplicity spectrum $M(n)_{meas}$ can be used. The resulting ratios are only dependent upon the efficiency ϵ. These equations can be solved graphically. Using the following ratios: M(3)/M(4), M(3)/M(5), and M(4)/M(5) the total efficiency ϵ was calculated to be 12.8 ± 0.5 % and 12.7 ± 0.3 % for the experimental data and simulation respectively. The quoted uncertainty for the total efficiency ϵ only includes statistical uncertainty. The results for each multiplicity distribution ratio are displayed in Table 4.1. Agreement between experimental data and simulation was observed for all ratios within 1σ.

Table 4.1: Various multiplicity ratios were used to calculate the total neutron detection efficiency measured with a Cf-252 source.

Ratio	Exp. ϵ (%)	Sim. ϵ (%)
M(3)/M(4)	13.0 ± 0.4	12.8 ± 0.2
M(3)/M(5)	12.8 ± 0.6	12.7 ± 0.4
M(4)/M(5)	12.6 ± 1.4	12.6 ± 0.8
Average	12.8 ± 0.5	12.7 ± 0.3

Using the same experimental data and simulation, the capture time distribution was

[1]This is a different time value than the fixed or expanding time-range trigger of Sec. 3.3. It is a coincidence requirement for the triggering algorithm, not the triggering algorithm itself.

calculated by

$$P_{capture}(t) = P_{meas}(t) - \sum_{n=3}^{n<N_{max}} \sum_{j=0}^{j<n} \sum_{i=0}^{N_{max}} \beta(i)\epsilon^j P_{bkg}(n-j,t), \tag{4.9}$$

where $P_{capture}(t)$ and $P_{meas}(t)$ are the background corrected and measured capture time distributions respectively, and all other parameters have previously been defined in Eq. 4.8. The capture distributions $P_{capture}(t)$ and $P_{meas}(t)$ are constructed using the individual deposition time after the tagging detector. For example, a multiplicity 3 event would have 3 entries in $P_{meas}(t)$. The experimental and simulated capture times were 18.7 $\pm$ 3.0 μs and 20.0 $\pm$ 0.1 μs respectively and the distributions are shown in Fig 4.9. The relatively small error on the simulated capture time only incorporated statistical uncertainty.

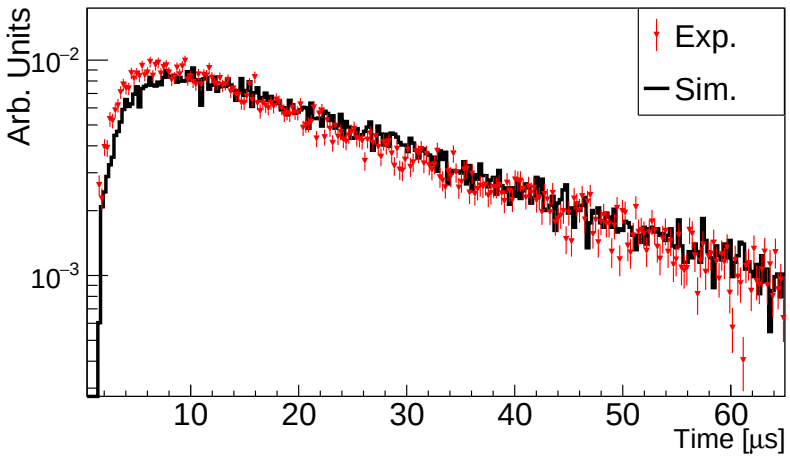

Figure 4.9: Capture time distribution for the experimental data and simulation from tagged multiplicity events from a Cf-252 neutron multiplicity source. Some disagreement exists at short capture times but the exponential shape matches reasonably well.

The modest agreement in the neutron capture time may be due to assuming that the fission neutrons from Cf-252 are emitted isotropically. However, the source was very close to the detector resulting in nearly 2π coverage. It is assumed that the regardless of the non-isotropic neutron emission, the above calibration was sufficient. This reasoning was based upon the excellent and uniform agreement of the calculated efficiency values. Systematic uncertainty for the event triggering efficiency, thus the neutron capture time and efficiency, is considered in individual measurement sections (Sec. 6.3 and Sec. 7.3).

4.6 Charged Particle Veto

In order to efficiently remove noise induced by cosmogenic charged particles, the MARS veto described in Sec. 4.1 and pictured in Fig. 4.3, is used to reject neutron detector events

within 200 μs of a veto deposition. The 200 μs veto time is based upon the time-since-muon distribution displayed in Fig. 3.6. This figure displays the time between depositions in a multiplicity event and the immediately preceding veto deposition. Of particular concern, a significant portion of the veto is only 1 inch thick. Given the muon minimum energy loss of $\sim$2 MeV/cm, muons are expected to deposit $\sim$5 MeV in the MARS veto with a wide Landau distribution. The spread of this deposited energy is very near the maximum ambient gamma-ray energy of 2.6 MeV. The lack of separation between these two values indicates that it will be very difficult to distinguish cosmogenic charged particles from the ambient gamma-ray flux.

To veto as much of the cosmogenic charged particle flux as possible, the muon veto energy hardware threshold was set as low as possible. This energy threshold was ultimately determined by the trigger rate of the veto; the detector trigger rate is fairly constant and the WFDs have a maximum write to disk capability. The veto rate was maximized, the energy threshold was minimized. For the 2 PMT veto panels, which are 1 inch thick, this hardware threshold was $\sim$2.0 MeV. The software threshold was set at the maximum hardware threshold given the gain drift described in Sec. 4.3. In this manner nearly all cosmogenic charged particles were detected. However, this low software energy threshold results in many veto depositions being due to the ambient gamma-ray flux.

The recorded energy spectrum from one week of data from one of the 1 inch veto panels at the 377 m.w.e. depth is displayed in Fig. 4.10. The Landau distribution centered at $\sim$5 MeV is due to the muon interaction in the veto. The exponential distribution at lower energies is due to the ambient gamma-ray flux. As observed in Fig. 4.10, a significant portion of veto depositions are due to gamma rays. This gamma-ray contamination could be removed

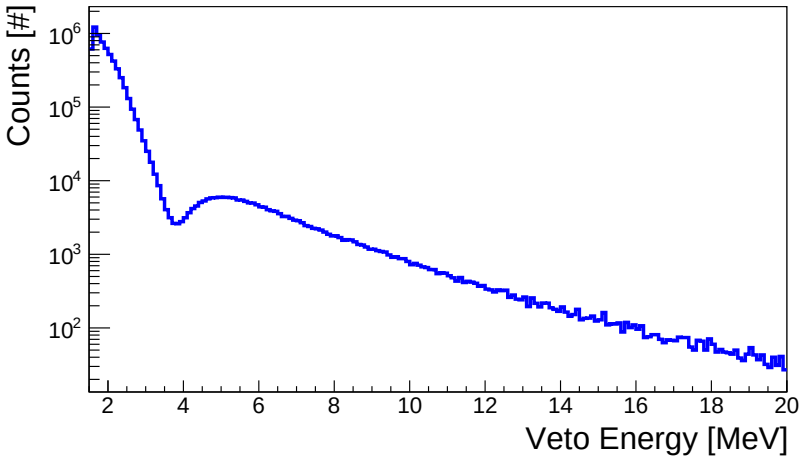

Figure 4.10: The recorded veto energy spectrum at the 377 m.w.e. depth

by raising the energy threshold. However, it was decided to keep the low software energy threshold in order to have a nearly 100% cosmogenic charged particle veto efficiency.

Modeling of the cosmogenic charged particle interactions in MARS and the associated veto is described in Appendix B. The charged particle veto efficiency is not formally calculated. It changes as a function of the measurement location, due primarily to the change in the muon energy and angular distribution and the associated minimum software energy threshold.

Chapter 5

The MARS Monte Carlo Model and Simulation

In order to estimate the detector response matrix and perform the inversion algorithm described in Chapter 3, a Monte Carlo model of MARS was constructed using Geant4.9.6p02 and the Shielding physics list [48, 49]. The reliability of the final result is heavily dependent upon the quality of the response matrix; the Monte Carlo model must be reasonably accurate. To ensure accurate modeling of the detector, several physics models were modified from the default Geant4 Shielding physics list and several experiments were performed to calibrate the Monte Carlo model with experimentally measured quantities. The following chapter describes the validation of the Monte Carlo model. In Sec. 5.1, the geometric dimensions and various configurations of the MARS Monte Carlo are described. In Sec. 5.2, the physics models which were changed from the default Shielding physics list models are described. In Sec. 5.3 the simulation of the MARS DAQ is described. Finally in Secs. 5.4-5.5, the previous calibrations are incorporated into the Monte Carlo model. Predictions of the effective area and the unfolding of simulated spectra are presented.

5.1 The Geometric Model

Using the dimensions described in Sec. 4.1, two variations of the Monte Carlo model were created: the full geometry model and the partial geometry model. There are several reasons for creating the two models. First, modeling the specific environment of each experiment is incredibly time consuming. In order to not model the specific environment for each measurement, two models were created that should bound most measurements. A comparison of the system response and associated unfolded spectra using these two models produces a conservative estimate of the systematic uncertainties that may exist, when the specific detailed environment of a measurement is not included. Second, specific and detailed simulation of the environment require a significant allocation of CPU-time, more than is reasonably achievable.

The full geometry model is displayed in Fig. 5.1 and includes the neutron detectors, the lead, the veto system, the deployment platform, and a 2.5 m thick rock floor with the same density as KURF (2.69 g/cm^3) [67]. The full Monte Carlo model requires a significant

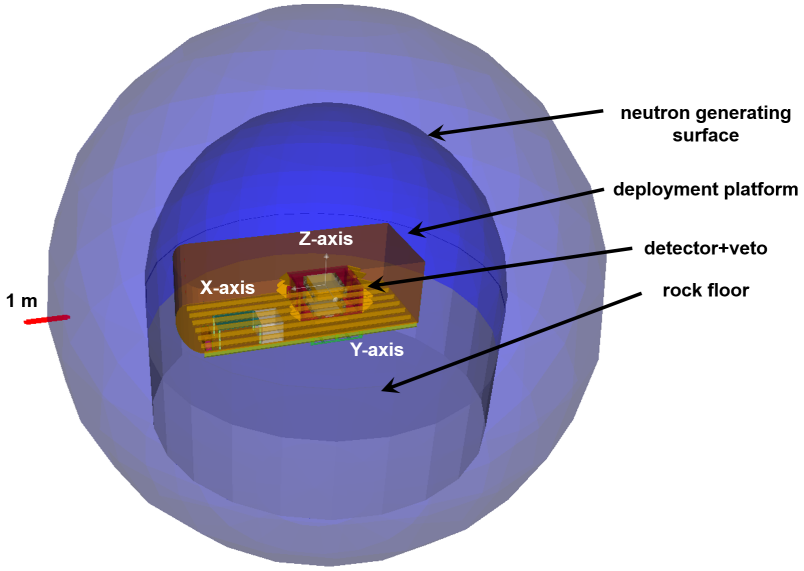

Figure 5.1: A computer rendering of the full geometry Monte Carlo Model. Axes are labeled and the scale is included.

amount of CPU-time (∼100,000 CPU-hours) to produce the statistics necessary to form the detector response matrix. It is assumed that the full geometry model roughly approximates most measurement scenarios as long as there is not a rock wall or large neutron scattering surface closer than the distance from the rock floor to the detector.

The partial geometry model was created to quickly simulate incident neutron events using the MARS Monte Carlo model. It only includes the detector, lead, steel table, and veto. The deployment platform and associated surrounding environment was not modeled. The partial model is displayed in Fig. 5.2.

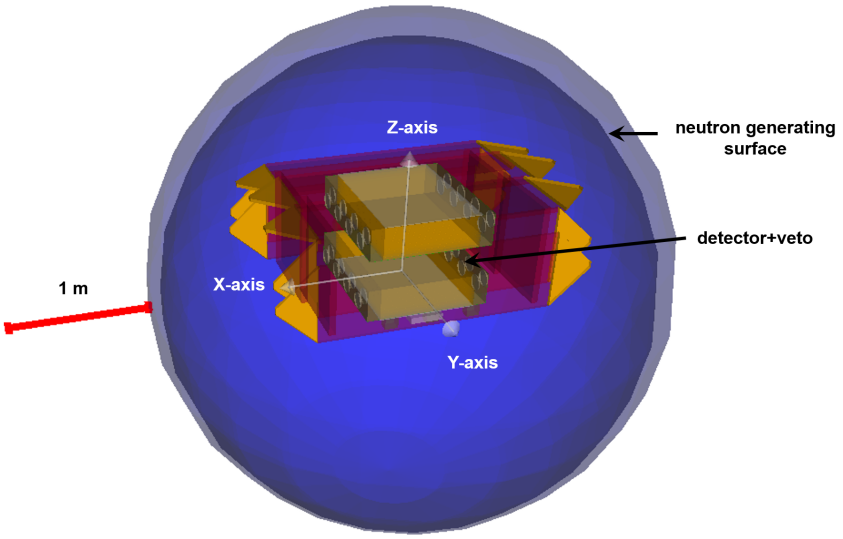

Figure 5.2: A computer rendering of the partial geometry Monte Carlo Model. Axes are labeled and the scale is included. The steel table and lead are included in the model; the rendering struggled to effectively display these components.

5.2 The Physics Models

Two problems were encountered in regards to simulating the predicted neutron response with the default Geant4 Shielding physics list: poor Monte Carlo modeling of the multiplicity and energy of Gd de-excitation gamma rays originally identified by Horton-Smith [68] and a poor reproduction of the inelastic reaction channels and kinematics for neutron-carbon interactions above 20 MeV as shown first by Roeder [69]. Solutions to alleviating the inaccuracy from the two above models are described below.

Additionally, an issue was discovered while performing muon simulations (Sec. B): Geant4.9.6p02 would occasionally enter an infinite loop when a Geant4 multiple scattering interaction was performed across two geometry boundaries resulting in a transportation step. This problem only occurred during muon simulations. It appears to be a Geant4 issue. To run the simulations without encountering this infinite loop, multiple scattering interactions were turned off. It is not known what effect this has on the muon simulations. However, it was necessary in order to predict the muon contamination of the neutron signal.

Gd De-Excitation

Modeling of the Gd de-excitation gamma rays is inherently difficult. When the two isotopes of Gd with the largest neutron capture cross-section (Gd-155 and Gd-157) absorb a neutron, they are excited into the continuum energy levels of the nucleus. Decay from the continuum to the discrete energy levels is difficult to model. Significant progress has been made by the DANCE collaboration to measure this phenomenon as well as the decay from the discrete

energy levels [70]. However, the models from the DANCE collaboration require estimation of a nuclear density state and an algorithm which must randomly choose approximate levels from the continuum. Due to this random choice of levels, a significant number of models must be investigated in order to find the best set of approximate levels. Due to the inherent complexity of these models and the lack of a published best fit continuum energy level scheme, an accurate representation of the Gd de-excitation has not been incorporated into Geant4.

In contrast to the best attempt to model the Gd de-excitation by the DANCE collaboration, the default final state model of Geant4 is woefully inadequate. The default final state model does not conserve energy and a significant number of Gd de-excitations liberate a total energy far from the expected Q-value. To solve some of the issues with the default final state model, Geant4 offers the evaporation model, which does conserve energy. A comparison of the total energy liberated during a Gd de-excitation between the two Geant4 models is provided in Fig. 5.3. The evaporation model correctly predicts the expected Q values of

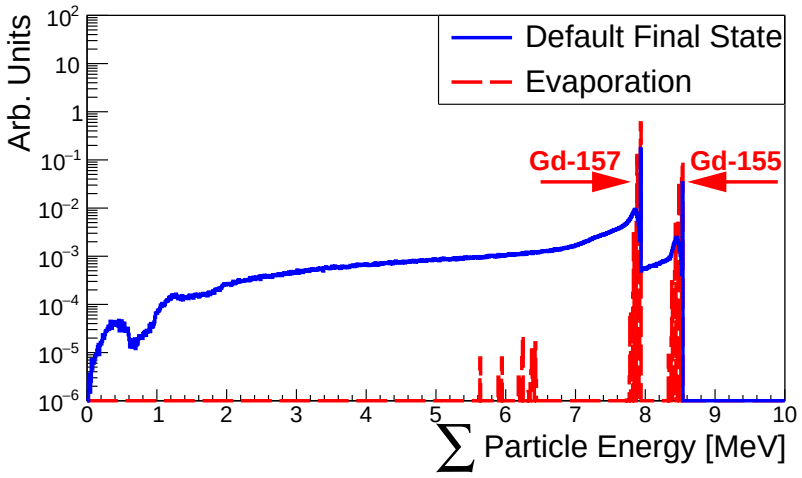

Figure 5.3: A comparison of the total kinetic energy of all particles produced in a Gd de-excitation between the evaporation and default final state model. The Evaporation model correctly predicts the Q-values of the reactions.

the Gd nuclei decays. A comparison of the gamma ray multiplicity between the two models is provided in Fig. 5.4. The predicted gamma ray multiplicity for the evaporation model seems slightly incorrect. A higher number of multiplicity 1 gamma ray de-excitations is expected [68]. However, no corrections are made to the evaporation model.

MENATE_R

Modeling of the high-energy neutron inelastic reactions on carbon is inherently less difficult than the Gd de-excitation. The problem is using accurate data from experiments which

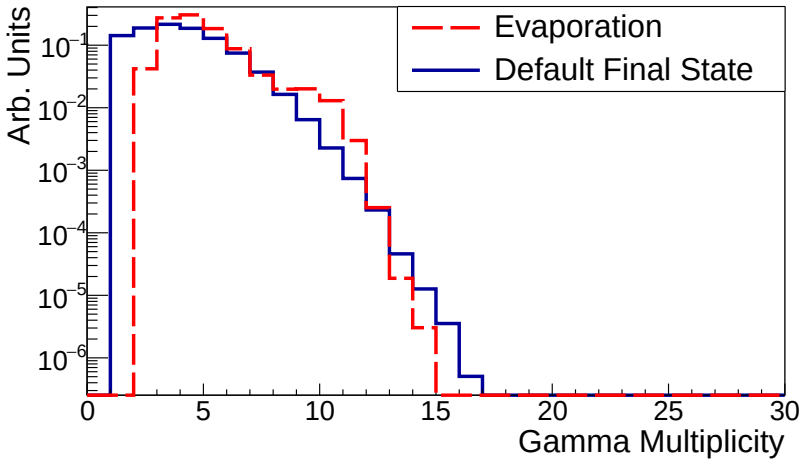

Figure 5.4: A comparison of the gamma ray multiplicity produced in a Gd de-excitation between the evaporation and default final state model.

have quasi mono-energetic neutron spectra. Geant4 has been shown to over-predict the (n,γ) reaction and under-predict or not predict at all a host of other interactions which may produce secondary neutrons. If MARS were to be used in a capture-gated/recoil manner these secondary neutrons are incredibly important for calculating the detector response. Additionally, these secondary neutrons may slightly shift the multiplicity based detector response to higher multiplicity values, particularly at lower energy.

Instead of using the Geant4 default model, the MENATE_R package [69, 71] was used to simulate inelastic neutron carbon interactions. MENATE_R considers six inelastic reaction channels: (n,n'3α), (n,α), (n,n'p), (n,γ), (n,n'n), and (n,p) which were tuned to results from several experiments [72, 73]. The (n,t) and (n,d) reactions are lumped into the (n,p) reaction. In contrast to several Geant4 cascade models, MENATE_R does not over-predict the (n,γ) reaction channel [69, 71].

MENATE_R was shared through Nuclear Science and Security Consortium partners at Michigan State University. The code arrived in a state that was incompatible with other Geant4 physics lists. It was modified to overwrite the neutron carbon inelastic reactions for several of the default physics lists provided in Geant4.9.6.p02. Comparisons between MENATE_R and the default Geant4 Shielding physics list were performed using the experimental results and a very basic model of the detector from Nakao *et al.* [74]. Nakao *et al.* was an accelerator experiment using NE213, a liquid hydrocarbon based scintillator. A 12.7 cm by 12.7 cm NE213 neutron detector was modeled in a quasi mono-energetic neutron beam line. One million incident neutrons were simulated. No position-dependent detector response modeling was performed. The deposited energy was quenched using Birk's Law [75]

$$E_{quenched} = \frac{E_{deposited}}{1 + k_b \frac{dE}{dX}}, \tag{5.1}$$

where k_b is Birk's constant. Here a Birk's constant of 1.61 μm/MeV was used, given the NE213 scintillator [74]. MENATE_R better reproduces features of the measured response from Nakao *et al.* [74] than the default Geant4 Shielding physics list (Fig. 5.5). The main feature differences between the two models are due to more accurate modeling of the the (n,p) reaction with MENATE_R . While MENATE_R is by no means a perfect fit to the

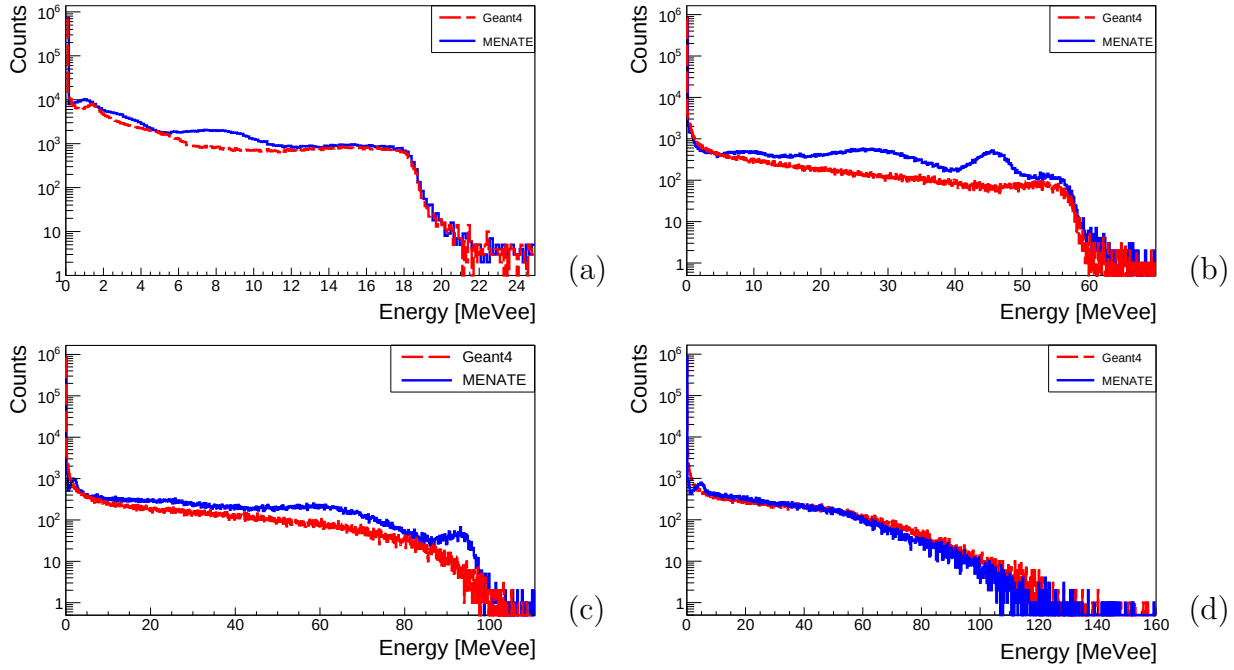

Figure 5.5: A comparison of the high energy neutron response on NE213 using MENATE_R and the default Geant4 shielding physics list. (a) Depicts a simulation with incident neutrons of energy between 29 and 30 MeV. (b) Depicts a simulation with incident neutrons of energy between 74 and 78 MeV. (c) Depicts a simulation with incident neutrons of energy between 131 and 133 MeV. (d) Depicts a simulation with incident neutrons of energy between 206 and 208 MeV. Experimental comparisons can be found in Nakao *et al.* [74].

data by Nakao *et al.*, it shows better qualitative agreement. Without a better model, the MARS Monte Carlo model used MENATE_R to model high-energy inelastic neutron carbon reactions.

5.3 Simulating the MARS DAQ

In addition to the specifically chosen Monte Carlo models described above, the MARS analysis attempts to crudely model the response of the DAQ. The MARS simulation analysis records the time, energy deposited, detector volume, and position of all particle interactions in the Monte Carlo simulation. The deposited energy is quenched using Birk's Law [75], with

coefficients for BC-408 measured by Zhang [76]. No pulse shape modeling is performed. The ADC clock frequency is used to bin the particle interactions on a per volume basis, resulting in a vector of integrated energy depositions as a function of WFD sample.

A trapezoidal filter with a gap time of 4 samples and a peaking time of 8 samples is used to process the time integrated energy vector. This is the same filter used in the MARS DAQ. Due to the hardware energy threshold not being known precisely, the simulated DAQ triggers on pulses above 10 keV. Minimal changes were observed in the recorded multiplicity events if the threshold was raised to the known software energy threshold of 850 keV. Using the same time ranges described in Sec. 4.2, the triggered simulation data is integrated and processed to form depositions. These depositions are identified with same algorithm as the experimental data. Application of the software energy threshold (850 keV) is applied with the same code as used in the experimental analysis.

5.4 Effective Area Predictions

In order to calculate the detector response matrix, high-energy neutrons from 20 to 2500 MeV were simulated using the partial geometry MARS Monte Carlo model described in Sec. 5.1. Incident neutrons were generated on a half sphere of radius 1.9 m surrounding the detector. The recorded energy depositions for all active detector and veto volumes were grouped by the time ranges described in Sec. 4.2 to determine the energy, weighted position, and WFD sample. Energy and position dependent responses outlined in Sec. 4.4 were used to convolve the simulated response. The expanding time range triggering algorithm described in Sec. 3.3 was used to determine the multiplicity, capture energy, and thermalization energy. These simulation results were used to examine the multiplicity, capture energy, and thermalization energy response as a function of the incident neutron energy and predict the effective area for incident high-energy neutrons in MARS.

In Fig.5.6 the three components of the measured response are displayed as a function of the incident neutron energy. The y-axis of each part of Fig.5.6 represents the discretization of the respective component. The x-axis is composed of 20 MeV wide bins. Each column is a probability distribution of the respective component in the respective 20 MeV wide bin. As observed in Fig.5.6, the multiplicity and capture energy exhibit response changes between 200 MeV and 400 MeV. This feature is represented by the change in the slope of the maximum multiplicity or capture energy at a respective energy. The slope in both responses significantly decreases past this point. This feature limits the energy resolution at higher energies. The thermalization energy does not exhibit this trend and plays a larger role in the reconstruction at higher energies. This very complicated response is atypical and presented a significant challenge for inferring the incident neutron flux.

Typically, experiments which require inversion analysis have a detector response matrix $\mathbf{A}$ which is nearly diagonal. This results in the inversion algorithm balancing statistical concerns: the experiment is nearly a direct or quasi-direct measurement. Figure 5.7 is a graphical representation of the detector response matrix. The matrix has been normalized

by its maximum value. The three component measured signal is shown versus the basis spline number[1]. Bins at the top of the histogram (near bin 0 on the y-axis) represent events with the minimum multiplicity, capture energy, and thermalization energy to be considered an event. Bins at the bottom of the histogram (near bin 2800 on the y-axis) represent events with the maximum multiplicity, capture energy, and thermalization energy. The basis spline knots for this matrix were at [20, 30, 40, 50, 90, 200, 650, 900, 1150, 2000, 2500] in units of MeV. As observed in Fig. 5.7, the detector response matrix **A** has a complicated shape which appears similar to the superposition of several upper triangular matrices. This matrix does not have the standard quasi-diagonal appearance. The complexity and correlation of the three component signal makes the inversion process challenging. Great care must be used to produce reliable and consistent results. This is why direct or less rigorous inversion methods would fail to reliably reconstruct the MARS data: using MCMC with a regularization optimization and a bias reduction step is critical to producing consistent results.

In spite of the algorithmic challenges to reconstructing a reliable neutron flux, MARS has a large effective area. This trade-off: the ease of analysis versus a sensitive detector is critical to making the below ground measurements discussed in Chapter 7. The effective area of the multiplicity technique for incident neutrons with isotropic, $\cos^2(\theta)$, $\cos^3(\theta)$, and $\cos^4(\theta)$ angular distributions is shown in Fig. 5.8. The effective area was calculated by

$$A_{eff}[cm^2](E) = \frac{N_{interacting}(E) * (2\pi * 190 * 190)[cm^2]}{N_{simulated}(E)}, \tag{5.2}$$

where $A_{eff}[cm^2](E)$ is the effective area, $N_{interacting}(E)$ is the number of neutrons events passing the respective threshold, $(2\pi * 190 * 190)[cm^2]$ is the surface area of the generating surface, and $N_{simulated}(E)$ is the total number of neutrons simulated. A more generic description of calculating the effective area is described by Sullivan [77]. The above effective calculations, produce results which are not dependent upon the detector shape or Monte Carlo world volume radius. A factor of 2π, instead of 4π, was used due to the assumption that the incident neutron is pointed only in the downward direction [12, 16]. The impact of the contribution of neutrons that may scatter upward off the ground is explored by the full vs. partial geometries described in Sec. 5.1.

Above ground the angular distribution is expected to be $\cos^3(\theta)$ [12]. Below ground, the incident neutron angular distribution is expected to be an energy-dependent combination of isotropic and highly peaked along the initiating muon direction [16]. Isotropic neutrons are due to muon capture and are likely below the detection threshold used by MARS. Incident neutrons which follow the initial muon angular distribution may be removed from the recorded data set due to muon actuating the charged particle veto.

[1]Note the y-axis has been reversed from a typical histogram.

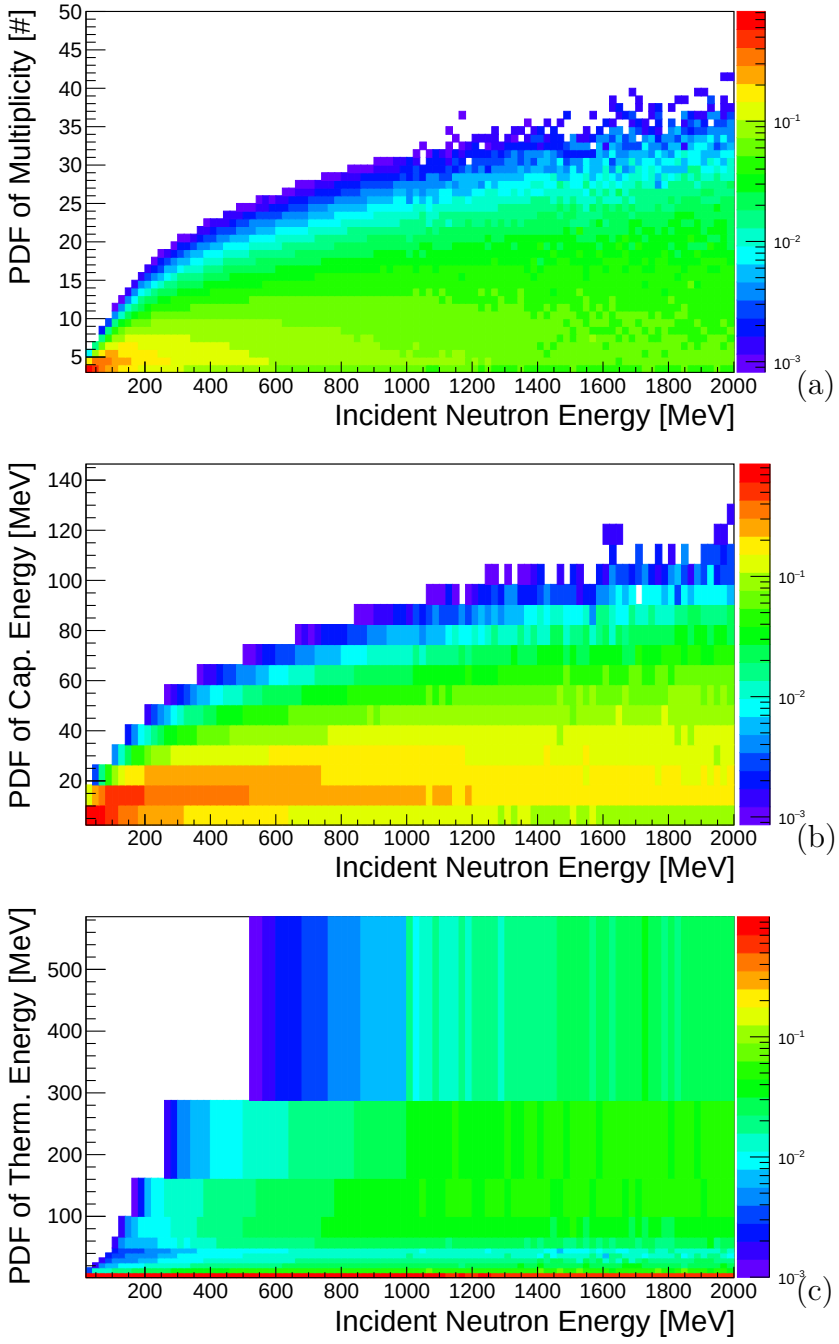

Figure 5.6: (a) Depicts the multiplicity response as a function of the incident neutron energy. (b) Depicts the capture energy response as a function of the incident neutron energy. (c) Depicts the thermalization energy response as a function of the incident neutron energy. All three components are binned in the same manner used in the MCMC reconstruction algorithm. Each column of the respective histogram is a probability distribution of the events at that respective energy.

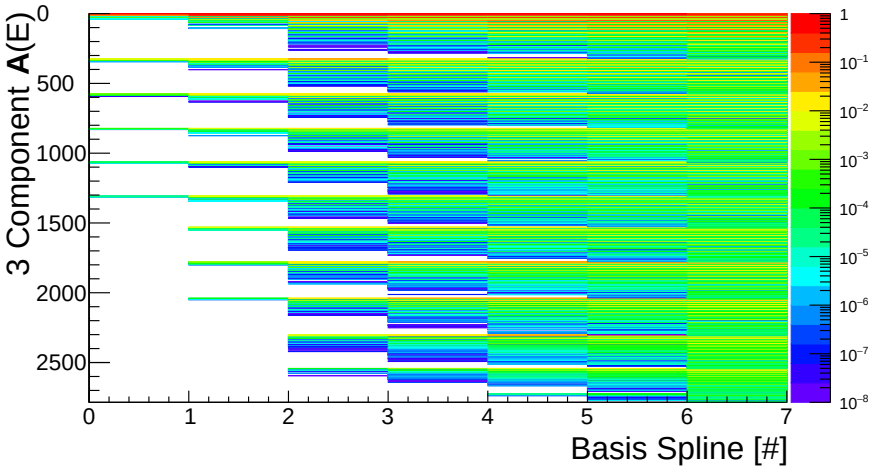

Figure 5.7: The histogram representation of the MARS detector response matrix **A**. Note the matrix looks like the superposition of several upper triangular matrices. The matrix in this representation is not quasi-diagonal.

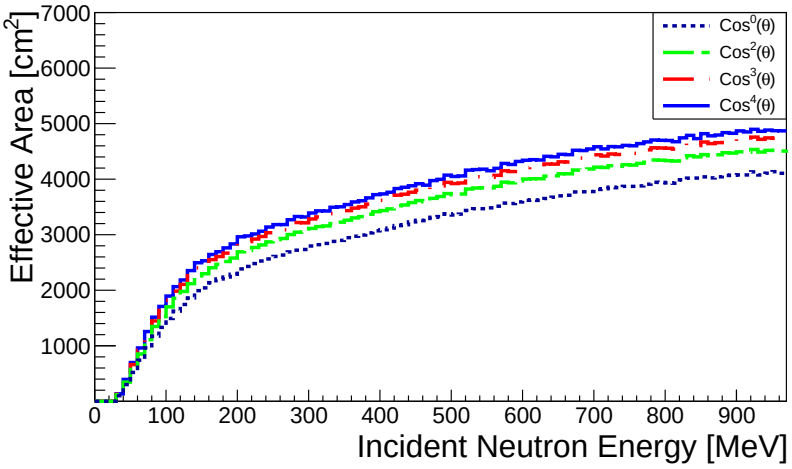

Figure 5.8: The predicted effective area for incident high-energy neutrons with angular distributions of isotropic, $\cos^2(\theta)$, $\cos^3(\theta)$, and $\cos^4(\theta)$.

5.5 MCMC Reconstruction of Simulated Spectra

Incorporating the techniques presented above, the calibrated MARS Monte Carlo detector response matrix was used to reconstruct several incident high-energy neutron spectra. Five groups of neutrons were simulated at 100, 200, 300, 500, and 700 MeV. Neutrons were generated on the half sphere surface of the partial geometry model in a cosine distribution. The measured detector response of Sec. 4.4 and the triggering algorithm described in Sec. 4.5 were applied to the simulated mono-energetic neutrons. Finally the event requirements described in Sec. 3.3 were applied to both the simulated mono-energetic data and the detector response.

To test the MARS reconstruction analysis, incident neutrons were simulated until 100,000 events were recorded. The capture energy was binned in 8 MeV increments from 0.8 MeV to 800.8 MeV. The thermalization energy was binned given an energy resolution 30 percent worse than determined in Sec. 4.3 with the caveat that each bin must be $\geq$8 MeV in width. The thermalization energy bin edges were at [0.8, 8.8, 16.8, 24.8, 32.8, 40.8, 66.49, 100.08, 161.76, 287.8, 585.35, 2000.00] MeV. This coarse energy binning in the thermalization and capture energy ensures that energy calibration or gain correction measurements do not dominate the systematic uncertainty. In Fig. 5.9 the simulated "measured" data ($\vec{g}_{sim}$) for the 100 MeV and 700 MeV incident neutrons are displayed. Significant differences can be observed in the data: higher values of the simulated $\vec{g}$ are populated as the incident neutron energy increases. With experimental data a plot of this nature will be used to compared the measured signal ($\vec{g}$) and the predicted noise ($\vec{b}$).

The MCMC algorithm described in Sec. 3.5 was used to reconstruct the input neutron counts for each of the 5 mono-energetic spectra. The distribution of reconstructed and input counts in the basis spline space is observed in Fig. 5.10. The reconstructed uncertainty only incorporated statistical concerns. The output energy knot spacing for each of the 5 simulated energies was fine near the respective energy and became more coarse at a greater distances from the mono-energetic peak. The binning was made fine enough that multiple $\vec{f_i}$ had Gaussian distributions, but not so small that Gibbs phenomenon [53] was observed in the reconstructed output.

Examining Fig. 5.10, a perfect reconstruction of the amplitude is not expected. Instead, a broadening of the reconstructed energy which quantifies the reconstruction algorithm energy resolution, given the detector response is observed. Additionally, consistent integral events which are displayed in Table 5.1 are observed. The quoted uncertainty in Table 5.1 only includes statistical considerations.

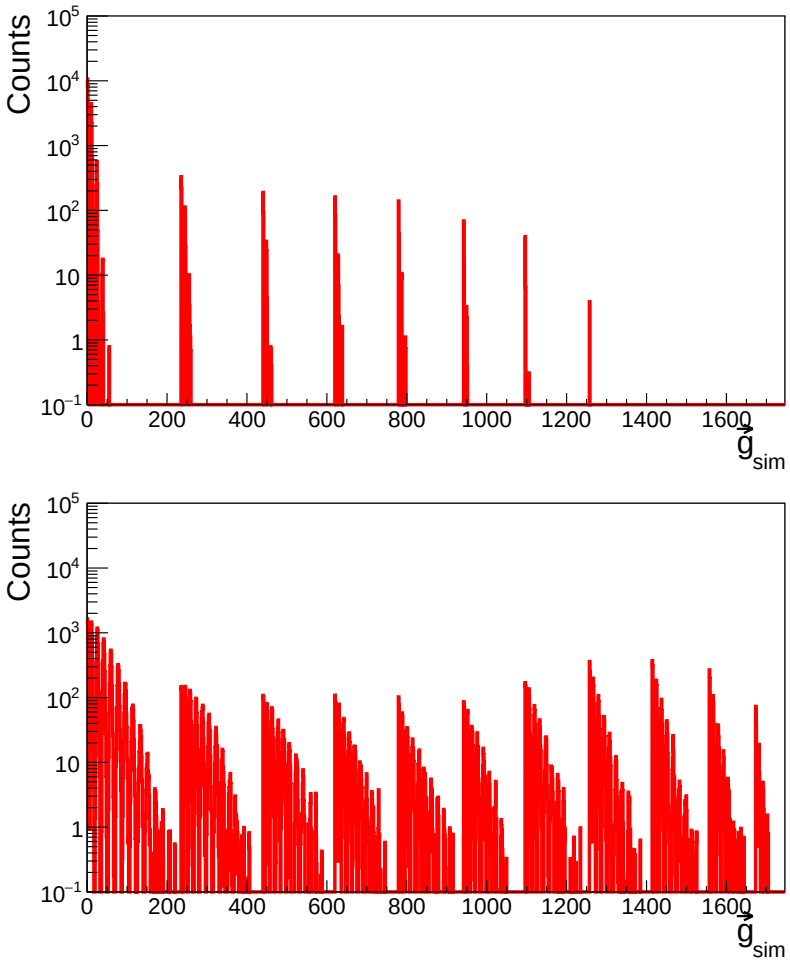

Figure 5.9: (a) Depicts the simulated 3 component response ($\vec{g}$) from 100 MeV neutrons incident on MARS. (b) Depicts the simulated 3 component response ($\vec{g}$) from 700 MeV neutrons incident on MARS. Higher values of the simulated $\vec{g}$ are populated as the incident neutron energy increases.

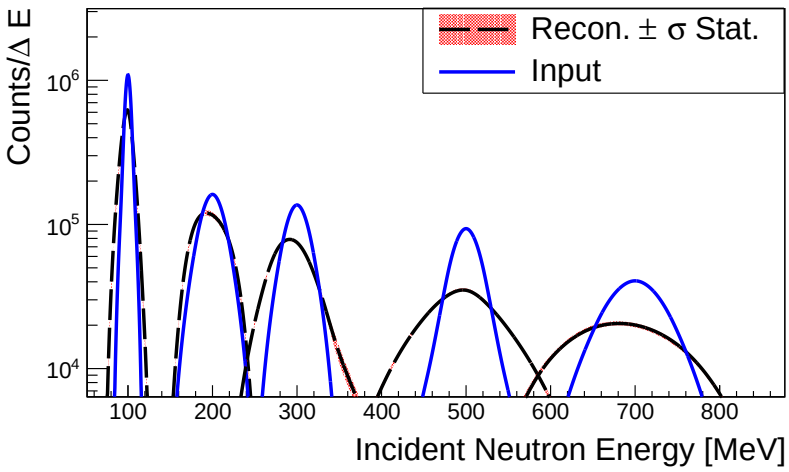

Figure 5.10: The reconstructed counts/ΔE of the 5 mono-energetic neutron simulations. The input spectra in the basis spline space is displayed as a blue line. Reconstructed spectra are displayed in a dash black line. Confidence intervals around the reconstructed spectra are displayed as a patterned red area.

Table 5.1: The integral number of neutrons simulated for the 5 mono-energetic neutron energies. The truth, bias corrected reconstruction, and the integral of the $\pm 1\sigma$ confidence interval functions are displayed.

Energy	Truth 10^6	$f(E)^{+\sigma}_{-\sigma}$ 10^6
100	10.6	$10.9^{+0.4}_{-0.4}$
200	6.47	$6.60^{+0.2}_{-0.2}$
300	5.46	$5.55^{+0.2}_{-0.2}$
500	4.55	$4.59^{+0.2}_{-0.1}$
700	4.06	$4.11^{+0.2}_{-0.2}$

Chapter 6

Measurement of the High-Energy Neutron Energy-Dependent Flux Above Ground

Above ground, the high-energy neutron energy-dependent flux has been poorly measured. Most of these measurements, and some of the environmental factors resulting in the variation of the measurements, have been summarized by Ziegler [12]. Significant variation exists between the set of measurements: an order of magnitude variation is observed in the MARS measurement energy regime ($\geq$90 MeV). Additionally, the most referenced experiments do not provide robust statistical or systematic uncertainty estimates [10, 41, 39]. Above 300 MeV, the only measurements that exist are Bonner spheres or IGY meter experiments [10, 41, 39] and one telescope measurement by Ashton *et al.* [78]. These measurements are not independent. Ashton *et al.* scales their data based upon measurements by Hughes [41]. Therefore above 300 MeV, all measurements are correlated. Of particular concern with all results, the incident energy-dependent neutron angular distribution is poorly measured. This uncertainty, which is described to a greater degree in Sec. 6.1, allows Ziegler to scale recoil based measurements to match Bonner sphere and IGY meter measurements. For certain measurements this can be a factor of 2 [12]. This scaling misleads the reader and results in a trend-line that appears to have small uncertainty and matches most of the data.

MARS has two purposes for measuring the above ground high-energy neutron flux: to provide a new and independent measurement, and to prove the feasibility of below ground measurements by comparing the MARS above ground measurement to the spread of previous above ground measurements. In Sec. 6.1 previous above ground neutron measurements are described. In Sec. 6.2 the MARS above ground measurement scenario is presented. In Sec. 6.3 the measured data, preliminary MCMC convergence figures, and the systematic uncertainty estimates are presented. Finally, in Sec. 6.4 the result of the MARS above ground measurement is presented.

6.1 Previous Measurements

The early and most referenced work in detecting high-energy neutrons was performed by Hess *et al.* [10]. Hess used a Bi-209 fission chamber, a CH_2 gas proportional detector, a BF-3 detector surrounded by paraffin, and an array of gold foils to infer the neutron energy distribution from thermal energies to 10 GeV. Hess did not account for charged particle spallation in certain detectors. Particularly at high energies, this resulted in measurements reporting an elevated flux. Hughes later corrected these measurements [41].

The most robust above ground neutron energy-dependent flux measurements were Bonner sphere [39] and IGY meter experiments [41, 79]. These detection methods were described in Sec. 2.3. Due to the uniform angular response of Bonner spheres, these measurements contain no information relevant to the incident neutron angular distribution. IGY meters do not have uniform response.

Other experiments have used a recoil based telescope design [78, 80, 81, 82, 83]. These detection methods were described in Sec. 2.3. Spark chambers have also been employed to perform similar recoil based measurements [84]. If segmentation is used, telescopes and spark chambers are capable of reconstructing the incident neutron angular distribution. In contrast to MARS, Bonner sphere arrays, and IGY meters, telescopes are capable of measuring the incident neutron energy on a per event basis. These recoil based experiments typically have much lower event rates.

Cloud chambers have also been used to measure the incident neutron flux [85]. This experiment reports a measured flux, given the non-uniform angular response of the chamber. Using this measured flux the authors inferred the incident neutron angular distribution by comparing to the predicted vertical flux.

The results from these experiments (except for Gordon *et al.* [39]) were summarized by Ziegler in Fig. 18 of [12]. Unfortunately Ziegler did not include the reported statistical or systematic uncertainty from these results. Additionally, Ziegler did not describe the scaling of these results in a fashion that is repeatable.

Several other problems exist when comparing the above previous measurements. Of particular concern, a robust measurement of the incident neutron angular distribution is lacking. Several experiments have performed this measurement with poor statistics [80, 81, 82, 83]. Typically the incident neutron angular distribution is characterized as $\propto cos^n(\theta)$, where θ is the angle relative to the zenith [12]. This poorly measured angular distribution becomes problematic when comparing results between different experiments: most detectors do not have uniform response as a function of the incident neutron angular distribution. However Bonner sphere experiments, generally considered the most reliable measurements over a large energy range [1], have uniform angular response. This often results in comparisons quoting the total neutron energy-dependent flux not the angular neutron energy-dependent flux: [n/cm^2/sec/MeV] vs. [n/cm^2/sec/MeV/sr]. This conversion has potential to introduce

[1] Bonner sphere experiments claim dynamic range from thermal neutron energies to an energy regime of ~15 GeV.

large systematic uncertainty in comparisons, which is often not considered. The conversion from angular flux to total flux can be calculated by multiplying the angular neutron flux by $2\pi/(n+1)$ [12], where n is the cosine power, assuming uniform response as a function of energy.

Slightly less troubling, a standardized correction does not exist for scaling results based upon the measurement location's elevation and geomagnetic rigidity. At higher elevations a reduction in atmospheric shielding is observed, resulting in a higher flux [10, 11]. Geomagnetic rigidity is a measure of a cosmogenic charged particle's ability to penetrate Earth's magnetic field. Rigidity can be calculated by: $\frac{pc}{Ze}$, where p is the particle momentum in units of [eV/c], c is the speed of light, Z is the atomic number, and e is charge of an electron. A geomagnetic rigidity cutoff exists, as a function of latitude and longitude, after which charged particles with less rigidity will be deflected away from Earth. Above ground, high-energy neutrons are created by these cosmogenic charged particles. The rigidity cutoff thus partially controls the high-energy neutron flux. Hess *et al.* measured this effect [10]. Gordon *et al.* has recently described a procedure for correcting both the elevation and geomagnetic rigidity. As standardized by many papers [12], the flux is normally corrected to a latitude of 44N corresponding to New York city.

The MARS results presented below attempt to address several of the above listed problems. In Fig. 6.10, the MARS results are compared to the data summarized by Ziegler. Uncertainty from the summarized measurements are displayed in all comparisons made in this work. The only data that was scaled to account for the incident neutron angular distribution based upon the average neutron angular distribution was Ashton *et al.* [78]. The assumed incident neutron angular distribution was $\cos^3(\theta)$. Most other experiments measured the incident angular distribution and their results are easily converted to the total high-energy neutron flux. The MARS results also characterize the systematic uncertainty associated with the poorly measured incident neutron angular distribution. MARS results report the total neutron flux, not the angular neutron flux, in order to compare to the Bonner sphere measurements. Additionally the MARS results use the Gordon *et al.* corrections to account for elevation and geomagnetic rigidity.

6.2 Measurement Campaign

MARS measured the above ground neutron flux at the surface of Earth, above KURF. The measurement location was at an atmospheric depth of 1029.76 g/cm^3 ($\sim$500 m above sea level) near 37-23-00.4 North, 080-39-29.2 West. The location was not on a plain: two mountain ridges surround the location on 2 sides (Fig. 6.1). These mountain ridges were not accounted for in the MARS Monte Carlo simulation due to the already significant simulation time incurred to generate detector response matrices.

The measurement was performed after the three below ground measurements from April 24th, 2015 until July 17th, 2015. Geomagnetic rigidity was not measured and published results for this time period were not found. Based upon the 11 year solar cycle a geomagnetic

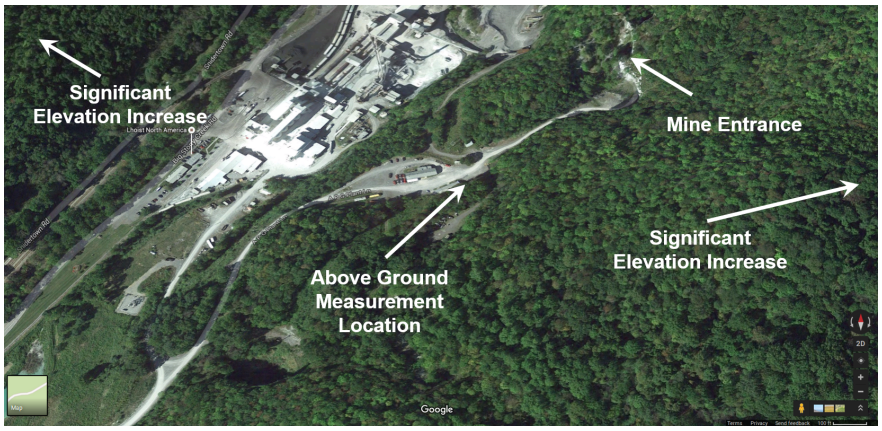

Figure 6.1: A Google maps quasi 3-D representation of the above ground KURF measurement location. The measurement location is near the center of the figure. The mine entrance is near the top right of the figure. Significant elevation increases are observed at the bottom right and top left of the figure.

rigidity calculation using 2004 data was used to estimate a rigidity of 2.49 GV [86]. Due to the measurement location, the geomagnetic rigidity is not expected to significantly fluctuate and the results are insensitive to small fluctuations in the rigidity. Geomagnetic rigidity corrections in the fashion of Gordon *et al.* [39] were applied to the detector response matrix.

High voltage problems were experienced intermittently after the first week of the measurement. During week 6, veto channels were lost and in the final month no useful data was taken. Due to this set of circumstances, MARS had a total measurement time of ∼9 days where all detector components were working in proper fashion. Primarily due to the veto deposition rate (Sec. 4.6), a dead-time of 19.6% was observed.

6.3 The Measured Data and MCMC Preliminary Results

In spite of the measurement complications MARS recorded ∼2.9 million neutron-like events. Events were identified using the requirements of Sec. 3.1, the triggering algorithm of Sec. 3.3, and the binning of Sec. 5.5. By recording ∼2.9 million events, MARS significantly surpasses the statistics acquired by the previous measurements. Often considered the most reliable measurements, the Bonner spheres measurements only attempt to record at least 10,000 neutron captures per sphere [39]. Generally only two Bonner spheres are used to measure the high-energy neutron flux. Due to the sharply decreasing neutron energy spectrum, it is assumed that these spheres are likely the statistically limiting spheres. Using this assumption, MARS records ∼2 orders of magnitude more events above 90 MeV in roughly the same measurement time as the Bonner sphere measurements [39].

Background Predictions

Using this measured data, the background which passed all neutron event cuts was modeled using the gamma-ray background model and the CRY package [87] as described in Appendix B. This background estimation quantifies the number of "neutron" events which may be misidentified gamma-ray or muon events. Gamma-ray background predictions are described below. The cosmogenic charged particle CRY background model predicted 970±15 contamination events corresponding to 0.03% of the measured event number. Due to this insignificant percentage, the cosmogenic charged particle contamination was not considered in the background subtraction.

Each component of the measured vector $\vec{g}_{meas}$ and the predicted gamma-ray background $\vec{b}$ is displayed in Fig. 6.2. The plots are logarithmic on the y-axis: the background contamination is not significant. As observed in Fig. 6.2 the predicted gamma ray contaminated events follow the same trend as the measured data. This is expected since each neutron event has a roughly constant but small probability of being contaminated by a single gamma ray deposition.

The full measured vector $\vec{g}_{meas}$ and predicted background $\vec{b}$ are displayed in Fig. 6.3. This quasi-sawtooth wave structure is expected given the detector response matrix of Fig 5.7. As before with the individual components, it appears the predicted background $\vec{b}$ is a constant fraction of the measured bins in $\vec{g}_{meas}$. Multiple attempts were made to reduce the total gamma ray contamination by raising the average deposition energy threshold for all multiplicity events (threshold 6 of Sec. 3.3). No improvements were observed. No attempt was made to raise the individual deposition threshold (threshold 1 of Sec. 3.3). This would have proven computationally expensive since the threshold could not be raised for the below ground data, and the same processing code was used to generate the detector response matrix $\mathbf{A}$. Most of the uncorrelated gamma rays which contaminate neutron events appear to have energies near the Tl-208 gamma-ray energy (2.6 MeV). These concerns indicate the only way to reduce the gamma ray contamination is probably through changing the event identification algorithm either through reducing the first time range or the expanding time range. This was not performed due to it being computationally expensive to reprocess the measured data. Regardless, the ∼9% multiplicity event contamination is considered during the MCMC algorithm and the noise is removed.

MCMC Algorithm Convergence

Using the measured data from Fig. 6.2 and the algorithm in Sec. 3.5, the MCMC analysis performed several iterations to first optimize the regularization parameter. The regularization parameter α converged quickly for all reconstructions. Figure 6.4 displays the convergence of α for the full geometry model assuming an incident neutron angular distribution of $\cos^3(\theta)$ using the default expanding time triggering algorithm. Convergence is achieved after ∼2 iterations. This figure is representative of all the reconstructions used to determine the systematic uncertainty.

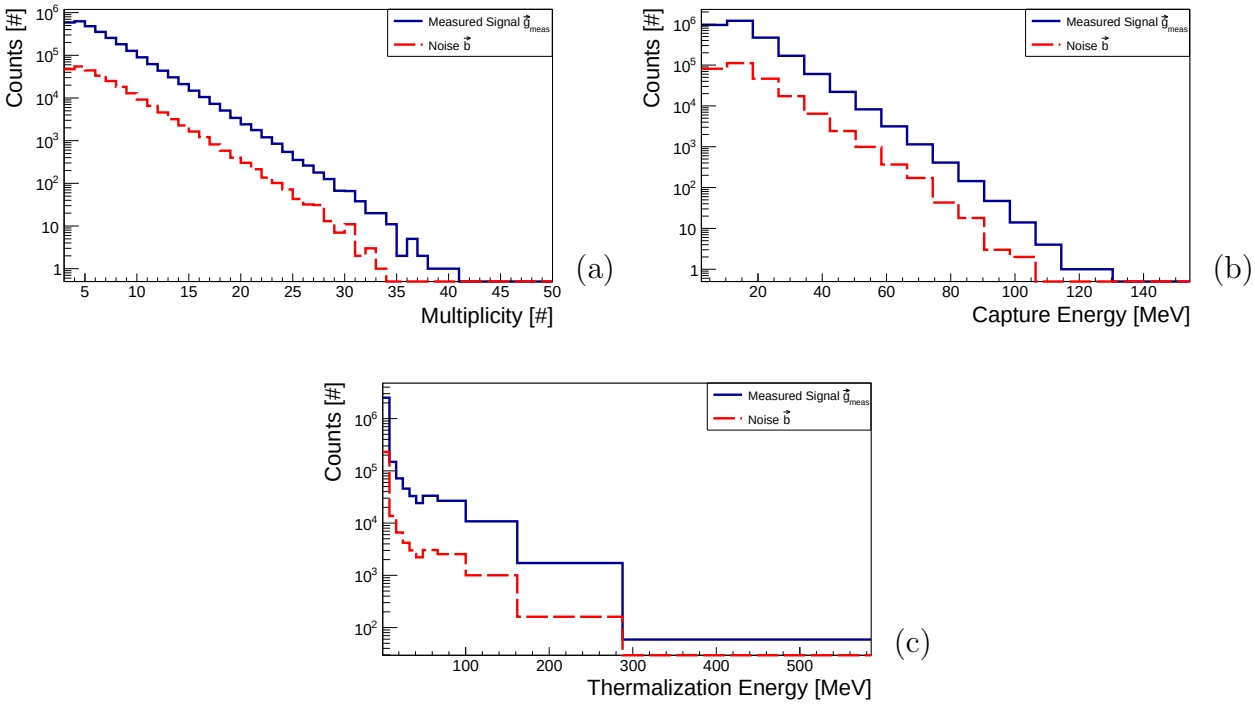

Figure 6.2: The measured neutron data and the predicted gamma ray contaminated events from the measurement above ground at KURF. (a) Depicts the measured multiplicity and the predicted contaminated multiplicity data. (b) Depicts the measured capture energy and the predicted contaminated capture energy data. (c) Depicts the measured thermalization energy and the predicted contaminated thermalization energy data. The three components of each x-axis represents the measured binning for the respective component. A similar percent of contaminated events is observed across the range of measured data consistent with a small constant probability for contamination.

After finding the optimal regularization parameter, the MCMC reconstruction removed the bias from all reconstructions. Figure 6.5 displays the percent difference between the final bias reduced reconstruction and all iterations of the bias subtraction. While the solution appears to marginally improve after one or two iterations, the percent change between the non-bias reduced solution $\vec{f}^{0}_{BC}$ and the bias reduced solution $\vec{f}^{5}_{BC}$ was minimal. The algorithm estimated that minimal bias existed before performing the bias subtraction. This is most likely due to the conservative basis spline knot spacing used by the analysis.

After removing the bias, plots of the final MCMC solution ($\vec{f}^{5}_{BC}$) convergence criteria are observed for element $\vec{f}_0$ in Fig. 6.6. These plots are representative of all $\vec{f}_i$ and display convergence. Figure 6.6a presents the autocorrelation of $\vec{f}_0$ as a function of the post burn-in sample. Figure 6.6b presents the cumulative running mean of $\vec{f}_0$ as a function of the post burn-in sample. Figure 6.6c presents $\vec{f}_0$ as a function of the post burn-in sample.

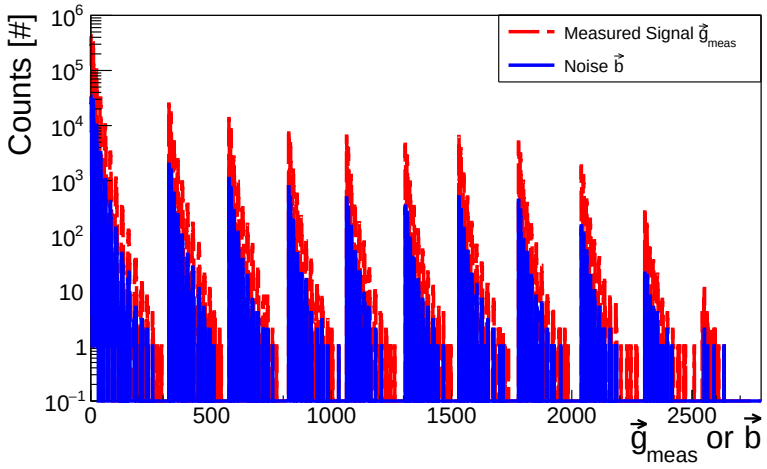

Figure 6.3: The measured three component data vector $\vec{g}_{meas}$ and the predicted background $\vec{b}$. It appears the predicted background is a nearly constant percentage of the measured vector bin value.

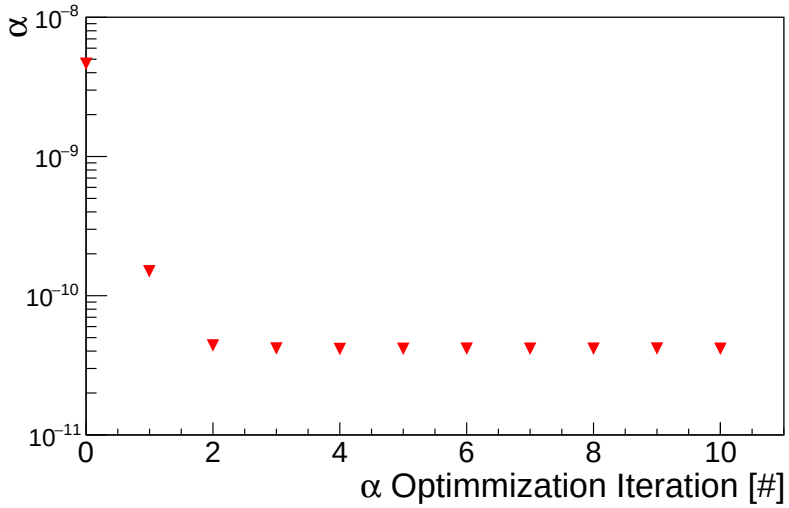

Figure 6.4: The regularization parameter α iteration update values from step 2c of the MCMC algorithm from Sec. 3.5.

Figure 6.6d presents the distribution of $\vec{f}_0$. Figure 6.6a-c exhibit convergence: the autocorrelation approaches 0, the running mean appears to flat-line, and $\vec{f}_0$ appears to be composed of white noise around $\sim 0.54e^{-3}[\#/cm^2/sec/MeV]$. Additionally Figure 6.6d displays the desired quasi-Gaussian form. The convergence criteria for the rest of $\vec{f}$ is displayed in Appendix G.

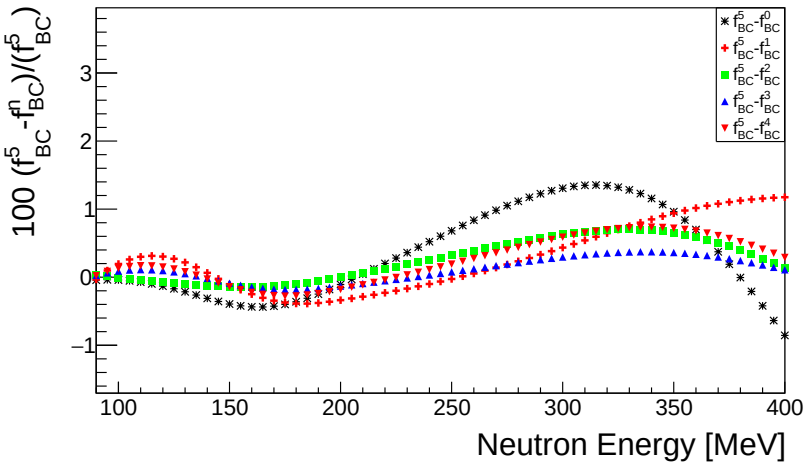

Figure 6.5: The percent difference between the final bias reduced answer $\vec{f}^{5}_{BC}$ and the previous iterations $\vec{f}^{n}_{BC}$ where n varies from 0 to 4. A minimal amount of bias was removed from the solution. This is probably due to conservative knot spacing of the final answer.

Systematic Uncertainty Analysis

In contrast to the work of Hess, Hughes, and Gordon [10, 41, 39], estimates of the statistical and many systematic uncertainty considerations inherent in all MARS measurements are estimated and reported. The statistical uncertainty was estimated using the MCMC algorithm. In the following section the systematic uncertainty analysis is presented. The following systematic concerns are described below: the incident neutron angular distribution, the surrounding environment considered by the Monte Carlo model, and the multiplicity event triggering efficiency. Other systematic uncertainty that may be of concern to the reader: the secondary neutron capture efficiency, the uncertainty of the gain drift in the PMTs, and the energy calibration of the detector are not considered. The neutron capture efficiency shows excellent agreement between experimental data and simulation (see Sec. 4.5). The binning of the measured capture energy and thermalization energy was intentionally coarse. By making this binning coarse, it is unlikely that PMT gain drift or a slight bias in the detector energy calibration significantly contribute to systematic uncertainty.

The Incident Neutron Angular Distribution

Of the measurements described in Sec. 6.1, the telescope measurements of Heidbreder [80], Preszler [81], and Moser and Saxena [82, 83] account for the incident neutron angular distribution. Excluding Heidbreder due to limited statistics, these measurements are at the low end of the energy range MARS has measured. Above 300 MeV, previous measurements do not consider the incident angular distribution. Several of the experiments referenced by Ziegler indicate that the angular distribution is probably dependent upon the incident

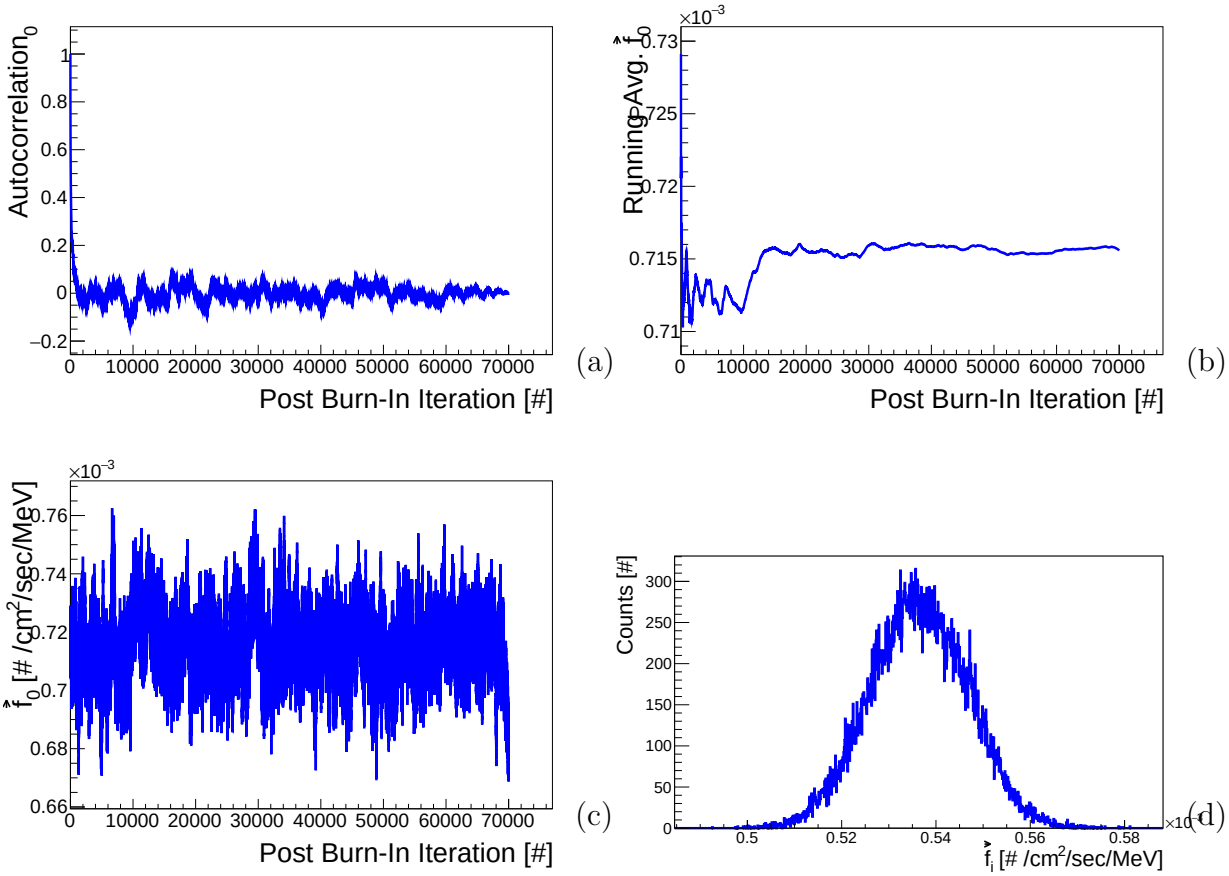

Figure 6.6: (a) Depicts the autocorrelation of $\vec{f_0}$ as a function of the post burn-in iteration. (b) Depicts the running average of $\vec{f_0}$ as a function of the post burn-in iteration. (c) Depicts the value of $\vec{f_0}$ as a function of the post burn-in iteration. (d) Depicts the histogram of $\vec{f_0}$ values. As described in the text the sub-figures are representative of all parameters and indicate sufficient convergence.

neutron energy. However, MARS does not consider the energy dependence due to a lack of robust measurements. In order for MARS to estimate a systematic uncertainty based upon the incident neutron angular distribution, measurements described by Ziegler are characterized by a mean and variance: $\propto cos^{n\pm\sigma_n}(\theta)$.

In calculating a mean and variance of the angular distribution of the incident neutron flux the following measurements were used: Barford reported a value of $\cos^{2.5\pm1}(\theta)$ [88]. Conversi calculated two values: $\cos^{2.1\pm0.3}(\theta)$ and $\cos^{2.6\pm0.}(\theta)$ at 60 and 750 MeV respectively [84]. Heidbreder *et al.* reported a value of $\cos^{3.5\pm1.2}(\theta)$ [80]. This is calculated from only 29 neutron like events. Lohrmann *et al.* reported a best fit of $\cos^{1}(\theta)$ with an upper limit of $\cos^{4}(\theta)$ [89]. However, Lohrmann stated that the fits are quite poor. Additionally this data

does not closely agree with other measurements. Lohrmann was not considered in calculating an average. Miyake *et al.* calculated the angular distribution by comparing the recorded flux to the predicted vertical flux. Between 100 MeV and 1 GeV this indicated an angular distribution varying from $\cos^3(\theta)$ to $\cos^5(\theta)$ [85]. The distribution becomes more peaked as the neutron energy increases. Moser *et al.* reported a best fit of $\cos^{2.9\pm0.3}(\theta)$ for neutrons of energy 20 to 170 MeV [82]. This is an average of four measurements at significantly different elevations and is an update to the original work by Saxena [83]. Preszler *et al.* reported a value of $\cos^{3.0}(\theta)$. These measurements, excluding the results of Lohrmann *et al.*, indicate a mean angular distribution of $\cos^{3.0\pm0.6}(\theta)$. The MARS analysis used this mean value and a standard deviation of ±1.0 to describe the systematic variation due to the unknown incident neutron angular distribution. The percent variation without uncertainty between the assumed $\cos^{3.0}(\theta)$ and $\cos^{2.0}(\theta)$ and $\cos^{4.0}(\theta)$ is shown in Fig. 6.7 as a function of the reconstructed neutron energy.

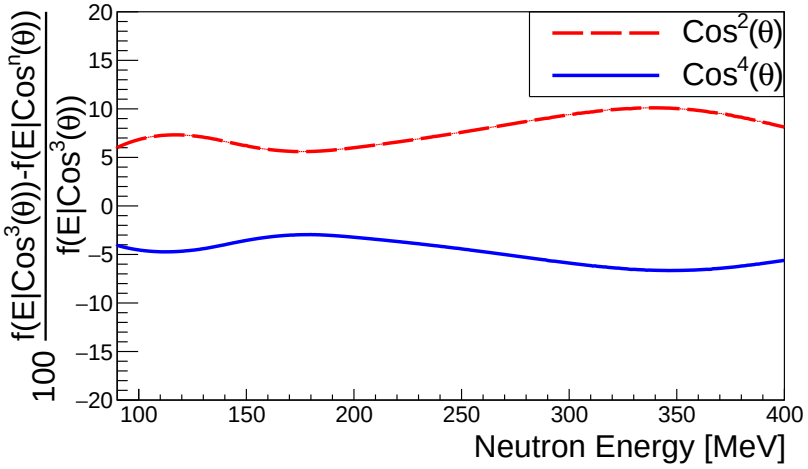

Figure 6.7: The percent difference in the reconstructed neutron flux versus energy, between the preferred ($\cos^3(\theta)$) and alternative choices of the neutron angular distribution. The partial geometry model was used for this comparison.

The Surrounding Environment Monte Carlo Model

The MARS Monte Carlo model consists of two environmental scenarios: the full and partial geometry models described in Sec. 5.1. The partial geometry model only includes the MARS detector. The full geometry model includes the MARS deployment platform and an associated model of the surrounding earth. The variation of the MARS results as a function of the surrounding environmental model were on the same order as the incident angular distribution (Fig. 6.7). However, a multitude of environmental models do not exist, making it difficult to calculate a systematic uncertainty. The distributions as a function of energy between the partial and full geometry model are therefore averaged using a convolution and

each individual distribution was used to construct the systematic uncertainties presented in Fig. 6.8. Other Geant4 physics lists and environmental models could be considered. However, additional models are prohibitively expensive given the CPU-time required to produce acceptable statistics.

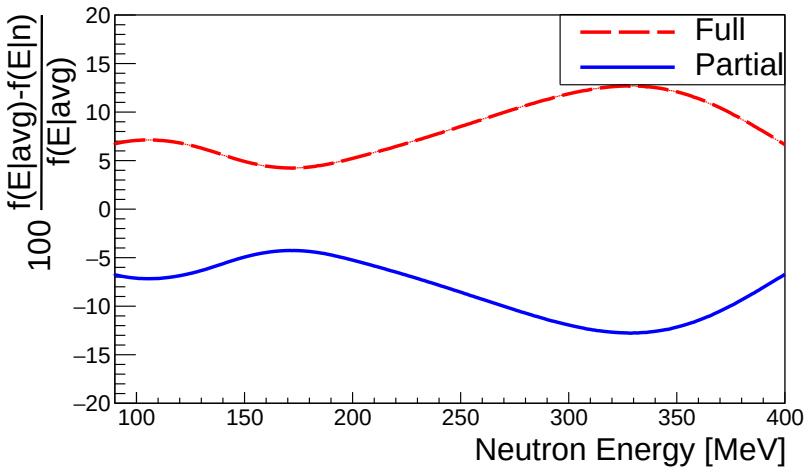

Figure 6.8: The percent difference in the reconstructed neutron flux versus energy, between the partial and full geometry models given an incident angular distribution of $\cos^3(\theta)$.

The Multiplicity Event Identification

The secondary neutron capture characteristics for MARS were well characterized using a Cf-252 source in [90]. Excellent agreement between the neutron capture efficiency and reasonable agreement between the neutron capture time was observed. The slight discrepancy in the capture time produces a small deviation in the MARS event tagging efficiency. The triggering analysis described in Sec. 5.4 used an initial time range of 25 μs with a possible expansion of 75 μs from the second to last deposition. To characterize the uncertainty in the event tagging efficiency, the initial time range was varied from 22μs to 28μs. The secondary time range was left fixed at 75μs. The variation in the initial time range is based upon the ratio of the initial time range and the capture time:

$$\frac{25\mu s}{t_{sim}} \approx \frac{25\mu s + x\mu s}{t_{exp}}, \tag{6.1}$$

where t_{sim} is the capture time from the simulation, t_{exp} is the capture time from the measured data (Sec. 4.5), and x is the variation [2]. The variation x was conservatively rounded up to 3 μs, and it is assumed the variation is symmetric ($\pm$ 3 μs). This systematic uncertainty was found to be relatively small when compared to the angular distribution and environmental model systematic uncertainty (Figs. 6.7-6.8).

[2]The Poisson distribution is dependent upon the ratio of the trigger time range and the capture time.

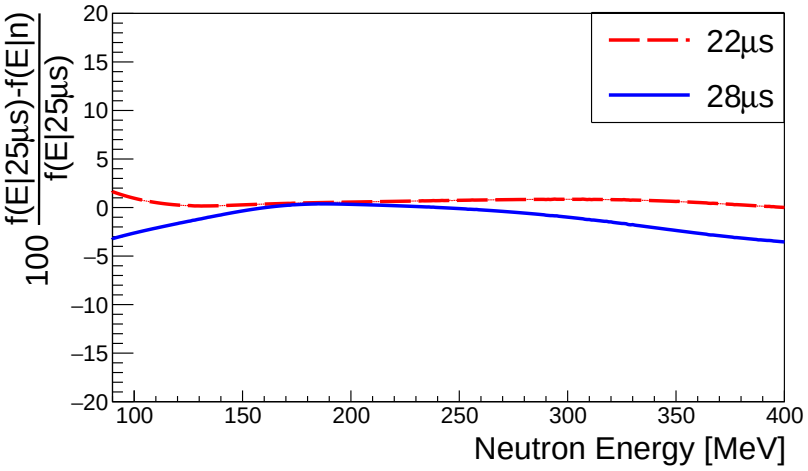

Figure 6.9: The percent difference in the reconstructed neutron flux versus energy, between the default initial time range structure of 25 μs and initial time ranges of 22 μs and 28 μs given an incident angular distribution of $\cos^3(\theta)$.

6.4 Final Results and Discussion

Given the above measured data and systematic uncertainty analysis, Fig. 6.10 displays the final reconstructed high-energy neutron energy-dependent flux. The total uncertainty was calculated by a sum in quadrature, given the concerns presented in Sec. 6.3 and the statistical uncertainty. The MARS results are compared to the previous measurements summarized by Ziegler [12] and to the measurement of Gordon [39]. Additionally, the uncertainty of previous measurements ignored by Ziegler was included in Fig. 6.10.

The above ground results in Fig. 6.10 are comparable with the results of Gordon *et al.* [39] and Hess *et al.* [10, 41] between 90 MeV and 250 MeV. Below 90 MeV the result is constrained by the detector efficiency and boundary conditions employed by the MCMC reconstruction analysis. Above 250 MeV, MARS predicts a slightly lower flux than most previous measurements. Regardless of the energy regime, the MARS results are contained within the spread of previous measurements.

Many factors in MARS or in the previous measurements could induce the lack of agreement above 250 MeV. The MARS measurement could be biased by the large hills on two sides of the detector. These hills could decrease the flux of high-energy neutrons particularly as the incident neutron energy increases. More importantly, MARS only uses the Geant4 Shielding physics list. This is generally considered the best physics list in Geant4 for modeling high-energy background measurements. However, if MARS were to use multiple physics lists or use a different modeling application (e.g. MCNP or FLUKA), a larger uncertainty may be calculated, which could cover the previous measurements. These simulations are not performed in MARS due to the simulation time required to produce acceptable statistics. While this is not an acceptable excuse: no other experiments characterize this systematic

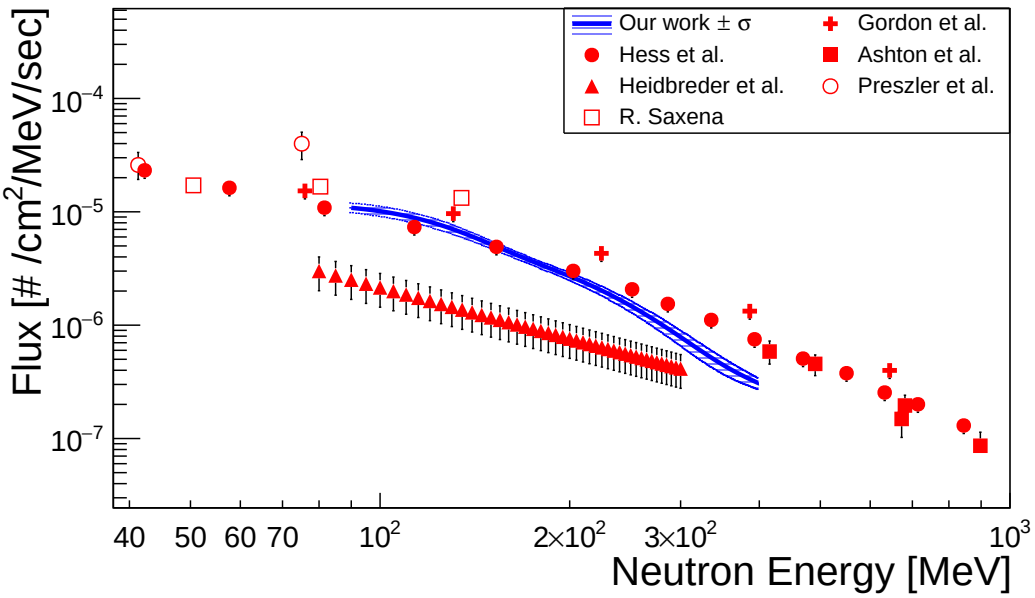

Figure 6.10: The above ground reconstructed neutron energy-dependent flux at KURF compared to previous experiments. The previous experimental data correspond to the following shapes: Ashton *et al.* ■[78], Gordon *et al.* +[39], Heidbreder *et al.* ▲[80], Hess *et al.* ●[10, 41], Preszler *et al.* ○[81], and R. Saxena □[83]. The results from Ashton [78] were scaled by Ziegler [12] due to the unknown incident angular distribution.

uncertainty.

Some previous experiments may be biased because of the lack of a charged particle veto [10, 41, 39]. Charged particles may artificially inflate the measured neutron flux. Ziegler estimates that the hadron flux is 90% neutrons at 100 MeV, but may be 50% protons by 1 GeV [12]. MARS would appropriately veto these protons. If this charged particle flux is considered, an over-prediction of the neutron flux may be present in the previous data. Additionally, if the incident neutron angular distribution becomes more peaked at higher energies it may reduce the inferred flux by other experiments. This reduction is primarily due to a slightly increased efficiency from high-energy neutrons, due to less clipping of detector edges in detectors with non-uniform angular response.

Finally, no experiment calculates the systematic uncertainty due to the varying magnetic strength of the heliosphere. With these caveats, the MARS results and 1σ uncertainty are not expected to completely cover the previous measurements. The MARS results should not be considered superior to previous measurements because MARS has not been independently calibrated at these energies (e.g. at an accelerator facility). The results provide confidence that the below ground results described in the next chapter have reconstructed an appropriate flux.

Chapter 7

Measurement of the High-Energy Neutron Energy Dependent Flux Below Ground

In contrast to above ground, below ground the high-energy neutron flux is due to muon spallation and evaporation on the surrounding rock. The high-energy neutron flux is location dependent. These high-energy neutrons are capable of inducing indirect backgrounds for many rare-event neutral particle detectors (e.g. antineutrino reactor monitors [19], WIMP dark matter detectors [20], neutrinoless double beta decay detectors [21], coherent neutrino nucleus scattering detector [91]). To characterize this below ground neutron flux MARS made measurements at three depths: 377, 540, and 1450 m.w.e.

The primary purpose of this chapter is to report the results from the three below ground measurements. Where appropriate, the MARS results are compared to previous experiments and simulation predictions. In Sec. 7.1 previous measurements by other groups are described and a discussion as to why they are inadequate is presented. In Sec. 7.2 the three measurement locations are described. In Sec. 7.3 results from the three depths are presented. In Sec. 7.4 the results are summarized and comparisons are made to simulation predictions from Mei and Hime [16] and measured data from Garrison [13] and Malgin [15, 14]. Finally in Sec. 7.5, the energy integrated neutron is examined as a function of the respective muon flux. Preliminary implications are drawn regarding future depth-dependent models.

7.1 Previous Measurements

In general, the existing data relevant to the muogenic high-energy neutron flux below ground falls into three classes:

1. *In Situ* measurements of the neutron multiplicity and spectra from cosmic muons propagating through scintillator [92, 93, 94, 95, 96, 97, 98]

2. Fixed target experiments in which the neutron multiplicity and spectrum resulting from a mono-energetic muon beam incident on a target are measured [99]

3. *In Situ* measurements of the muogenic neutron background anti-coincident from the initiating muon [13, 14, 15, 43, 47, 46, 44]

With regards to the first class, the relevant quantity tracking with depth is the average muon energy: site-specific geological parameters such as overburden type and rock composition affect the average muon energy for a given depth [16]. Current measurements quantify neutron production as a function of average muon energy spanning a range from 20 GeV to almost 400 GeV, roughly corresponding to an equivalent flat overburden depth of 20 to 5200 m.w.e [98]. Several validations of both FLUKA [33, 34] and Geant4 [48, 49] have demonstrated a consistent under production of neutrons at all average muon energies compared to data. The overall shape of the neutron energy spectrum resulting from cosmic muon interactions with matter appears to be well predicted with these two Monte Carlo packages [100, 101]. Recent improvements to FLUKA [102, 103] give neutron yields that are in better agreement with data than compared to Geant4 [104].

The fixed target data class consists of a single experiment performed at CERN on three different target elements at one muon energy. The NA55 experiment studied neutron production from 190 GeV/c muons incident on thin targets of graphite, copper, and lead [99]. Later simulations preformed with Geant4.8.1 demonstrated significant underproduction of neutrons which worsened for high-Z targets [105]. Predictions with the more recent versions of Geant4 have not been performed, so the degree to which the gap has been closed is not clear at this time. However, the increasing discrepancy as a function of Z demonstrates the need for validation with other targets. Various measurements of muogenic neutron production in high-Z materials are summarized in [106].

Regardless of the accuracy of the simulations for the two previous categories, neither measurement class directly measures the high-energy neutron flux emitted from rock as a function of depth or average muon energy. Muon correlated neutron measurements in scintillator only quantify production in detector materials, not the neutron flux emitted from the cavern walls. Muon beam experiments have not used rock targets or tested a suite of elements capable of predicting a representative rock response. Therefore both the first and second class of experiments are only useful for benchmarking Monte Carlo simulations.

Finally, *in situ* measurements of the cosmogenic neutron background, anti-coincident with the initiating muon in the detector, are sparse. Five measurement attempts, each at a single depth are known:

1. Garrison at 265 m.w.e. [13]

2. Malgin *et al.* at 550 m.w.e. [14, 15]

3. Langford *et al.* at 1450 m.w.e. [43]

4. Sweany *et al.* at 1950 m.w.e. [47, 46]

5. Zhang and Mei at 2100 m.w.e. [44]

Of the five measurements, only two report measured neutron spectra in the relevant energy regime. Garrison recently measured the high-energy neutron flux (25 to 150 MeV) at a depth of 265 m.w.e. [13]. This measurement was at a depth slightly above the shallowest MARS measurement. However, the results will be included in the final measurement comparison figure (Fig. 7.18). Malgin *et al.* measured an integrated neutron energy flux (20 to 80 MeV) at 550 m.w.e of 2.3x10^{-4} [$\#/m^2/sec$]. The energy-dependent flux was presented in arbitrary units in a separate paper [15], which allowed for calculating the incident neutron flux. While the measured energy regime of the Malgin measurement does not overlap with MARS, it still provides a useful comparison at a very similar depth. Langford *et al.* performed a measurement at Kimballton Underground Research Facility (KURF) (1450 m.w.e.), the same location as the deepest MARS measurement, and only observed neutron energies indicative of (α,n) reactions [43]. The measurement by Sweany *et al.* is at a depth below what has been measured by this effort (1950 m.w.e.) and lacks a detailed energy spectral measurement [47, 46]. Zhang and Mei recently performed a recoil measurement at 2100 m.w.e. However, no spectral unfolding was performed. Only the measured data of 5 MeVee to 50 MeVee proton recoils was presented [44].

The five previous experiments span a large overburden range and use different measurement techniques, detectors, and rock types which make comparisons of the results difficult without benchmarked Monte Carlo simulations. Additionally only two of the measurements reports results in a format which can be used by other experimenters [13, 14, 15]. One of these measurements [14, 15], was performed in the early 1980's and the results were translated from Russian journals.

In contrast to the disjointed information from the previous measurements, MARS has measured the high-energy neutron energy-dependent flux at three depths, with the same general rock composition, to ensure as uniform relative systematic bias as possible. Results in Sec. 7.3 report the energy dependent flux, with statistical and systematic uncertainty. These results are in a format which allow for the future creation of a depth dependent model of the high-energy neutron energy-dependent flux.

7.2 Measurement Campaign

MARS performed three neutron energy-dependent flux measurements at KURF at depths of: 377, 540, and 1450 m.w.e. The measurements were performed from June to December 2013 (540 m.w.e.), from January until May 2014 (377 m.w.e.), and from May 2014 to May 2015 (1450 m.w.e.). The three measurement locations differed greatly in terms of the surrounding environment. At the 377 m.w.e depth, the experimental cavern was roughly hemispherical with a large radius ($\geq$15 m). MARS was positioned near the center of the cavern. The cavern dimensions were not precisely measured due to persistent fog clouding attempted laser rangefinders measurements. At the 540 m.w.e. depth, the experimental cavern hall had a

rectangular cross section on the order of ∼40 ft. wide and ∼20 ft. tall. MARS was positioned within 10 ft. of one of the side walls to avoid mine traffic. At the 1450 m.w.e. depth, MARS was placed on a concrete pad inside the KURF scientific facility. The cavern width was similar to the 540 m.w.e. depth but the ceiling was significantly higher. Unfortunately the 377 m.w.e. and 540 m.w.e. locations did not have sufficient lighting to provide detailed pictures. At the 1450 m.w.e. depth, Virginia Tech researchers have provided pictures of the cavern before the installation of the scientific facility (Fig. 7.1) and of the inside of the scientific facility after construction (Fig. 7.2) [107]. Examining Fig. 7.2, MARS was positioned at location B.

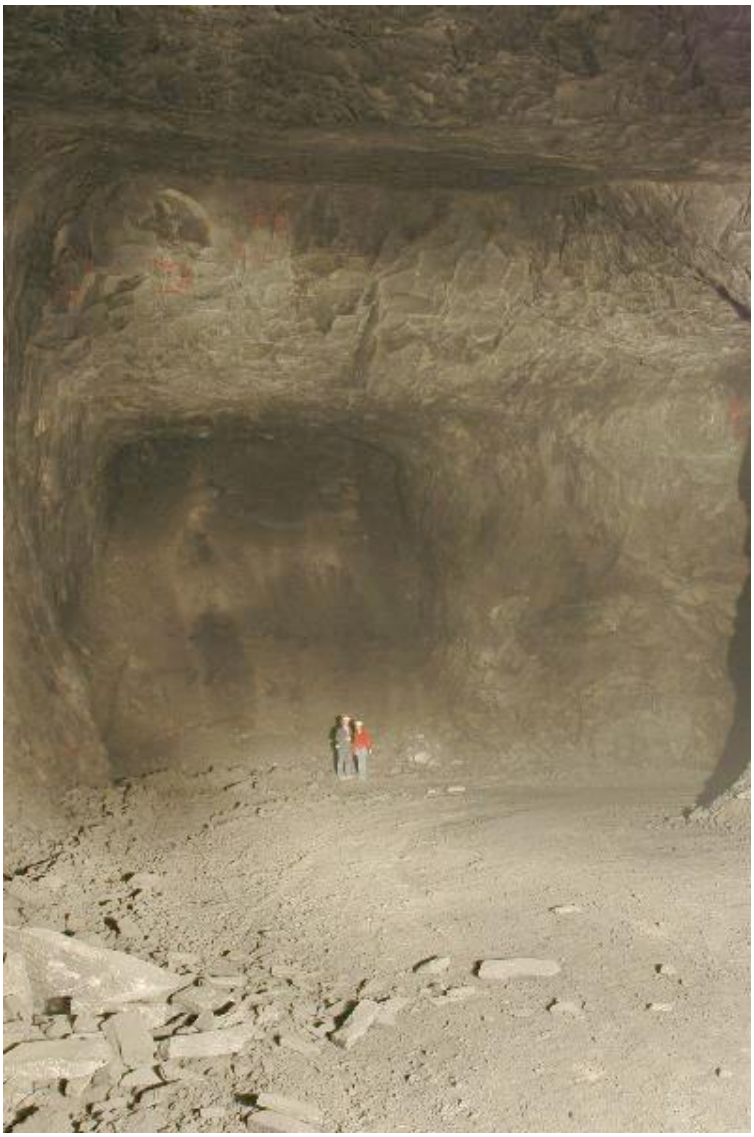

Figure 7.1: A picture of the cavern before construction of the KURF scientific facility.

Figure 7.2: A picture of the inside of the KURF scientific facility. The MARS deployment platform was parked at location B.

The MARS reconstruction analysis ignores the respective cavern geometries. Previous analysis using the above ground data (Sec. 6.3) indicated that the difference between a rock floor and no surrounding environment should be less than the statistical uncertainty below ground. Additionally, it is assumed that the closer a rock surface is to the detector, the more it will shift the results. The rock floor below the detector is the nearest rock surface to the detector; the rock floor is included in the full geometry Monte Carlo model.

7.3 Results

Using the measured data described above and the algorithm in Sec. 3.5, the MCMC analysis was performed in the nearly the same manner as Sec. 6.4. Two differences exist between the above and below ground measurements: the multiplicity event thresholds as described in Sec. 3.3, and the assumed incident neutron angular distribution. Below ground the distribution is expected to be a combination of an isotropic distribution from evaporation and a highly forward peaked with the incident muon direction distribution. Therefore, the MARS analysis assumes an incident angular distribution of $\cos^2(\theta)$. Angular distributions of $\cos^1(\theta)$ and $\cos^3(\theta)$ are used to estimate the systematic uncertainty.

As above ground, a minimal number of muon generated events are expected to contaminate the MARS neutron measurement: the below ground noise subtraction only considers the gamma ray contamination. Muon-induced neutron-like events, in each below ground

measurement, were predicted to contribute less than 1 measured event. Examining the multiplicity identification algorithm of Sec. 3.3 one should note that the final threshold is significantly different for the below ground data. This more stringent threshold requires all events to have an average recorded Gd de-excitation energy of >2.2 MeV which significantly removes the uncorrelated ambient gamma-ray background. Below ground, all three measurements have an estimated ∼4% gamma-ray contamination of the neutron multiplicity signal.

Similar results were observed for optimizing the regularization parameter α. Bias reduction and systematic uncertainty estimates were more crucial for obtaining consistent results below ground. Due to lower statistics, the histogram convergence values (see Fig. 6.6d) of the individual basis splines do not always have a Gaussian distribution. The output energy knot spacing was increased until consistent results were achieved. For each respective reconstruction the knot spacing will be provided below. It is assumed that if the $\vec{f_i}$ values do not have a Gaussian distribution, the mean value should decease as a function of the i-th basis spline coefficient. The rest of the section describes the calculation and uncertainty at each respective equivalent flat overburden depth. The next section presents all three results together and compares the results to previous measurements and simulation.

The 377 m.w.e. Flux

The measurement at 377 m.w.e. was performed over a 5 month period with a live-time of 79.5 days. Due primarily to the ambient gamma ray flux, a dead-time of 4.2% was observed. During the last month of the measurement, the HV modules supplying power exhibited intermittent performance. This data was discarded and the HV modules were replaced. The data for the first four months exhibited stable triggering rates and was used for the following analysis. During this measurement period, 1234 neutron-like events were measured. As expected, this is a significant decrease from the rate observed above ground. The measured neutron data and gamma-ray and muon background predictions in the three component measured space are shown in Fig. 7.3. Note, these background predictions are for gamma-ray contaminated or muon induced events in the measured data; they are predicted using simulation.

These neutron events were processed with the MCMC algorithm of Sec. 3.5. An energy knot spacing of [20, 30, 40, 50, 90, 400, 800, 1200, 1600, 2500] in units of MeV was used. The support of the reconstruction is (90 MeV, 400 MeV). The optimization of the regularization parameter α and the amount of bias correction performed are presented in Fig. 7.4. Convergence of α is achieved by iteration 3; only 5 iterations were used due to the analysis quickly converging. As opposed to the above ground measurements, significant bias reduction is observed. This is most likely due to the limited statistics at the 377 m.w.e. depth.

After optimizing the regularization parameter α and reducing the bias, the convergence criteria were calculated and are presented for $\vec{f_0}$ in Fig. 7.5. Other vector coefficient convergence criteria are presented in Appendix H.

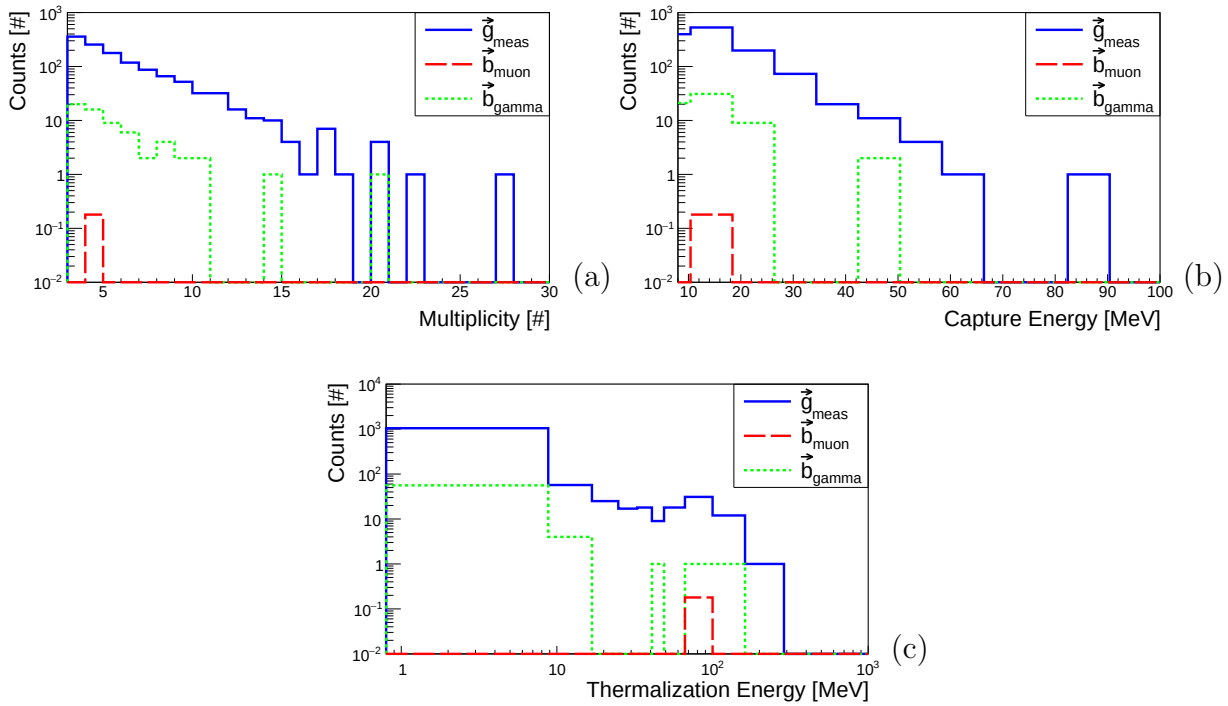

Figure 7.3: The measured neutron data and the simulation predicted gamma-ray and muon background from the measurement at 377 m.w.e. depth at KURF. (a) Depicts the measured multiplicity and the predicted contaminated multiplicity data. (b) Depicts the measured capture energy and the predicted contaminated capture energy data. (c) Depicts the measured thermalization energy and the predicted contaminated thermalization energy data. The three components of each x-axis represents the measured binning for the respective component. A similar percent of contaminated events is observed across the range of measured data consistent with a small constant probability for contamination.

As with the above ground data, systematic uncertainty quantification was performed and the results are displayed in Fig. 7.6. The total uncertainty was calculated by a sum in quadrature. However, below ground the dominate uncertainty is due to statistical concerns. The final reconstructed flux with total uncertainty at 377 m.w.e. is presented in Fig. 7.7.

The 540 m.w.e. Flux

The measurement at 540 m.w.e. was performed over a 6 month period with a live-time of 126 days. Due primarily to the ambient gamma-ray flux, a dead-time of 4.1% was observed. No issues were observed with the data or hardware during the measurement. During this measurement period, 720 neutron-like events were measured. As expected, this is a significant decrease from the rate observed above ground and a slight decrease from the rate observed during the 377 m.w.e. measurement. The measured data and gamma-ray and muon noise

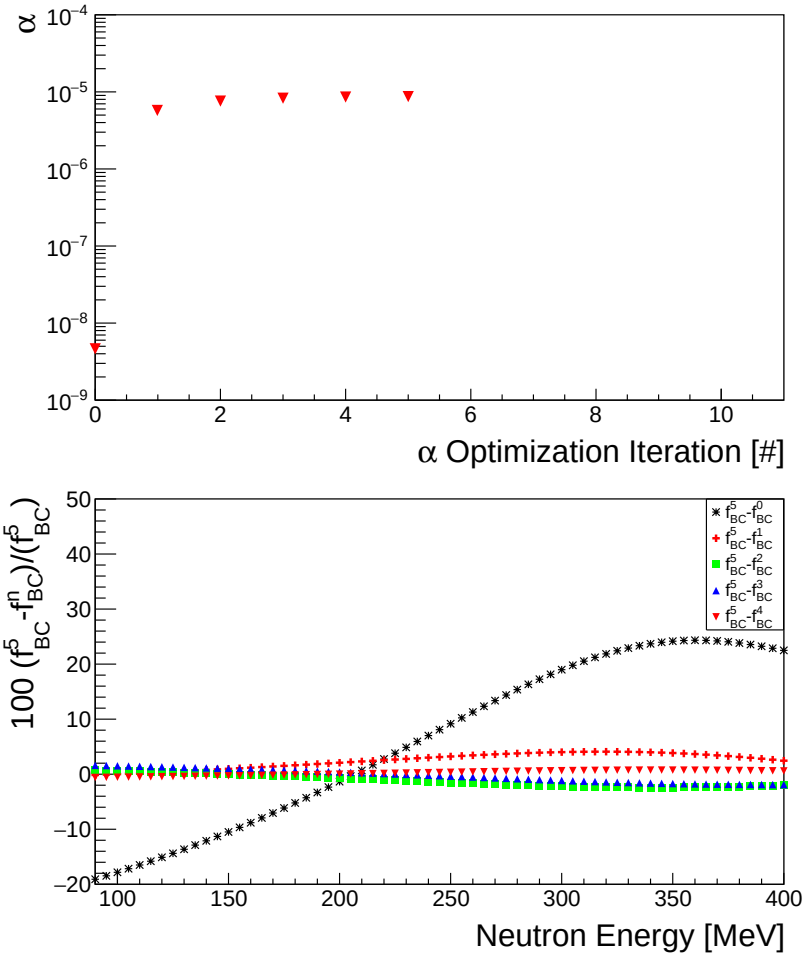

Figure 7.4: For the 377 m.w.e. depth: Redo (a)(a) depicts the regularization parameter α iteration update values from step 2c of the MCMC algorithm from Sec. 3.5. (b) Depicts the percent difference between the final bias reduced answer $\vec{f}^{5}_{BC}$ and the previous iterations $\vec{f}^{n}_{BC}$ where n varies from 0 to 4.

predictions in the three component measured space are shown in Fig. 7.8.

These neutron events were processed with the MCMC algorithm of Sec. 3.5. An energy knot spacing of [20, 30, 40, 50, 90, 400, 800, 1200, 1600, 2500] in units of MeV was used. This is the same knot spacing as the 377 m.w.e. measurement. The optimization of the regularization parameter α and the amount of bias correction performed are presented in Fig. 7.9. Convergence of α is achieved by iteration 3. As opposed to the above ground measurements, significant bias reduction is observed. This is most likely due to the limited statistics at the 540 m.w.e. depth.

After optimizing the regularization parameter α and reducing the bias, the convergence criteria were calculated and are presented for $\vec{f}_0$ in Fig. 7.10. Other vector coefficient con-

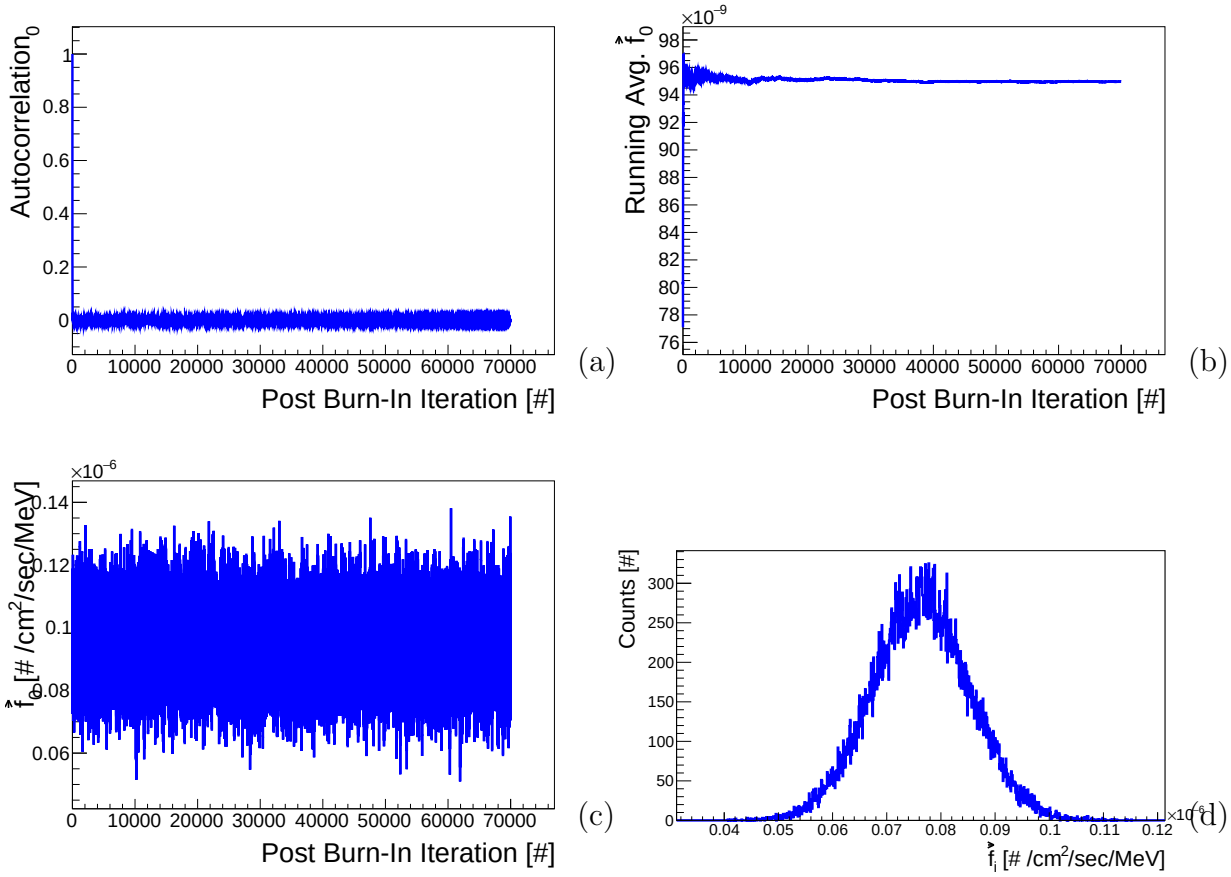

Figure 7.5: For the 377 m.w.e. depth: (a) depicts the autocorrelation of $\vec{f}_0$ as a function of the post burn-in iteration. (b) Depicts the running average of $\vec{f}_0$ as a function of the post burn-in iteration. (c) Depicts the value of $\vec{f}_0$ as a function of the post burn-in iteration. (d) Depicts the histogram of $\vec{f}_0$ values. As described in the text the sub-figures are representative of all parameters and indicate sufficient convergence.

vergence criteria are presented in Appendix H.

As with the above ground data, systematic uncertainty quantification was performed and the results are displayed in Fig. 7.11. The total uncertainty was calculated by a sum in quadrature. However, below ground the dominate uncertainty is due to statistical concerns. Figure 7.11c is significantly different than the triggering systematic uncertainty observed in the above ground measurement and the 377 m.w.e. measurement. The 22 μs and 28 μs reconstructions do not bound the 25 μs reconstruction. The same initial parameters were used to start the MCMC reconstruction and convergence was observed for all reconstructions. The observed non-bounding feature was consistent between both the full and partial Monte Carlo models. If one were to correctly combine the three systematic uncertainties, a sum in

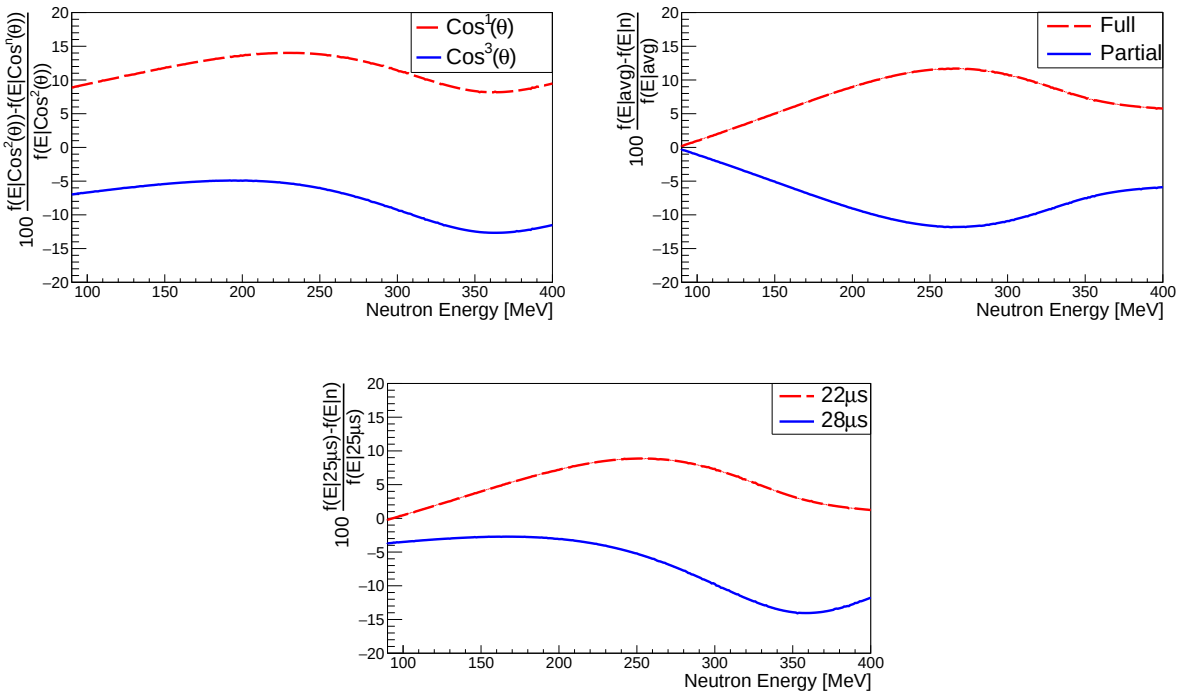

Figure 7.6: For the 377 m.w.e. depth: (a) Depicts the percent difference in the reconstructed neutron flux versus energy, between the preferred ($\cos^2(\theta)$) and alternative choices of the neutron angular distribution. The partial geometry model was used for this comparison. (b) Depicts the reconstructed neutron energy-dependent flux for the partial and full geometry models given an incident angular distribution of $\cos^2(\theta)$. (c) Depicts the reconstructed neutron energy-dependent flux with variation in the initial gate triggering time given an incident angular distribution of $\cos^2(\theta)$.

quadrature can no longer be used: the uncertainty for the triggering variation is no longer symmetric. However, dealing with non-symmetric uncertainty distribution requires a model or multiple reconstructions of the distribution as a function of the triggering time. This was not considered computationally feasible; the distributions were conservatively assumed to be symmetric. The final reconstructed flux with total uncertainty at 540 m.w.e. is presented in Fig. 7.12.

The 1450 m.w.e. Flux

The measurement at 1450 m.w.e. was performed over a 12 month period with a live-time of 207 days. Due primarily to the ambient gamma ray flux, a dead-time of 3.6% was observed. During several weeks no data was taken, due to issues with changing data hard drives. No issues were observed with the data or hardware during the measurement. During this measurement period, 279 neutron-like events were measured. As expected, this is a significant

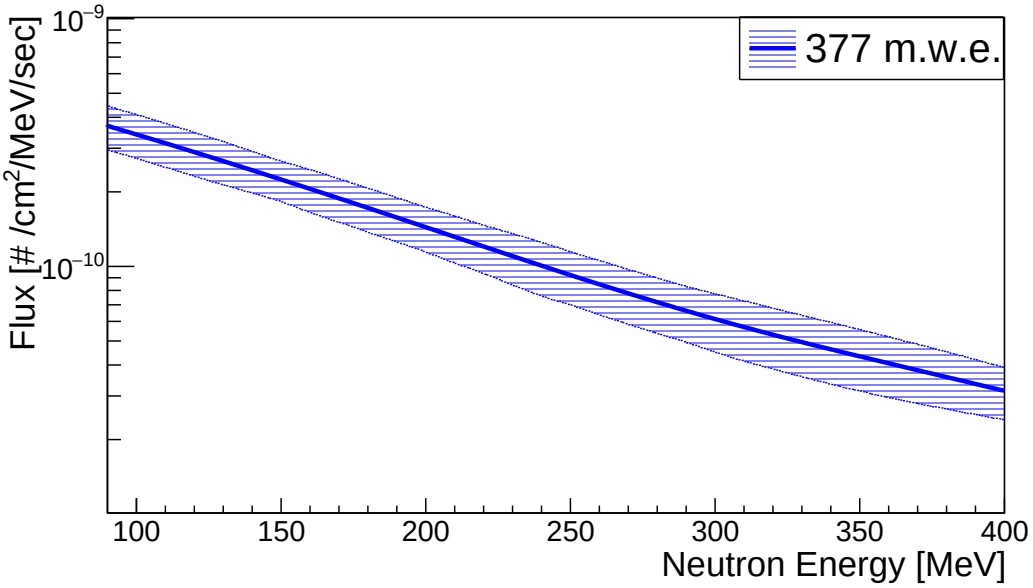

Figure 7.7: The reconstructed high-energy neutron energy-dependent flux with total uncertainty at 377 m.w.e.

decrease from the rate observed above ground and a slight decrease from the rate observed during the 377 m.w.e. and 540 m.w.e. measurements. The measured neutron data and gamma-ray and muon background predictions in the three component measured space are shown in Fig. 7.13.

These neutron events were processed with the MCMC algorithm of Sec. 3.5. An energy knot spacing of [20, 30, 40, 50, 90, 300, 800, 1200, 1600, 2500] in units of MeV was used. This is not the same knot spacing as the 377 m.w.e. and 540 m.w.e. measurements. The highest energy with full support, 300 MeV, was decreased from 400 MeV. The reconstruction was found to have significant variation past 300 MeV. If the highest support energy was 400 MeV, the mean value of the basis spline coefficients ($\vec{f}_i$, Fig. 7.15c) was found to fluctuate as the basis spline number increased [1]. The coefficients are expected to have a Gaussian distribution or the mean is expected to decrease as the basis spline number increases. The optimization of the regularization parameter α and the amount of bias correction performed are presented in Fig. 7.14. Convergence of α is achieved by iteration 3. As opposed to the above ground measurements, significant bias reduction is observed. However, significantly more bias correction iterations were required to achieve stability. This is most likely due to the limited statistics at the 1450 m.w.e. depth.

After optimizing the regularization parameter α and reducing the bias, the convergence criteria were calculated and are presented for $\vec{f}_0$ in Fig. 7.15. Other vector coefficient con-

[1] For example $\vec{f}_4$ vs. $\vec{f}_5$.

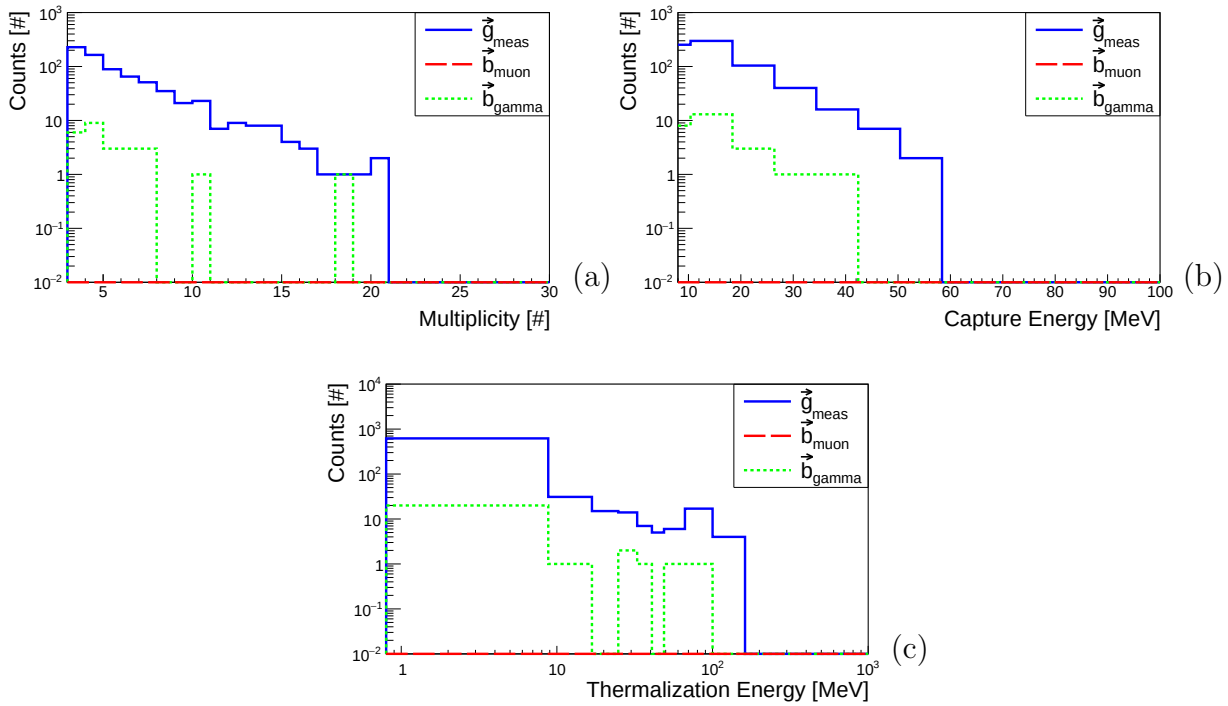

Figure 7.8: The measured neutron data and the simulation predicted gamma-ray and muon background from the measurement at 540 m.w.e. depth at KURF. (a) Depicts the measured multiplicity and the predicted contaminated multiplicity data. (b) Depicts the measured capture energy and the predicted contaminated capture energy data. (c) Depicts the measured thermalization energy and the predicted contaminated thermalization energy data. The three components of each x-axis represents the measured binning for the respective component. A similar percent of contaminated events is observed across the range of measured data consistent with a small constant probability for contamination. No muon predicted background events were observed. This is an artifact of the simulation time and small muon contamination probability.

vergence criteria are presented in Appendix H.

As with the above ground data, systematic uncertainty quantification was performed and the results are displayed in Fig. 7.16. The total uncertainty was calculated by a sum in quadrature. Similar to the reconstructions at 540 m.w.e. non-symmetric uncertainty is observed in Fig. 7.16c. The final reconstructed flux with total uncertainty at 1450 m.w.e. is presented in Fig. 7.17.

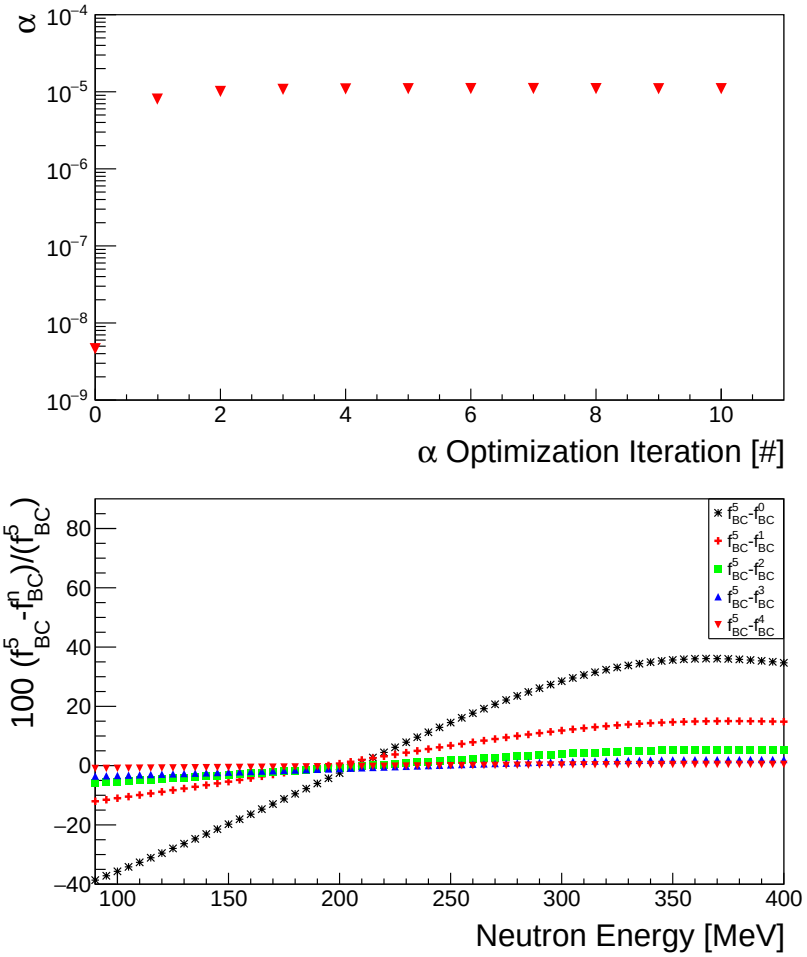

Figure 7.9: For the 540 m.w.e. depth: (a) depicts the regularization parameter α iteration update values from step 2c of the MCMC algorithm from Sec. 3.5. (b) Depicts the percent difference between the final bias reduced answer $\vec{f}^{5}_{BC}$ and the previous iterations $\vec{f}^{n}_{BC}$ where n varies from 0 to 4.

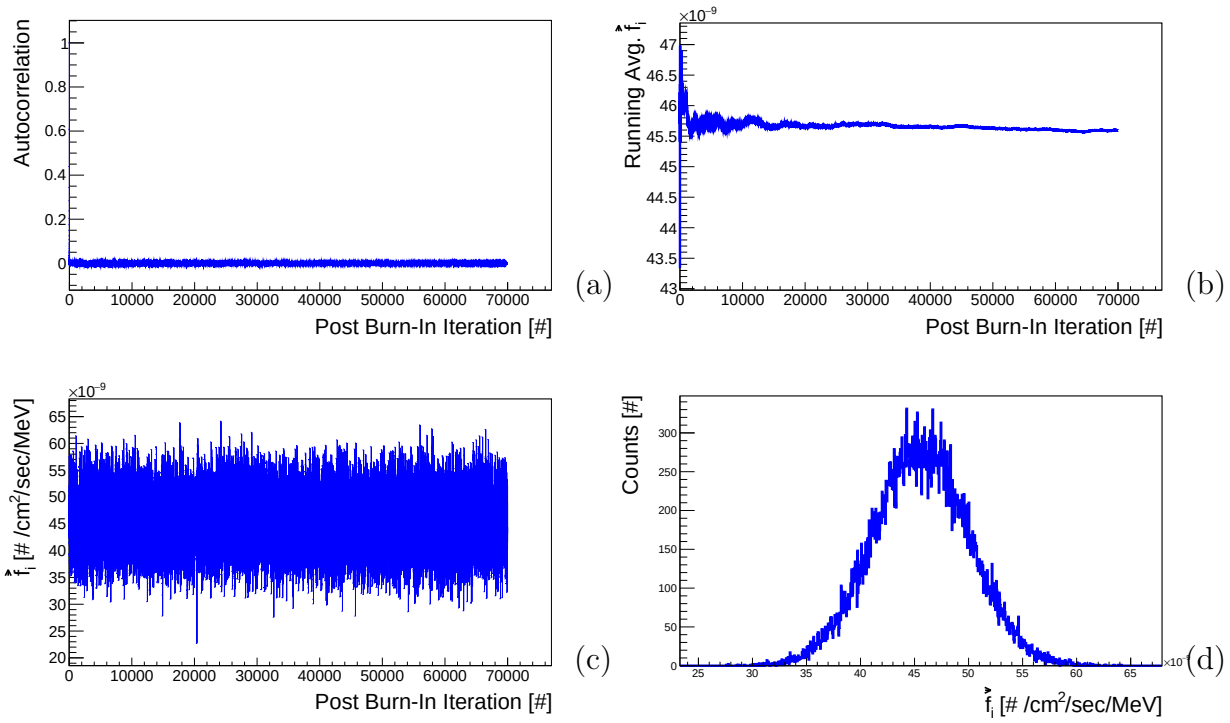

Figure 7.10: For the 540 m.w.e. depth: (a) depicts the autocorrelation of $\vec{f_0}$ as a function of the post burn-in iteration. (b) Depicts the running average of $\vec{f_0}$ as a function of the post burn-in iteration. (c) Depicts the value of $\vec{f_0}$ as a function of the post burn-in iteration. (d) Depicts the histogram of $\vec{f_0}$ values. As described in the text the sub-figures are representative of all parameters and indicate sufficient convergence.

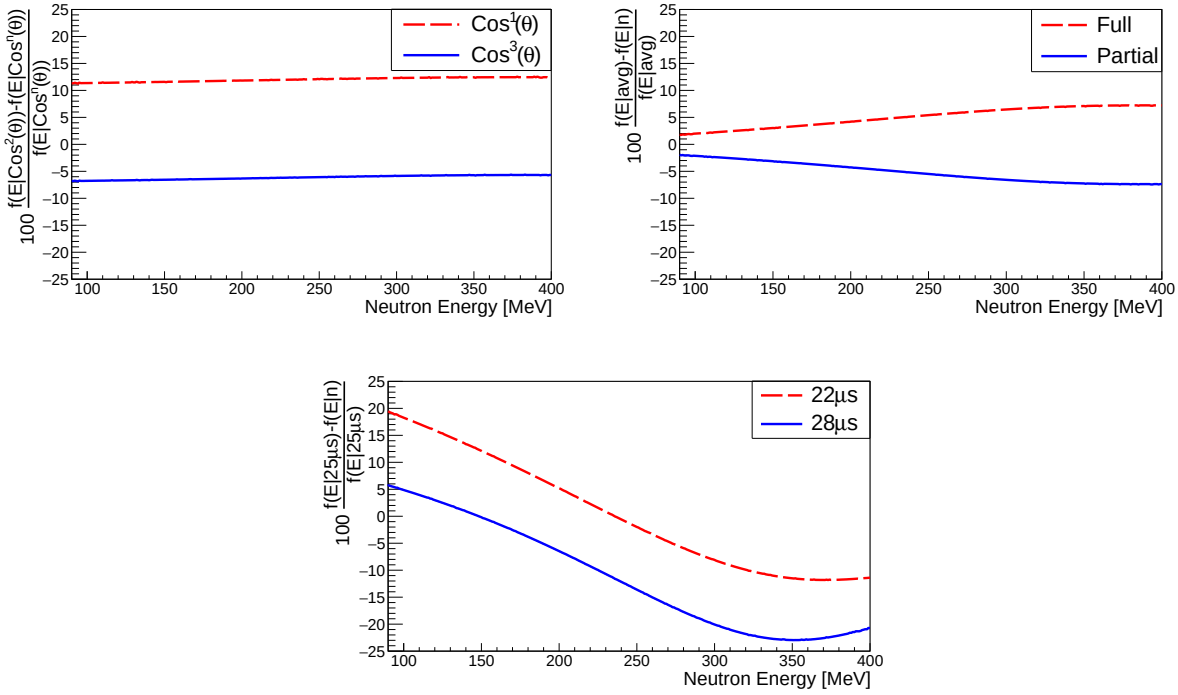

Figure 7.11: For the 540 m.w.e. depth: (a) Depicts the percent difference in the reconstructed neutron flux versus energy, between the preferred ($\cos^2(\theta)$) and alternative choices of the neutron angular distribution. The partial geometry model was used for this comparison. (b) Depicts the reconstructed neutron energy-dependent flux for the partial and full geometry models given an incident angular distribution of $\cos^2(\theta)$. (c) Depicts the reconstructed neutron energy-dependent flux with variation in the initial gate triggering time given an incident angular distribution of $\cos^2(\theta)$.

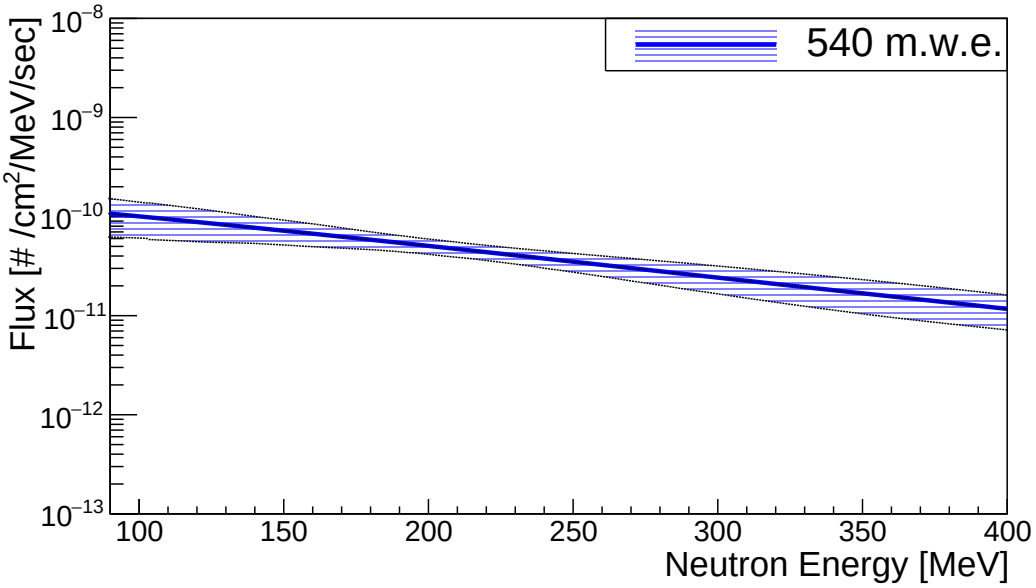

Figure 7.12: The reconstructed high-energy neutron energy-dependent flux with total uncertainty at 540 m.w.e.

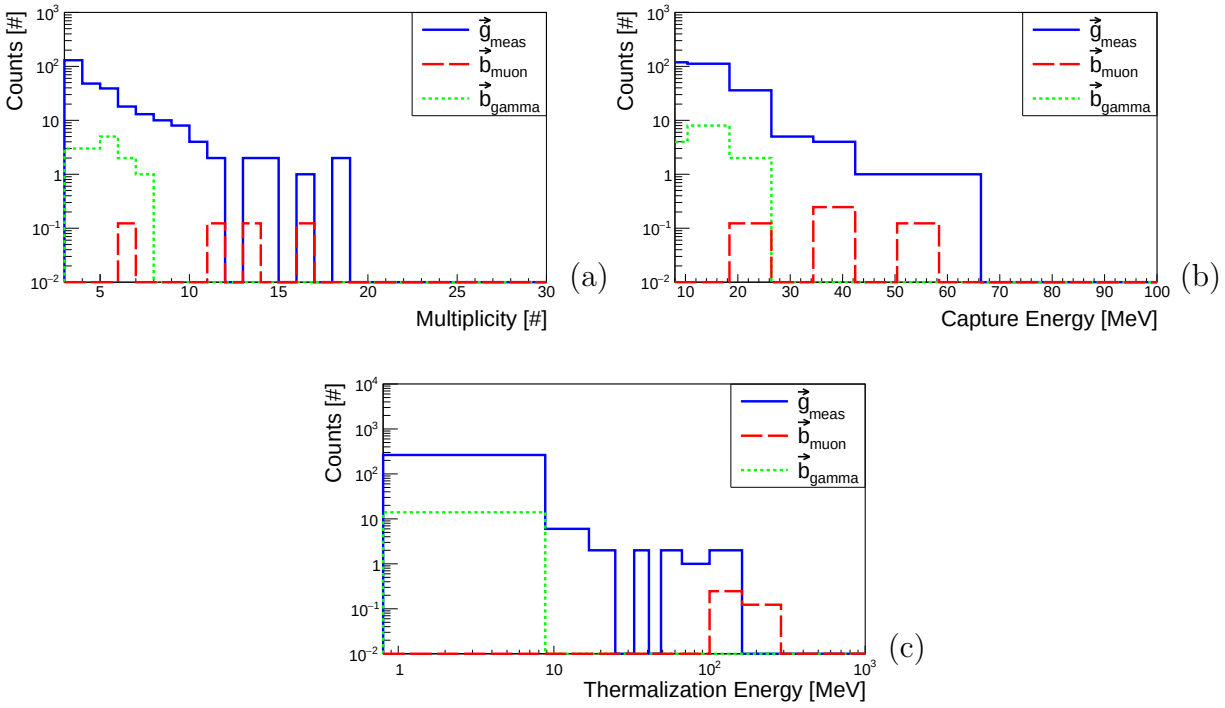

Figure 7.13: The measured neutron data and the simulation predicted gamma-ray and muon background from the measurement at 1450 m.w.e. depth at KURF. (a) Depicts the measured multiplicity and the predicted contaminated multiplicity data. (b) Depicts the measured capture energy and the predicted contaminated capture energy data. (c) Depicts the measured thermalization energy and the predicted contaminated thermalization energy data. The three components of each x-axis represents the measured binning for the respective component. A similar percent of contaminated events was observed across the range of measured data consistent with a small constant probability for contamination.

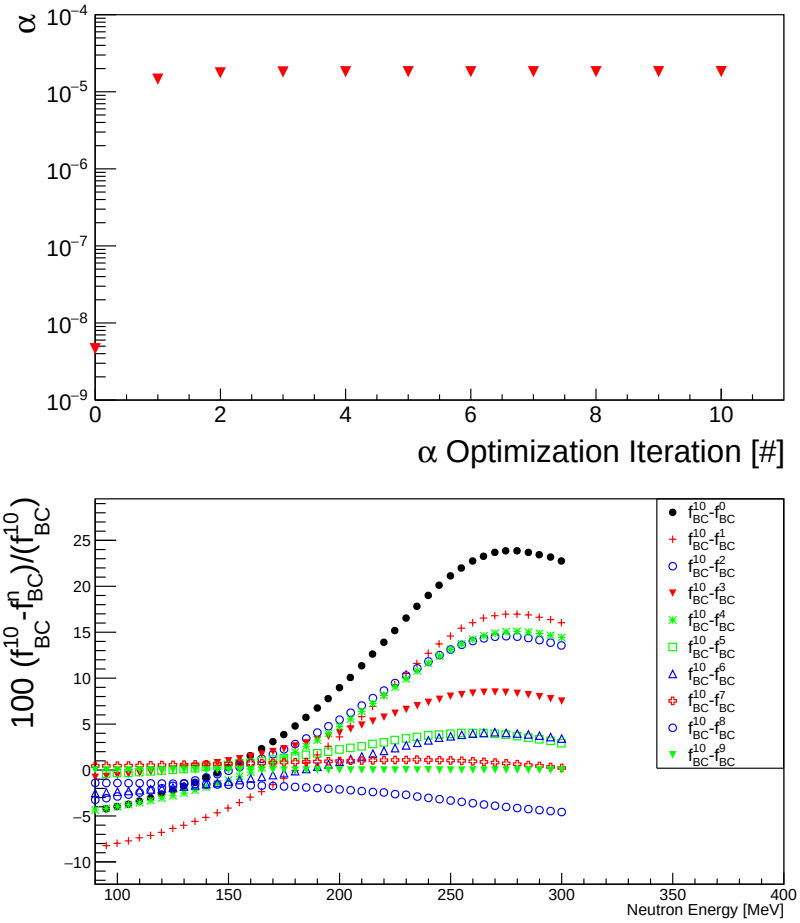

Figure 7.14: For the 1450 m.w.e. depth: (a) depicts the regularization parameter α iteration update values from step 2c of the MCMC algorithm from Sec. 3.5. (b) Depicts the percent difference between the final bias reduced answer $\vec{f}^{5}_{BC}$ and the previous iterations $\vec{f}^{n}_{BC}$ where n varies from 0 to 4.

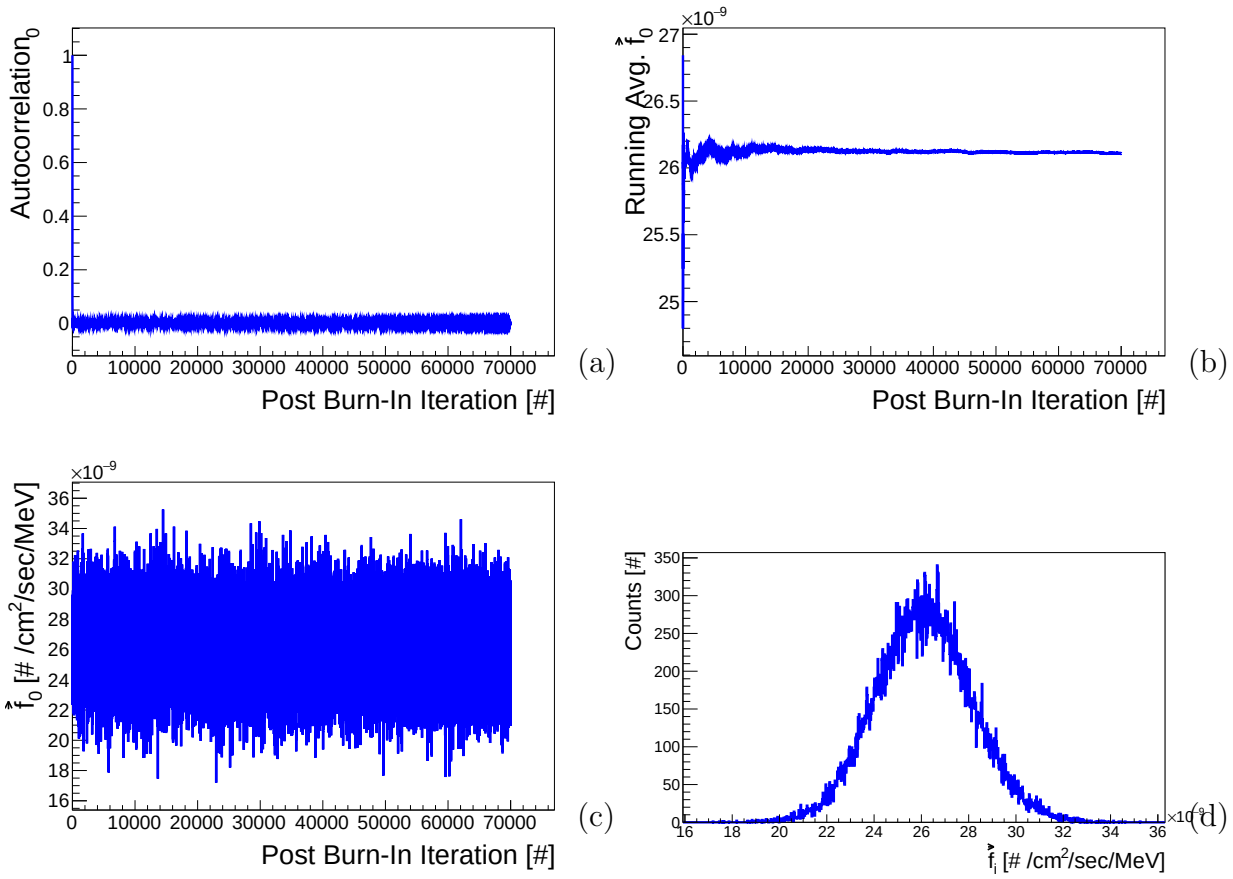

Figure 7.15: For the 1450 m.w.e. depth: (a) depicts the autocorrelation of $\vec{f_0}$ as a function of the post burn-in iteration. (b) Depicts the running average of $\vec{f_0}$ as a function of the post burn-in iteration. (c) Depicts the value of $\vec{f_0}$ as a function of the post burn-in iteration. (d) Depicts the histogram of $\vec{f_0}$ values. As described in the text the sub-figures are representative of all parameters and indicate sufficient convergence.

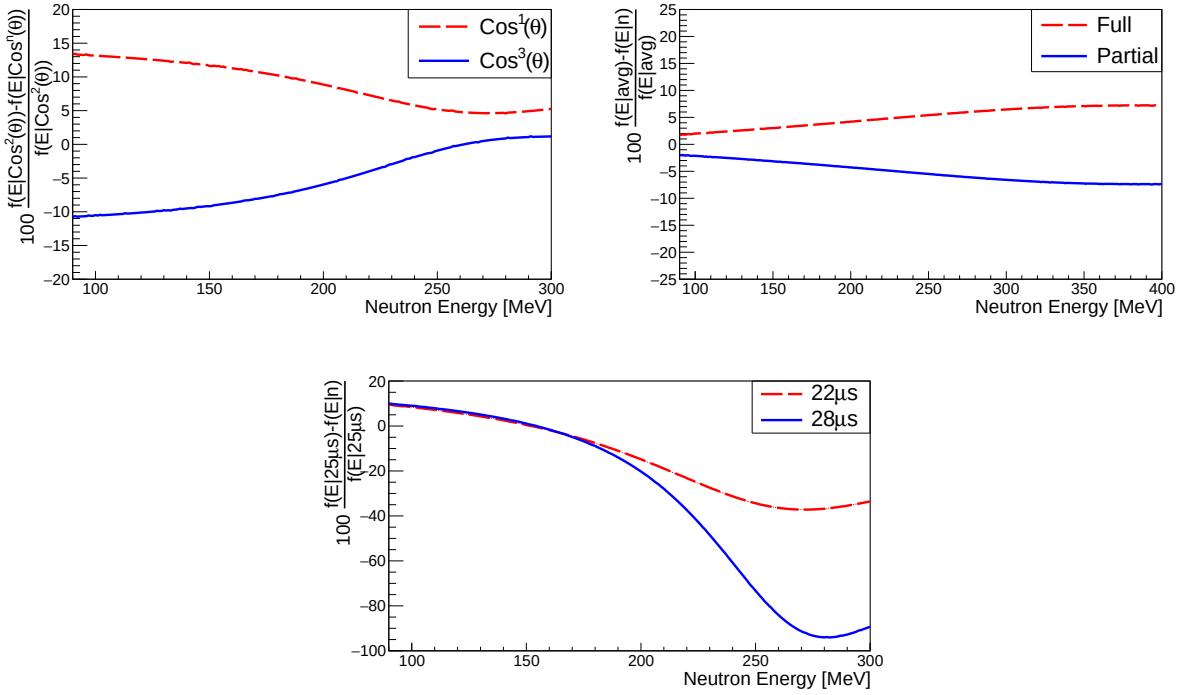

Figure 7.16: For the 1450 m.w.e. depth: (a) Depicts the percent difference in the reconstructed neutron flux versus energy, between the preferred ($\cos^2(\theta)$) and alternative choices of the neutron angular distribution. The partial geometry model was used for this comparison. (b) Depicts the reconstructed neutron energy-dependent flux for the partial and full geometry models given an incident angular distribution of $\cos^2(\theta)$. (c) Depicts the reconstructed neutron energy-dependent flux with variation in the initial gate triggering time given an incident angular distribution of $\cos^2(\theta)$.

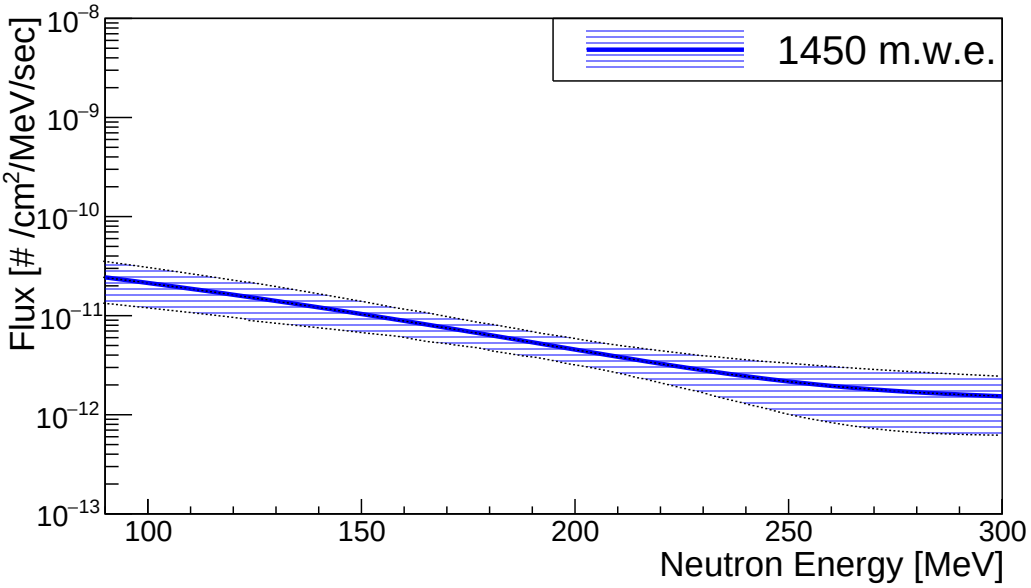

Figure 7.17: The reconstructed high-energy neutron energy-dependent flux with total uncertainty at 1450 m.w.e.

7.4 Summary and Comparison to Previous Work

The three high-energy neutron energy-dependent flux results were compared to the previous measurements by Garrison [13] and Malgin [14, 15]. The results quoted by Garrison were divided by a factor of 2, due to the incorrect effective area normalization by Garrison [13][2]. The arbitrary scaled energy-dependent flux from Malgin was integrated and scaled based upon the reported integrated flux of 2.3x10^{-4} #/m^2/sec. The scaled values were divided by the bin width from [15] to provide results in #/cm^2/sec/MeV. Malgin did not provide the assumed incident neutron angular distribution or uncertainty estimates. Both of these previous measurements performed measurements at a lower energy range than the MARS measurements.

Additionally, a comparison was made to the predicted Mei and Hime spectra [16] at the 1450 m.w.e. depth. No comparison was made at the two shallow depths; Mei and Hime claim their prediction should not be used at depths less than 1000 m.w.e. Mei and Hime predicted spectra are characterized by a function with several fitting coefficients (Eq. 14 from [16]). WIPP data fitting coefficients from Tab. VII of [16] were used. It appears that several of the coefficients (a_0 and a_3) are dependent upon the measurement depth; WIPP is the closest site in terms of depth, but not rock composition. The problematic energy-dependent scaling coefficient A_μ was calculated by matching the total integrated flux values from Tab. V of [16] with integrated Eq. 14 values from [16]. The lower limit integration values of 1, 10, and 100 MeV were used. The upper limit was fixed at 10 GeV. The integration range of 100 MeV to 10 GeV was used to predict the quoted scaling factor and the quoted energy-dependent flux. The integration ranges of 1 MeV to 10 GeV and 10 MeV to 10 GeV were used to construct uncertainty estimates for the Mei and Hime predicted flux. No uncertainty based upon the rock composition was considered.

The final below ground results compared to these measurements and simulation are displayed in Fig. 7.18. While no scaling has been performed to correct the neutron flux for varying rock composition, the MARS reconstructed data appears to be in rough agreement with the Malgin measurement. A 2σ error bar from the MARS measurement would overlap the highest energy measurement from Malgin. Full agreement at this energy might be possible if Malgin quoted the uncertainty in their measurement. No direct or nearly direct comparison can be made to the Garrison data given the MARS measurement locations. However, given the change in overburden and the resulting energy-dependent flux between the 377 m.w.e. and 540 m.w.e. measurements, the Garrison data seems elevated.

Surprisingly, the Mei and Hime prediction is very close to the MARS measured flux at 1450 m.w.e. over the energy range from 90 MeV to 300 MeV. While this is only one spectrum at one depth, the comparison provides credence that the Mei and Hime predictions may be moderately accurate at deep depths (>1000 m.w.e.). This of course assumes that the scaling parameter A_μ was appropriately calculated; Mei and Hime give no guidance in regards to

[2]See pg 116-117 of Garrison [13]. Garrison claims a correction of 4, but incorrectly assumes that the neutron flux has an upward component.

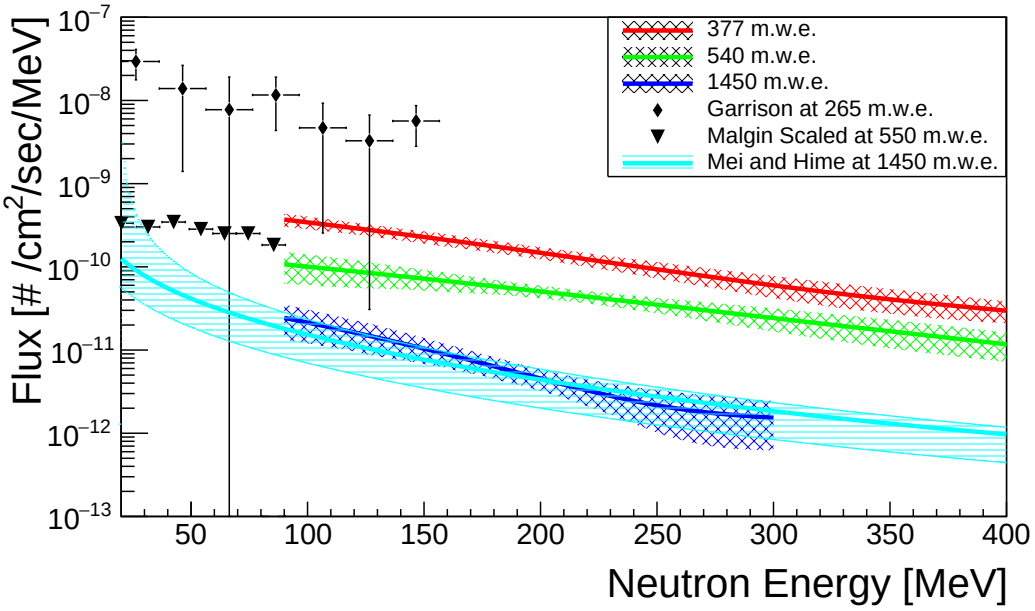

Figure 7.18: The reconstructed high-energy neutron energy-dependent flux at 377, 540, and 1450 m.w.e. at KURF compared to previous measurements [15, 14, 13] and simulation predictions [16].

this calculation.

More importantly, the collection of MARS measurements will allow future work to construct a shallow depth dependent model of the high-energy neutron energy-dependent flux. This model will allow for the prediction of high-energy neutron induced noise in rare-event detectors at depths between 377 m.w.e. and 1450 m.w.e. Future and current rare-event detectors operating in this range of overburden are likely to be antineutrino based nuclear reactor monitoring experiments.

7.5 MARS Results Implications

Given the reasonable agreement of the MARS results with previous measurements and simulations, it is instructive to examine the energy integrated neutron flux as a function of the muon flux (Fig. 7.19). Recall that below ground the neutron flux is created by the muon flux, primarily through muon spallation on rock. The neutron yield as a function of the mean muon energy is predicted to increase in a non-linear fashion with the mean muon energy [16]. As an experiment is placed deeper below ground, the muon flux decreases, but the mean muon energy increases. Therefore, it is expected that the integrated neutron flux should increase in a non-linear fashion with the incident muon flux. The energy integrated neutron flux between 90 MeV and 300 MeV and the muon flux for the 3 below ground measurements

are displayed versus the measurement depth in Fig. 7.19. The neutron flux is represented by the red squares and red y-axis; the muon flux is represented by the black triangles and black y-axis. Uncertainty in the integrated neutron flux is calculated using the 1-σ uncertainty distributions of Fig. 7.18. The muon flux is calculated using the measured muon flux, the experiment live-time at each location, and the MARS effective area to muons. The muon flux uncertainty is described in Appendix C.

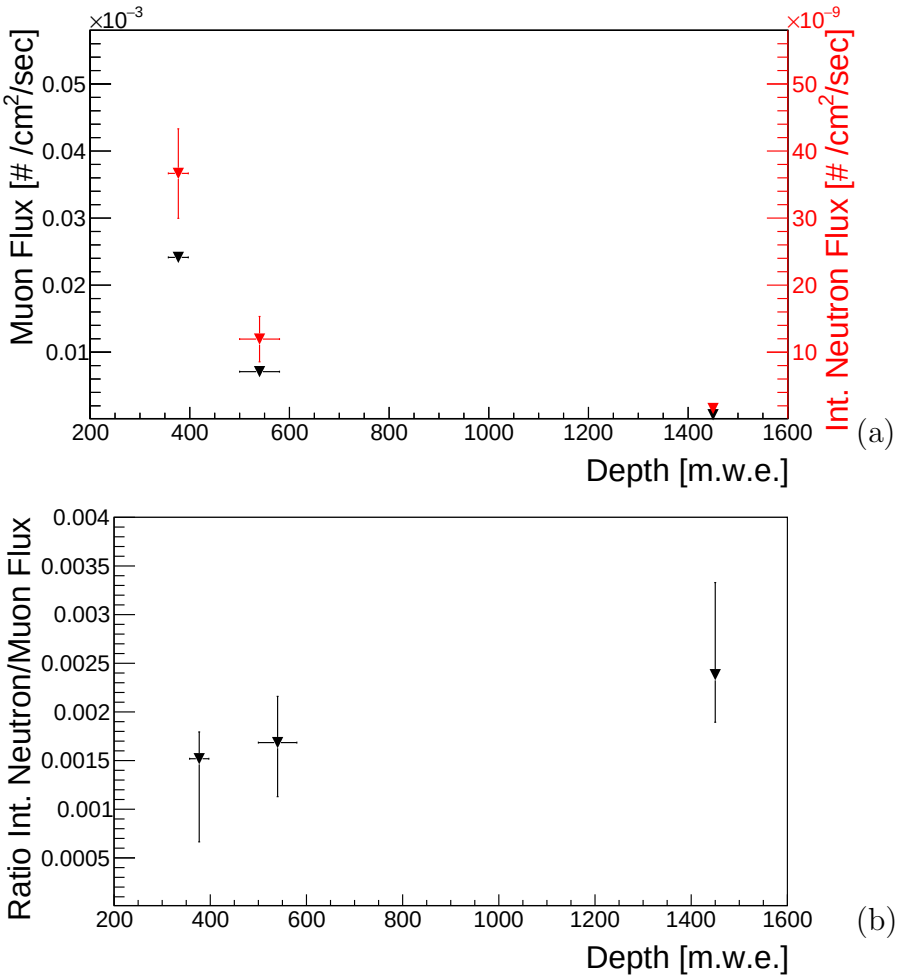

Figure 7.19: (a) The energy integrated neutron flux and the muon flux versus the depth for the three MARS measurements. The neutron flux is represented by the square markers and the right y-axis. The muon flux is represented by the triangle markers and the left y-axis. The neutron energy integration was performed over the energy range of 90 MeV to 300 MeV. (b) The ratio of the integrated neutron flux and the muon flux versus the measurement depth.

Examining Fig. 7.19, it appears that the relationship could be non-linear. However, significant uncertainty exists. If it could be shown that the relationship was conclusively non-linear, it would indicate that the creation mechanism is not consistent: the neutron

yield increases as a function of the mean muon energy; the MARS results exhibit the correct trend [16]. Whether, the trend has the correct form is difficult to ascertain with only three data points. Regardless of the weak conclusion surrounding Fig. 7.19, it should caution future experimenters to not linearly extrapolate the high-energy neutron flux from shallow depths to deeper depths.

Chapter 8

Summary

High-energy neutrons produce secondary particles through spallation, which create a ubiquitous and prominent background in a wide range of particle and nuclear physics experiments. Examples of high-energy neutron induced backgrounds include: the generation of secondary radiation which may impact gamma ray and neutron based measurements [12, 108, 109] and indirect backgrounds for many rare-event neutral particle experiments such as antineutrino based reactor monitors [19], WIMP dark matter detectors [20], and neutrinoless double beta decay detectors [21].

Above ground the high-energy neutron energy-dependent flux has been measured, but with significantly varying results. Below ground, many attempts have tried to measure the high-energy neutron energy-dependent flux. Only two previous measurements succeeded in measuring these neutrons and communicated their results in a fashion useful to others [13, 14, 15]. A model of the neutron energy-dependent flux was previously developed for measurements below 1000 m.w.e. No comparisons to this model and the measured neutron flux have previously been performed.

In an effort to provide new and independent measurements above and below ground, the Multiplicity And Recoil Spectrometer (MARS) was designed, constructed, and deployed to the Kimballton Underground Research Facility (KURF). MARS is a $\sim$1 m^3 transportable detector composed of plastic scintillator, Gd based neutron detectors, and a lead spallation target. Measurements were made at surface of Earth and at depths of 377 m.w.e., 540 m.w.e., and 1450 m.w.e.

To perform these four measurements, MARS used a new spallation based multiplicity concept to transform an incident high-energy neutron into many lower energy secondary neutrons. By measuring the multiplicity of correlated secondary neutrons, the energy deposited by these secondary neutrons when captured on a Gd nucleus, and any high-energy charged particles created during the spallation process, the MARS analysis is capable of inferring the incident neutron energy-dependent flux. To perform these reconstructions, a new Markov Chain Monte Carlo (MCMC) inversion algorithm [57] was developed for MARS which uses a calibrated Monte Carlo model of the MARS detector. In order to have an accurate Monte Carlo model of MARS, position-dependent energy calibrations were performed

in all radiation sensitive regions of the detector. Additionally, the secondary neutron capture efficiency, a key component of the detected flux, was calibrated by using a Cf-252 source.

Figure 8.1 presents the four MARS measurements with comparisons to previous measurements and simulation. Results are also presented for the four MARS measurements in tabular form in Appendix A. in At Earth's surface, the MARS measurement results agree with previous Bonner sphere measurements [41, 39] in the energy range between 90 MeV and 250 MeV. Above 250 MeV the MARS results are slightly lower than previous measurements. Below ground, no previous measurements exist which can be compared to the 377 m.w.e. measurement. However, at 540 m.w.e. the MARS result appears to be in reasonable agreement with the result from Malgin [15] at the one measured energy where the results overlap. The 1450 m.w.e. MARS measurement shows agreement with the predicted flux from Mei and Hime [16] [1].

The agreement of the MARS results with previous measurements and existing simulation, where applicable, provide confidence that all MARS measurements have produced the correct high-energy neutron energy-dependent flux. Beyond this agreement, the MARS results make new contributions to the measured high-energy neutron energy-dependent flux. These new contributions are at different depths, at a deeper depth than has previously been measured, have the same rock composition surrounding them, are at higher neutron energies, and have uniform detector related systematic bias due to the transportable nature of MARS. The characteristics of these new contributions will allow for the development of a depth-dependent high-energy neutron energy-dependent flux model. This model will impact the design of future rare-event physics experiments, enabling better background estimates and detector design optimization to mitigate high-energy neutron induced backgrounds. Additionally, this model will allow current experiments to better estimate the high-energy neutron induced background component of their measured signal.

[1] Mei and Hime predictions were not compared to the 377 m.w.e. and 540 m.w.e. measurement. The results from Mei and Hime are assumed to only be reliable at depths greater than 1000 m.w.e. [16]

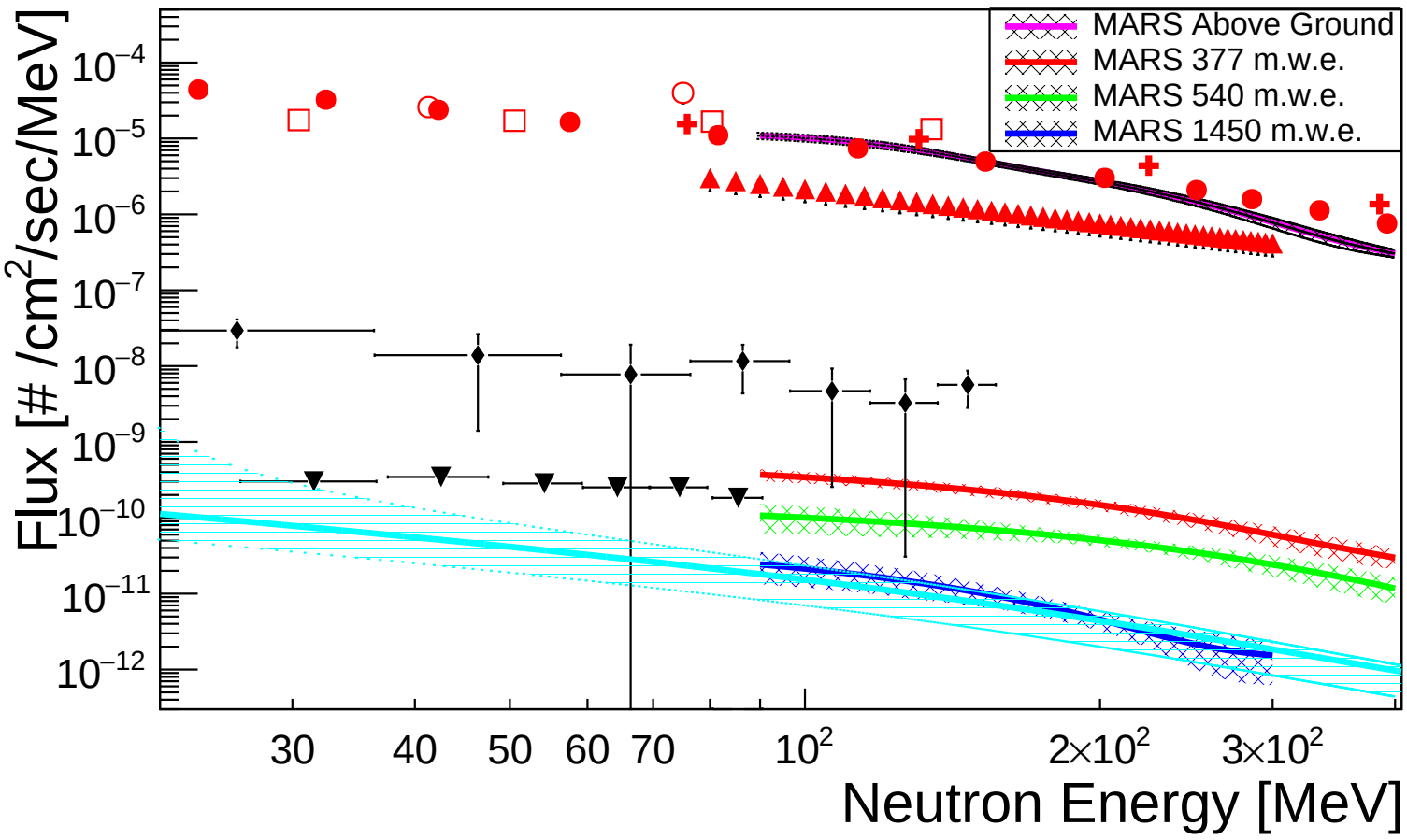

Figure 8.1: The MARS reconstructed high-energy neutron energy-dependent flux above ground and at depths of 377 m.w.e, 540 m.w.e, and 1450 m.w.e. at KURF. The previous experimental data above ground correspond to the following shapes: Ashton *et al.* ■[78], Gordon *et al.* +[39], Heidbreder *et al.* ▲[80], Hess *et al.* ●[10, 41], Preszler *et al.* ○[81], and R. Saxena □[83]. The previous experimental data below ground correspond to the following shapes: Garrison ◆[13] and Malgin ▼[15, 14]. The previous simulation predictions are by Mei and Hime [16] and correspond to the cyan curve and systematic uncertainty.

Chapter 9

Future Work

Regardless of the agreement of MARS results with previous measurements and simulation, several remaining questions and challenges still exist to improve confidence in the MARS results. These tasks are categorized below into two categories: the use of the MARS results to predict high-energy neutron backgrounds, and improvements to the MARS modeling and system response.

9.1 Continuation of Measurements

Currently, an effort has already begun to use the MARS results at 377 m.w.e. to predict the high-energy neutron induced background in the WATCHBOY experiment [110]. WATCHBOY is also part of the WATCHMAN [19] effort. It has measured a limit on muon-induced β-neutron emitters in water. The MARS measurement at 377 m.w.e. was within 10 m of the WATCHBOY detector. By incorporating this high-energy neutron induced background into the WATCHBOY analysis, their measured limit may be reduced.

Separately, an effort will soon begin to use the three MARS below ground measurements to create a depth-dependent model of the high-energy neutron flux below ground. This model will be used to predict high-energy neutron induced background in future antineutrino nuclear reactor monitoring experiments. This model and in particular the 1450 m.w.e. measurement could be used to revise or improve Mei and Hime predictions, further enhancing high-energy neutron flux predictions below ground relevant for current and future rare-event physics experiments.

9.2 Improvements in Modeling and System Response

The MARS results could be improved by more accurate modeling and system response predictions. The most troubling uncertainty in the MARS results is due to the reliance on Monte Carlo simulations, which have not been robustly validated, to predict the neutron lead spallation reaction. The understanding presented in this work is that those models are

based upon proton spallation in lead. How much these two different reactions disagree is not known. To perform a measurement of the neutron lead spallation would be challenging. This measurement would require a nearly mono-energetic high-energy neutron source and a thin target of lead. The surrounding environment response to the neutron beam would have to be minimal. Large solid angle coverage would be necessary to characterize the secondary neutron response.

In the absence of measured neutron lead spallation data, it may be possible to benchmark the MARS response to high-energy neutrons. Such a measurement could be performed at LANSCE [37]. However, due to the MARS capture time and multiplicity event time, the accelerator pulse-rate would have to be less than 5 kHz and the incident neutron flux could only initiate 1 spallation interaction in MARS per pulse. LANSCE personal indicated such a beam configuration existed for one measurement of the CAPTAIN experiment [111], but this beam configuration was not common. No indication was provided on how accurately the neutron energy could be measured, given the beam conditions.

In the absence of performing the above measurements, different Geant4 physics list could be used to characterize the current variation in high-energy neutron physics models. These models may use slightly different total cross-section predictions as well as different secondary neutron distributions. The variation between these models would be incorporated as a systematic uncertainty. This systematic uncertainty, in the absence of measurements, would attempt to incorporate the uncertainty due to neutron lead spallation. Additionally, more recent versions of Geant4 could be used. Version Geant4.9.6.p02 was used due to it being available at the start of the project. Separate Monte Carlo models using different Monte Carlo packages could be constructed [1]. All of these proposals would require significant computational time.

Given the above concerns, the uncertainty surrounding neutron lead spallation reactions may seem detrimental to the accuracy of the MARS measurements. However, the uncertainty surrounding neutron lead spallation data and the MARS response to high-energy neutrons probably does not significantly impact the MARS results. This conclusion is based on comparisons of the above ground MARS measurements to previous recoil based and Bonner sphere measurements. Recoil based measurements do not rely on the neutron lead spallation reaction; their results are independent of the neutron lead reaction uncertainty. Separate Bonner sphere measurements have been independently calibrated at the LANSCE [112]. These Bonner spheres calibrations found reasonable agreement between the measured and and unfolded high-energy neutron flux from LANSCE. Additionally, LANSCE Bonner sphere measurements [112] used the same Monte Carlo model and unfolding code as the Bonner sphere experiments used to measure the above ground high-energy neutron cosmogenic flux [39, 11].

In addition to the neutron lead reaction uncertainty, the MARS energy calibration and light propagation yield poor results outside of the calibrated energy regime. These results could be improved by using a full light propagation model, using more and varied gamma-

[1] For example MCNP or FLUKA.

ray sources for the energy calibration, and using the muon energy distribution to improve the position-dependent energy calibration. However, these calibrations are time consuming given their position-dependent nature and they may produce marginal improvement of the MARS results. Additionally, the Gd de-excitation could be incorporated into the energy calibration. This would require that the evaporation model be replaced with the DANCE DICEBOX model [70].

More accurate muon propagation models could be used in place of the Reyna muon generator and propagation model [113]. Additionally, an overburden map for the 1450 m.w.e. depth could be produced and used to predict the associated muon flux and muon induced noise more accurately.

Finally, if all of the above were performed, it may be possible to optimize the binning of the MARS measured 3-component space [2]. Such an optimized binning may make it possible to improve the MCMC reconstruction algorithm energy resolution. This may provide valuable insight as to why the above ground measurement does not match with previous measurements above 250 MeV.

[2]Multiplicity, Capture Energy, and Thermalization Energy.

Appendix A

MARS Results Data

The following tables contain the MARS results from all four measurements. All energy-dependent neutron flux values and uncertainties are quoted in units of [# /cm^2/sec/MeV].

Table A.1: The high-energy neutron energy-dependent flux results from the four MARS measurements at KURF. All results are quoted in units of [#/cm^2/sec/MeV].

Energy [MeV]	Above Ground	377 m.w.e.	540 m.w.e.	1450 m.w.e.
90	1.08423e-05	3.69721e-10	1.07148e-10	2.43534e-11
91	1.0782e-05	3.67055e-10	1.06538e-10	2.40443e-11
92	1.07188e-05	3.64128e-10	1.05794e-10	2.3737e-11
93	1.06529e-05	3.61356e-10	1.05185e-10	2.34339e-11
94	1.05843e-05	3.58604e-10	1.04511e-10	2.31327e-11
95	1.05132e-05	3.55868e-10	1.03784e-10	2.28349e-11
96	1.04397e-05	3.5327e-10	1.03117e-10	2.25395e-11
97	1.03637e-05	3.50564e-10	1.02523e-10	2.22464e-11
98	1.02854e-05	3.47743e-10	1.01866e-10	2.19562e-11
99	1.02049e-05	3.45075e-10	1.01146e-10	2.1671e-11
100	1.01222e-05	3.42412e-10	1.00499e-10	2.13858e-11
101	1.00388e-05	3.39883e-10	9.98527e-11	2.1104e-11
102	9.95096e-06	3.37137e-10	9.92087e-11	2.0826e-11
103	9.86244e-06	3.34523e-10	9.85718e-11	2.05683e-11
104	9.77213e-06	3.31931e-10	9.79312e-11	2.02769e-11
105	9.68011e-06	3.2935e-10	9.72991e-11	2.00057e-11
106	9.58649e-06	3.26779e-10	9.67246e-11	1.97381e-11
107	9.49133e-06	3.24241e-10	9.60384e-11	1.94905e-11
108	9.39472e-06	3.21696e-10	9.54718e-11	1.92097e-11
109	9.29671e-06	3.1918e-10	9.47969e-11	1.895e-11

110	9.19866e-06	3.16776e-10	9.41779e-11	1.86926e-11
111	9.09819e-06	3.14185e-10	9.36211e-11	1.84378e-11
112	8.99555e-06	3.11808e-10	9.2955e-11	1.82019e-11
113	8.89298e-06	3.09251e-10	9.23474e-11	1.79359e-11
114	8.78954e-06	3.06812e-10	9.17433e-11	1.77041e-11
115	8.68525e-06	3.04475e-10	9.11418e-11	1.74449e-11
116	8.58017e-06	3.01965e-10	9.05419e-11	1.72178e-11
117	8.47443e-06	2.99568e-10	8.99459e-11	1.6963e-11
118	8.36812e-06	2.97274e-10	8.93561e-11	1.67406e-11
119	8.26123e-06	2.94903e-10	8.87658e-11	1.64919e-11
120	8.15407e-06	2.92459e-10	8.8182e-11	1.62597e-11
121	8.04652e-06	2.90123e-10	8.75982e-11	1.60301e-11
122	7.93872e-06	2.87883e-10	8.70173e-11	1.58037e-11
123	7.83076e-06	2.85569e-10	8.64431e-11	1.55781e-11
124	7.72273e-06	2.83191e-10	8.58703e-11	1.53561e-11
125	7.61474e-06	2.80904e-10	8.53e-11	1.51366e-11
126	7.50761e-06	2.78638e-10	8.47308e-11	1.49196e-11
127	7.39919e-06	2.76389e-10	8.41677e-11	1.47047e-11
128	7.2925e-06	2.74148e-10	8.36084e-11	1.44916e-11
129	7.18475e-06	2.71924e-10	8.30494e-11	1.4282e-11
130	7.07814e-06	2.69713e-10	8.24937e-11	1.40741e-11
131	6.97274e-06	2.67518e-10	8.19432e-11	1.38689e-11
132	6.86729e-06	2.65412e-10	8.13939e-11	1.36654e-11
133	6.76255e-06	2.63169e-10	8.08475e-11	1.34756e-11
134	6.65798e-06	2.61018e-10	8.03443e-11	1.3266e-11
135	6.55498e-06	2.58878e-10	7.97651e-11	1.30696e-11
136	6.45285e-06	2.56823e-10	7.92289e-11	1.28755e-11
137	6.35184e-06	2.5464e-10	7.86919e-11	1.26837e-11
138	6.25196e-06	2.52542e-10	7.81628e-11	1.24947e-11
139	6.15388e-06	2.50461e-10	7.76353e-11	1.23072e-11
140	6.05653e-06	2.4839e-10	7.71453e-11	1.21218e-11
141	5.96002e-06	2.46335e-10	7.65864e-11	1.1939e-11
142	5.86552e-06	2.44291e-10	7.60674e-11	1.17672e-11
143	5.77264e-06	2.42324e-10	7.55494e-11	1.15882e-11
144	5.68143e-06	2.40248e-10	7.50699e-11	1.14035e-11
145	5.59246e-06	2.38243e-10	7.45275e-11	1.12291e-11
146	5.50425e-06	2.3632e-10	7.40203e-11	1.10654e-11
147	5.41836e-06	2.34281e-10	7.35118e-11	1.08872e-11
148	5.33427e-06	2.32321e-10	7.30118e-11	1.07193e-11
149	5.25187e-06	2.30372e-10	7.25117e-11	1.05536e-11
150	5.17125e-06	2.28439e-10	7.20163e-11	1.03973e-11
151	5.0923e-06	2.26576e-10	7.1555e-11	1.02352e-11

152	5.01499e-06	2.24607e-10	7.10325e-11	1.00683e-11
153	4.93932e-06	2.22711e-10	7.05747e-11	9.91065e-12
154	4.86526e-06	2.20827e-10	7.00577e-11	9.75516e-12
155	4.79278e-06	2.18957e-10	6.95759e-11	9.60154e-12
156	4.72184e-06	2.17103e-10	6.91254e-11	9.45e-12
157	4.65242e-06	2.15257e-10	6.86208e-11	9.30702e-12
158	4.58448e-06	2.13432e-10	6.81447e-11	9.15303e-12
159	4.51801e-06	2.11612e-10	6.76735e-11	9.01369e-12
160	4.45346e-06	2.09806e-10	6.72047e-11	8.86353e-12
161	4.38934e-06	2.08014e-10	6.67398e-11	8.7217e-12
162	4.32708e-06	2.06232e-10	6.62772e-11	8.58192e-12
163	4.26616e-06	2.04466e-10	6.58165e-11	8.44404e-12
164	4.20658e-06	2.02712e-10	6.53574e-11	8.308e-12
165	4.14828e-06	2.00971e-10	6.49035e-11	8.17376e-12
166	4.09126e-06	1.99239e-10	6.44504e-11	8.04137e-12
167	4.03545e-06	1.97521e-10	6.40015e-11	7.91061e-12
168	3.98088e-06	1.95815e-10	6.35544e-11	7.78204e-12
169	3.92745e-06	1.94177e-10	6.311e-11	7.65522e-12
170	3.87522e-06	1.92444e-10	6.26683e-11	7.53017e-12
171	3.82406e-06	1.90779e-10	6.22293e-11	7.40695e-12
172	3.77447e-06	1.89169e-10	6.1793e-11	7.28572e-12
173	3.72506e-06	1.87525e-10	6.13592e-11	7.16581e-12
174	3.67712e-06	1.85843e-10	6.09279e-11	7.04788e-12
175	3.63019e-06	1.84226e-10	6.04986e-11	6.93151e-12
176	3.58423e-06	1.82619e-10	6.00732e-11	6.81706e-12
177	3.53925e-06	1.81021e-10	5.96492e-11	6.70821e-12
178	3.49517e-06	1.79438e-10	5.92285e-11	6.59702e-12
179	3.45199e-06	1.77867e-10	5.88105e-11	6.48371e-12
180	3.40968e-06	1.76304e-10	5.83942e-11	6.37613e-12
181	3.36821e-06	1.74757e-10	5.79818e-11	6.26991e-12
182	3.32755e-06	1.73264e-10	5.75708e-11	6.16536e-12
183	3.28769e-06	1.71694e-10	5.71621e-11	6.06278e-12
184	3.24856e-06	1.70181e-10	5.67574e-11	5.96154e-12
185	3.21019e-06	1.68677e-10	5.63536e-11	5.86191e-12
186	3.1725e-06	1.67186e-10	5.59529e-11	5.76737e-12
187	3.13548e-06	1.65749e-10	5.5555e-11	5.67088e-12
188	3.09908e-06	1.64238e-10	5.51761e-11	5.57253e-12
189	3.06333e-06	1.62783e-10	5.47665e-11	5.47935e-12
190	3.02815e-06	1.61336e-10	5.43915e-11	5.38736e-12
191	2.99353e-06	1.59902e-10	5.39863e-11	5.2971e-12
192	2.95982e-06	1.58519e-10	5.36012e-11	5.20824e-12
193	2.92584e-06	1.57068e-10	5.32172e-11	5.12094e-12

194	2.89311e-06	1.55708e-10	5.28372e-11	5.03524e-12
195	2.86006e-06	1.54315e-10	5.24732e-11	4.9508e-12
196	2.82779e-06	1.52898e-10	5.20821e-11	4.86798e-12
197	2.79593e-06	1.51569e-10	5.17083e-11	4.78643e-12
198	2.76442e-06	1.50174e-10	5.13363e-11	4.70639e-12
199	2.73323e-06	1.48825e-10	5.0981e-11	4.62774e-12
200	2.70236e-06	1.47491e-10	5.06007e-11	4.5505e-12
201	2.67176e-06	1.46165e-10	5.02365e-11	4.47464e-12
202	2.64145e-06	1.44892e-10	4.98874e-11	4.40011e-12
203	2.61139e-06	1.43548e-10	4.95148e-11	4.32701e-12
204	2.58162e-06	1.42298e-10	4.91572e-11	4.25527e-12
205	2.55212e-06	1.40975e-10	4.88024e-11	4.18741e-12
206	2.52287e-06	1.39704e-10	4.84492e-11	4.1181e-12
207	2.49389e-06	1.38481e-10	4.80985e-11	4.04765e-12
208	2.46518e-06	1.3723e-10	4.7751e-11	3.9811e-12
209	2.43675e-06	1.3595e-10	4.74053e-11	3.91577e-12
210	2.40888e-06	1.34721e-10	4.70617e-11	3.85175e-12
211	2.38064e-06	1.33501e-10	4.67205e-11	3.78892e-12
212	2.35299e-06	1.3233e-10	4.63815e-11	3.7298e-12
213	2.32558e-06	1.3109e-10	4.60453e-11	3.66943e-12
214	2.29845e-06	1.29901e-10	4.57096e-11	3.61017e-12
215	2.27156e-06	1.28722e-10	4.53778e-11	3.55227e-12
216	2.24522e-06	1.27552e-10	4.50471e-11	3.49309e-12
217	2.21886e-06	1.26432e-10	4.47313e-11	3.43751e-12
218	2.19273e-06	1.25244e-10	4.43934e-11	3.38525e-12
219	2.16657e-06	1.24103e-10	4.40703e-11	3.3297e-12
220	2.14096e-06	1.22972e-10	4.37485e-11	3.27744e-12
221	2.11557e-06	1.21852e-10	4.343e-11	3.22859e-12
222	2.09046e-06	1.20742e-10	4.31125e-11	3.17637e-12
223	2.06584e-06	1.1964e-10	4.2797e-11	3.12745e-12
224	2.04094e-06	1.18548e-10	4.24848e-11	3.07959e-12
225	2.01655e-06	1.17506e-10	4.21737e-11	3.03494e-12
226	1.99268e-06	1.16392e-10	4.18655e-11	2.9871e-12
227	1.9685e-06	1.15331e-10	4.15587e-11	2.94441e-12
228	1.94484e-06	1.14276e-10	4.12544e-11	2.89865e-12
229	1.92141e-06	1.13231e-10	4.09518e-11	2.85599e-12
230	1.89822e-06	1.12198e-10	4.06509e-11	2.81429e-12
231	1.87525e-06	1.11172e-10	4.03532e-11	2.77351e-12
232	1.8528e-06	1.10156e-10	4.00575e-11	2.73371e-12
233	1.83005e-06	1.09148e-10	3.97632e-11	2.69485e-12
234	1.80779e-06	1.08148e-10	3.94702e-11	2.65892e-12
235	1.78602e-06	1.07198e-10	3.91802e-11	2.61993e-12

236	1.76397e-06	1.06179e-10	3.89049e-11	2.58388e-12
237	1.74241e-06	1.05207e-10	3.86064e-11	2.54876e-12
238	1.72106e-06	1.04244e-10	3.83225e-11	2.51441e-12
239	1.69994e-06	1.03289e-10	3.80403e-11	2.48089e-12
240	1.67905e-06	1.02384e-10	3.77606e-11	2.44837e-12
241	1.65862e-06	1.01408e-10	3.7482e-11	2.41654e-12
242	1.63792e-06	1.00479e-10	3.7206e-11	2.38565e-12
243	1.6177e-06	9.95619e-11	3.69307e-11	2.35551e-12
244	1.59768e-06	9.8651e-11	3.66595e-11	2.3262e-12
245	1.57788e-06	9.77489e-11	3.63885e-11	2.29757e-12
246	1.55831e-06	9.68568e-11	3.61203e-11	2.26985e-12
247	1.53917e-06	9.60105e-11	3.58542e-11	2.24458e-12
248	1.5198e-06	9.50941e-11	3.55886e-11	2.21828e-12
249	1.50085e-06	9.42259e-11	3.53257e-11	2.19093e-12
250	1.48212e-06	9.33653e-11	3.50649e-11	2.16616e-12
251	1.46361e-06	9.25117e-11	3.48059e-11	2.142e-12
252	1.44552e-06	9.16716e-11	3.45486e-11	2.12029e-12
253	1.42719e-06	9.08338e-11	3.42935e-11	2.09572e-12
254	1.40953e-06	9.00085e-11	3.40396e-11	2.07534e-12
255	1.39183e-06	8.91869e-11	3.38001e-11	2.05217e-12
256	1.37411e-06	8.83764e-11	3.35386e-11	2.03134e-12
257	1.35704e-06	8.75742e-11	3.32902e-11	2.01108e-12
258	1.33972e-06	8.67759e-11	3.30444e-11	1.99317e-12
259	1.32306e-06	8.60279e-11	3.27995e-11	1.97411e-12
260	1.30614e-06	8.52457e-11	3.25698e-11	1.95403e-12
261	1.28964e-06	8.44381e-11	3.23165e-11	1.93782e-12
262	1.27334e-06	8.36734e-11	3.20773e-11	1.92051e-12
263	1.25722e-06	8.29157e-11	3.18398e-11	1.90207e-12
264	1.24131e-06	8.21688e-11	3.16034e-11	1.8874e-12
265	1.22559e-06	8.1427e-11	3.13703e-11	1.87002e-12
266	1.21005e-06	8.06911e-11	3.11378e-11	1.85481e-12
267	1.19469e-06	7.99648e-11	3.09071e-11	1.83996e-12
268	1.17954e-06	7.92823e-11	3.06898e-11	1.82737e-12
269	1.16456e-06	7.8534e-11	3.04511e-11	1.81187e-12
270	1.14976e-06	7.7828e-11	3.02259e-11	1.79848e-12
271	1.13516e-06	7.7132e-11	3.00023e-11	1.78545e-12
272	1.12073e-06	7.64406e-11	2.978e-11	1.7729e-12
273	1.10648e-06	7.57941e-11	2.95719e-11	1.76066e-12
274	1.09242e-06	7.50821e-11	2.93408e-11	1.74895e-12
275	1.07853e-06	7.44132e-11	2.91243e-11	1.73755e-12
276	1.06502e-06	7.37508e-11	2.89091e-11	1.72651e-12
277	1.05127e-06	7.30962e-11	2.86949e-11	1.71577e-12

278	1.03811e-06	7.24463e-11	2.84825e-11	1.70545e-12
279	1.02473e-06	7.18061e-11	2.82724e-11	1.69535e-12
280	1.01171e-06	7.11716e-11	2.80626e-11	1.68728e-12
281	9.98857e-07	7.05439e-11	2.78552e-11	1.6762e-12
282	9.86176e-07	6.99238e-11	2.76493e-11	1.667e-12
283	9.73653e-07	6.93081e-11	2.74448e-11	1.65816e-12
284	9.61508e-07	6.87385e-11	2.72424e-11	1.64944e-12
285	9.49125e-07	6.81365e-11	2.7041e-11	1.64107e-12
286	9.37103e-07	6.75034e-11	2.68412e-11	1.63286e-12
287	9.25253e-07	6.69176e-11	2.66425e-11	1.6249e-12
288	9.13558e-07	6.6371e-11	2.64587e-11	1.61872e-12
289	9.02023e-07	6.57597e-11	2.62514e-11	1.61108e-12
290	8.90824e-07	6.51867e-11	2.60575e-11	1.60212e-12
291	8.79604e-07	6.46628e-11	2.58648e-11	1.59482e-12
292	8.68533e-07	6.407e-11	2.56749e-11	1.58771e-12
293	8.57443e-07	6.35194e-11	2.5485e-11	1.58072e-12
294	8.46674e-07	6.29753e-11	2.52975e-11	1.57381e-12
295	8.36074e-07	6.24343e-11	2.51112e-11	1.56701e-12
296	8.25614e-07	6.19017e-11	2.49261e-11	1.56035e-12
297	8.153e-07	6.13747e-11	2.47426e-11	1.55374e-12
298	8.05143e-07	6.08905e-11	2.45602e-11	1.54719e-12
299	7.95119e-07	6.03401e-11	2.43797e-11	1.54066e-12
300	7.8526e-07	5.98684e-11	2.42007e-11	1.53416e-12
301	7.75533e-07	5.93638e-11	2.40227e-11	-
302	7.6595e-07	5.8831e-11	2.38465e-11	-
303	7.5651e-07	5.83396e-11	2.36706e-11	-
304	7.47208e-07	5.78538e-11	2.34968e-11	-
305	7.38036e-07	5.74074e-11	2.33248e-11	-
306	7.29012e-07	5.68943e-11	2.31536e-11	-
307	7.20119e-07	5.64255e-11	2.2984e-11	-
308	7.11517e-07	5.5998e-11	2.2815e-11	-
309	7.02895e-07	5.55018e-11	2.26486e-11	-
310	6.94254e-07	5.50485e-11	2.24823e-11	-
311	6.86044e-07	5.45994e-11	2.23185e-11	-
312	6.77656e-07	5.41561e-11	2.21547e-11	-
313	6.69708e-07	5.3755e-11	2.19931e-11	-
314	6.61579e-07	5.32857e-11	2.18322e-11	-
315	6.53719e-07	5.28921e-11	2.16725e-11	-
316	6.46001e-07	5.24702e-11	2.15145e-11	-
317	6.38396e-07	5.20515e-11	2.13576e-11	-
318	6.30903e-07	5.16033e-11	2.12015e-11	-
319	6.23545e-07	5.11948e-11	2.10475e-11	-

320	6.16299e-07	5.0792e-11	2.0894e-11	-
321	6.09176e-07	5.03922e-11	2.07414e-11	-
322	6.02166e-07	4.99982e-11	2.06029e-11	-
323	5.9527e-07	4.96087e-11	2.04408e-11	-
324	5.88484e-07	4.92235e-11	2.02928e-11	-
325	5.81815e-07	4.88448e-11	2.01451e-11	-
326	5.7526e-07	4.84692e-11	1.99989e-11	-
327	5.688e-07	4.8096e-11	1.98537e-11	-
328	5.62601e-07	4.77651e-11	1.97218e-11	-
329	5.56368e-07	4.73669e-11	1.95666e-11	-
330	5.50099e-07	4.70432e-11	1.94252e-11	-
331	5.44075e-07	4.66558e-11	1.92843e-11	-
332	5.38288e-07	4.63062e-11	1.91449e-11	-
333	5.32331e-07	4.59623e-11	1.90064e-11	-
334	5.26614e-07	4.5619e-11	1.88692e-11	-
335	5.20998e-07	4.52819e-11	1.87321e-11	-
336	5.15606e-07	4.49492e-11	1.85974e-11	-
337	5.1005e-07	4.46196e-11	1.84636e-11	-
338	5.0472e-07	4.42937e-11	1.83416e-11	-
339	4.99487e-07	4.4006e-11	1.81976e-11	-
340	4.94338e-07	4.3655e-11	1.80666e-11	-
341	4.8929e-07	4.33727e-11	1.79363e-11	-
342	4.8432e-07	4.30305e-11	1.78074e-11	-
343	4.79452e-07	4.2724e-11	1.76794e-11	-
344	4.74661e-07	4.24223e-11	1.7552e-11	-
345	4.69968e-07	4.21206e-11	1.7426e-11	-
346	4.6546e-07	4.18258e-11	1.73007e-11	-
347	4.60921e-07	4.15328e-11	1.71761e-11	-
348	4.56358e-07	4.12452e-11	1.70531e-11	-
349	4.51987e-07	4.0958e-11	1.69306e-11	-
350	4.47703e-07	4.06782e-11	1.6809e-11	-
351	4.43489e-07	4.04267e-11	1.66993e-11	-
352	4.39352e-07	4.01223e-11	1.65685e-11	-
353	4.35295e-07	3.98495e-11	1.645e-11	-
354	4.3131e-07	3.95786e-11	1.63322e-11	-
355	4.27393e-07	3.93131e-11	1.62148e-11	-
356	4.23554e-07	3.90791e-11	1.60988e-11	-
357	4.19784e-07	3.87894e-11	1.59833e-11	-
358	4.16182e-07	3.85322e-11	1.5869e-11	-
359	4.12454e-07	3.8277e-11	1.57557e-11	-
360	4.08882e-07	3.80254e-11	1.56528e-11	-
361	4.05375e-07	3.77762e-11	1.55304e-11	-

362	4.01938e-07	3.75292e-11	1.54296e-11	-
363	3.98561e-07	3.72864e-11	1.53091e-11	-
364	3.95245e-07	3.70453e-11	1.51991e-11	-
365	3.92083e-07	3.68066e-11	1.50907e-11	-
366	3.88881e-07	3.65715e-11	1.49824e-11	-
367	3.85652e-07	3.63384e-11	1.48749e-11	-
368	3.82566e-07	3.61068e-11	1.47686e-11	-
369	3.79539e-07	3.58784e-11	1.46629e-11	-
370	3.7656e-07	3.56522e-11	1.45578e-11	-
371	3.73634e-07	3.54268e-11	1.44537e-11	-
372	3.7076e-07	3.52052e-11	1.43501e-11	-
373	3.67932e-07	3.49858e-11	1.42562e-11	-
374	3.65159e-07	3.47681e-11	1.41444e-11	-
375	3.62426e-07	3.45528e-11	1.40432e-11	-
376	3.59816e-07	3.43398e-11	1.3942e-11	-
377	3.57174e-07	3.41278e-11	1.38418e-11	-
378	3.54504e-07	3.39198e-11	1.37425e-11	-
379	3.51942e-07	3.37122e-11	1.36436e-11	-
380	3.49426e-07	3.35057e-11	1.35538e-11	-
381	3.46946e-07	3.33014e-11	1.34474e-11	-
382	3.44506e-07	3.31236e-11	1.33504e-11	-
383	3.42104e-07	3.28993e-11	1.32542e-11	-
384	3.39734e-07	3.27006e-11	1.31584e-11	-
385	3.37397e-07	3.25027e-11	1.30718e-11	-
386	3.35159e-07	3.23075e-11	1.29683e-11	-
387	3.3282e-07	3.21124e-11	1.28741e-11	-
388	3.30642e-07	3.19197e-11	1.27808e-11	-
389	3.2836e-07	3.1728e-11	1.26876e-11	-
390	3.26175e-07	3.156e-11	1.2595e-11	-
391	3.24012e-07	3.13485e-11	1.25033e-11	-
392	3.21874e-07	3.11616e-11	1.2412e-11	-
393	3.19758e-07	3.09974e-11	1.23294e-11	-
394	3.17665e-07	3.07893e-11	1.22387e-11	-
395	3.15596e-07	3.06064e-11	1.21408e-11	-
396	3.13539e-07	3.04428e-11	1.20513e-11	-
397	3.11504e-07	3.02401e-11	1.19624e-11	-
398	3.09538e-07	3.00594e-11	1.1882e-11	-
399	3.07531e-07	2.98792e-11	1.17862e-11	-
400	3.0554e-07	2.96986e-11	1.16986e-11	-

Table A.2: The high-energy neutron energy-dependent flux positive uncertainty σ_+ results from the four MARS measurements at KURF. All results are quoted in units of [#/cm^2/sec/MeV].

Energy [MeV]	σ_+ Above Ground	σ_+ 377 m.w.e.	σ_+ 540 m.w.e.	σ_+ 1450 m.w.e.
90	9.80047e-06	3.03647e-10	6.21525e-11	1.33525e-11
91	9.73762e-06	3.0154e-10	6.21594e-11	1.31885e-11
92	9.67264e-06	2.99093e-10	6.19005e-11	1.3096e-11
93	9.6053e-06	2.97099e-10	6.18785e-11	1.29479e-11
94	9.53637e-06	2.94883e-10	6.17354e-11	1.28008e-11
95	9.46554e-06	2.9264e-10	6.13808e-11	1.26741e-11
96	9.39291e-06	2.90594e-10	6.13174e-11	1.25095e-11
97	9.31898e-06	2.88328e-10	6.11889e-11	1.24008e-11
98	9.24327e-06	2.86314e-10	6.11031e-11	1.22465e-11
99	9.16583e-06	2.84158e-10	6.08611e-11	1.2134e-11
100	9.08698e-06	2.82016e-10	6.07753e-11	1.20212e-11
101	9.00658e-06	2.80187e-10	6.05694e-11	1.18608e-11
102	8.92558e-06	2.7817e-10	6.04731e-11	1.17583e-11
103	8.84277e-06	2.76257e-10	6.01592e-11	1.16261e-11
104	8.75906e-06	2.74419e-10	5.864e-11	1.151e-11
105	8.67415e-06	2.72596e-10	5.8451e-11	1.13679e-11
106	8.58847e-06	2.70778e-10	5.8289e-11	1.12584e-11
107	8.50178e-06	2.68957e-10	5.80686e-11	1.11322e-11
108	8.41406e-06	2.67001e-10	5.80152e-11	1.10208e-11
109	8.32546e-06	2.64996e-10	5.7794e-11	1.08857e-11
110	8.23621e-06	2.63046e-10	5.75837e-11	1.07847e-11
111	8.14643e-06	2.61175e-10	5.74428e-11	1.06527e-11
112	8.05645e-06	2.59296e-10	5.73236e-11	1.05336e-11
113	7.96533e-06	2.57332e-10	5.71303e-11	1.04249e-11
114	7.8741e-06	2.55396e-10	5.69394e-11	1.03049e-11
115	7.78233e-06	2.53692e-10	5.67476e-11	1.02025e-11
116	7.69018e-06	2.51704e-10	5.65535e-11	1.00853e-11
117	7.59764e-06	2.49784e-10	5.64535e-11	9.95602e-12
118	7.5052e-06	2.48133e-10	5.62341e-11	9.8707e-12
119	7.41206e-06	2.46213e-10	5.60675e-11	9.74487e-12
120	7.31926e-06	2.44383e-10	5.58767e-11	9.62704e-12
121	7.22633e-06	2.42484e-10	5.5681e-11	9.51118e-12
122	7.13333e-06	2.40843e-10	5.55749e-11	9.39687e-12
123	7.04034e-06	2.3894e-10	5.53644e-11	9.2576e-12
124	6.94748e-06	2.36885e-10	5.51876e-11	8.94044e-12
125	6.85476e-06	2.34861e-10	5.50538e-11	8.86031e-12

126	6.76309e-06	2.32922e-10	5.49642e-11	8.75605e-12
127	6.67034e-06	2.30943e-10	5.4851e-11	8.67787e-12
128	6.5791e-06	2.28978e-10	5.48161e-11	8.57562e-12
129	6.48695e-06	2.27031e-10	5.46766e-11	8.49909e-12
130	6.39598e-06	2.25254e-10	5.46499e-11	8.4001e-12
131	6.30639e-06	2.23362e-10	5.45251e-11	8.32606e-12
132	6.21562e-06	2.21671e-10	5.44553e-11	8.22993e-12
133	6.12672e-06	2.19721e-10	5.43412e-11	8.14555e-12
134	6.03853e-06	2.17861e-10	5.43186e-11	8.06381e-12
135	5.95082e-06	2.16161e-10	5.42174e-11	7.97146e-12
136	5.86296e-06	2.14559e-10	5.41495e-11	7.90126e-12
137	5.77751e-06	2.12661e-10	5.40054e-11	7.81134e-12
138	5.6922e-06	2.11001e-10	5.39307e-11	7.72264e-12
139	5.60784e-06	2.09353e-10	5.37834e-11	7.65474e-12
140	5.52529e-06	2.0772e-10	5.36884e-11	7.56811e-12
141	5.44262e-06	2.05899e-10	5.34823e-11	7.47914e-12
142	5.3615e-06	2.04003e-10	5.33295e-11	7.40239e-12
143	5.28159e-06	2.02151e-10	5.31098e-11	7.34144e-12
144	5.20308e-06	2.00386e-10	5.29712e-11	7.25147e-12
145	5.12573e-06	1.98531e-10	5.27382e-11	7.16983e-12
146	5.04997e-06	1.9672e-10	5.25013e-11	7.09423e-12
147	4.97537e-06	1.94869e-10	5.22984e-11	7.00832e-12
148	4.90203e-06	1.93179e-10	5.2142e-11	6.93419e-12
149	4.8301e-06	1.91383e-10	5.19216e-11	6.85764e-12
150	4.75939e-06	1.89602e-10	5.17051e-11	6.77275e-12
151	4.69011e-06	1.87853e-10	5.15917e-11	6.69855e-12
152	4.6221e-06	1.86075e-10	5.13238e-11	6.61914e-12
153	4.55531e-06	1.84334e-10	5.11194e-11	6.56145e-12
154	4.4898e-06	1.82607e-10	5.09384e-11	6.48698e-12
155	4.42558e-06	1.80902e-10	5.07191e-11	6.43252e-12
156	4.36249e-06	1.79301e-10	5.05141e-11	6.35933e-12
157	4.30061e-06	1.77831e-10	5.03336e-11	6.30837e-12
158	4.23981e-06	1.76475e-10	5.0081e-11	6.23691e-12
159	4.1802e-06	1.75227e-10	4.98929e-11	6.15885e-12
160	4.1218e-06	1.73982e-10	4.97221e-11	6.05298e-12
161	4.06441e-06	1.72636e-10	4.95029e-11	5.95241e-12
162	4.0081e-06	1.71395e-10	4.93306e-11	5.84229e-12
163	3.95292e-06	1.70155e-10	4.91549e-11	5.73529e-12
164	3.89888e-06	1.68822e-10	4.90216e-11	5.64028e-12
165	3.84591e-06	1.67587e-10	4.88443e-11	5.54108e-12
166	3.79389e-06	1.66353e-10	4.87066e-11	5.46174e-12
167	3.74289e-06	1.65029e-10	4.85662e-11	5.39872e-12

168	3.69278e-06	1.63626e-10	4.83812e-11	5.34446e-12
169	3.64369e-06	1.6216e-10	4.82355e-11	5.28073e-12
170	3.59563e-06	1.60674e-10	4.80863e-11	5.22877e-12
171	3.54849e-06	1.59216e-10	4.79345e-11	5.15685e-12
172	3.50276e-06	1.57777e-10	4.77791e-11	5.06739e-12
173	3.45684e-06	1.56337e-10	4.75842e-11	5.006e-12
174	3.41221e-06	1.54895e-10	4.74238e-11	4.94461e-12
175	3.36865e-06	1.5348e-10	4.72608e-11	4.87681e-12
176	3.32562e-06	1.52051e-10	4.71291e-11	4.82382e-12
177	3.28363e-06	1.50689e-10	4.69584e-11	4.77115e-12
178	3.24228e-06	1.49271e-10	4.67869e-11	4.69228e-12
179	3.20174e-06	1.47915e-10	4.66124e-11	4.5914e-12
180	3.16198e-06	1.46503e-10	4.64346e-11	4.49319e-12
181	3.12281e-06	1.4518e-10	4.62863e-11	4.39284e-12
182	3.08439e-06	1.43828e-10	4.609e-11	4.32619e-12
183	3.04666e-06	1.42444e-10	4.5893e-11	4.25802e-12
184	3.00948e-06	1.41183e-10	4.56334e-11	4.19657e-12
185	2.97298e-06	1.40032e-10	4.53675e-11	4.13499e-12
186	2.93708e-06	1.38889e-10	4.51544e-11	4.06181e-12
187	2.90178e-06	1.37824e-10	4.49914e-11	3.9996e-12
188	2.86705e-06	1.36674e-10	4.47625e-11	3.93009e-12
189	2.8327e-06	1.35578e-10	4.45134e-11	3.88584e-12
190	2.79906e-06	1.34533e-10	4.42515e-11	3.84026e-12
191	2.76574e-06	1.33369e-10	4.39581e-11	3.79826e-12
192	2.73297e-06	1.32348e-10	4.36751e-11	3.73478e-12
193	2.70061e-06	1.31219e-10	4.34163e-11	3.67109e-12
194	2.66868e-06	1.3008e-10	4.31849e-11	3.59749e-12
195	2.63708e-06	1.28797e-10	4.30457e-11	3.52465e-12
196	2.60586e-06	1.27555e-10	4.28517e-11	3.4572e-12
197	2.57509e-06	1.26301e-10	4.26035e-11	3.37643e-12
198	2.54464e-06	1.24935e-10	4.23093e-11	3.30747e-12
199	2.51438e-06	1.23629e-10	4.20213e-11	3.24892e-12
200	2.48454e-06	1.22465e-10	4.17153e-11	3.19875e-12
201	2.45496e-06	1.21382e-10	4.14365e-11	3.14818e-12
202	2.42558e-06	1.20189e-10	4.11444e-11	3.09729e-12
203	2.39651e-06	1.19008e-10	4.08489e-11	3.04355e-12
204	2.36775e-06	1.17833e-10	4.05276e-11	2.98755e-12
205	2.33917e-06	1.16649e-10	4.01914e-11	2.93296e-12
206	2.3108e-06	1.15414e-10	3.98963e-11	2.87685e-12
207	2.28276e-06	1.14196e-10	3.96541e-11	2.82178e-12
208	2.25494e-06	1.13097e-10	3.93835e-11	2.76513e-12
209	2.22745e-06	1.1183e-10	3.9119e-11	2.70986e-12

210	2.20012e-06	1.10549e-10	3.8859e-11	2.64827e-12
211	2.17316e-06	1.09305e-10	3.86106e-11	2.59448e-12
212	2.14647e-06	1.08129e-10	3.83741e-11	2.54813e-12
213	2.12001e-06	1.06995e-10	3.81533e-11	2.47818e-12
214	2.09384e-06	1.05871e-10	3.79078e-11	2.4121e-12
215	2.0679e-06	1.04808e-10	3.76052e-11	2.35811e-12
216	2.04225e-06	1.03756e-10	3.73241e-11	2.318e-12
217	2.01679e-06	1.02667e-10	3.70506e-11	2.27126e-12
218	1.99157e-06	1.01626e-10	3.67443e-11	2.21599e-12
219	1.96661e-06	1.006e-10	3.64014e-11	2.16321e-12
220	1.94195e-06	9.95827e-11	3.61214e-11	2.11264e-12
221	1.91753e-06	9.85783e-11	3.58331e-11	2.06208e-12
222	1.89335e-06	9.75824e-11	3.55447e-11	2.01363e-12
223	1.8694e-06	9.65404e-11	3.52459e-11	1.96732e-12
224	1.84572e-06	9.55621e-11	3.4963e-11	1.92025e-12
225	1.82226e-06	9.45818e-11	3.46719e-11	1.87761e-12
226	1.79903e-06	9.36218e-11	3.43882e-11	1.83515e-12
227	1.77606e-06	9.26852e-11	3.41094e-11	1.79255e-12
228	1.75333e-06	9.17015e-11	3.38211e-11	1.75383e-12
229	1.73086e-06	9.07792e-11	3.35462e-11	1.71889e-12
230	1.7086e-06	8.9872e-11	3.32666e-11	1.6781e-12
231	1.68654e-06	8.89693e-11	3.29697e-11	1.63048e-12
232	1.66472e-06	8.80771e-11	3.27126e-11	1.58221e-12
233	1.64319e-06	8.70954e-11	3.23955e-11	1.53661e-12
234	1.62188e-06	8.6208e-11	3.20966e-11	1.49907e-12
235	1.60079e-06	8.53886e-11	3.17911e-11	1.4645e-12
236	1.57996e-06	8.44701e-11	3.15149e-11	1.42989e-12
237	1.55908e-06	8.35551e-11	3.1222e-11	1.39702e-12
238	1.53892e-06	8.26031e-11	3.09145e-11	1.36372e-12
239	1.51878e-06	8.16575e-11	3.05814e-11	1.33228e-12
240	1.49886e-06	8.0828e-11	3.02391e-11	1.29843e-12
241	1.47907e-06	7.99525e-11	2.99314e-11	1.26414e-12
242	1.45956e-06	7.91205e-11	2.96585e-11	1.23582e-12
243	1.44026e-06	7.83371e-11	2.94211e-11	1.21019e-12
244	1.4212e-06	7.73856e-11	2.91777e-11	1.18228e-12
245	1.40232e-06	7.64927e-11	2.89176e-11	1.15362e-12
246	1.38364e-06	7.56106e-11	2.86502e-11	1.12248e-12
247	1.36526e-06	7.47348e-11	2.83747e-11	1.09386e-12
248	1.34704e-06	7.37636e-11	2.80902e-11	1.06432e-12
249	1.32903e-06	7.29028e-11	2.78129e-11	1.03862e-12
250	1.31125e-06	7.20503e-11	2.76006e-11	1.01382e-12
251	1.29368e-06	7.12548e-11	2.73256e-11	9.91377e-13

252	1.27631e-06	7.04728e-11	2.70485e-11	9.71874e-13
253	1.25917e-06	6.96944e-11	2.67951e-11	9.51851e-13
254	1.24222e-06	6.89284e-11	2.65233e-11	9.33058e-13
255	1.22546e-06	6.82179e-11	2.62677e-11	9.1501e-13
256	1.20892e-06	6.75689e-11	2.60064e-11	8.97712e-13
257	1.19257e-06	6.69283e-11	2.575e-11	8.82865e-13
258	1.17644e-06	6.62405e-11	2.54745e-11	8.66386e-13
259	1.16047e-06	6.5572e-11	2.5219e-11	8.52177e-13
260	1.1448e-06	6.47992e-11	2.49803e-11	8.35792e-13
261	1.12924e-06	6.39764e-11	2.47183e-11	8.23797e-13
262	1.11388e-06	6.32207e-11	2.44688e-11	8.10406e-13
263	1.09876e-06	6.25212e-11	2.42376e-11	7.97232e-13
264	1.08378e-06	6.17815e-11	2.39898e-11	7.84623e-13
265	1.06906e-06	6.11747e-11	2.3738e-11	7.72934e-13
266	1.05446e-06	6.05252e-11	2.34961e-11	7.62729e-13
267	1.04009e-06	5.98899e-11	2.32372e-11	7.53208e-13
268	1.02587e-06	5.92863e-11	2.29807e-11	7.45043e-13
269	1.01188e-06	5.86486e-11	2.27345e-11	7.34724e-13
270	9.98067e-07	5.80425e-11	2.25049e-11	7.2571e-13
271	9.84424e-07	5.74485e-11	2.22804e-11	7.17387e-13
272	9.70957e-07	5.6864e-11	2.20575e-11	7.10385e-13
273	9.5767e-07	5.62456e-11	2.18426e-11	7.02785e-13
274	9.4458e-07	5.56225e-11	2.16388e-11	6.94815e-13
275	9.31658e-07	5.4964e-11	2.14166e-11	6.88949e-13
276	9.18905e-07	5.44193e-11	2.1223e-11	6.83605e-13
277	9.06346e-07	5.38326e-11	2.10064e-11	6.77171e-13
278	8.93967e-07	5.33046e-11	2.08002e-11	6.72807e-13
279	8.81778e-07	5.27884e-11	2.05976e-11	6.67424e-13
280	8.69755e-07	5.22315e-11	2.03789e-11	6.64696e-13
281	8.57885e-07	5.16022e-11	2.01816e-11	6.59952e-13
282	8.46114e-07	5.10322e-11	1.99675e-11	6.55161e-13
283	8.34592e-07	5.0464e-11	1.97737e-11	6.51333e-13
284	8.23248e-07	4.98636e-11	1.95494e-11	6.47945e-13
285	8.12076e-07	4.93062e-11	1.9344e-11	6.46252e-13
286	8.01058e-07	4.87461e-11	1.91403e-11	6.4349e-13
287	7.90222e-07	4.8155e-11	1.89229e-11	6.41608e-13
288	7.79453e-07	4.76222e-11	1.87291e-11	6.39414e-13
289	7.68939e-07	4.70825e-11	1.85392e-11	6.37445e-13
290	7.58737e-07	4.65485e-11	1.83453e-11	6.34912e-13
291	7.4844e-07	4.60545e-11	1.81676e-11	6.33358e-13
292	7.38248e-07	4.55692e-11	1.79932e-11	6.30578e-13
293	7.28368e-07	4.50587e-11	1.78135e-11	6.29326e-13

294	7.18525e-07	4.46068e-11	1.76415e-11	6.28289e-13
295	7.08966e-07	4.41547e-11	1.74911e-11	6.27937e-13
296	6.99517e-07	4.36238e-11	1.73398e-11	6.25013e-13
297	6.9014e-07	4.32216e-11	1.71661e-11	6.24259e-13
298	6.81013e-07	4.27993e-11	1.6985e-11	6.23517e-13
299	6.71873e-07	4.23654e-11	1.68107e-11	6.22835e-13
300	6.63099e-07	4.19774e-11	1.66587e-11	6.20739e-13
301	6.54411e-07	4.15721e-11	1.64888e-11	-
302	6.45772e-07	4.11188e-11	1.63217e-11	-
303	6.37368e-07	4.07133e-11	1.61547e-11	-
304	6.28867e-07	4.02792e-11	1.59929e-11	-
305	6.2088e-07	3.99369e-11	1.58317e-11	-
306	6.12803e-07	3.95201e-11	1.56926e-11	-
307	6.04901e-07	3.91146e-11	1.55356e-11	-
308	5.97128e-07	3.88007e-11	1.53811e-11	-
309	5.89652e-07	3.83775e-11	1.52325e-11	-
310	5.82061e-07	3.80067e-11	1.50776e-11	-
311	5.74814e-07	3.76384e-11	1.49286e-11	-
312	5.67469e-07	3.72759e-11	1.4782e-11	-
313	5.60363e-07	3.69303e-11	1.4637e-11	-
314	5.53393e-07	3.65671e-11	1.45144e-11	-
315	5.4653e-07	3.62306e-11	1.43741e-11	-
316	5.39672e-07	3.58775e-11	1.4235e-11	-
317	5.3319e-07	3.55613e-11	1.40982e-11	-
318	5.26697e-07	3.52101e-11	1.39634e-11	-
319	5.20271e-07	3.48552e-11	1.38302e-11	-
320	5.14146e-07	3.45581e-11	1.36991e-11	-
321	5.0799e-07	3.42105e-11	1.35644e-11	-
322	5.0196e-07	3.39211e-11	1.3448e-11	-
323	4.96032e-07	3.35859e-11	1.33163e-11	-
324	4.90305e-07	3.33049e-11	1.31928e-11	-
325	4.84597e-07	3.30317e-11	1.30707e-11	-
326	4.79019e-07	3.26983e-11	1.29547e-11	-
327	4.736e-07	3.24396e-11	1.28317e-11	-
328	4.68306e-07	3.22222e-11	1.27198e-11	-
329	4.63027e-07	3.19171e-11	1.25998e-11	-
330	4.57841e-07	3.16268e-11	1.24863e-11	-
331	4.52749e-07	3.13662e-11	1.23742e-11	-
332	4.47844e-07	3.11202e-11	1.22527e-11	-
333	4.42959e-07	3.08806e-11	1.2147e-11	-
334	4.38256e-07	3.06389e-11	1.20328e-11	-
335	4.3357e-07	3.04042e-11	1.19327e-11	-

336	4.29047e-07	3.01749e-11	1.18163e-11	-
337	4.24546e-07	2.99478e-11	1.17207e-11	-
338	4.20203e-07	2.97234e-11	1.161e-11	-
339	4.15959e-07	2.95181e-11	1.15107e-11	-
340	4.11718e-07	2.92433e-11	1.14173e-11	-
341	4.07644e-07	2.90866e-11	1.13012e-11	-
342	4.03648e-07	2.88684e-11	1.12145e-11	-
343	3.99741e-07	2.86622e-11	1.11054e-11	-
344	3.95843e-07	2.84635e-11	1.10196e-11	-
345	3.92104e-07	2.82595e-11	1.09312e-11	-
346	3.88429e-07	2.8067e-11	1.08168e-11	-
347	3.84793e-07	2.78295e-11	1.07341e-11	-
348	3.81253e-07	2.7643e-11	1.0649e-11	-
349	3.77786e-07	2.74545e-11	1.0546e-11	-
350	3.74399e-07	2.72768e-11	1.04619e-11	-
351	3.71149e-07	2.71024e-11	1.03882e-11	-
352	3.67903e-07	2.69197e-11	1.02786e-11	-
353	3.64739e-07	2.67454e-11	1.01978e-11	-
354	3.61641e-07	2.65292e-11	1.01178e-11	-
355	3.58609e-07	2.6364e-11	1.00378e-11	-
356	3.55649e-07	2.62086e-11	9.96311e-12	-
357	3.52756e-07	2.60368e-11	9.88154e-12	-
358	3.49926e-07	2.58774e-11	9.78703e-12	-
359	3.47171e-07	2.56782e-11	9.71519e-12	-
360	3.44522e-07	2.55244e-11	9.63992e-12	-
361	3.41876e-07	2.53723e-11	9.56072e-12	-
362	3.39294e-07	2.52123e-11	9.49158e-12	-
363	3.36769e-07	2.50205e-11	9.41416e-12	-
364	3.34252e-07	2.4892e-11	9.34064e-12	-
365	3.31906e-07	2.47484e-11	9.26972e-12	-
366	3.29547e-07	2.45715e-11	9.19857e-12	-
367	3.27179e-07	2.44343e-11	9.12753e-12	-
368	3.24924e-07	2.42587e-11	9.05813e-12	-
369	3.22727e-07	2.41262e-11	8.98948e-12	-
370	3.2057e-07	2.39952e-11	8.92114e-12	-
371	3.18386e-07	2.3825e-11	8.85337e-12	-
372	3.16399e-07	2.36985e-11	8.78952e-12	-
373	3.14303e-07	2.35735e-11	8.72355e-12	-
374	3.12455e-07	2.34495e-11	8.65301e-12	-
375	3.10442e-07	2.33276e-11	8.60424e-12	-
376	3.08615e-07	2.31932e-11	8.53903e-12	-
377	3.06818e-07	2.30882e-11	8.47474e-12	-

378	3.04945e-07	2.29745e-11	8.40771e-12	-
379	3.0317e-07	2.28939e-11	8.34787e-12	-
380	3.01361e-07	2.27778e-11	8.28838e-12	-
381	2.99717e-07	2.26634e-11	8.22238e-12	-
382	2.98002e-07	2.26169e-11	8.17612e-12	-
383	2.96282e-07	2.24768e-11	8.11511e-12	-
384	2.94691e-07	2.23678e-11	8.0541e-12	-
385	2.93093e-07	2.22911e-11	7.99765e-12	-
386	2.91486e-07	2.2184e-11	7.93361e-12	-
387	2.89834e-07	2.20619e-11	7.89149e-12	-
388	2.88371e-07	2.20036e-11	7.8297e-12	-
389	2.86664e-07	2.18974e-11	7.76992e-12	-
390	2.85193e-07	2.18385e-11	7.71158e-12	-
391	2.83606e-07	2.172e-11	7.66812e-12	-
392	2.82067e-07	2.16182e-11	7.61077e-12	-
393	2.80501e-07	2.15756e-11	7.5576e-12	-
394	2.79089e-07	2.14304e-11	7.50009e-12	-
395	2.77584e-07	2.13753e-11	7.45334e-12	-
396	2.76099e-07	2.12784e-11	7.39673e-12	-
397	2.74629e-07	2.1201e-11	7.3407e-12	-
398	2.73165e-07	2.1102e-11	7.28909e-12	-
399	2.71675e-07	2.10311e-11	7.24591e-12	-
400	2.70224e-07	2.09285e-11	7.18777e-12	-

Table A.3: The high-energy neutron energy-dependent flux negative uncertainty σ_- results from the four MARS measurements at KURF. All results are quoted in units of [#/cm^2/sec/MeV].

Energy [MeV]	σ_- Above Ground	σ_- 377 m.w.e.	σ_- 540 m.w.e.	σ_- 1450 m.w.e.
90	1.18841e-05	4.35795e-10	1.52144e-10	3.53544e-11
91	1.18263e-05	4.3257e-10	1.50916e-10	3.49001e-11
92	1.1765e-05	4.29164e-10	1.49688e-10	3.4378e-11
93	1.17005e-05	4.25613e-10	1.48491e-10	3.39199e-11
94	1.16323e-05	4.22325e-10	1.47287e-10	3.34646e-11
95	1.1561e-05	4.19095e-10	1.46186e-10	3.29956e-11
96	1.14864e-05	4.15945e-10	1.44916e-10	3.25694e-11
97	1.14085e-05	4.128e-10	1.43856e-10	3.20921e-11
98	1.13276e-05	4.09173e-10	1.42629e-10	3.16659e-11

99	1.1244e-05	4.05992e-10	1.41431e-10	3.1208e-11
100	1.11575e-05	4.02809e-10	1.40224e-10	3.07504e-11
101	1.10711e-05	3.99578e-10	1.39136e-10	3.03472e-11
102	1.09763e-05	3.96105e-10	1.37944e-10	2.98938e-11
103	1.08821e-05	3.92789e-10	1.36984e-10	2.95105e-11
104	1.07852e-05	3.89442e-10	1.37222e-10	2.90438e-11
105	1.06861e-05	3.86104e-10	1.36147e-10	2.86434e-11
106	1.05845e-05	3.82779e-10	1.3516e-10	2.82177e-11
107	1.04809e-05	3.79524e-10	1.34008e-10	2.78488e-11
108	1.03754e-05	3.7639e-10	1.32928e-10	2.73985e-11
109	1.0268e-05	3.73363e-10	1.318e-10	2.70143e-11
110	1.01611e-05	3.70507e-10	1.30772e-10	2.66005e-11
111	1.00499e-05	3.67194e-10	1.298e-10	2.62229e-11
112	9.93465e-06	3.64321e-10	1.28587e-10	2.58702e-11
113	9.82063e-06	3.61171e-10	1.27564e-10	2.54469e-11
114	9.70498e-06	3.58227e-10	1.26547e-10	2.51033e-11
115	9.58818e-06	3.55257e-10	1.25536e-10	2.46872e-11
116	9.47017e-06	3.52227e-10	1.2453e-10	2.43503e-11
117	9.35122e-06	3.49352e-10	1.23438e-10	2.39699e-11
118	9.23104e-06	3.46416e-10	1.22478e-10	2.36106e-11
119	9.1104e-06	3.43593e-10	1.21464e-10	2.32389e-11
120	8.98888e-06	3.40536e-10	1.20487e-10	2.28924e-11
121	8.8667e-06	3.37763e-10	1.19515e-10	2.2549e-11
122	8.74411e-06	3.34924e-10	1.1846e-10	2.22105e-11
123	8.62117e-06	3.32197e-10	1.17522e-10	2.18986e-11
124	8.49798e-06	3.29498e-10	1.16553e-10	2.17718e-11
125	8.37473e-06	3.26947e-10	1.15546e-10	2.14129e-11
126	8.25213e-06	3.24354e-10	1.14497e-10	2.10832e-11
127	8.12804e-06	3.21834e-10	1.13484e-10	2.07316e-11
128	8.00591e-06	3.19318e-10	1.12401e-10	2.04075e-11
129	7.88254e-06	3.16816e-10	1.11422e-10	2.00648e-11
130	7.76031e-06	3.14173e-10	1.10338e-10	1.9748e-11
131	7.63909e-06	3.11674e-10	1.09361e-10	1.94118e-11
132	7.51896e-06	3.09152e-10	1.08333e-10	1.91008e-11
133	7.39837e-06	3.06617e-10	1.07354e-10	1.88056e-11
134	7.27743e-06	3.04174e-10	1.0637e-10	1.84681e-11
135	7.15915e-06	3.01595e-10	1.05313e-10	1.81677e-11
136	7.04274e-06	2.99088e-10	1.04308e-10	1.78498e-11
137	6.92617e-06	2.96619e-10	1.03378e-10	1.7556e-11
138	6.81172e-06	2.94084e-10	1.02395e-10	1.72667e-11
139	6.69992e-06	2.91568e-10	1.01487e-10	1.69597e-11
140	6.58778e-06	2.8906e-10	1.00602e-10	1.66754e-11

141	6.47742e-06	2.8677e-10	9.96905e-11	1.63988e-11
142	6.36954e-06	2.84579e-10	9.88053e-11	1.6132e-11
143	6.26369e-06	2.82498e-10	9.79891e-11	1.5835e-11
144	6.15979e-06	2.80111e-10	9.71686e-11	1.55556e-11
145	6.05919e-06	2.77954e-10	9.63168e-11	1.52885e-11
146	5.95853e-06	2.7592e-10	9.55393e-11	1.50366e-11
147	5.86135e-06	2.73692e-10	9.47253e-11	1.47661e-11
148	5.7665e-06	2.71463e-10	9.38816e-11	1.45044e-11
149	5.67364e-06	2.69362e-10	9.31018e-11	1.42496e-11
150	5.58311e-06	2.67275e-10	9.23276e-11	1.40219e-11
151	5.49449e-06	2.65299e-10	9.15184e-11	1.37719e-11
152	5.40788e-06	2.63139e-10	9.07412e-11	1.35174e-11
153	5.32334e-06	2.61087e-10	9.00299e-11	1.32599e-11
154	5.24072e-06	2.59048e-10	8.91769e-11	1.30233e-11
155	5.15998e-06	2.57012e-10	8.84327e-11	1.27706e-11
156	5.08119e-06	2.54905e-10	8.77368e-11	1.25407e-11
157	5.00422e-06	2.52684e-10	8.69081e-11	1.23057e-11
158	4.92915e-06	2.50388e-10	8.62085e-11	1.20691e-11
159	4.85582e-06	2.47997e-10	8.54541e-11	1.18685e-11
160	4.78512e-06	2.4563e-10	8.46872e-11	1.16741e-11
161	4.71426e-06	2.43391e-10	8.39766e-11	1.1491e-11
162	4.64606e-06	2.41068e-10	8.32239e-11	1.13215e-11
163	4.5794e-06	2.38776e-10	8.24782e-11	1.11528e-11
164	4.51429e-06	2.36603e-10	8.16932e-11	1.09757e-11
165	4.45066e-06	2.34355e-10	8.09627e-11	1.08064e-11
166	4.38863e-06	2.32125e-10	8.01943e-11	1.0621e-11
167	4.32801e-06	2.30012e-10	7.94368e-11	1.04225e-11
168	4.26897e-06	2.28004e-10	7.87276e-11	1.02196e-11
169	4.21122e-06	2.26193e-10	7.79845e-11	1.00297e-11
170	4.15481e-06	2.24215e-10	7.72504e-11	9.83157e-12
171	4.09962e-06	2.22342e-10	7.65242e-11	9.65706e-12
172	4.04618e-06	2.20561e-10	7.58068e-11	9.50405e-12
173	3.99327e-06	2.18712e-10	7.51343e-11	9.32563e-12
174	3.94202e-06	2.1679e-10	7.44319e-11	9.15116e-12
175	3.89172e-06	2.14971e-10	7.37363e-11	8.98621e-12
176	3.84284e-06	2.13186e-10	7.30173e-11	8.8103e-12
177	3.79486e-06	2.11353e-10	7.23401e-11	8.64527e-12
178	3.74806e-06	2.09606e-10	7.16701e-11	8.50175e-12
179	3.70224e-06	2.07819e-10	7.10086e-11	8.37602e-12
180	3.65738e-06	2.06104e-10	7.03539e-11	8.25906e-12
181	3.61362e-06	2.04334e-10	6.96772e-11	8.14697e-12
182	3.57072e-06	2.027e-10	6.90515e-11	8.00453e-12

183	3.52871e-06	2.00944e-10	6.84312e-11	7.86754e-12
184	3.48765e-06	1.99179e-10	6.78813e-11	7.7265e-12
185	3.4474e-06	1.97321e-10	6.73396e-11	7.58883e-12
186	3.40791e-06	1.95484e-10	6.67513e-11	7.47294e-12
187	3.36917e-06	1.93675e-10	6.61186e-11	7.34217e-12
188	3.33112e-06	1.91803e-10	6.55897e-11	7.21496e-12
189	3.29396e-06	1.89987e-10	6.50195e-11	7.07287e-12
190	3.25724e-06	1.88139e-10	6.45315e-11	6.93445e-12
191	3.22132e-06	1.86436e-10	6.40144e-11	6.79593e-12
192	3.18666e-06	1.8469e-10	6.35273e-11	6.68171e-12
193	3.15107e-06	1.82918e-10	6.30181e-11	6.5708e-12
194	3.11754e-06	1.81336e-10	6.24895e-11	6.47298e-12
195	3.08304e-06	1.79834e-10	6.19006e-11	6.37696e-12
196	3.04973e-06	1.7824e-10	6.13124e-11	6.27876e-12
197	3.01676e-06	1.76837e-10	6.0813e-11	6.19642e-12
198	2.9842e-06	1.75412e-10	6.03634e-11	6.10532e-12
199	2.95208e-06	1.74022e-10	5.99407e-11	6.00656e-12
200	2.92018e-06	1.72517e-10	5.94861e-11	5.90226e-12
201	2.88857e-06	1.70949e-10	5.90365e-11	5.80111e-12
202	2.85733e-06	1.69595e-10	5.86305e-11	5.70292e-12
203	2.82627e-06	1.68088e-10	5.81808e-11	5.61046e-12
204	2.79549e-06	1.66763e-10	5.77867e-11	5.523e-12
205	2.76507e-06	1.65302e-10	5.74134e-11	5.44186e-12
206	2.73493e-06	1.63993e-10	5.7002e-11	5.35936e-12
207	2.70502e-06	1.62767e-10	5.65429e-11	5.27351e-12
208	2.67543e-06	1.61363e-10	5.61184e-11	5.19707e-12
209	2.64605e-06	1.60071e-10	5.56916e-11	5.12169e-12
210	2.61764e-06	1.58893e-10	5.52643e-11	5.05522e-12
211	2.58812e-06	1.57697e-10	5.48303e-11	4.98337e-12
212	2.55952e-06	1.56532e-10	5.43889e-11	4.91148e-12
213	2.53116e-06	1.55185e-10	5.39372e-11	4.86067e-12
214	2.50306e-06	1.53931e-10	5.35115e-11	4.80824e-12
215	2.47522e-06	1.52635e-10	5.31503e-11	4.74644e-12
216	2.4482e-06	1.51349e-10	5.27701e-11	4.66817e-12
217	2.42093e-06	1.50198e-10	5.2412e-11	4.60375e-12
218	2.39389e-06	1.48862e-10	5.20424e-11	4.55451e-12
219	2.36653e-06	1.47606e-10	5.17391e-11	4.49618e-12
220	2.33996e-06	1.4636e-10	5.13755e-11	4.44224e-12
221	2.31362e-06	1.45125e-10	5.1027e-11	4.3951e-12
222	2.28757e-06	1.43901e-10	5.06803e-11	4.33911e-12
223	2.26229e-06	1.42739e-10	5.03481e-11	4.28759e-12
224	2.23615e-06	1.41533e-10	5.00065e-11	4.23893e-12

225	2.21084e-06	1.4043e-10	4.96755e-11	4.19226e-12
226	2.18632e-06	1.39162e-10	4.93428e-11	4.13905e-12
227	2.16094e-06	1.37977e-10	4.90079e-11	4.09627e-12
228	2.13636e-06	1.36851e-10	4.86877e-11	4.04346e-12
229	2.11196e-06	1.35682e-10	4.83573e-11	3.99308e-12
230	2.08783e-06	1.34523e-10	4.80351e-11	3.95047e-12
231	2.06396e-06	1.33374e-10	4.77367e-11	3.91654e-12
232	2.04087e-06	1.32234e-10	4.74024e-11	3.8852e-12
233	2.01691e-06	1.312e-10	4.71309e-11	3.85308e-12
234	1.9937e-06	1.30089e-10	4.68438e-11	3.81877e-12
235	1.97124e-06	1.29007e-10	4.65693e-11	3.77536e-12
236	1.94798e-06	1.27888e-10	4.62948e-11	3.73788e-12
237	1.92573e-06	1.26858e-10	4.59908e-11	3.7005e-12
238	1.90319e-06	1.25885e-10	4.57304e-11	3.6651e-12
239	1.88111e-06	1.24921e-10	4.54992e-11	3.6295e-12
240	1.85925e-06	1.23939e-10	4.52822e-11	3.5983e-12
241	1.83816e-06	1.22864e-10	4.50326e-11	3.56893e-12
242	1.81628e-06	1.21838e-10	4.47534e-11	3.53548e-12
243	1.79514e-06	1.20787e-10	4.44404e-11	3.50083e-12
244	1.77416e-06	1.19916e-10	4.41414e-11	3.47012e-12
245	1.75345e-06	1.19005e-10	4.38595e-11	3.44152e-12
246	1.73298e-06	1.18103e-10	4.35904e-11	3.41723e-12
247	1.71309e-06	1.17286e-10	4.33336e-11	3.39529e-12
248	1.69255e-06	1.16425e-10	4.3087e-11	3.37223e-12
249	1.67267e-06	1.15549e-10	4.28384e-11	3.34324e-12
250	1.65299e-06	1.1468e-10	4.25292e-11	3.3185e-12
251	1.63353e-06	1.13769e-10	4.22861e-11	3.29263e-12
252	1.61474e-06	1.1287e-10	4.20486e-11	3.2687e-12
253	1.59521e-06	1.11973e-10	4.17919e-11	3.23958e-12
254	1.57684e-06	1.11089e-10	4.15558e-11	3.21762e-12
255	1.5582e-06	1.10156e-10	4.13325e-11	3.18934e-12
256	1.5393e-06	1.09184e-10	4.10708e-11	3.16497e-12
257	1.52152e-06	1.0822e-10	4.08304e-11	3.1393e-12
258	1.50301e-06	1.07311e-10	4.06143e-11	3.11996e-12
259	1.48564e-06	1.06484e-10	4.03801e-11	3.09604e-12
260	1.46749e-06	1.05692e-10	4.01593e-11	3.07227e-12
261	1.45004e-06	1.049e-10	3.99147e-11	3.05185e-12
262	1.43281e-06	1.04126e-10	3.96858e-11	3.03062e-12
263	1.41569e-06	1.0331e-10	3.94419e-11	3.00691e-12
264	1.39884e-06	1.02556e-10	3.9217e-11	2.99018e-12
265	1.38211e-06	1.01679e-10	3.90026e-11	2.9671e-12
266	1.36564e-06	1.00857e-10	3.87795e-11	2.94689e-12

267	1.3493e-06	1.0004e-10	3.8577e-11	2.9267e-12
268	1.3332e-06	9.92783e-11	3.83988e-11	2.9097e-12
269	1.31723e-06	9.84194e-11	3.81676e-11	2.88902e-12
270	1.30146e-06	9.76135e-11	3.79469e-11	2.87125e-12
271	1.2859e-06	9.68155e-11	3.77242e-11	2.85351e-12
272	1.27051e-06	9.60173e-11	3.75026e-11	2.83541e-12
273	1.2553e-06	9.53427e-11	3.73013e-11	2.81853e-12
274	1.24027e-06	9.45417e-11	3.70428e-11	2.80308e-12
275	1.2254e-06	9.38625e-11	3.68321e-11	2.78616e-12
276	1.21113e-06	9.30822e-11	3.65952e-11	2.76941e-12
277	1.1962e-06	9.23599e-11	3.63834e-11	2.75437e-12
278	1.18226e-06	9.15881e-11	3.61647e-11	2.73809e-12
279	1.16767e-06	9.08237e-11	3.59473e-11	2.72328e-12
280	1.15367e-06	9.01117e-11	3.57464e-11	2.70987e-12
281	1.13983e-06	8.94857e-11	3.55288e-11	2.69245e-12
282	1.12624e-06	8.88153e-11	3.53311e-11	2.67884e-12
283	1.11271e-06	8.81523e-11	3.51158e-11	2.66499e-12
284	1.09977e-06	8.76134e-11	3.49355e-11	2.65093e-12
285	1.08617e-06	8.69669e-11	3.47381e-11	2.63589e-12
286	1.07315e-06	8.62607e-11	3.45422e-11	2.62223e-12
287	1.06028e-06	8.56802e-11	3.43621e-11	2.6082e-12
288	1.04766e-06	8.51198e-11	3.41883e-11	2.59802e-12
289	1.03511e-06	8.44369e-11	3.39636e-11	2.58471e-12
290	1.02291e-06	8.38249e-11	3.37698e-11	2.56933e-12
291	1.01077e-06	8.32712e-11	3.3562e-11	2.55628e-12
292	9.98818e-07	8.25708e-11	3.33566e-11	2.54485e-12
293	9.86518e-07	8.19801e-11	3.31564e-11	2.5321e-12
294	9.74823e-07	8.13438e-11	3.29536e-11	2.51934e-12
295	9.63183e-07	8.07138e-11	3.27314e-11	2.50609e-12
296	9.51711e-07	8.01795e-11	3.25123e-11	2.49569e-12
297	9.4046e-07	7.95278e-11	3.23192e-11	2.48321e-12
298	9.29273e-07	7.89817e-11	3.21354e-11	2.47087e-12
299	9.18366e-07	7.83148e-11	3.19487e-11	2.45849e-12
300	9.0742e-07	7.77594e-11	3.17428e-11	2.44759e-12
301	8.96655e-07	7.71555e-11	3.15566e-11	-
302	8.86128e-07	7.65432e-11	3.13714e-11	-
303	8.75652e-07	7.5966e-11	3.11866e-11	-
304	8.65548e-07	7.54283e-11	3.10006e-11	-
305	8.55193e-07	7.4878e-11	3.08178e-11	-
306	8.45221e-07	7.42684e-11	3.06146e-11	-
307	8.35337e-07	7.37363e-11	3.04324e-11	-
308	8.25906e-07	7.31953e-11	3.02489e-11	-

309	8.16139e-07	7.26261e-11	3.00646e-11	-
310	8.06447e-07	7.20903e-11	2.9887e-11	-
311	7.97273e-07	7.15603e-11	2.97085e-11	-
312	7.87843e-07	7.10364e-11	2.95275e-11	-
313	7.79054e-07	7.05797e-11	2.93493e-11	-
314	7.69764e-07	7.00043e-11	2.91499e-11	-
315	7.60908e-07	6.95535e-11	2.89708e-11	-
316	7.5233e-07	6.90629e-11	2.8794e-11	-
317	7.43603e-07	6.85417e-11	2.86169e-11	-
318	7.35109e-07	6.79965e-11	2.84396e-11	-
319	7.26819e-07	6.75345e-11	2.82647e-11	-
320	7.18453e-07	6.7026e-11	2.8089e-11	-
321	7.10361e-07	6.6574e-11	2.79183e-11	-
322	7.02373e-07	6.60753e-11	2.77578e-11	-
323	6.94508e-07	6.56314e-11	2.75653e-11	-
324	6.86662e-07	6.51421e-11	2.73928e-11	-
325	6.79033e-07	6.46578e-11	2.72195e-11	-
326	6.71501e-07	6.42401e-11	2.70431e-11	-
327	6.64e-07	6.37524e-11	2.68758e-11	-
328	6.56897e-07	6.33081e-11	2.67238e-11	-
329	6.49709e-07	6.28167e-11	2.65334e-11	-
330	6.42356e-07	6.24596e-11	2.63641e-11	-
331	6.35402e-07	6.19455e-11	2.61945e-11	-
332	6.28731e-07	6.14922e-11	2.60372e-11	-
333	6.21703e-07	6.1044e-11	2.58658e-11	-
334	6.14972e-07	6.05992e-11	2.57055e-11	-
335	6.08426e-07	6.01595e-11	2.55316e-11	-
336	6.02164e-07	5.97235e-11	2.53785e-11	-
337	5.95554e-07	5.92914e-11	2.52065e-11	-
338	5.89237e-07	5.8864e-11	2.50731e-11	-
339	5.83015e-07	5.84938e-11	2.48846e-11	-
340	5.76958e-07	5.80667e-11	2.4716e-11	-
341	5.70935e-07	5.76589e-11	2.45714e-11	-
342	5.64992e-07	5.71926e-11	2.44003e-11	-
343	5.59164e-07	5.67857e-11	2.42534e-11	-
344	5.5348e-07	5.6381e-11	2.40844e-11	-
345	5.47831e-07	5.59817e-11	2.39208e-11	-
346	5.42492e-07	5.55846e-11	2.37847e-11	-
347	5.37049e-07	5.52361e-11	2.36181e-11	-
348	5.31464e-07	5.48473e-11	2.34571e-11	-
349	5.26187e-07	5.44615e-11	2.33151e-11	-
350	5.21007e-07	5.40795e-11	2.31562e-11	-

351	5.1583e-07	5.3751e-11	2.30104e-11	-
352	5.10801e-07	5.3325e-11	2.28583e-11	-
353	5.05851e-07	5.29536e-11	2.27022e-11	-
354	5.00979e-07	5.2628e-11	2.25466e-11	-
355	4.96176e-07	5.22622e-11	2.23918e-11	-
356	4.91458e-07	5.19497e-11	2.22344e-11	-
357	4.86812e-07	5.1542e-11	2.2085e-11	-
358	4.82438e-07	5.1187e-11	2.19509e-11	-
359	4.77738e-07	5.08759e-11	2.17963e-11	-
360	4.73242e-07	5.05264e-11	2.16657e-11	-
361	4.68874e-07	5.01802e-11	2.15001e-11	-
362	4.64581e-07	4.98462e-11	2.13677e-11	-
363	4.60353e-07	4.95523e-11	2.1204e-11	-
364	4.56238e-07	4.91987e-11	2.10576e-11	-
365	4.5226e-07	4.88647e-11	2.09117e-11	-
366	4.48215e-07	4.85715e-11	2.07662e-11	-
367	4.44126e-07	4.82425e-11	2.06223e-11	-
368	4.40207e-07	4.79548e-11	2.04791e-11	-
369	4.36352e-07	4.76305e-11	2.03364e-11	-
370	4.32551e-07	4.73092e-11	2.01945e-11	-
371	4.28883e-07	4.70287e-11	2.00541e-11	-
372	4.25121e-07	4.67118e-11	1.99107e-11	-
373	4.21561e-07	4.63981e-11	1.97889e-11	-
374	4.17863e-07	4.60868e-11	1.96358e-11	-
375	4.14411e-07	4.57779e-11	1.94821e-11	-
376	4.11016e-07	4.54865e-11	1.9345e-11	-
377	4.07531e-07	4.51673e-11	1.92089e-11	-
378	4.04063e-07	4.48651e-11	1.90772e-11	-
379	4.00714e-07	4.45305e-11	1.89393e-11	-
380	3.9749e-07	4.42336e-11	1.88192e-11	-
381	3.94175e-07	4.39394e-11	1.86724e-11	-
382	3.9101e-07	4.36303e-11	1.85248e-11	-
383	3.87925e-07	4.33217e-11	1.83933e-11	-
384	3.84777e-07	4.30335e-11	1.82626e-11	-
385	3.817e-07	4.27143e-11	1.8146e-11	-
386	3.78833e-07	4.2431e-11	1.80031e-11	-
387	3.75807e-07	4.21628e-11	1.78568e-11	-
388	3.72914e-07	4.18359e-11	1.77318e-11	-
389	3.70056e-07	4.15587e-11	1.76053e-11	-
390	3.67157e-07	4.12815e-11	1.74785e-11	-
391	3.64419e-07	4.0977e-11	1.73385e-11	-
392	3.6168e-07	4.07051e-11	1.72132e-11	-

393	3.59016e-07	4.04192e-11	1.71012e-11	-
394	3.56241e-07	4.01483e-11	1.69773e-11	-
395	3.53608e-07	3.98375e-11	1.68283e-11	-
396	3.50979e-07	3.96071e-11	1.67058e-11	-
397	3.48379e-07	3.92791e-11	1.65841e-11	-
398	3.45911e-07	3.90169e-11	1.64749e-11	-
399	3.43386e-07	3.87273e-11	1.63265e-11	-
400	3.40855e-07	3.84688e-11	1.62095e-11	-

Appendix B

Modeling of the Gamma-Ray and Cosmogenic Charged Particle Noise

With the correctly chosen physics models, the MARS Monte Carlo model was used to predict cosmogenic charged particle and gamma-ray noise. As described in Sec. 3.1, the primary noise to the MARS measured neutron signal is due to the uncorrelated ambient gamma-ray flux and cosmogenic charged particle flux. The gamma ray flux has a small probability as a function of time to produce $\geq$3 nearly time coincident gamma rays depositions in MARS satisfying the multiplicity trigger. However, over long measurement times this probability is non-negligible. Charged particles are capable of inducing spallation reactions in the lead, also actuating the multiplicity trigger. These backgrounds can be modeled using measured parameters as well as established Monte Carlo packages (CRY [87]).

A simple Monte Carlo model based upon the measured uncorrelated gamma ray background rate and the individual multiplicity event time range was used to estimate the gamma ray contamination of the multiplicity data. The gamma ray contamination probability for each measured multiplicity event was calculated by:

$$R = \sum_{j=1}^{Mult.} P_{bkg}(r,t,j)P(E)^j, \tag{B.1}$$

where R is the total probability that the event is contaminated, $P_{bkg}(r,t,j)$ is the Poisson probability for j gamma rays given the measured rate of the background (r) and the time considered by the triggering algorithm for the respective multiplicity event (t), $P(E)$ is the probability that the background gamma ray energy is within the triggering thresholds described above, and noise contamination from 1 to all depositions in the multiplicity event are considered. A uniform random value between 0 and 1 was sampled. If the random value was less than R, the appropriate element of the $\vec{b}$ from Equ. 3.2 is incremented. Note that traditionally, the noise would be calculated by the summation of $P_{bkg}(r,t,j|E > 0.85\ MeV)$. However, the inter-event time controlling the probability of gamma rays was calculated during the MARS data pre-processing. The MARS data is pre-processed with no software energy

threshold. It is assumed that the two probabilities are separable. The energy distribution, in PE, of gamma-ray depositions ($P(E)$) at the 377 m.w.e. depth is displayed in Fig. B.1. The model randomly samples the distribution in PE, then converts this value to the measured energy space. This was done in order to simplify new energy calibrations at a later date.

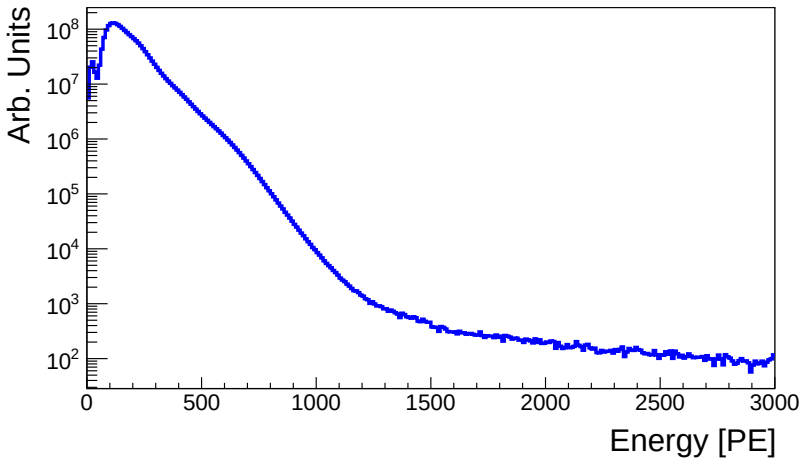

Figure B.1: The energy distribution in PE of ambient gamma rays at the 377 m.w.e. depth.

The charged-particle contamination simulation differs between above ground and below ground measurements. Above ground, charged particles were simulated using the CRY package [87] with all particles except neutrons. CRY simulates a host of particles, and given the expected rate at sea level calculates the equivalent measurement time. It should be noted that CRY only considers the cosmogenic flux initiated by galactic protons. While protons constitute most of the cosmic ray progenitors, they may not be responsible for the same percentage of the total cosmic ray flux: higher Z progenitors may produce more cosmic rays per progenitor.

Below ground, it is assumed that the only charged particles noise of concern is due to the muon flux. Muons were sampled from the distribution described by Reyna [113][1] and propagated to the appropriate depth using the site specific overburden map at 377 m.w.e. and 540 m.w.e and the Geant4 Monte Carlo model. At the 1450 m.w.e. depth the Reyna distribution was also used, but it was assumed that the overburden could be approximated as a flat earth overburden. Muons which did not have positive energy at the appropriate depth were culled from the simulation. The detector position-dependent energy response of Sec. 4.4 and the neutron triggering algorithm of Sec 3.3 were applied to the simulated data. In addition, the time offset between WFDs of the neutron detectors and vetoes was considered. The total time simulated was calculated by:

$$Time = \frac{N}{A\ N/M\ \int Reyna(E,\Omega)\ dEd\Omega}, \tag{B.2}$$

[1]This distribution has units of $\#/\mathrm{cm}^2/\mathrm{sec}/\mathrm{GeV}/\mathrm{sr}$

where A is the area near the detector over which muons where propagated, N is total number of muons that survived to the appropriate depth, M is the total number of muons simulated, and $\int Reyna(E,\Omega)\ dEd\Omega$ is the energy and solid angle integration of the distribution described by Reyna. For each depth, muons were simulated until a statistically sufficient number of neutron like events were recorded, or until the total simulation time exceeded the measurement time.

Both above and below ground, the noise simulations were run with the partial geometry model which only included the detector and the veto system: the surrounding environment was not modeled. In all measurement scenarios, the cosmogenic charged is predicted to have a negligible influence on the measured data. Therefore, the noise is assumed to be due to the ambient gamma-ray flux. Subtracting the noise from the measured data is not straightforward. The difference between two Poisson distributions is not a Poisson distribution; it is a Skellam distribution which is not bounded to positive real values. Additionaly, the Skellam distribution is significantly different than the assumed Poisson distribution. In order to maintain Poisson statistics and use the current MCMC reconstruction, the noise subtraction was performed inside the boot-strapping procedure. In practice this is done by bootstrapping both the forward projected vector $\mathbf{A}\vec{f}$ and $\vec{b}$ and adding the components (Sec. 3.5 Step 3(b)). While 2000 boostrap samples was proscribed by Efron and Tibshirani [58] for calculating confidence intervals, no guidance is provided given the additional bootstrap of the noise subtraction. Regardless, the confidence intervals as a function of the percent of the reconstructed value exhibits minimal change between the background subtracted and non-background subtracted reconstructions. The mean value however does change. It is therefore assumed that 2000 bootstrap samples is sufficient.

Appendix C

Determination of Depth Below Ground

With the correctly chosen physics models, the MARS Monte Carlo model was used to predict the equivalent flat overburden profile of each of the MARS below ground measurements. The overburden profile at KURF fluctuates: KURF sits below a crevice in a mountain. The two shallow measurements were performed at locations that traditionally have not been used for scientific work. The deep measurement was performed at a location with a dedicated science facility where the overburden has been previously measured. Virginia Tech researchers [114] have previously performed measurements of the muon angular flux at the 377 and 1450 m.w.e. depths. However the 540 m.w.e. depth has not been measured.

In order to better estimate the overburden at the two shallow locations, a surveying company was contracted. Overburden profiles were constructed using the topological grid from the United States Geological Survey (USGS) and voids were measured and subtracted. Measurements were made at azimuthal angles of 0 and 180, 45 and 225, 90 and 270, and 135 and 315 degrees. Elevation angles, at each of these azimuthal angles, were performed in 5 degree increments from 0 to 70 degrees.

Using the distance to the surface as a function of the azimuthal and elevation angle, an overburden profile was constructed. This data was used to make a triangular mesh using ROOT's Delaunay triangle package [64]. The overburden profile mesh for the 377 m.w.e. depth is shown in Fig. C.1. The overburden profile mesh for the 540 m.w.e. depth is shown in Fig. C.2.

Using the above ground muon distribution described by Reyna [113], the muon energy and angular distribution were sampled. This angular information was used with the triangular meshes and the Möller-Trumbore algorithm [115] to find the intersection of the incident muon and the respective triangle. The distance from the triangle intersection and the MARS detector was calculated. The energy loss due to the traveled rock distance was subtracted from the sampled energy assuming a dE/dx of 2.17 MeV g/cm^2. The rock at KURF was previously measured to have a density of 2.69 g/cm^3 [67]. In this fashion the energy and angle dependent muon flux could be calculated at the two shallow depths.

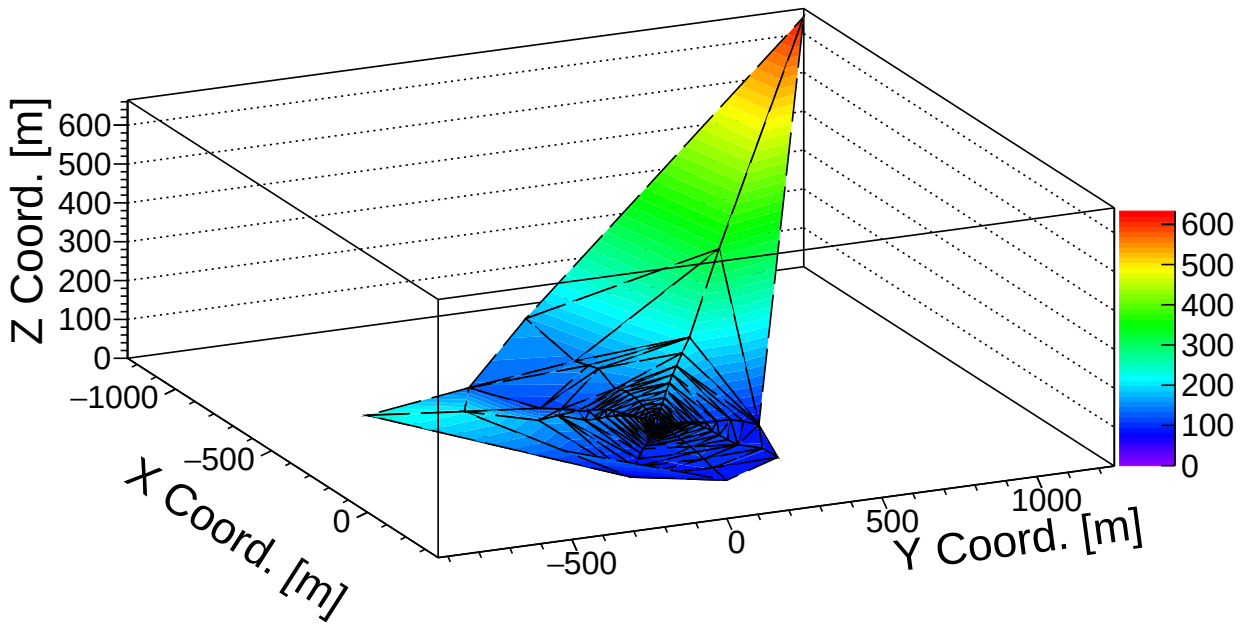

Figure C.1: A depiction of the measured 377 m.w.e. overburden profile. MARS is located at the (0,0,0) position directly below ∼150 m of rock. All dimensions are in meters, not m.w.e.

Muons with positive energy after traversing the rock overburden were simulated with the MARS Monte Carlo model to obtain the MARS simulated muon response. Using this technique, equivalent flat overburden profiles were also simulated. The muon flux rate between the surveyed and flat overburden scenarios were matched by changing the MARS depth for the flat overburden scenario. Using this method the Monte Carlo model predicts a depth of 365 m.w.e.±20 m.w.e. at the same location measured by the VT researchers to be at a depth of 377 m.w.e. with ±5% uncertainty [114]. With this verification at the 377 m.w.e. depth, the equivalent flat overburden depth at the second deepest measurement was estimated to be 540 m.w.e±40 m.w.e. The Monte Carlo simulations for both depths were ran until statistical uncertainty was negligible. The deep depth overburden is quoted based upon the previously measured KURF value.

Uncertainty was estimated by varying the overburden at elevation angles >70 degrees. The quoted depth is calculated by not considering muons with elevation angle >70 degrees. The lower bound of the depth estimate was made by assuming the elevation of Earth's surface is the same as the least measured point at 70 degrees. It was assumed that the uncertainty is symmetric.

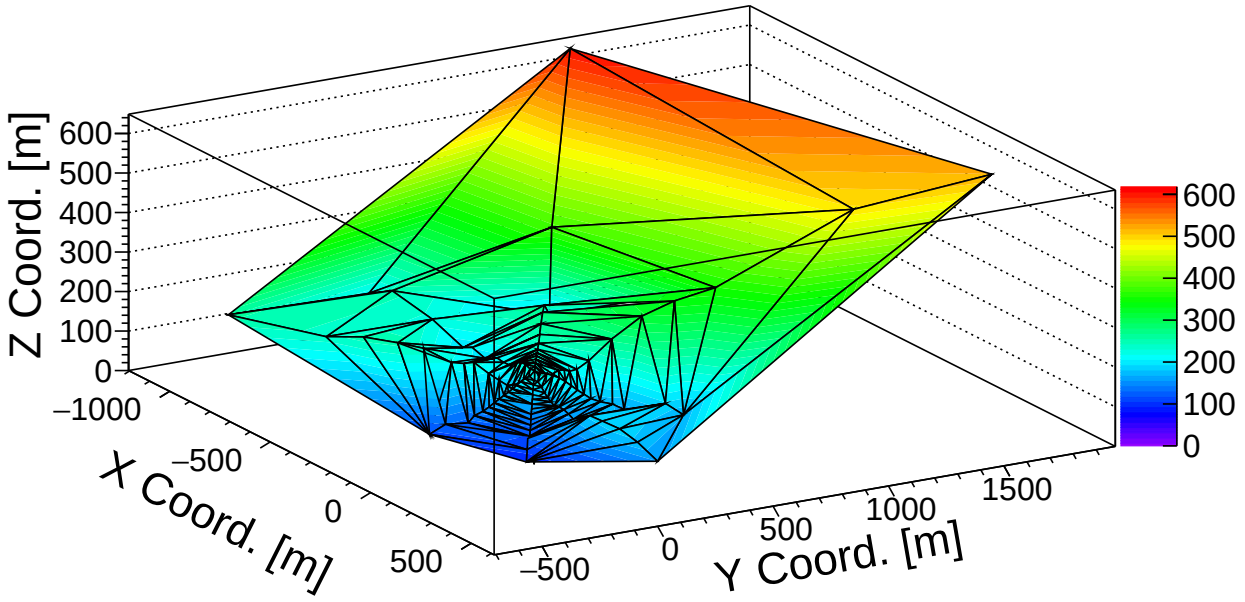

Figure C.2: A depiction of the measured 540 m.w.e. overburden profile. MARS is located at the (0,0,0) position directly above ∼250 m of rock. All dimensions are in meters, not m.w.e.

Appendix D

PMT Gain Drift

The measured gain drift of all PMTs is shown below. The neutron detector PMTs have corresponding serial numbers. The veto PMTs did not have serial numbers, or more likely they were not recorded. Not that the variation in the neutron detector PMT drift is significantly higher than the drift of the veto PMTs. This lends weight to the argument that mechanical coupling is the primary culprit for gain drift in the neutron detector PMTs.

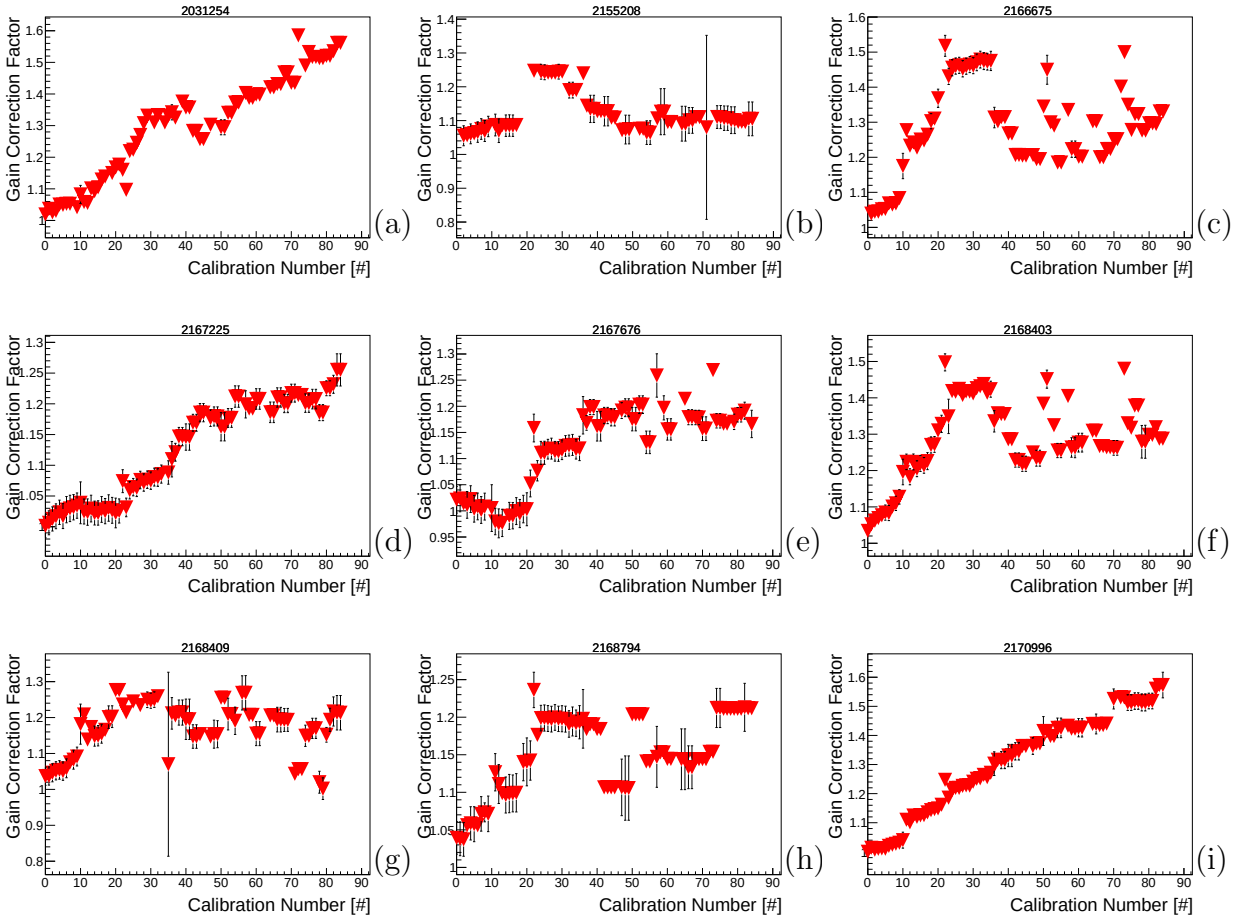

Figure D.1: The measured gain drift of neutron detector PMTs.

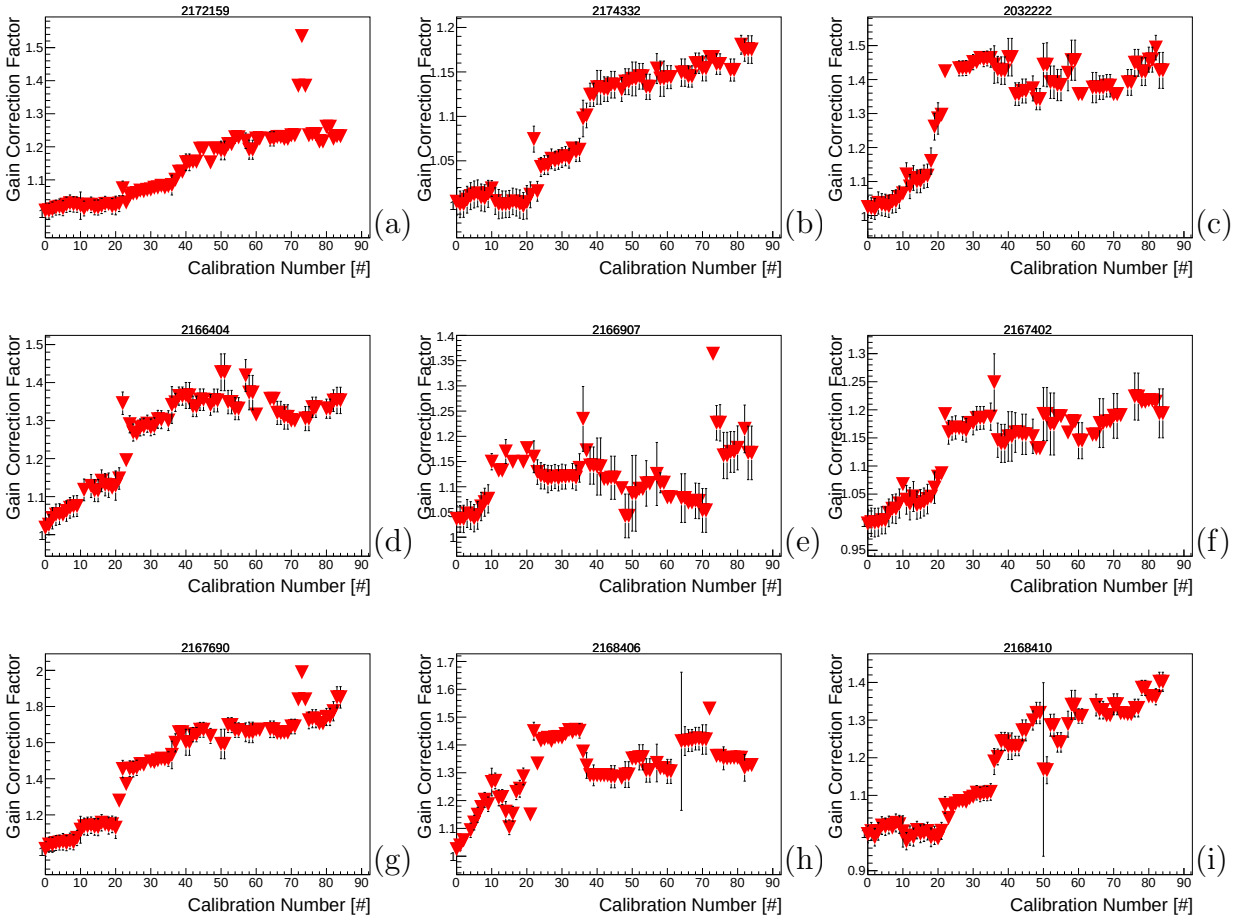

Figure D.2: The measured gain drift of neutron detector PMTs.

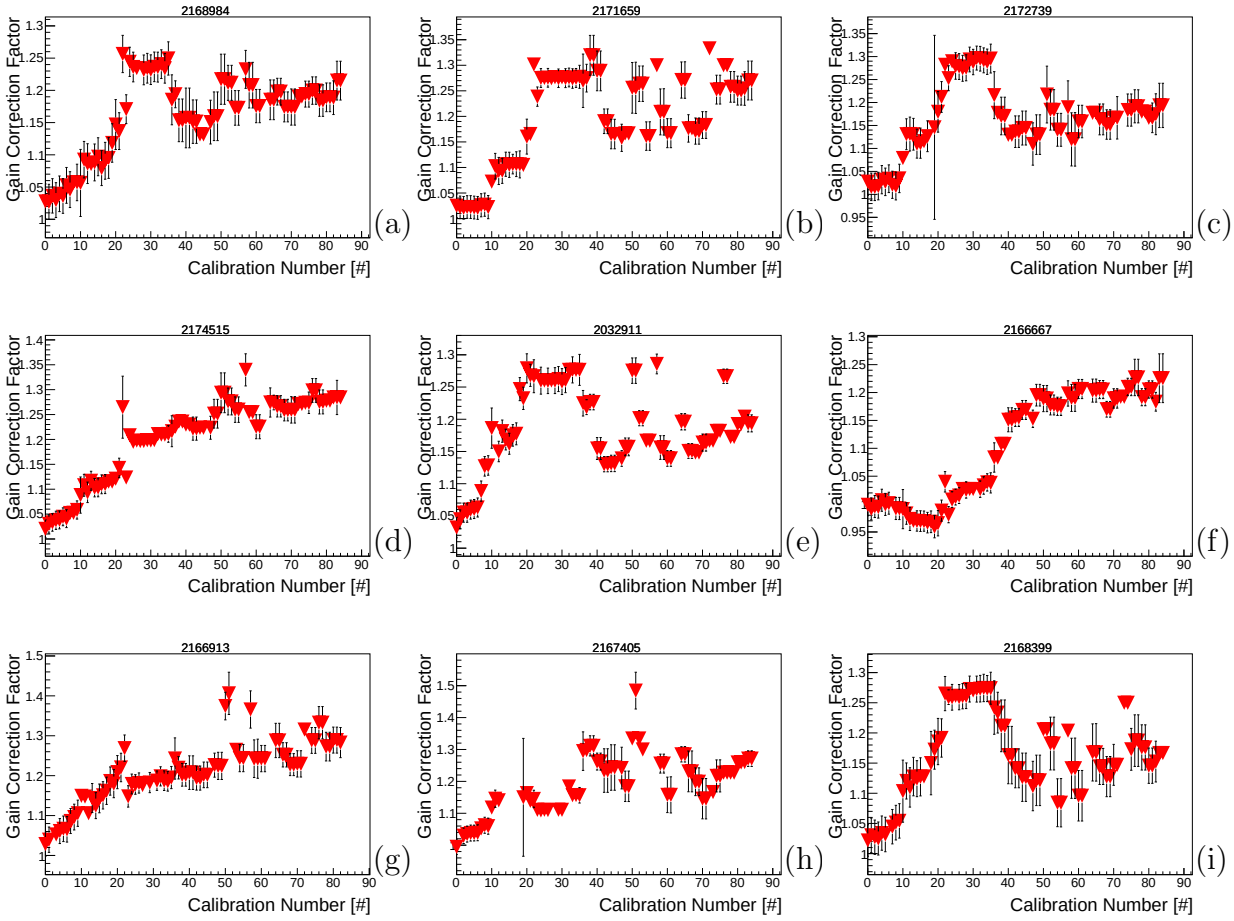

Figure D.3: The measured gain drift of neutron detector PMTs.

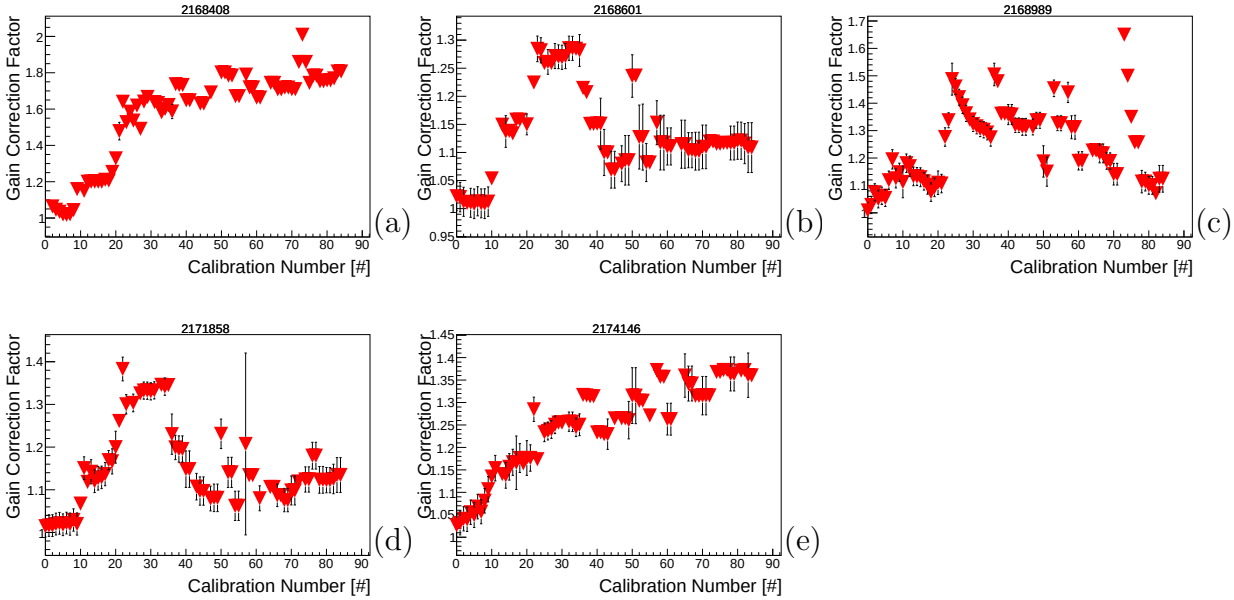

Figure D.4: The measured gain drift of neutron detector PMTs.

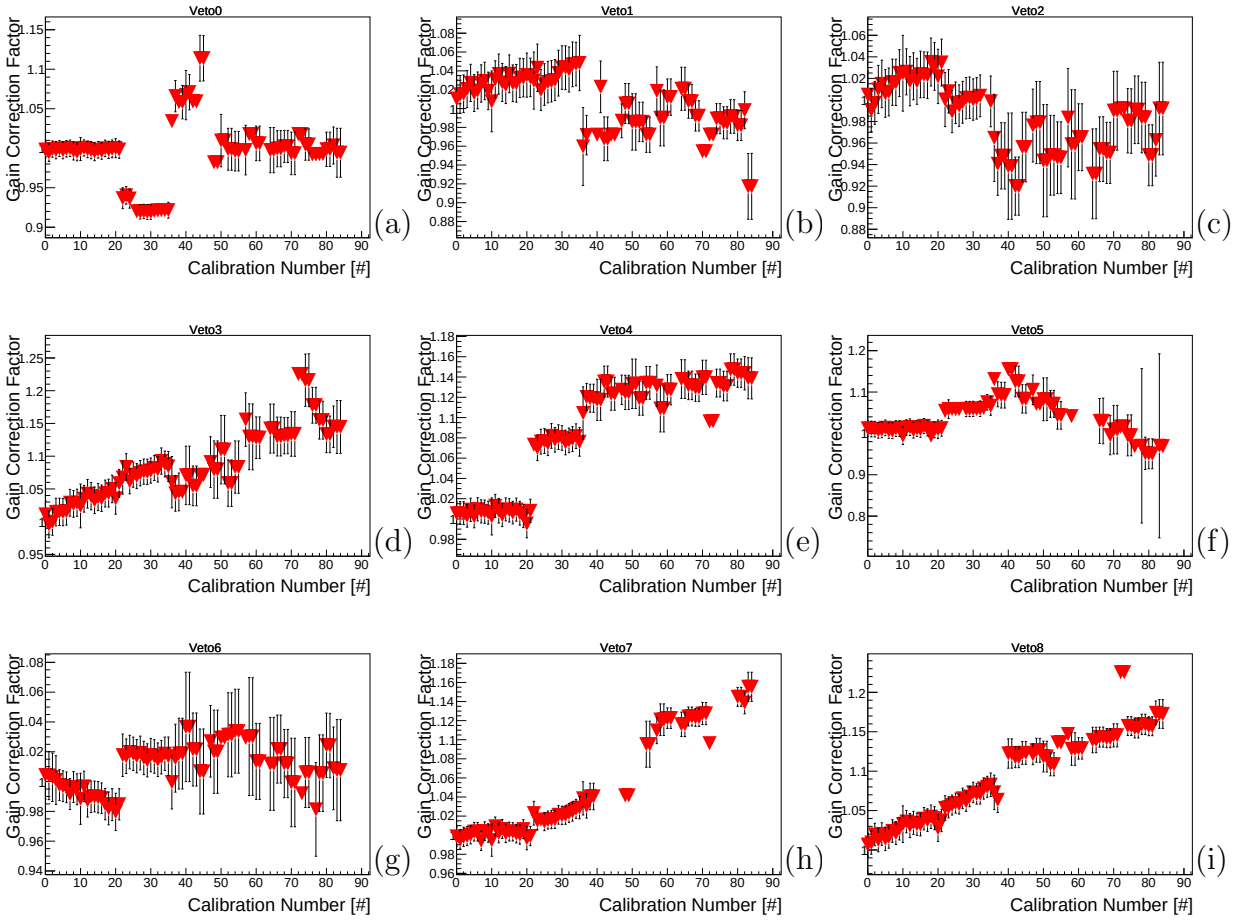

Figure D.5: The measured gain drift of veto PMTs

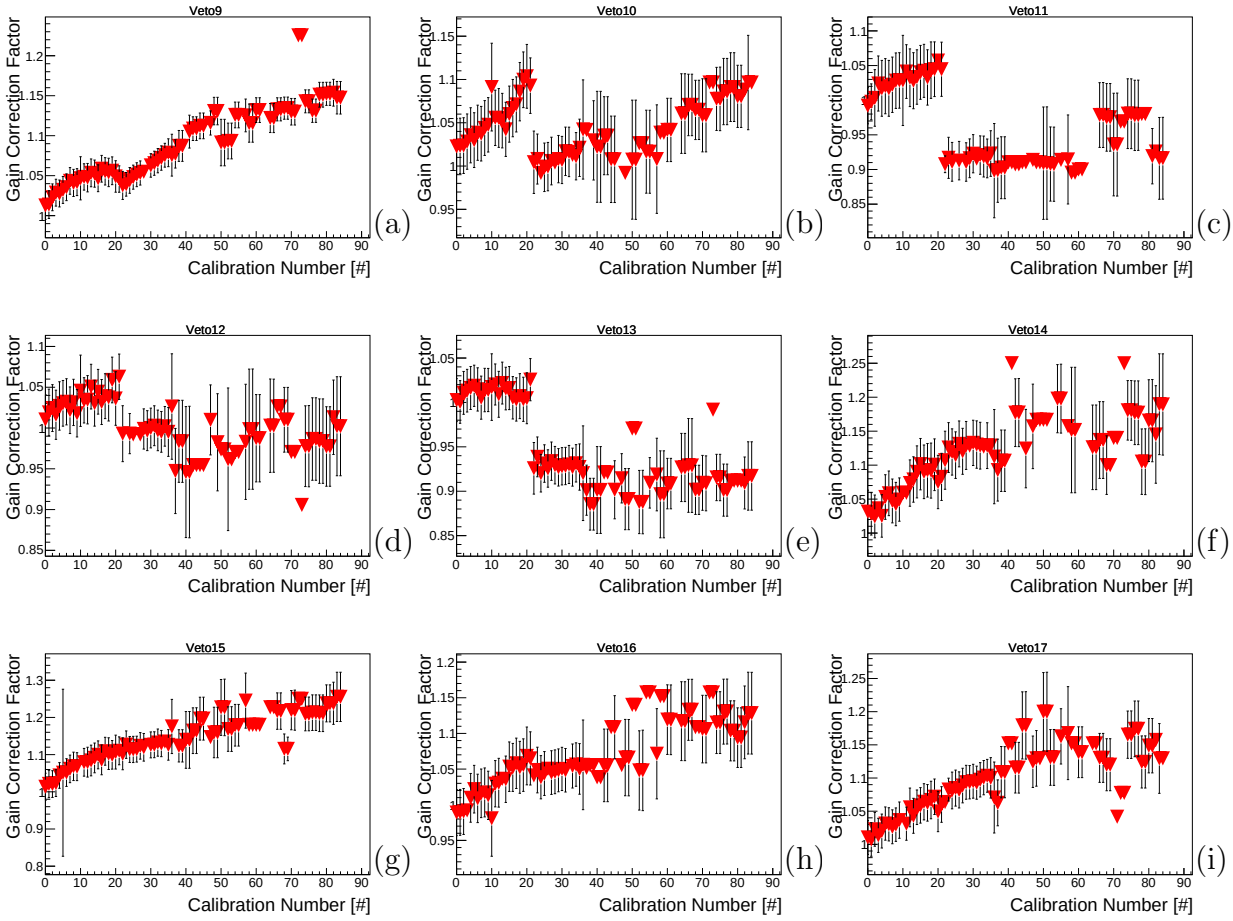

Figure D.6: The measured gain drift of veto PMTs

Appendix E

PMT Non-Linearity

PMT non-linearity was measured before the ADIT PMTs were installed into MARS. The PMT serial number is recorded at the top of each graph. The voltage varied between each PMT. The PMT response to a Cs-137 source and a liquid scintillator cell was used to roughly gain match all PMTs before testing the non-linearity.

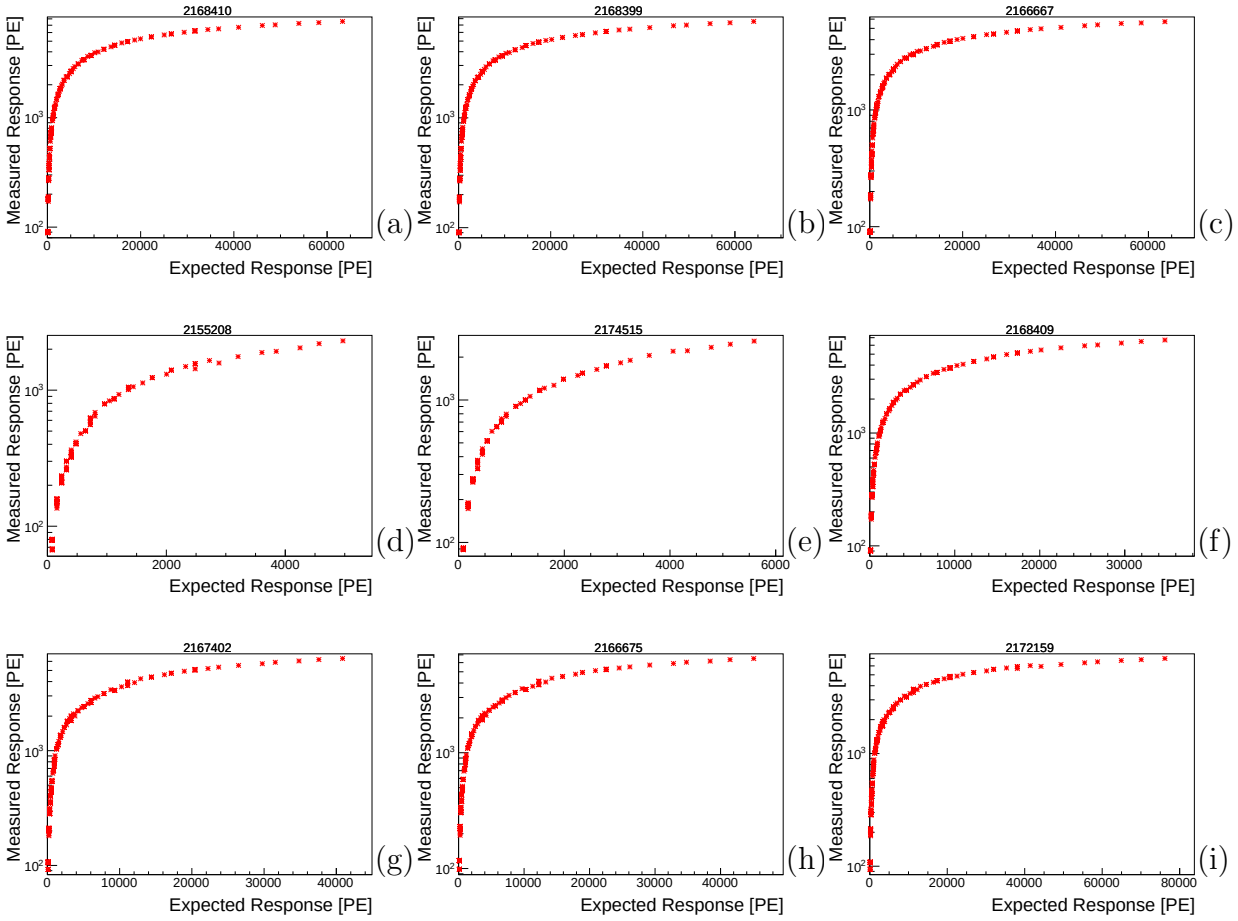

Figure E.1: The measured saturation of PMTs

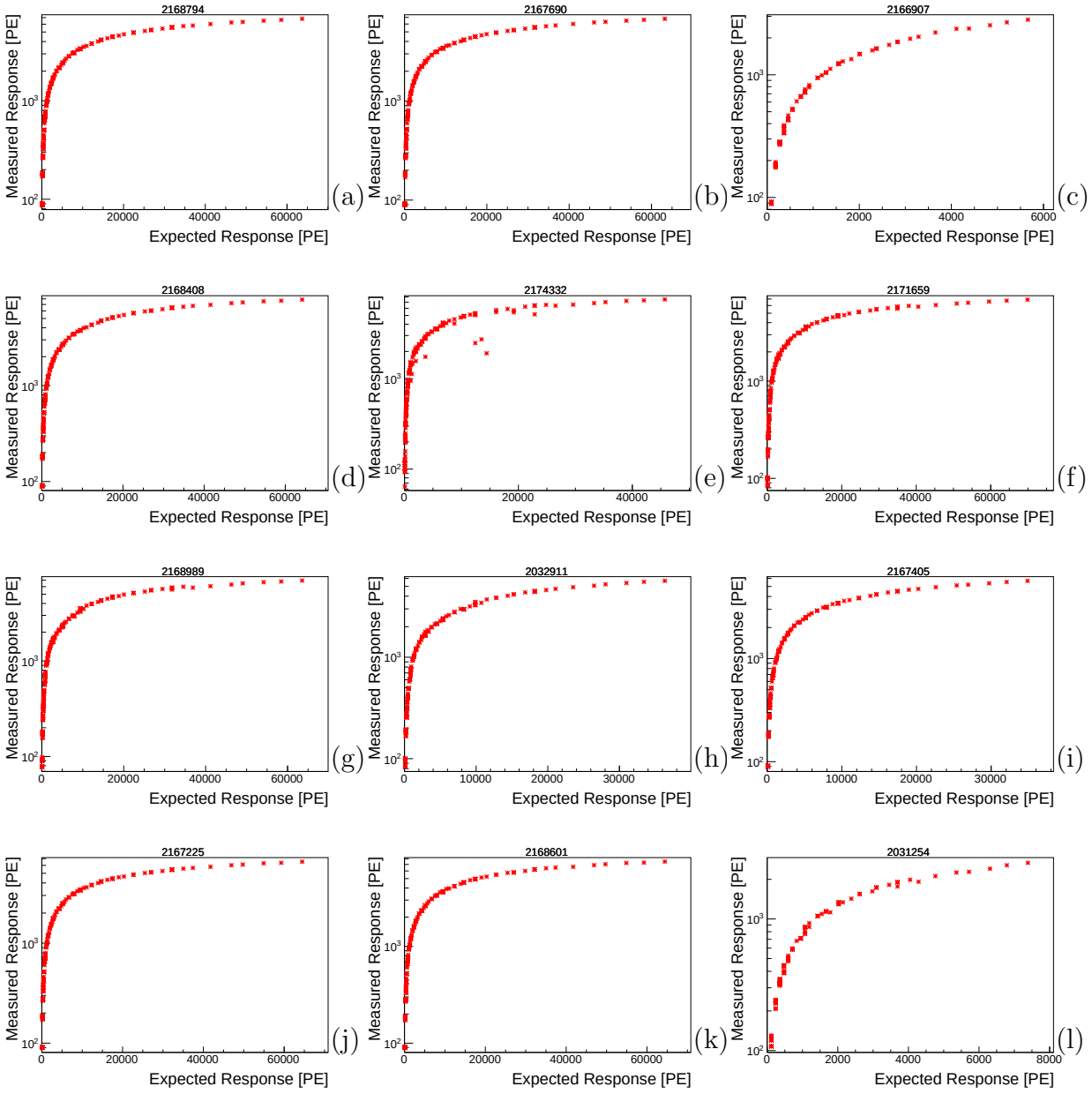

Figure E.2: The measured saturation of PMTs

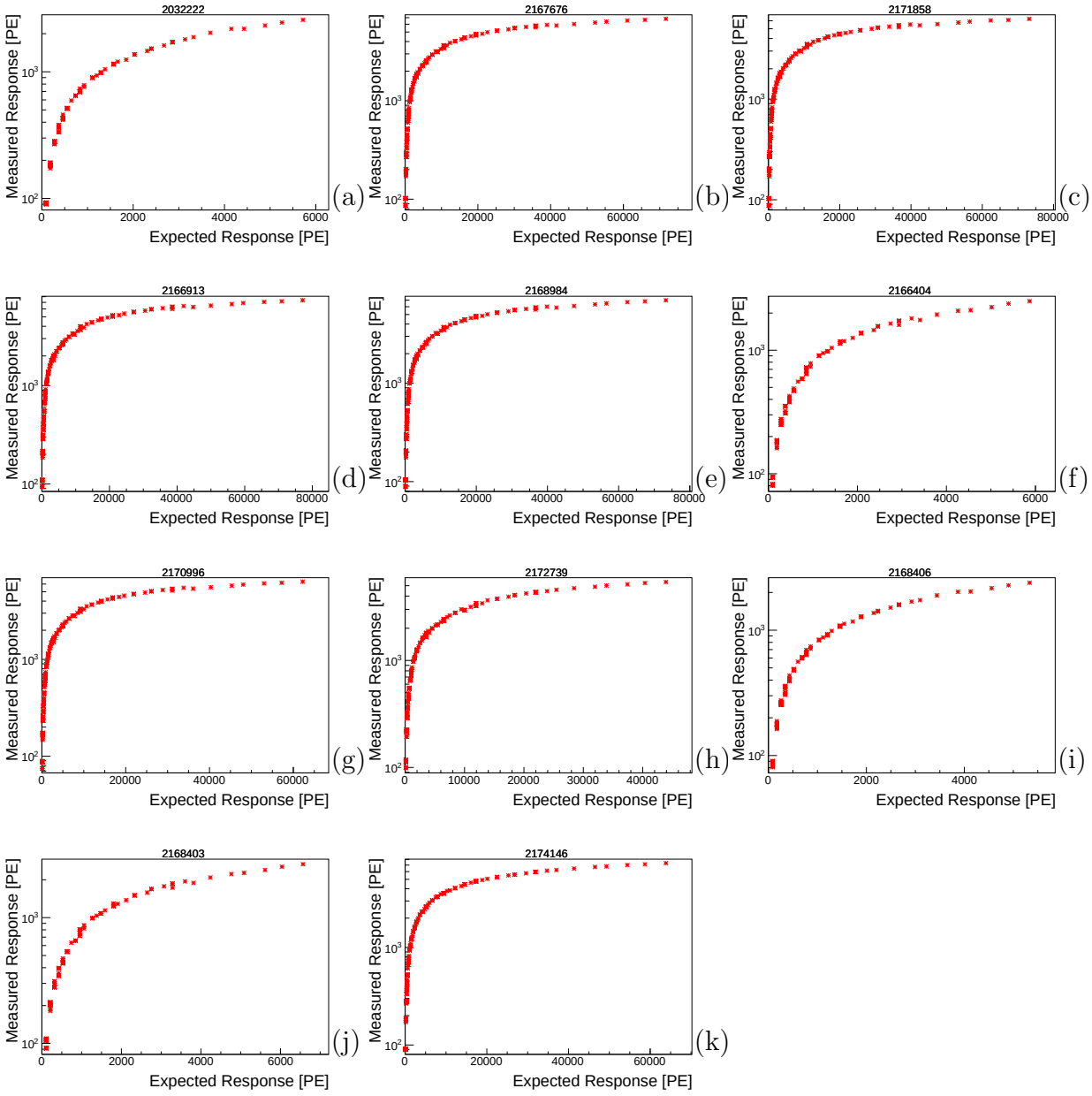

Figure E.3: The measured saturation of PMTs

Appendix F

Position-Dependent Energy Calibration

The position-dependent energy calibration for the top neutron detector is shown below. This calibration was done in a 5x5 grid as described in Sec. 4.4. The position of each measurement is recorded above the histogram. The origin is located in the center of the detector. The positive x-direction points from the driver side to the passenger side of the deployment platform. The positive y-direction points from the back of the deployment platform to the front of the deployment platform. Below the neutron detector calibrations the position dependent response for each veto detector is displayed. Veto detectors 0-6 are 2 PMT panels. Figure 4.3 is displayed again below with some of the veto detectors labeled. Veto detectors 7 and 8 are on the other side of the detector. Veto 7 is on the right side of the figure. Different measured positions have different colors or markers.

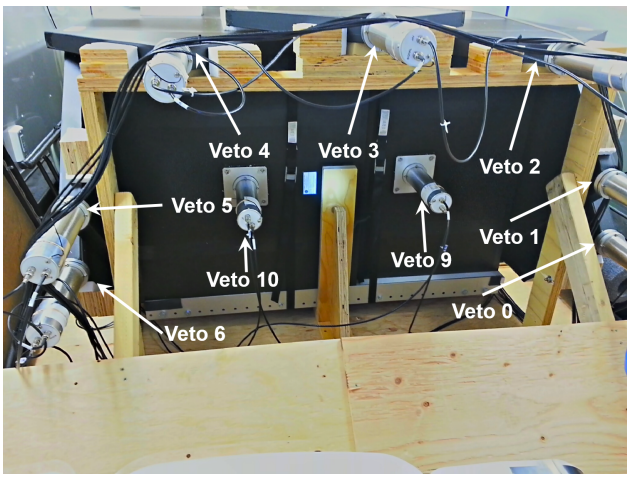

Figure F.1: A labeled view from one end of the assembled MARS veto.

F.1 Top Neutron Detector

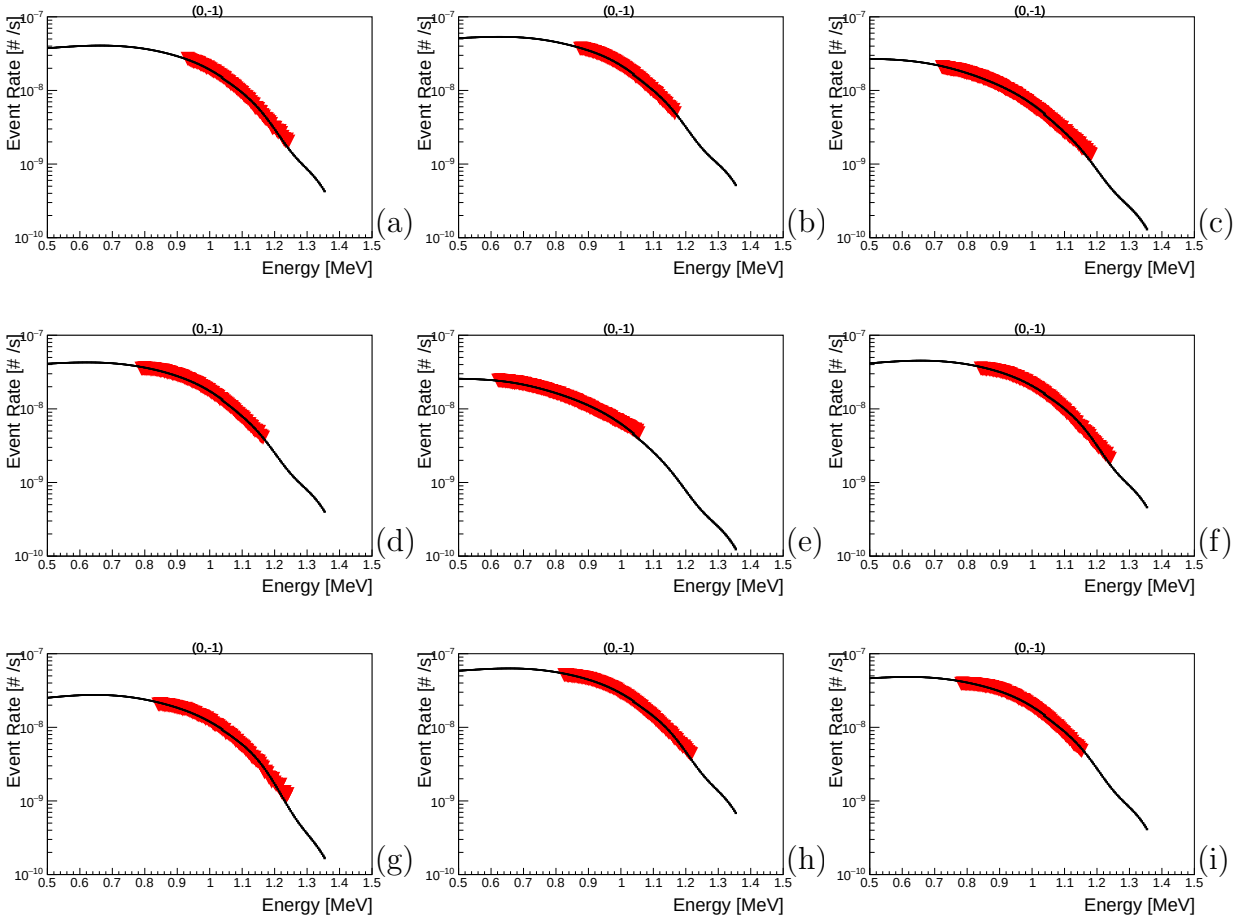

Figure F.2: The position-dependent energy calibration of the top neutron detector.

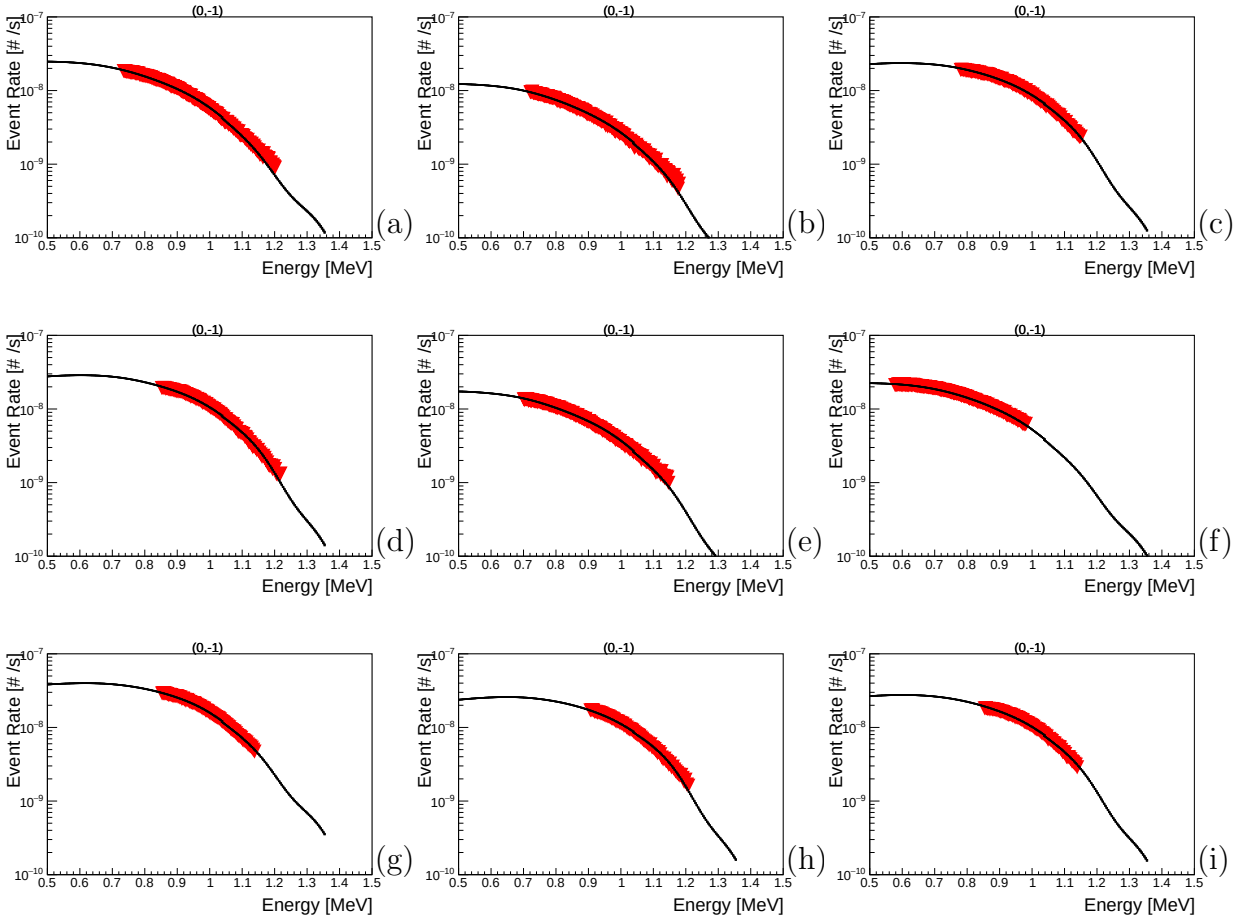

Figure F.3: The position-dependent energy calibration of the top neutron detector.

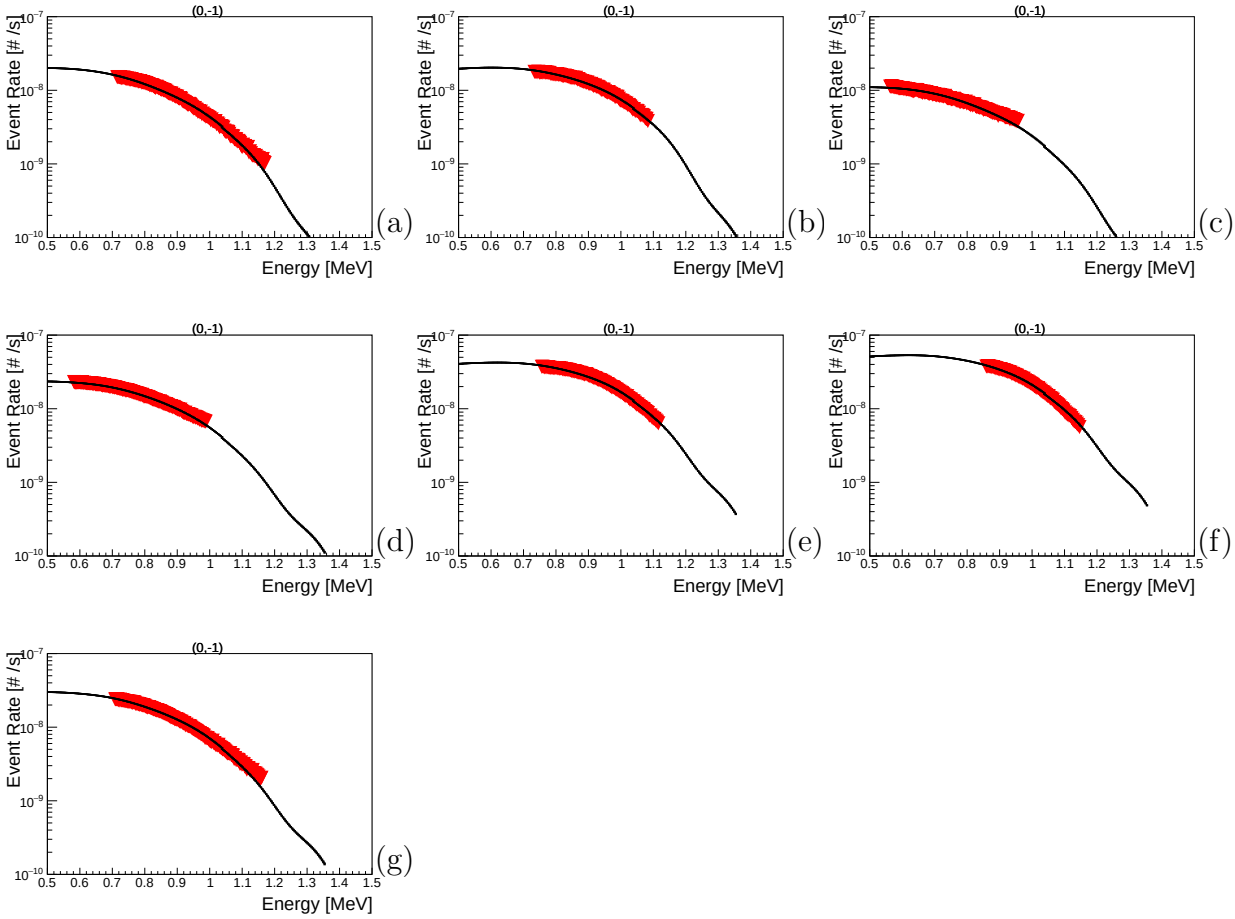

Figure F.4: The position-dependent energy calibration of the top neutron detector.

F.2 Veto Detectors

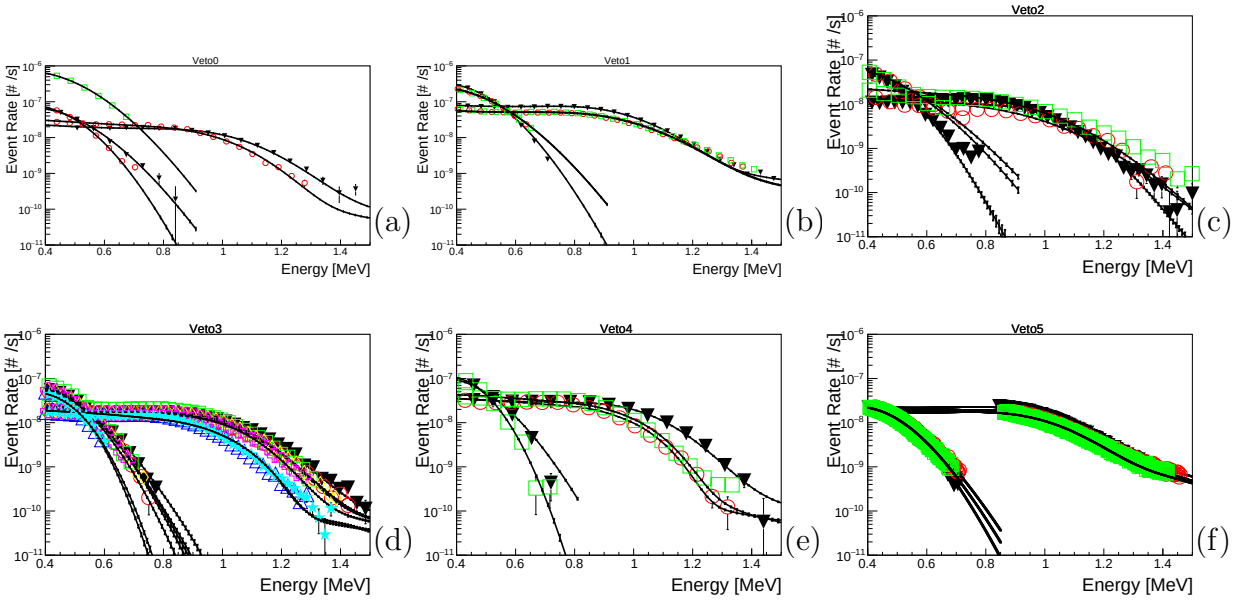

Figure F.5: The position-dependent energy calibration of veto detectors.

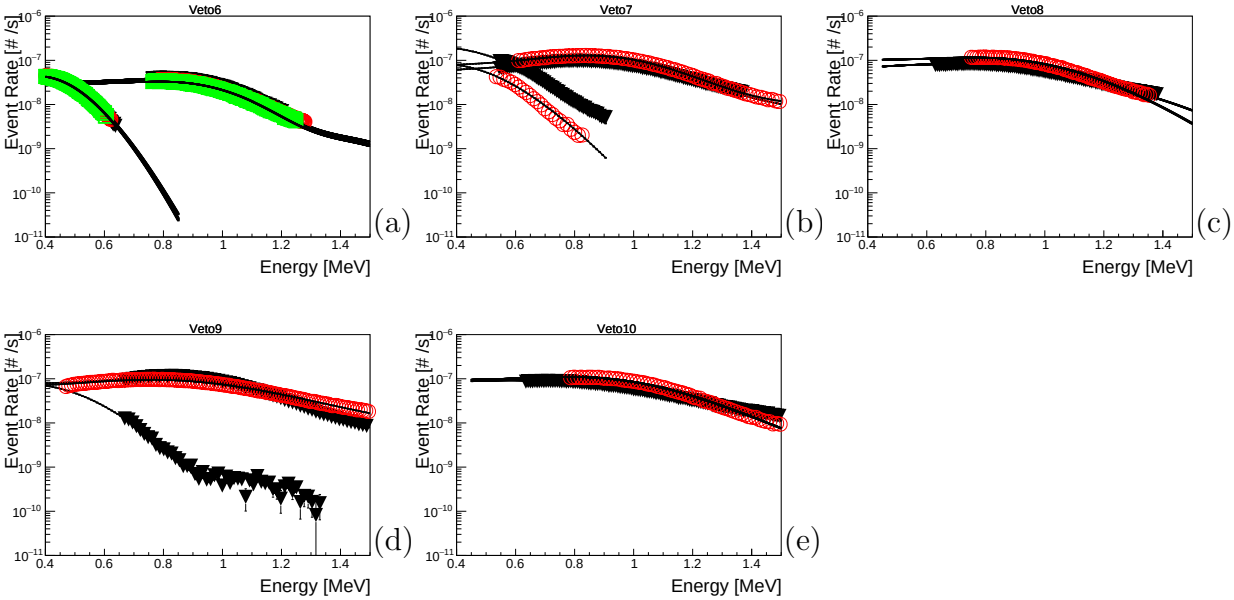

Figure F.6: The position-dependent energy calibration of veto detectors.

Appendix G

Convergence Criteria Above Ground

The following convergence criteria for the above ground measurement are shown assuming an incident neutron angular distribution of $\cos^3(\theta)$ using the full geometry model to populate the detector response matrix with the 25 μs initial time range expanding trigger.

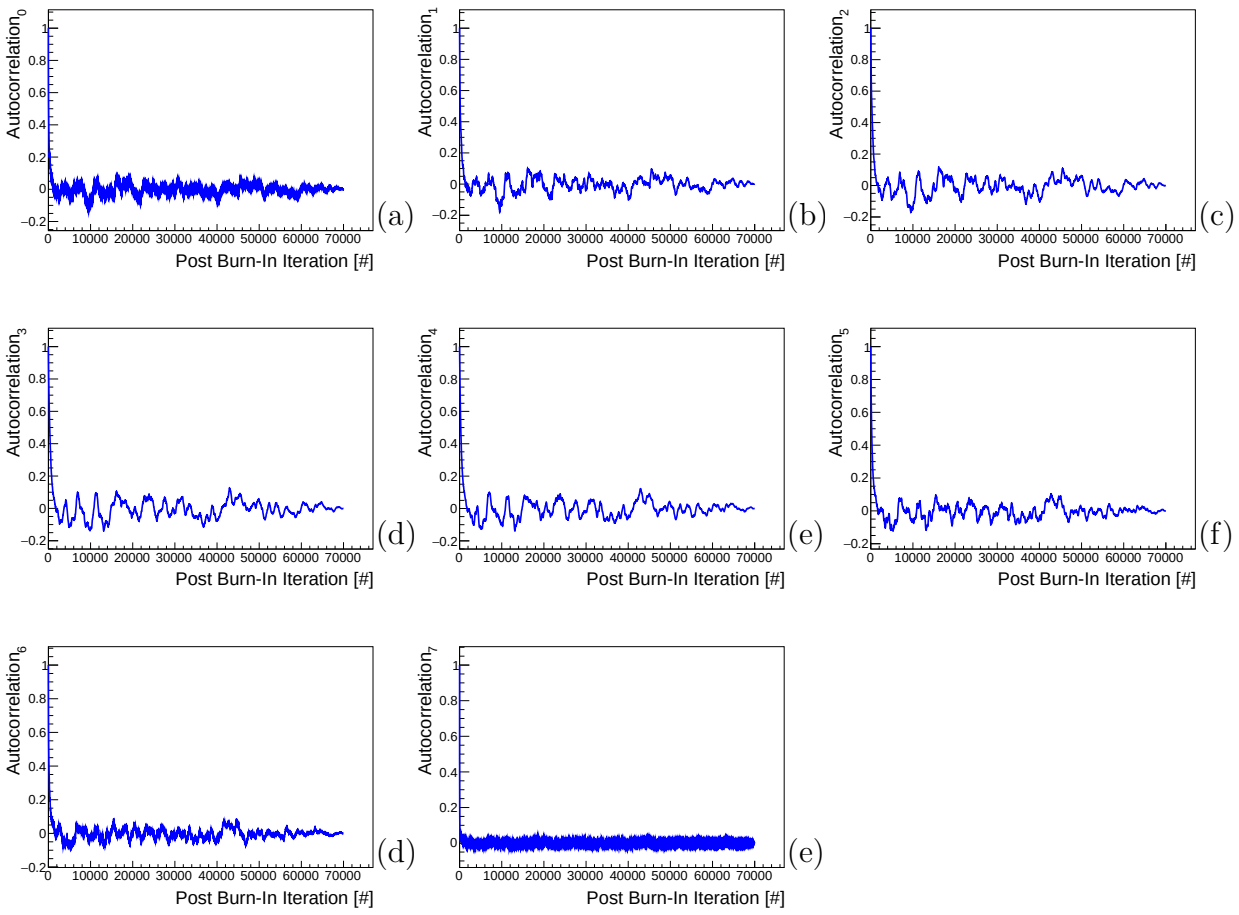

Figure G.1: The autocorrelation of each basis spline coefficient of the above ground measurement.

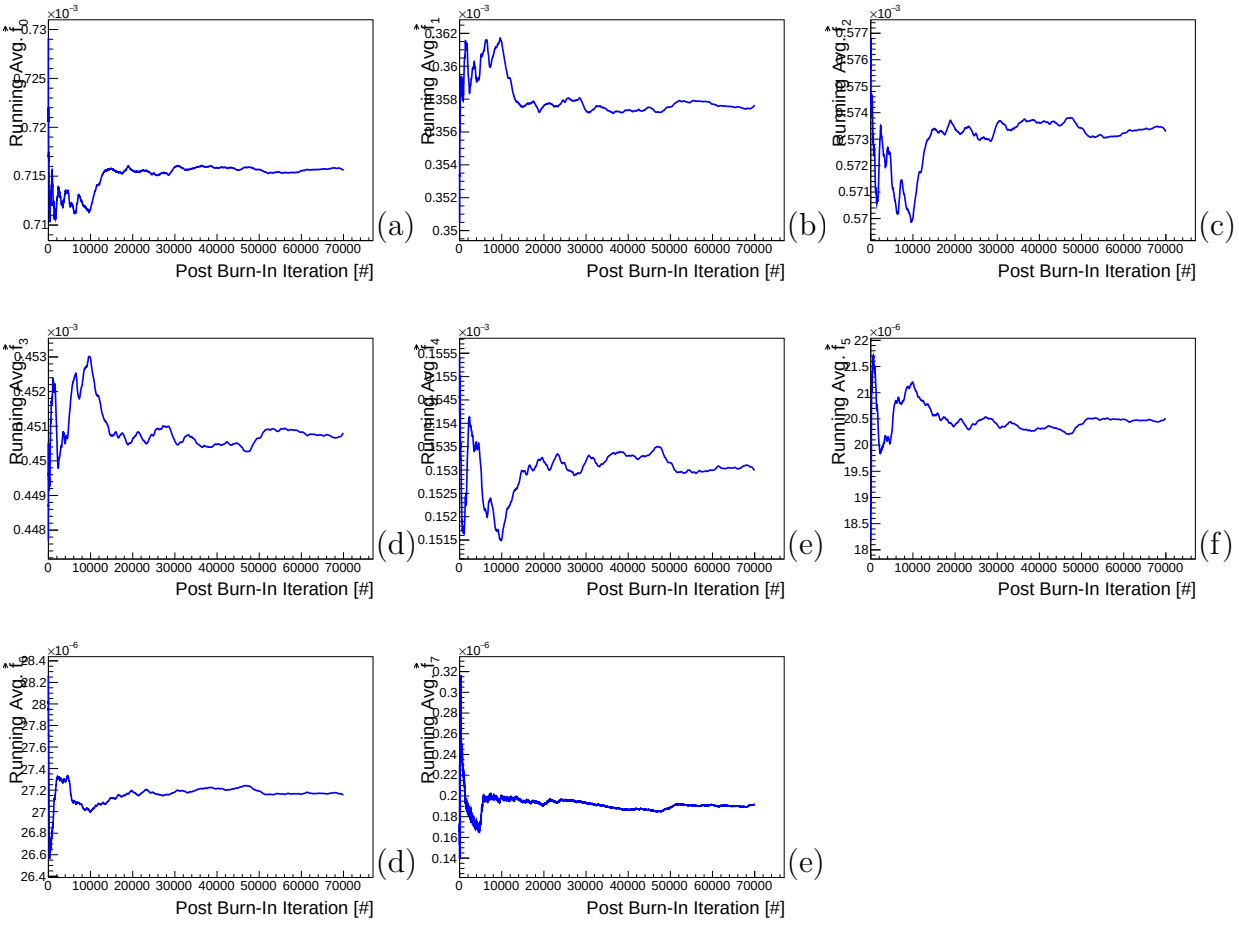

Figure G.2: The running mean of each basis spline coefficient of the above ground measurement.

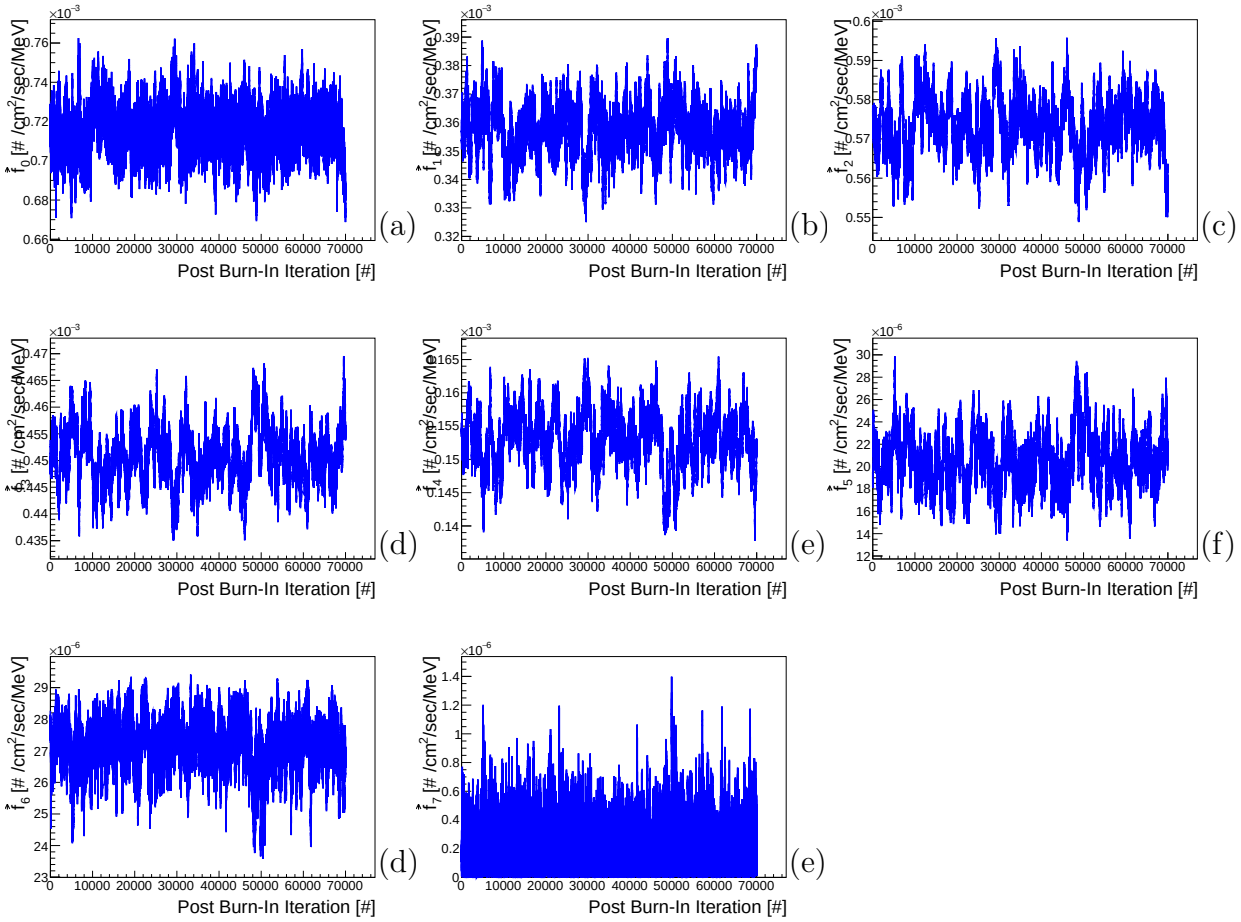

Figure G.3: The value of each basis spline coefficient as a function of the MCMC iteration post burn-in of the above ground measurement.

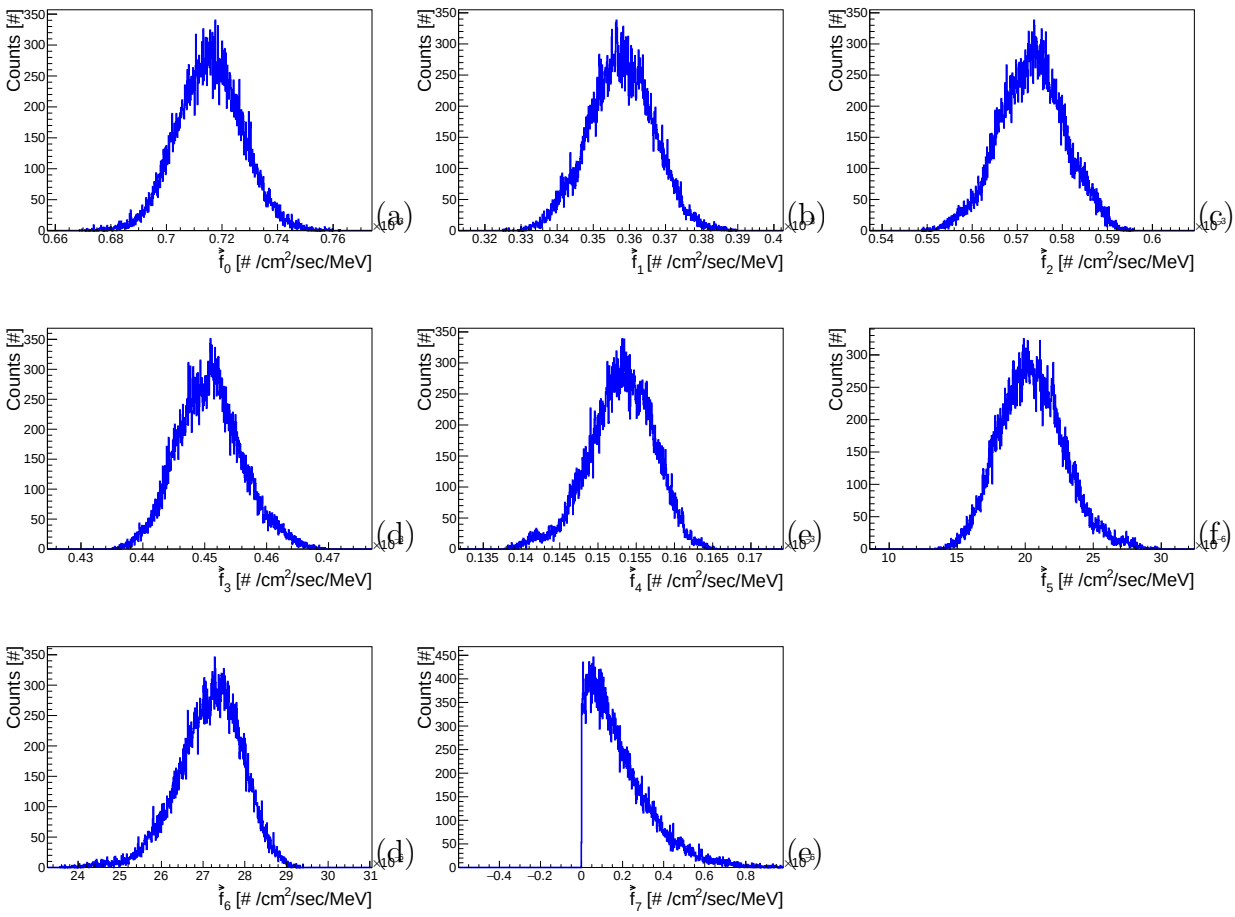

Figure G.4: The distribution of each basis spline coefficient of the above ground measurement.

Appendix H

Convergence Criteria Below Ground

The following convergence criteria for each of the below ground measurements are shown assuming an incident neutron angular distribution of $\cos^2(\theta)$ using the full geometry model to populate the detector response matrix with the 25 μs initial time range expanding trigger.

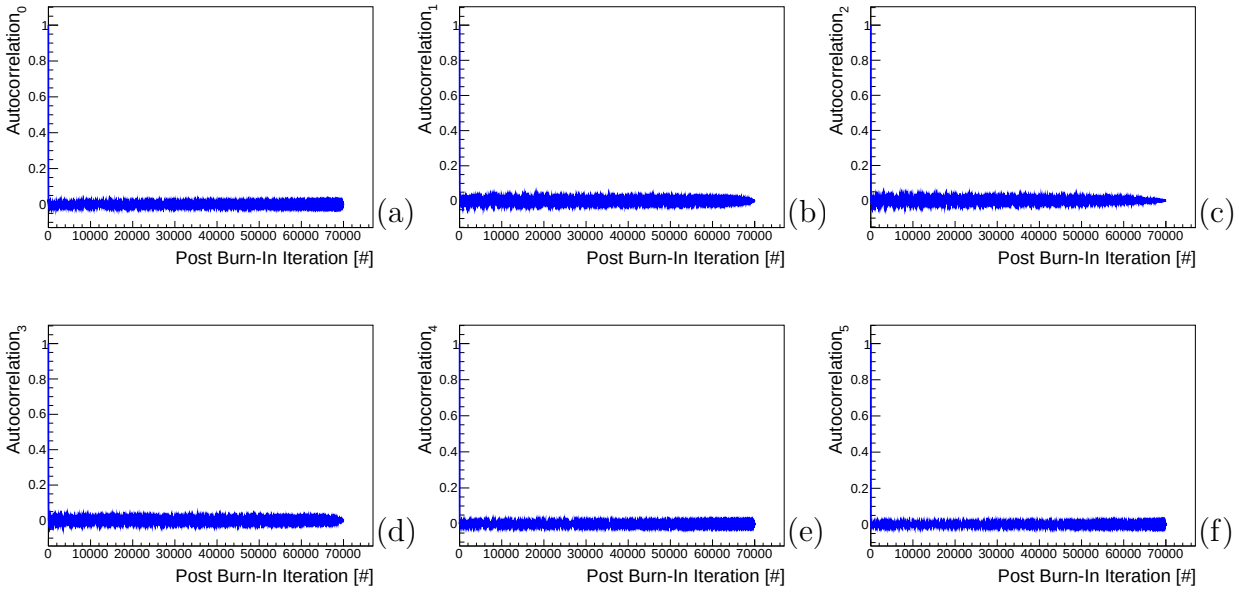

Figure H.1: The autocorrelation of each basis spline coefficient at the 377 m.w.e. depth.

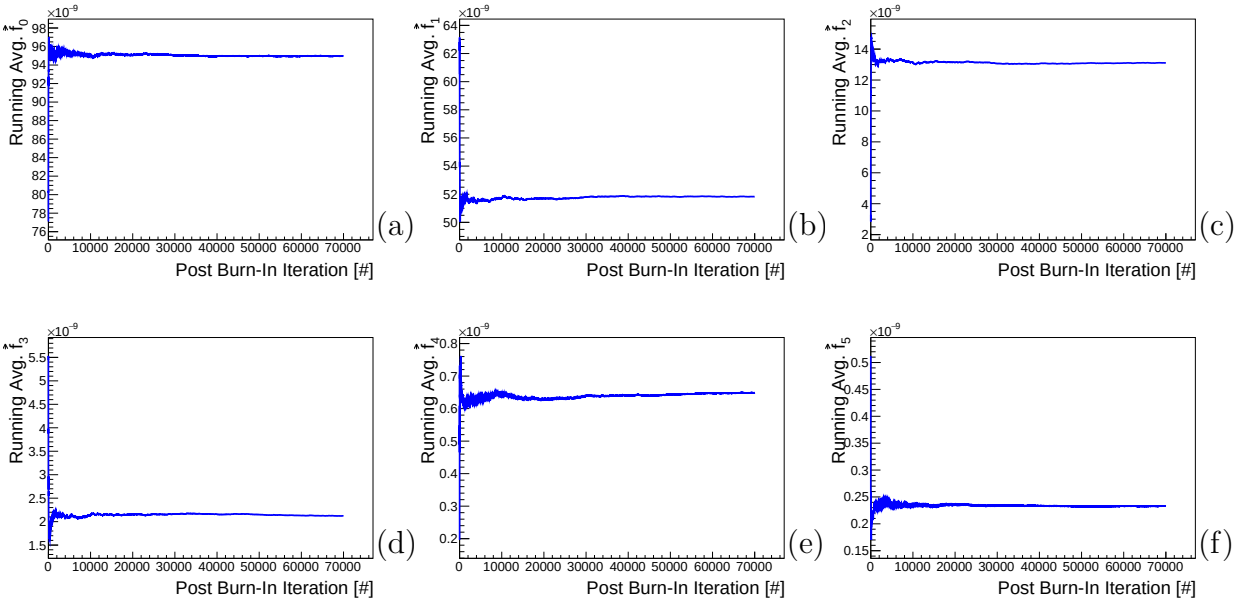

Figure H.2: The running mean of each basis spline coefficient at the 377 m.w.e. depth.

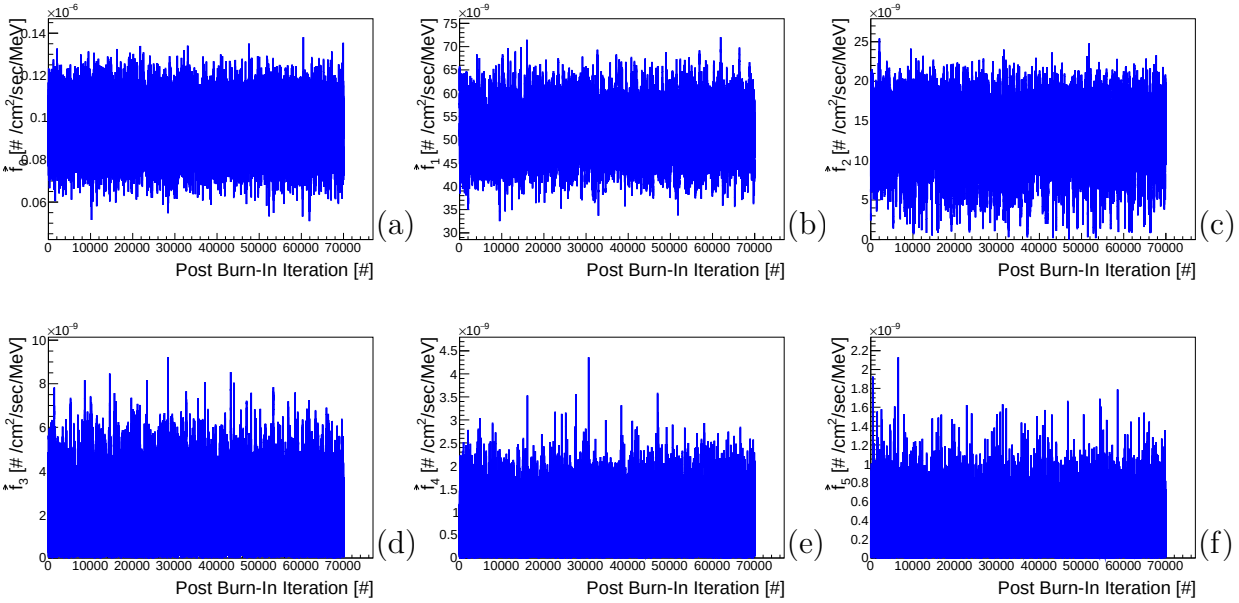

Figure H.3: The value of each basis spline coefficient as a function of the MCMC iteration post burn-in at the 377 m.w.e. depth.

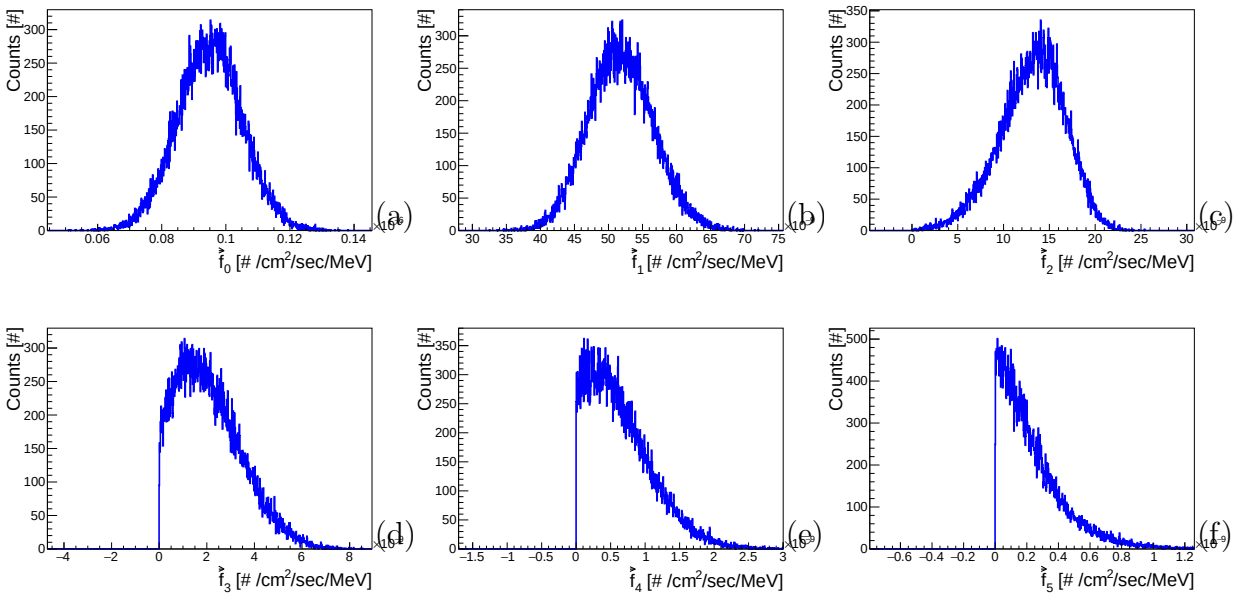

Figure H.4: The distribution of each basis spline coefficient at the 377 m.w.e. depth.

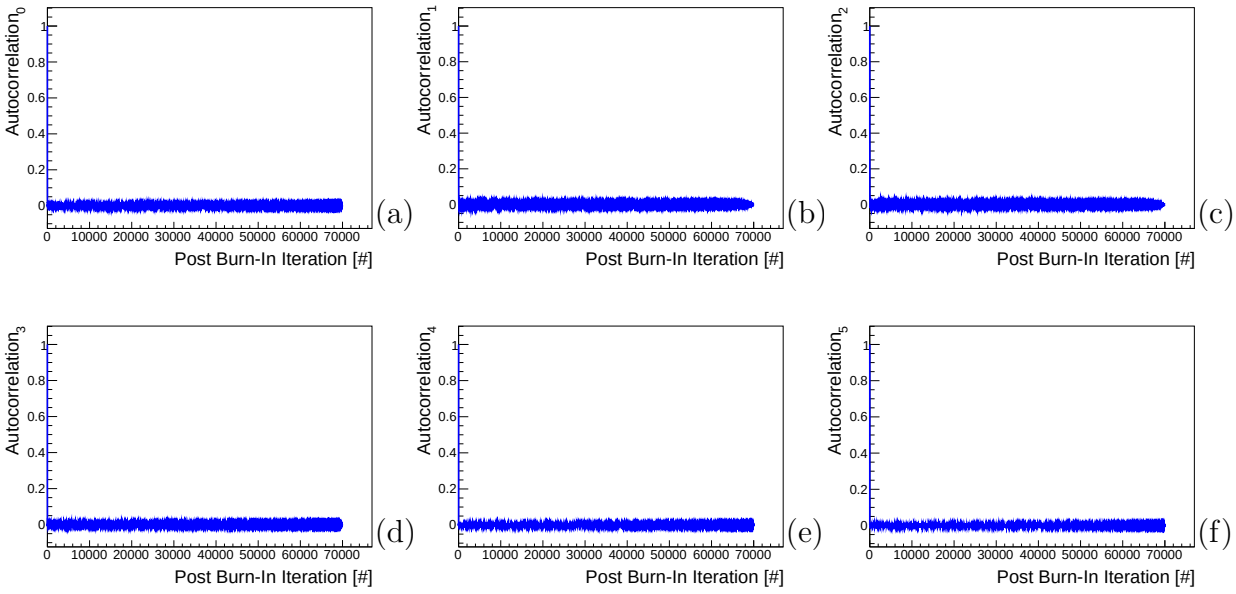

Figure H.5: The autocorrelation of each basis spline coefficient at the 540 m.w.e. depth.

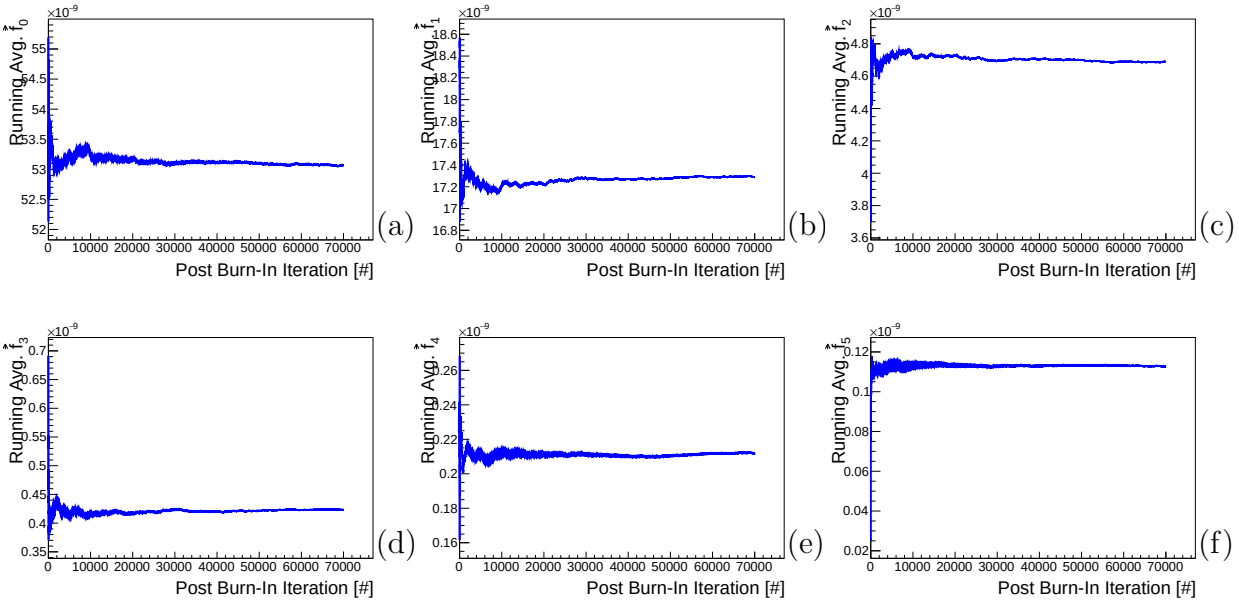

Figure H.6: The running mean of each basis spline coefficient at the 540 m.w.e. depth.

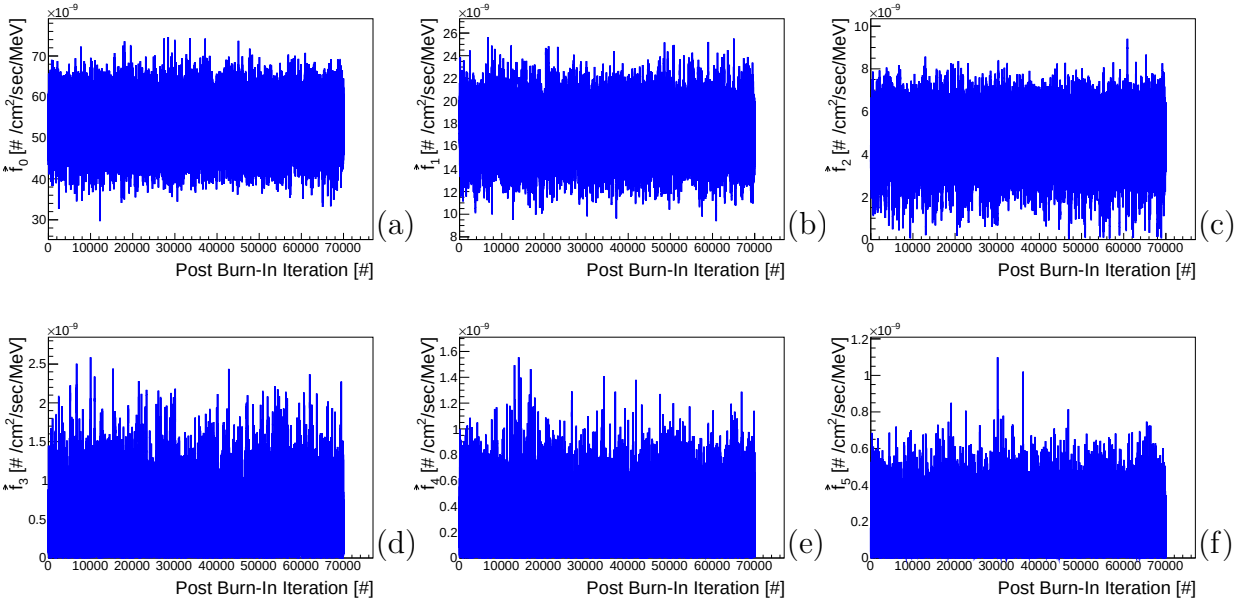

Figure H.7: The value of each basis spline coefficient as a function of the MCMC iteration post burn-in at the 540 m.w.e. depth.

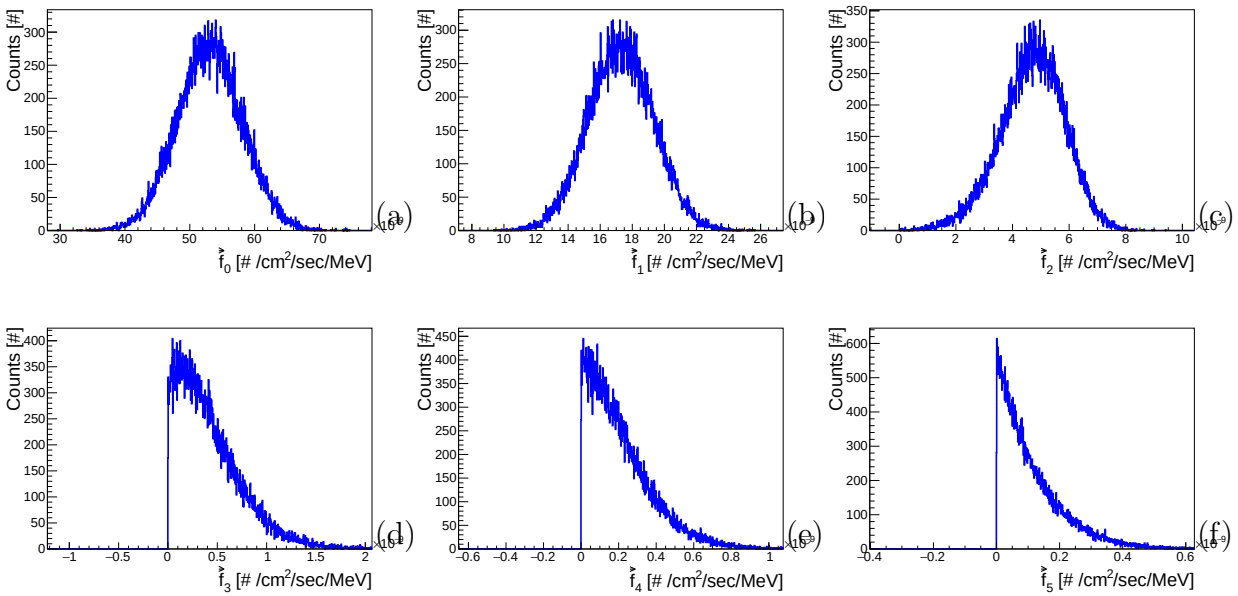

Figure H.8: The distribution of each basis spline coefficient at the 540 m.w.e. depth.

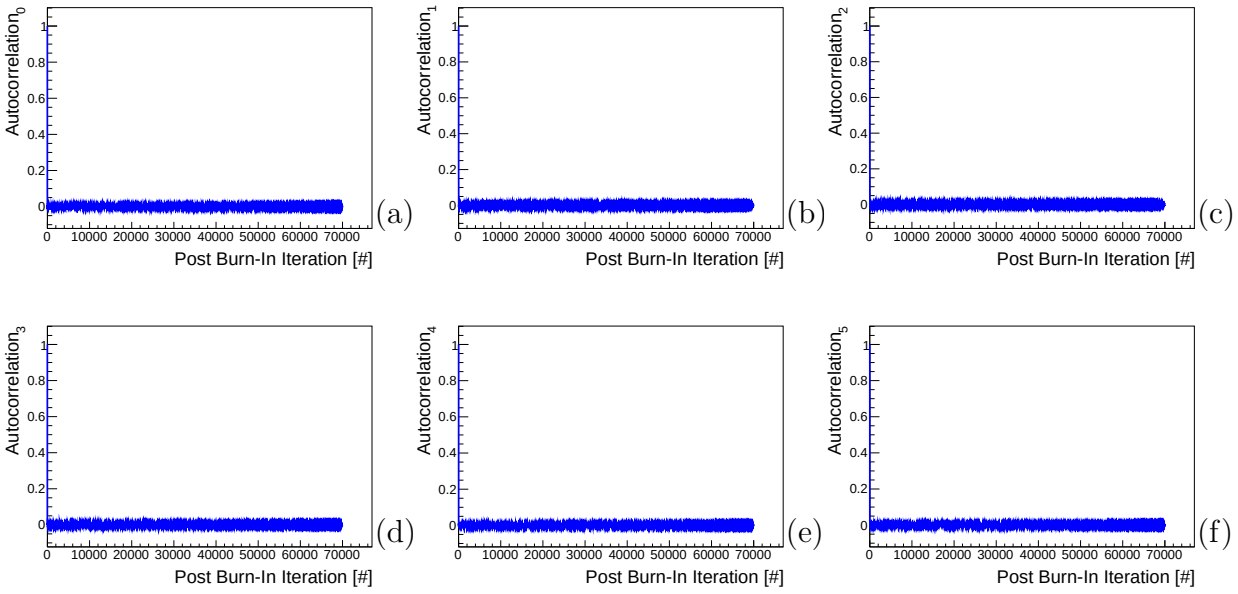

Figure H.9: The autocorrelation of each basis spline coefficient at the 1450 m.w.e. depth.

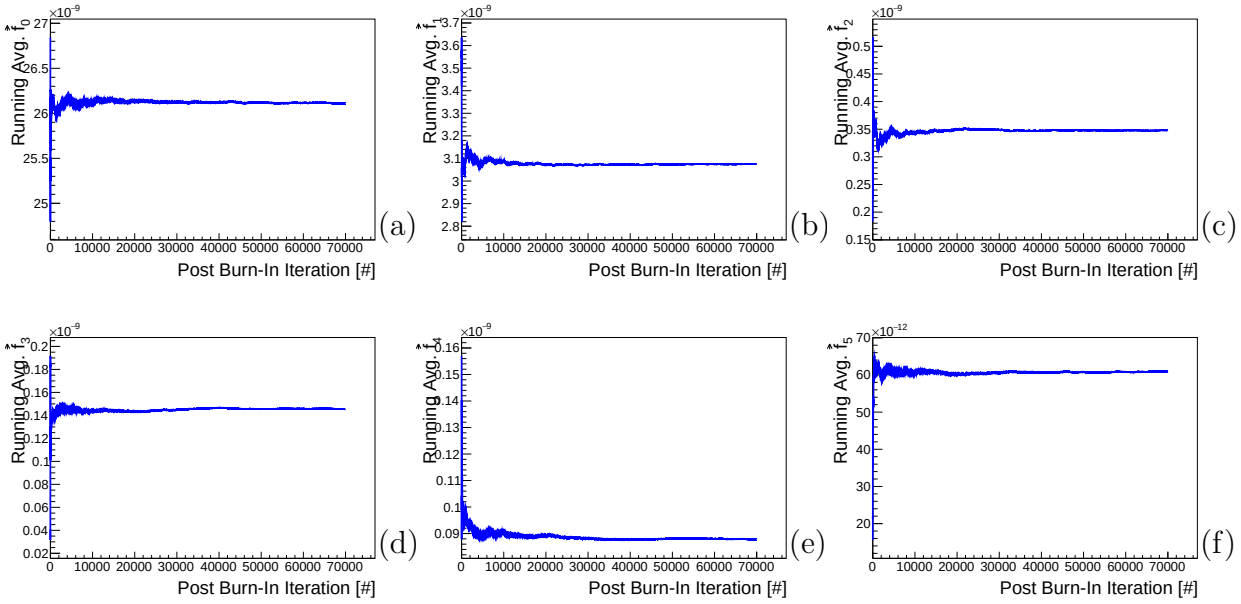

Figure H.10: The running mean of each basis spline coefficient at the 1450 m.w.e. depth.

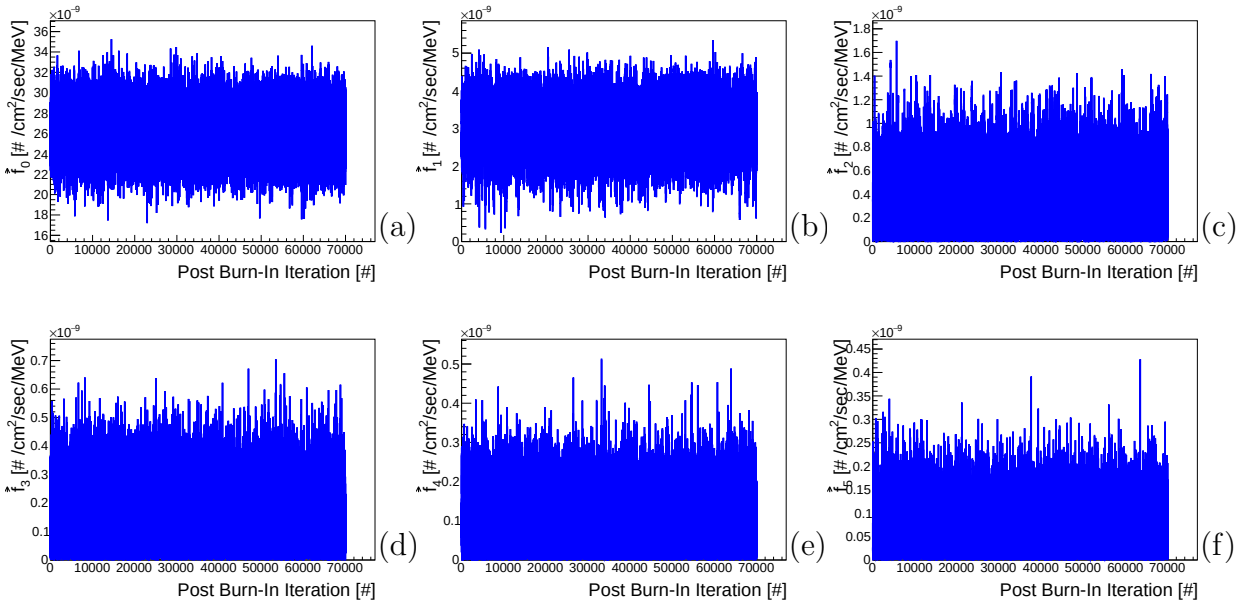

Figure H.11: The value of each basis spline coefficient as a function of the MCMC iteration post burn-in at the 1450 m.w.e. depth.

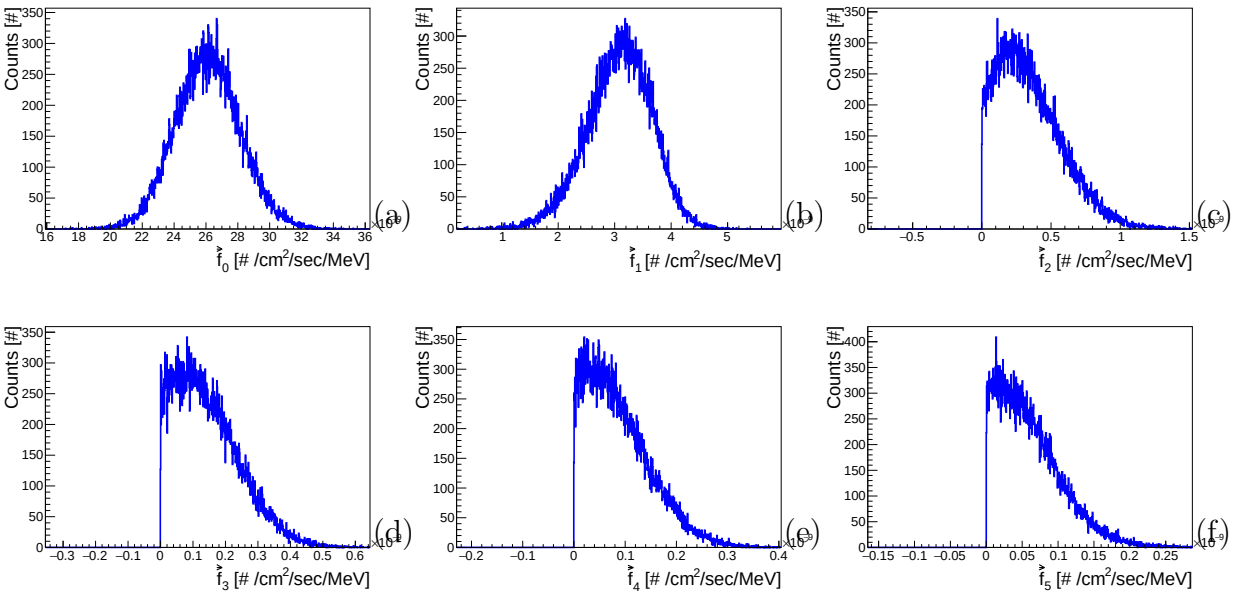

Figure H.12: The distribution of each basis spline coefficient at the 1450 m.w.e. depth.

Bibliography

[1] V.F. Hess. In: *Phys. Z.* 12 (1911), p. 998.

[2] V.F. Hess. In: *Wien. Sitz.-Ber.* 120 (1911), p. 1575.

[3] V.F. Hess. In: *Phys. Z.* 13 (1912), p. 1084.

[4] V.F. Hess. In: *Phys. Z.* 14 (1913), p. 610.

[5] L. H. Meredith et al. "Direct Detection of Soft Radiation above 50 Kilometers in the Auroral Zone". In: *Phys. Rev.* 97 (1 1955), pp. 201–205.

[6] W. Bothe and W. Kolhörster. "Das Wesen der Höhenstrahlung". In: *Zeitschrift fur Physik* 56 (Nov. 1929), pp. 751–777.

[7] M. Ambrosio et al. "The MACRO detector at Gran Sasso". In: *Nucl. Instr. Meth.* A486.3 (2002), pp. 663 –707.

[8] S.P. Ahlen et al. "Study of penetrating cosmic ray muons and search for large scale anisotropies at the Gran Sasso Laboratory". In: *Physics Letters B* 249.1 (1990), pp. 149 –156.

[9] T.J. Aucott. "Gamma-Ray Background Variability in Mobile Detectors ". PhD thesis. UC Berkeley: Nuclear Engineering, 2014.

[10] W.N. Hess et al. "Cosmic-Ray Neutron Energy Spectrum". In: *Phys. Rev.* 116 (2 1959), pp. 445–457.

[11] P. Goldhagen et al. "Measurement of the energy spectrum of cosmic-ray induced neutrons aboard an ER-2 high-altitude airplane". In: *Nucl. Instr. Meth.* A476.12 (2002), pp. 42 –51.

[12] J.F. Ziegler. "Terrestrial Cosmic Rays ". In: *IBM Journal of Research and Development* 40.1 (1996), pp. 19–39.

[13] L. Garrison. "Measurement of Neutron and Muon Fluxes 100 m Underground with the SciBath Detector". PhD thesis. Indiana U., Bloomington (main), 2014.

[14] A.S. Malgin et al. "High-Energy Hadrons Produced by Cosmic Ray Muons in the Earth as a Source of Background in Proton Decay Experiments". In: *JETP Lett.* 36 (1982), pp. 376–379.

[15] A.S. Malgin and O.G. Ryazhskaya. "Neutrons from Muons Underground". English. In: *Physics of Atomic Nuclei* 71.10 (2008), pp. 1769–1781.

[16] D. Mei and A. Hime. "Muon-Induced Background Study for Underground Laboratories". In: *Phys. Rev.* D73 (2006), p. 053004.

[17] D. S. Akerib et al. "Radiogenic and Muon-Induced Backgrounds in the LUX Dark Matter Detector". In: *Astropart. Phys.* 62 (2015), pp. 33–46.

[18] D. H. Hathaway, R. M. Wilson, and E. J. Reichmann. "The shape of the sunspot cycle". In: *Sol. Phys.* 151 (Apr. 1994), pp. 177–190.

[19] A. Bernstein et al. "Nuclear Security Applications of Antineutrino Detectors: Current Capabilities and Future Prospects". In: *Sci. Global Secur.* 18 (2010), pp. 127–192.

[20] M. J. Carson et al. In: *Astropart. Phys.* 21 (2004), pp. 667–687.

[21] M. S. Boswell et al. In: *Phys. Rev.* C87.6 (2013), p. 064607.

[22] Yu. V. Klimov et al. "Neutrino method remote measurement of reactor power and power output". In: *Atomic Energy* 76.2 (1994), pp. 123–127.

[23] N. S. Bowden et al. "Observation of the Isotopic Evolution of PWR Fuel Using an Antineutrino Detector". In: *J. Appl. Phys.* 105 (2009), p. 064902.

[24] S. Oguri et al. "Reactor antineutrino monitoring with a plastic scintillator array as a new safeguards method". In: *Nucl. Instrum. Meth.* A757 (2014), pp. 33–39.

[25] R. Wolf. In: *Acad. Sci. Comp. Rend.* 35 (1852), p. 704.

[26] *The Sunspot Cycle*. `http://solarscience.msfc.nasa.gov/SunspotCycle.shtml`. Accessed: 2016-07-25.

[27] J. C. Gosse and F. M. Phillips. "Terrestrial in situ cosmogenic nuclides: theory and application". In: *Quaternary Science Reviews* 20 (Aug. 2001), pp. 1475–1560.

[28] K. A. Olive et al. "Review of Particle Physics". In: *Chin. Phys.* C38 (2014), p. 090001.

[29] T. Araki et al. "Measurement of neutrino oscillation with KamLAND: Evidence of spectral distortion". In: *Phys. Rev. Lett.* 94 (2005), p. 081801.

[30] B. Schmidt et al. "Muon-induced background in the EDELWEISS dark matter search". In: *Astropart. Phys.* 44 (2013), pp. 28–39.

[31] M. Horn. "Simulations of the muon-induced neutron background of the EDELWEISS-II experiment for Dark Matter search ". PhD thesis. Universitat Karlsruhe (TH), 2007.

[32] S. Kamat. "Extending the Sensitivity to the Detection of WIMP Dark Matter with an Improved Understanding of the Limiting Nuetonr Backgrounds ". PhD thesis. Case Western Reserve University, 2005.

[33] Alfredo Ferrari et al. "FLUKA: A multi-particle transport code (Program version 2005)". In: (2005).

[34] T.T. Bhlen et al. "The {FLUKA} Code: Developments and Challenges for High Energy and Medical Applications". In: *Nuclear Data Sheets* 120.0 (2014), pp. 211 –214.

[35] S. R. Elliott. "The Majorana Project". In: *J. Phys. Conf. Ser.* 173 (2009), p. 012007.

[36] M.S. Boswell et al. "Neutron inelastic scattering in natural Cu as a background in neutrinoless double- decay experiments". In: *Phys. Rev.* C87.6 (2013), p. 064607.

[37] R.N. Silver. "The Los Alamos Neutron Scattering Center". In: *Physica B+C* 137.1 (1986), pp. 359 –372.

[38] R.L. Bramblett et al. "A new type of neutron spectrometer". In: *Nucl. Instr. Meth.* 9.1 (1960), pp. 1 –12.

[39] M.S. Gordon et al. "Measurement of the Flux and Energy Spectrum of Cosmic-Ray Induced Neutrons on the Ground". In: *IEEE Trans. Nucl. Sci.* 51.6 (2004), pp. 3427–3434.

[40] M. Reginatto and P. Goldhagen. "MAXED, A Computer Code For Maximum Entropy Deconvolution of Multisphere Neutron Spectrometer Data." In: *Health Physics* 77.5 (1999), pp. 579–583.

[41] E. B. Hughes and P. L. Marsden. "Response of a standard IGY neutron monitor". In: *Journal of Geophysical Research* 71.5 (1966), pp. 1435–1444.

[42] N. Mascarenhas et al. "Development of a Neutron Scatter Camera for Fission Neutrons". In: *2006 IEEE Nuclear Science Symposium Conference Record*. Vol. 1. 2006, pp. 185–188.

[43] T.J. Langford et al. "Fast neutron detection with a segmented spectrometer ". In: *Nucl. Instr. Meth.* A771.0 (2015), pp. 78 –87.

[44] C. Zhang and D.-M. Mei. "Measuring Muon-Induced Neutrons with Liquid Scintillation Detector at Soudan Mine". In: *Phys.Rev.* D90.12 (2014), p. 122003.

[45] J. D. Kinnison et al. "High-energy neutron spectroscopy with thick silicon detectors". In: *Radiat. Res.* 159.2 (2003), pp. 154–160.

[46] R. Hennings-Yeomans and D.S. Akerib. "A Neutron Multiplicity Meter for Deep Underground Muon-Induced High Energy Neutron Measurements". In: *Nucl. Instr. Meth.* A574 (2007), pp. 89–97.

[47] M. Sweany. "Characterization of Neutron Backgrounds for Direct Dark Matter Searches ". PhD thesis. University of California at Davis, 2011.

[48] S. Agostinelli et al. "Geant4 a Simulation Toolkit ". In: *Nucl. Instr. and Meth. A* 506.3 (2003), pp. 250 –303.

[49] J. Allison et al. "Geant4 developments and applications ". In: *IEEE Trans. Nucl. Sci.* 53.1 (2006), pp. 270–278.

[50] G.F. Knoll. *Radiation Detection and Measurement; 3rd ed.* New York, NY: Wiley, 2000.

[51] I. Fredholm. "Sur une classe d'équations fonctionnelles". In: *Acta Mathematica* 27.1 (1903), pp. 365–390.

[52] R. Penrose. "A Generalized Inverse for Matrices." In: *Proc. Cambridge Phil. Soc.* 51 (), pp. 406–413.

[53] E. Hewitt and R.E. Hewitt. "The Gibbs-Wilbraham phenomenon: An episode in fourier analysis". In: *Archive for History of Exact Sciences* 21.2 (1979), pp. 129–160.

[54] A.N. Tikhonov and V.Y. Arsenin. *Solutions of Ill-Posed Problems*. Winston, Washington, DC, 1977.

[55] N. Metropolis et al. "Equation of State Calculations by Fast Computing Machines". In: *J. Chem. Phys.* 21 (1953), pp. 1087–1092.

[56] W. K. Hastings. "Monte Carlo sampling methods using Markov chains and their applications". In: *Biometrika* 57.1 (1970), pp. 97–109.

[57] M. Kuusela and V. M. Panaretos. "Statistical unfolding of elementary particle spectra: Empirical Bayes estimation and bias-corrected uncertainty quantification". In: *ArXiv e-prints* (May 2015). arXiv: `1505.04768 [stat.AP]`.

[58] B. Efron and R. Tibshirani. *An Introduction to the Bootstrap*. Macmillan Publishers Limited. All rights reserved, 1993.

[59] C.D. Boor. *A Practical Guide to Splines*. New York: Springer Verlag, 1978.

[60] S. S. Saquib et al. "ML parameter estimation for Markov random fields with applications to Bayesian tomography". In: *IEEE Transactions on Image Processing* 7.7 (1998), pp. 1029–1044.

[61] *B133D01 Photomultiplier Tube*. `http://www.aditpmt.com/pmt-datasheets/B133D01W.pdf`. Accessed: 2015-06-30.

[62] *SIS3316 16 Channel VME Digitizer Family*. `http://www.struck.de/sis3316.html`. Accessed: 2015-06-30.

[63] *Technical Information Manual MOD. V1495 General Purpose VME Board*. `http://www.caen.it/servlet/checkCaenManualFile?Id=11043`. Accessed: 2015-09-30.

[64] R. Brun and F. Rademakers. "ROOT - An Object Oriented Data Analysis Framework". In: *Nucl. Instr. Meth.* A389 (1997), pp. 81–86.

[65] *Photomultiplier Tubes Basics and Applications*. `https://www.hamamatsu.com/resources/pdf/etd/PMT_handbook_v3aE.pdf`. Accessed: 2016-02-29.

[66] Norman E. Holden and Martin S. Zucker. "Prompt Neutron Multiplicities for the Transplutonium Nuclides ". In: *Radiation Effects* 96.1-4 (1986), pp. 289–292.

[67] E.T. Guarnaccia. "Modeling and Measurement of the Cosmic Muon Flux at Underground Sites". PhD thesis. Virginia Polytechnic Institute and State University, 2014.

[68] G. Horton-Smith. *Additional Gadolinium Support for GLG4sim*. `http://neutrino.phys.ksu.edu/~GLG4sim/Gd.html`. Accessed: 2015-07-08.

[69] B. Roeder. "Development and Validation of Neutron Detection Simulations for EURISOL ". In: *EURISOL Design Study* 3.0 (2008), pp. 31 –44.

[70] A. Chyzh et al. "Measurement of the ^{157}Gd(n,γ) reaction with the DANCE γ calorimeter array". In: *Phys. Rev. C* 84 (1 2011), p. 014306.

[71] P. Désesquelles et al. "Cross Talk and Diaphony in Neutron Detectors ". In: *Nucl. Inst. and Meth. A* 307.23 (1991), pp. 366 –373.

[72] R.A. Cecil et al. "Improved Predections of Neutron Detection Efficiency for Hydrocarbon Scintillators from 1 MeV to About 300 MeV ". In: *Nucl. Instr. and Meth.* 161.3 (1979), pp. 439 –447.

[73] A. Del Guerra. "A Compilation of n-p and n-C Cross Sections and Their Use in a Monte Carlo Program to Calculate the Neutron Detection Efficiency in Plastic Scintillator in the Energy Range 1-300 MeV ". In: *Nucl. Instr. and Meth.* 135.2 (1976), pp. 337 –352.

[74] Noriaki N. et al. "Absolute measurements of the response function of an NE213 organic liquid scintillator for the neutron energy range up to 206 MeV". In: *Nucl. Instr. Meth.* A463.12 (2001), pp. 275 –287.

[75] J.B. Birks, ed. *Front Matter*. International Series of Monographs in Electronics and Instrumentation. Pergamon, 1964, pp. iii –. ISBN: 978-0-08-010472-0.

[76] Zhang Jian-Fu et al. "Measurements of the light output functions of plastic scintillator using 9 Be(d, n) 10 B reaction neutron source". In: *Chinese Physics C* 34.7 (2010), p. 988.

[77] J.D. Sullivan. "Geometric factor and directional response of single and multi-element particle telescopes". In: *Nucl. Instr. Meth.* 95.1 (1971), pp. 5 –11.

[78] F. Ashton et al. "The spectrum of cosmic ray neutrons at sea level in the range 04-1.2 GeV". In: *J. Phys. A: Gen. Phys.* 4 (1971).

[79] J.A. Simpson. "cosmic-radiation neutron intensity monitor". In: *Annals of the IGY* 4 (1957), pp. 351–373.

[80] E. Heidbreder et al. "Measurements of the Distribution in Energy and Angle of High-Energy Neutrons in the Lower Atmosphere". In: *Journal of Geophysical Research* 76.13 (1971), pp. 2905–2916.

[81] A. M. Preszler et al. "Atmospheric Neutron Measurements in the 10-170 MeV Range". In: *Journal of Geophysical Research* 81.25 (1976), pp. 4715–4722.

[82] M.R. Moser et al. "Atmospheric Neutron Measurements in the 10-170 MeV Range". In: *29th International Cosmic Ray Conference Pune* 00 (2005), pp. 101–104.

[83] R. Saxena. "Ground Level Atmospheric Neutron Flux Measurements in the 10-170 MeV Range ". PhD thesis. University of New Hampshire, 1990.

[84] M. Conversi and P. Rothwell. "Angular Distributions in Cosmic Ray Stars at 3500 Meters". In: *Il Nuovo Cimento* 12.2 (1954), pp. 191–210.

[85] S. Miyake et al. "Cosmic Ray Nuclear Interactions in Nitrogen Gas". In: *Journal of the Physical Society of Japan* 12.8 (1957), pp. 845–854.

[86] *Web model / GeoMag-05.* `http://www.geomagsphere.org/data/vertical_cutoff_2004_table.dat`. Accessed: 2016-06-29.

[87] C. Hagmann et al. *Monte Carlo Simulation of Proton-Induced Cosmic-ray Cascades in the Atmosphere*. `http://nuclear.llnl.gov/simulation/doc_cry_v1.7/cry_physics.pdf`. Accessed: 2015-07-08.

[88] N.C. Barford and G. Davis. In: *Proc. Roy. Soc. Lond.* 214.225 (1952).

[89] E. Lohrmann. "Angular Distribution in Cosmic Ray Stars". In: *Il Nuovo Cimento* 1.6 (1955), pp. 1126–1140.

[90] C. Roecker et al. "Design of a transportable high efficiency fast neutron spectrometer ". In: *Nucl. Instr. Meth. A* 826.21 (2016).

[91] J. I. Collar et al. "Coherent neutrino-nucleus scattering detection with a CsI[Na] scintillator at the SNS spallation source ". In: *Nucl. Instr. Meth.* A773 (2014), p. 56.

[92] R. Hertenberger et al. "Muon-induced neutron and pion production in an organic liquid scintillator at a shallow depth". In: *Phys. Rev. C* 52 (6 1995), pp. 3449–3459.

[93] L.B. Bezrukov et al. In: *Sov. J. Nucl. Phys.* 17 (1983), p. 51.

[94] F. Boehm et al. "Neutron production by cosmic-ray muons at shallow depth". In: *Phys. Rev. D* 62 (9 2000), p. 092005.

[95] R.I. Enikeev et al. In: *Sov. J. Nucl. Phys.* 46 (1987), p. 883.

[96] M. Aglietta et al. "Study of single muons with the large volume detector at Gran Sasso laboratory". In: *Phys.Atom.Nucl.* 66 (2003), pp. 123–129.

[97] M. Aglietta et al. "Neutron flux generated by cosmic-ray mouns at 5200 hg/cm2 s.r. underground. Depth-neutron intensity curve". In: *Il Nuovo Cimento C* 12.4 (1989), pp. 467–477.

[98] S. Abe et al. "Production of radioactive isotopes through cosmic muon spallation in KamLAND". In: *Phys. Rev. C* 81 (2 2010), p. 025807.

[99] V. Chazal et al. "Investigations of Fast Neutron Production by 190!GeV/c Muon Interactions on Graphite Target". In: *Nucl. Instr. Meth.* A490 (2002), pp. 334–343.

[100] Y.F. Wang et al. "Predicting neutron production from cosmic ray muons". In: *Phys.Rev.* D64 (2001), p. 013012.

[101] L. Reichhart et al. "Measurement and simulation of the muon-induced neutron yield in lead". In: *Astroparticle Physics* 47.0 (2013), pp. 67 –76.

[102] A. Empl et al. "A Fluka study of underground cosmogenic neutron production". In: *Journal of Cosmology and Astroparticle Physics* 2014.08 (2014), p. 064.

[103] A. Empl et al. "Study of Cosmogenic Neutron Backgrounds at LNGS". In: (2012). arXiv: 1210.2708 [astro-ph.IM].

[104] G. Bellini et al. "Cosmogenic Backgrounds in Borexino at 3800 m water-equivalent depth". In: *Journal of Cosmology and Astroparticle Physics* 2013.08 (2013), p. 049. URL: http://stacks.iop.org/1475-7516/2013/i=08/a=049.

[105] M.G. Marino et al. "Validation of spallation neutron production and propagation within Geant4". In: *Nucl. Instr. Meth.* A582.2 (2007), pp. 611 –620.

[106] J.A. Formaggio and C.J. Martoff. "Backgrounds to Sensitive Experiments Underground". In: *Annual Review of Nuclear and Particle Science* 54.1 (2004), pp. 361–412.

[107] *Kimballton Underground Research Facility*. http://www.phys.vt.edu/~kimballton/kurf/pub/w.shtml?home. Accessed: 2016-06-29.

[108] J. Kiener et al. "Fast-neutron induced background in LaBr3:Ce detectors ". In: *Nucl. Instr. Meth. A* 798 (2015), pp. 152 –161.

[109] R.T. Kouzes et al. "Cosmic-ray-induced ship-effect neutron measurements and implications for cargo scanning at borders ". In: *Nucl. Instr. Meth. A* 587.1 (2008), pp. 89–100.

[110] S. Dazeley et al. "A search for cosmogenic production of -neutron emitting radionuclides in water". In: *Nucl. Instrum. Meth.* A821 (2016), pp. 151–159.

[111] H. Berns et al. "The CAPTAIN Detector and Physics Program". In: *Community Summer Study 2013: Snowmass on the Mississippi (CSS2013) Minneapolis, MN, USA, July 29-August 6, 2013*. 2013.

[112] E.A. Burgett. "A broad spectrum neutron spectrometer utilizing a high energy Bonner sphere extension". MA thesis. Georgia Institute of Technology, 2008.

[113] D. Reyna. "A Simple Parameterization of the Cosmic-Ray Muon Momentum Spectra at the Surface as a Function of Zenith Angle ". In: (2006). arXiv: hep-ph/0604145 [hep-ph].

[114] L.N. Kalusis et al. "Cosmic muon flux measurements at the Kimballton Underground Research Facility". In: *Journal of Instrumentation* 9.08 (2014), P08010.

[115] T. Möller and B. Trumbore. "Fast, Minimum Storage Ray-triangle Intersection". In: *J. Graph. Tools* 2.1 (Oct. 1997), pp. 21–28.